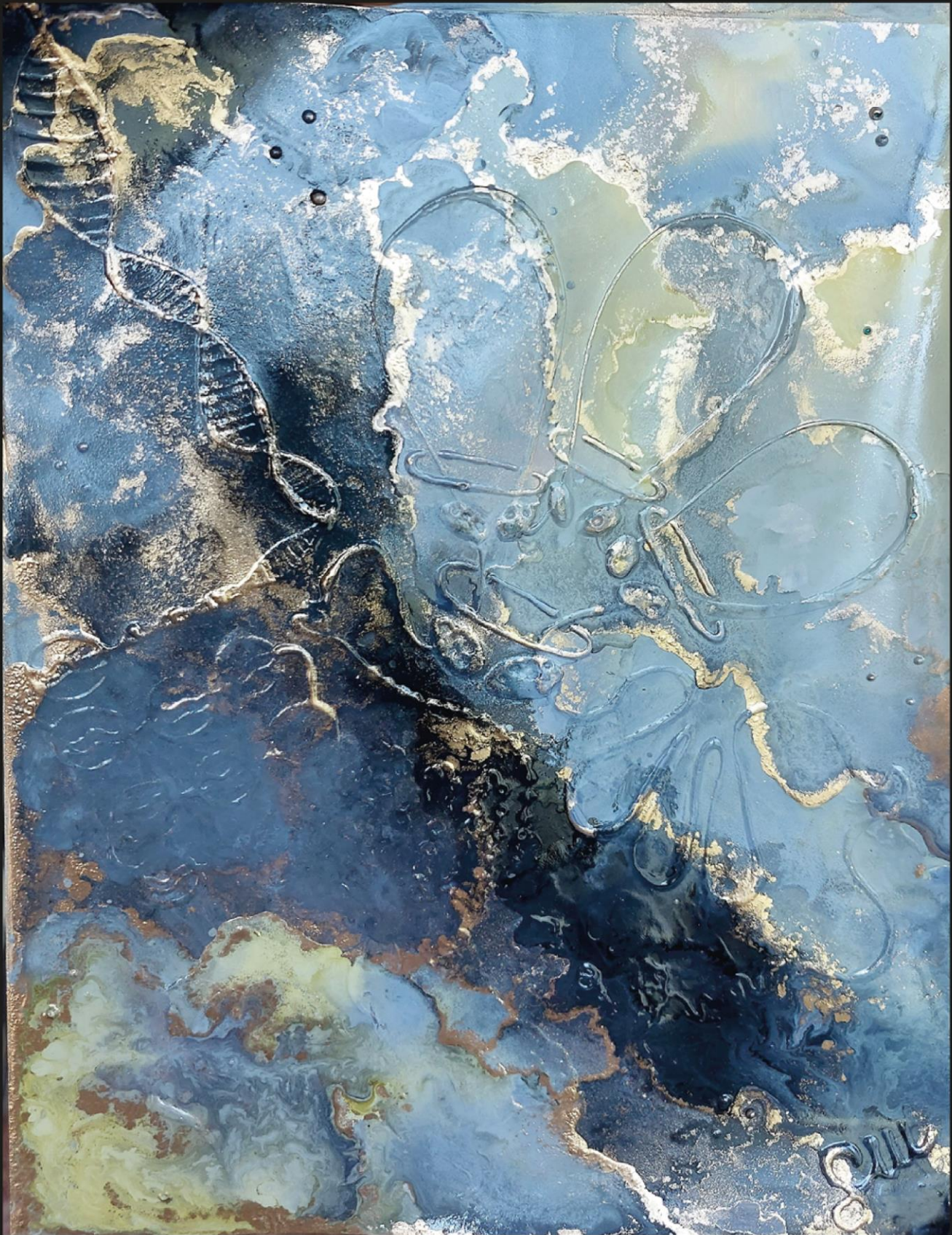


Interplay of DNA replication, repair and chromatin: structure versus function

Stefania Mamberti



Interplay of DNA replication, repair and chromatin: structure versus function

Zusammenspiel von DNA Replikation, Reparatur und Chromatin: Struktur versus Funktion



Dem Fachbereich Biologie der Technischen Universität Darmstadt
zur Erlangung des akademischen Grades
Doctor rerum naturalium
vorgelegte Dissertation von

Stefania Mamberti
M. Sc. in Molecular Biology and Genetics
aus Como, Italien

1. Referentin: Prof. Dr. M. Cristina Cardoso
2. Referent: Prof. Dr. Burkhard Jakob

Darmstadt 2022

Interplay of DNA replication, repair and chromatin: structure versus function
Zusammenspiel von DNA Replikation, Reparatur und Chromatin: Struktur versus Funktion
Genehmigte Dissertation von Mamberti Stefania, M.Sc. aus Como, Italien
1. Referent/Referentin: Prof. Dr. M. Cristina Cardoso
2. Referent/Referentin: Prof. Dr. Burkhard Jakob
Darmstadt, Technische Universität Darmstadt
Jahr der Veröffentlichung der Dissertation auf TUprints: 2023
URN: urn:nbn:de:tuda-tuprints-230395
URL: <https://tuprints.ulb.tu-darmstadt.de/id/eprint/23039>
Tag der Einreichung: 06.10.2022
Tag der mündlichen Prüfung: 13.12.2022
Veröffentlicht unter CC BY-SA 4.0 International
<https://creativecommons.org/licenses/>

“One of the basic rules of the universe is that nothing is perfect.

Perfection simply doesn't exist.

*Without imperfection,
neither you nor I would exist.”*

Stephen Hawking

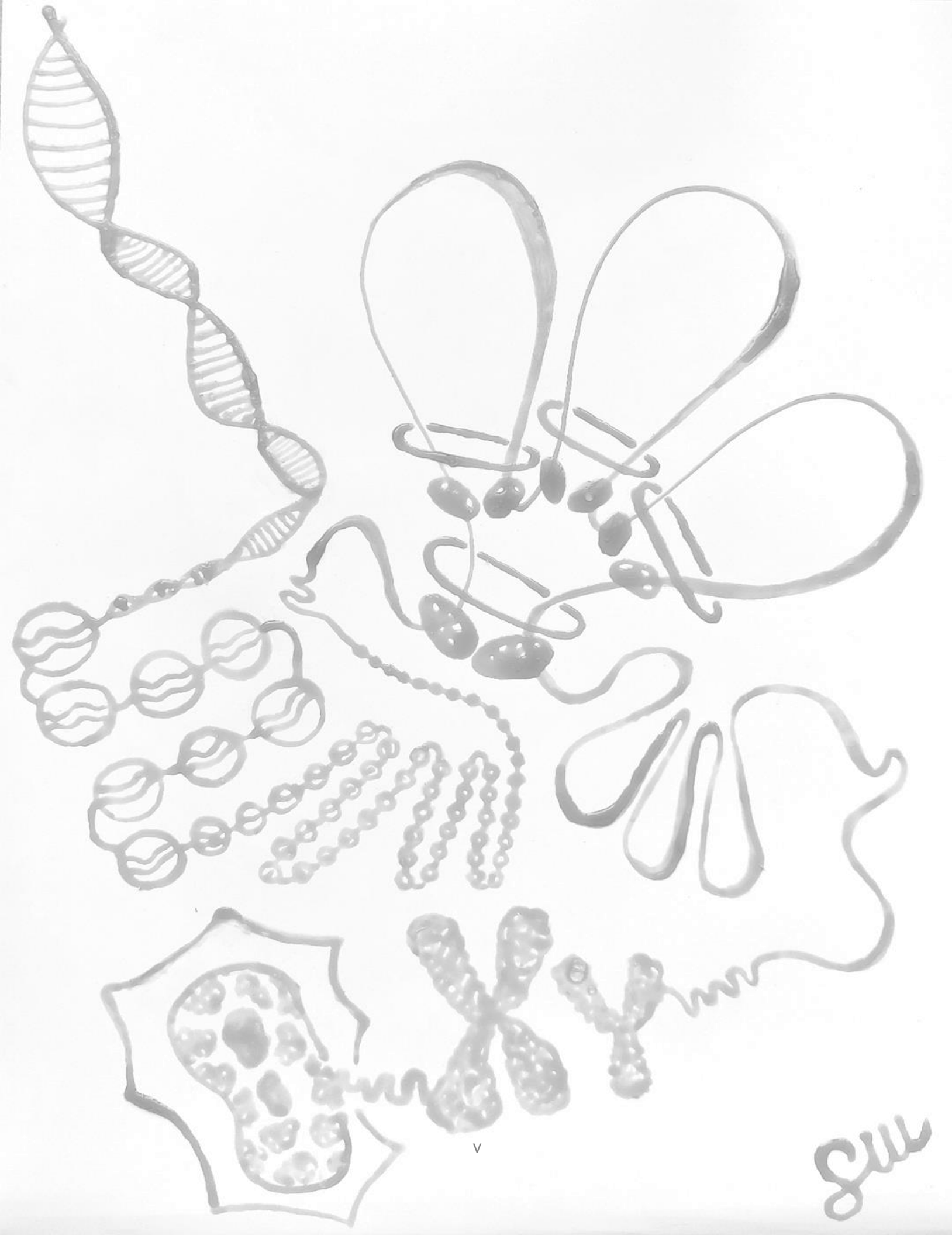
The abstract painting shown on the cover page is a free representation of the nucleoplasm, the complex liquid environment enclosed within the nuclear envelope, composed of water, ions, various molecules and enzymes.

This nucleoplasm painting made with alcohol inks actually covers a hidden drawing.

By tilting the painting towards light by different angles, the reflection unveils the three-dimensional folding of a double helix of DNA within a mammalian nucleus. The DNA molecule wraps around core histones and several nucleosomes line up as “beads on a string”. These beads then fold up in chromatin loops, which get extruded by the cohesin ring until reaching couples of convergent CTCF molecules at their anchors. Different loops get nested into larger chromatin domains and further fold into X, Y and the various somatic chromosomes, which eventually occupy distinct chromosome territories within the nucleus of a cell.

As the drawing is present within the painting but hidden by the alcohol ink on top of it, the molecules and mechanisms regulating DNA functions and ultimately governing the fate of a cell are enclosed within the nucleus and invisible to the naked eye. By the use of microscopy and different techniques, we are slowly uncovering the folding principles of the mammalian genome.

To unveil the three-dimensional drawing hidden within the painting, we need to tilt the painting by various degrees and achieve the correct reflection to light up each of the different parts of this drawing. In the same way, we need to design new methods and to further develop the existing ones to light up the different mechanisms regulating the various facets of genomic functions and ultimately achieve the full sight of the nuclear drawing that is hidden within our cells.



v

ms

Preface

The present work is aimed at investigating the relationship between chromatin structure and the genomic functions that allow the proper maintenance of the eukaryotic DNA within mammalian nuclei. The main representatives of these functions are the replication of the genome and its repair upon damage.

The present thesis starts with a general introductory chapter that defines the characteristics of chromatin architecture, DNA replication and repair units (based upon: Mamberti and Cardoso, 2020). In recent years, increasing evidence has highlighted the architectural proteins CTCF and cohesin as the major players in chromatin loop extrusion and in the definition of chromatin domains. The next two thesis chapters are therefore dedicated to each of these two proteins and their influence on the interrelationship between chromatin structural and functional units (parts thereof based upon: Cremer *et al.*, 2020; Mamberti *et al.*, 2022). Each chapter contains separate sections of introduction, results, discussion, material and methods. The thesis ends with a general discussion (parts of it based upon: Mamberti and Cardoso, 2020), followed by conclusions and outlook.

Summary

Hierarchical levels of chromatin organization allow different genomic functions to be spatio-temporally regulated within mammalian nuclei. Both DNA replication and DNA repair are global genomic processes. Their chromatin units have remarkable structural similarities and microscopically appear as clusters of nanofocal structures, each in the size range of chromatin loops. The present work aimed at relating genomic functions with the underlying structural organization by the two chromatin architectural proteins CTCF and cohesin, which cooperate to shape the genome into chromatin loops and domains.

Here, CTCF was shown to be critical for cellular survival after ionizing irradiation in a CTCF-dose dependent way. The results obtained in different cell lines upon CTCF-depletion were integrated into a biophysical model. The decreased clonogenic potential showed to derive from the increased probability of double strand breaks to cluster in larger chromatin domains lacking CTCF at their borders.

Moreover, CTCF proved to be enriched at the sites and at the time of DNA replication. CTCF intensity within replication foci was shown to decrease over a chase time after replication labeling, suggesting the occurrence of CTCF accumulation during ongoing DNA replication. The depletion of CTCF correlated with an impairment in cell cycle progression. CTCF-depleted cells stalled in G1 in a CTCF-dose dependent way, indicating that the chromatin structure provided by CTCF might be needed to properly enter S-phase. Additionally, CTCF resulted to be particularly enriched at the replicating inactive X and Y chromosomes. The depletion of CTCF led to the loss of synchrony in the DNA replication of the Y chromosome. Additionally, Y chromosome architecture showed changes of volume and shape upon CTCF reduction.

In the second part of this work, the cohesin subunit RAD21 was shown essential to determine the structure of chromatin loops. RAD21-depleted cells exhibited an increase in the size and shape heterogeneity of chromatin loops. The cohesin component SA1 was investigated for a role in DNA damage signaling. SA1 KO cells showed an impairment of the γ H2AX foci at all tested X-ray doses. The repair functional units decreased in number, volume and intensity in the absence of SA1.

In conclusion, the results presented here led to propose that the functions of DNA replication and repair are determined by the chromatin architecture, with the structure dictating the function.

Future work should further investigate the mechanisms behind the regulation of global genomic functions by these two chromatin architectural proteins and define the precise interplay between cohesin and CTCF within such regulation.

Zusammenfassung

Hierarchische Ebenen der Chromatinorganisation ermöglichen die räumlich-zeitliche Regulation verschiedener genomischer Funktionen in den Zellkernen von Säugetieren. Sowohl die DNA-Replikation als auch die DNA-Reparatur sind globale genomische Prozesse. Ihre Chromatineinheiten weisen bemerkenswerte strukturelle Ähnlichkeiten auf und erscheinen mikroskopisch als Cluster von nanofokalen Strukturen, die jeweils in der Größenordnung von Chromatinschleifen liegen. Ziel der vorliegenden Arbeit war es, die Genomfunktionen mit der zugrundeliegenden strukturellen Organisation durch die beiden Chromatinarchitekturproteine CTCF und Cohesin in Beziehung zu setzen, die zusammenarbeiten, um das Genom in Chromatinschleifen und Domänen zu formen.

Hier wurde gezeigt, dass CTCF dosisabhängig für das zelluläre Überleben nach ionisierender Bestrahlung entscheidend ist. Die Ergebnisse der CTCF-Depletion in verschiedenen Zelllinien wurden in ein biophysikalisches Modell integriert. Es zeigte sich, dass das verringerte klonogene Potenzial auf die erhöhte Wahrscheinlichkeit von DNA-Doppelstrangbrüchen zurückzuführen ist, die sich in größeren Chromatindomänen ohne CTCF an deren Rändern zusammenballen.

Außerdem erwies sich CTCF an den Stellen und zum Zeitpunkt der DNA-Replikation als angereichert. Es zeigte sich, dass die CTCF-Intensität innerhalb von Replikations-Foci nach der Replikationsmarkierung über eine Verfolgungszeit abnimmt, was auf eine CTCF-Akkumulation während der laufenden DNA-Replikation hindeutet. Die Verringerung von CTCF korrelierte mit einer Beeinträchtigung der Zellzyklusprogression. CTCF-depletierte Zellen verharrten CTCF-dosisabhängig in der G1 Phase, was darauf hindeutet, dass die von CTCF bereitgestellte Chromatinstruktur für den korrekten Eintritt in die S-Phase erforderlich sein könnte. Außerdem erwies sich CTCF als besonders angereichert an den replizierenden inaktiven X- und Y-Chromosomen. Die Verminderung von CTCF führte zu einem Verlust der Synchronität bei der DNA-Replikation des Y-Chromosoms. Außerdem veränderte sich die Architektur des Y-Chromosoms durch die Verringerung von CTCF in Bezug auf Volumen und Form.

Im zweiten Teil dieser Arbeit wurde gezeigt, dass die Cohesin-Untereinheit RAD21 für die Struktur der Chromatinschleifen entscheidend ist. RAD21-depletierte Zellen wiesen eine Zunahme der Größe und Formheterogenität von Chromatinschleifen auf. Die Cohesin-Komponente SA1 wurde auf ihre Rolle bei der Signalisierung von DNA-Schäden untersucht. SA1 KO-Zellen zeigten bei allen getesteten Röntgendosen eine Beeinträchtigung von γ H2AX. Die funktionalen Reparatereinheiten nahmen in Abwesenheit von SA1 in Anzahl, Volumen und Intensität ab.

Die hier vorgestellten Ergebnisse lassen den Schluss zu, dass die Funktion der DNA-Replikation und -Reparatur durch die Chromatinarchitektur bestimmt wird, wobei die Struktur die Funktion bestimmt.

Zukünftige Arbeiten sollten die Mechanismen hinter der Regulierung globaler genomischer Funktionen durch diese beiden Proteine der Chromatinarchitektur weiter untersuchen und das genaue Zusammenspiel zwischen Cohesin und CTCF innerhalb dieser Regulierung definieren.

Contents

| | |
|---|------|
| Preface | vi |
| Summary | vii |
| Zusammenfassung | viii |
| 1. General introduction | 1 |
| 1.1. Chromatin organization of the eukaryotic genome | 1 |
| 1.1.1. DNA loops..... | 1 |
| 1.1.2. A/B compartments..... | 5 |
| 1.1.3. Topologically associated domains | 5 |
| 1.1.4. Loop domains | 6 |
| 1.2. The chromatin architectural proteins CTCF and cohesin | 6 |
| 1.2.1. Effects of CTCF and cohesin depletion on chromatin | 8 |
| 1.3. Modeling of chromatin organization | 9 |
| 1.4. Global genomic processes: function versus structure | 11 |
| 1.4.1. DNA replication units..... | 12 |
| 1.4.2. Modeling of DNA replication | 16 |
| 1.4.3. DNA repair units..... | 16 |
| 2. Aims | 18 |
| 3. CTCF participates in defining the structural units of DNA repair and replication | 19 |
| 3.1. CTCF is critical for cellular survival upon ionizing radiation | 19 |
| 3.1.1. Introduction..... | 19 |
| 3.1.2. Results | 22 |
| 3.1.2.1. Validation of the genome size, CTCF basal levels and binding in different cancer cell lines..... | 22 |
| 3.1.2.2. CTCF knockdown and validation in different cancer cell lines | 24 |
| 3.1.2.3. CTCF depletion increases the radiosensitivity of cancer cells in a cell line dependent way | 26 |
| 3.1.2.4. GLOBLE model investigates the impact of DSB clustering in chromatin domains on cell kill | 28 |
| 3.1.2.5. CTCF effect on radiosensitivity is observed in mouse ES cells | |

| | |
|--|-----------|
| also and is CTCF dose-dependent..... | 30 |
| 3.1.3. Discussion..... | 35 |
| 3.1.4. Materials and Methods..... | 40 |
| 3.1.4.1. Cell culture..... | 40 |
| 3.1.4.2. CTCF knockdown..... | 41 |
| 3.1.4.3. CTCF immunostaining..... | 42 |
| 3.1.4.4. Microscopy imaging and quantification..... | 42 |
| 3.1.4.5. Clonogenic assay..... | 42 |
| 3.1.4.6. Modeling of cell survival using the Giant-Loop Binary Lesion (GLOBLE) model..... | 43 |
| 3.2. CTCF plays a role in DNA replication: a seXY hypothesis..... | 45 |
| 3.2.1. Introduction..... | 45 |
| 3.2.2. Results..... | 50 |
| 3.2.2.1. CTCF is enriched at the time and at the sites of DNA replication..... | 50 |
| 3.2.2.2. CTCF depletion affects cell cycle and S-phase progression..... | 52 |
| 3.2.2.3. CTCF is enriched at the replicating Xi and Y chromosomes and is necessary to maintain the synchrony of Y chromosome replication..... | 54 |
| 3.2.3. Discussion..... | 58 |
| 3.2.4. Material and methods..... | 63 |
| 3.2.4.1. Cell culture..... | 63 |
| 3.2.4.2. CTCF knock down..... | 63 |
| 3.2.4.3. EdU pulse labeling..... | 63 |
| 3.2.4.4. EdU detection, CTCF immunostaining and sex chromosomes FISH..... | 64 |
| 3.2.4.5. Microscopy imaging and analysis..... | 65 |
| 4. Cohesin is required to organize chromatin and DNA repair units..... | 68 |
| 4.1. Introduction..... | 68 |
| 4.2. Results..... | 79 |
| 4.2.1. RAD21 depletion and quantitation in HCT116-RAD21-mAC cells..... | 79 |
| 4.2.2. RAD21-depleted HCT116 cells display up to ten fold larger DNA loops..... | 79 |
| 4.2.3. Validation of SA1 KO in iMEF cells..... | 81 |
| 4.2.4. DNA damage signaling after ionizing radiation is impaired in | |

| | |
|--|------------|
| SA1 KO iMEF cells | 83 |
| 4.3. Discussion..... | 86 |
| 4.4. Material and Methods..... | 92 |
| 4.4.1. Cell culture..... | 92 |
| 4.4.2. RAD21 depletion in HCT116-RAD21-mAC cells | 92 |
| 4.4.3. DNA halo preparation | 92 |
| 4.4.4. X-rays irradiation of SA1 WT and SA1 KO iMEF cells..... | 93 |
| 4.4.5. RAD21 detection, SA1 and γ H2AX immunostaining | 93 |
| 4.4.6. Microscopy imaging and analysis | 94 |
| 5. General discussion | 96 |
| 6. Conclusions and outlook..... | 102 |
| 7. References..... | 104 |
| 8. Supplementary Material | 136 |
| 8.1. Supplementary figures..... | 136 |
| 8.2. Supplementary tables..... | 151 |
| 9. Annex | 170 |
| 9.1. List of abbreviations | 170 |
| 9.2. List of figures | 174 |
| 9.3. List of tables | 176 |
| 9.4. Declaration - Ehrenwörtliche Erklärung..... | 177 |
| 9.5. Own and external contributions..... | 177 |
| 9.6. Acknowledgements..... | 178 |
| 9.7. <i>Curriculum vitae</i> | 180 |

1. General introduction

1.1. Chromatin organization of the eukaryotic genome

The biggest polymer in cells happens to be DNA and the least is known about its structure and how this relates to its function.

In recent years, the 4D Nucleome program (4D Nucleome web portal: <https://www.4dnucleome.org>) was founded exactly to tackle the issue of how the genome is folded in three-dimensions, how this dynamically changes in time (the fourth dimension) and which are the functional consequences of such folding (Marti-Renom *et al.*, 2018; Tashiro and Lanctôt, 2015). It is also known for quite some time that genomic processes occur within discrete subnuclear sites. However, whether the structure of these sites is determined by or rather determines DNA metabolism remains to be elucidated. The major hallmarks of chromatin folding are depicted in Figure 1.1.

Indeed, in the last decades, a variety of methods have been developed towards unraveling how DNA is organized within the nucleus. These include: light and electron microscopy based approaches (e.g., Nishino *et al.*, 2012; Ou *et al.*, 2017; Ricci *et al.*, 2015), DNA metabolism-based techniques such as the incorporation and detection of nucleosides' analogues (reviewed in: Miron *et al.*, 2016), DNA halo visualization (e.g., Vogelstein *et al.*, 1980), fluorescent *in situ* hybridization (FISH) (e.g., Pinkel *et al.*, 1988), chromosome conformation capture (3C) based methods (Dekker *et al.*, 2002; reviewed in: Barutcu *et al.*, 2016) and polymer modeling (reviewed in: Nicodemi and Pombo, 2014; Tark-Dame *et al.*, 2011).

Here, the recent discoveries from our laboratory on the structural organization of chromatin units of the global genomic processes of DNA replication and repair (Chagin *et al.*, 2016; Löb *et al.*, 2016; Natale *et al.*, 2017) are presented in light of the interplay between genome structure and function.

1.1.1. DNA loops

A variety of studies investigating how genomic DNA is folded over multiple decades are listed in Table 1.1., the timeline Figure 1.2. and discussed below.

In 1976, Cook, Brazell & Jost proposed the involvement of loops in the superhelical organization of the genome, meant as organization level above the double helix (Cook *et al.*, 1976). They prepared nucleoids from human HeLa cells with a lysis solution containing a non-ionic detergent and variable concentrations of salt, up to a saturating level, thus depleting histones. Based on sedimentation ratios of these nucleoids through sucrose gradients containing the intercalating DNA dye ethidium bromide, they were able to deduce their DNA conformation. They did not observe any effect of the non-ionic

detergent and saturating concentration of salt (conditions that removed most chromatin proteins including histones) in the migration of the nucleoids through the gradient. Therefore, they concluded that additional constraints existed, which kept the superhelical organization of the DNA duplex intact.

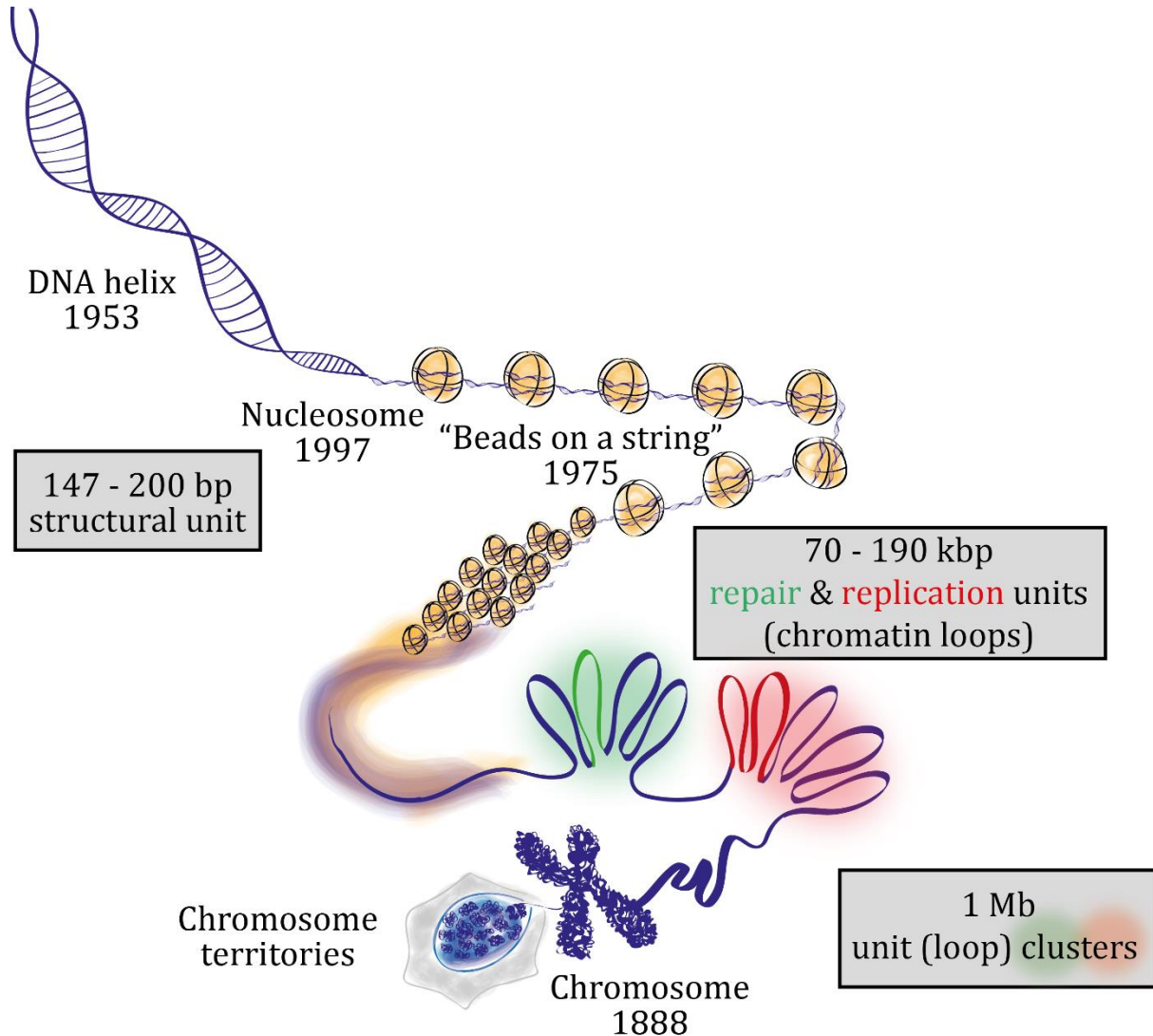


Figure 1.1. Hierarchical folding of DNA through chromatin organization and major hallmarks. The DNA helix is wrapped around an octamer of positively charged histones to form the nucleosome, with a DNA content of 147 bp. Multiple nucleosomes form the so-called "beads on a string" structure, which folds further into chromatin loops. The size of these loops corresponds to the one of functional units as measured with high resolution microscopy and DNA combing techniques, namely 75 kbp-sized DNA repair nano-foci and 190 kbp-sized DNA replication units. Clusters of these units build up Mb-sized domains as those observed relative to these genomic functions at lower resolution wide-field microscopy.

The year after, 1977, Paulson and Laemmli used electron microscopy to study histone-depleted metaphase chromosomes, obtained by treating purified HeLa cells chromosomes with dextran sulfate and heparin (Paulson and Laemmli, 1977). They showed that most of the DNA existed in loops of at least 10-30 μm , appearing as a halo, held together by a scaffold of non-histone proteins, or core, shaped characteristically as a metaphase chromosome. Assuming that 1 μm of DNA would equal 3000 base pairs (Chow *et al.*, 1975), they calculated a DNA content of 30-90 kb per loop. They proposed that their measurements might be underestimates, due to the fact that some DNA may not have been completely unfolded and to the observation that a few loops were longer than 60 μm . However, they pointed out that similar loop sizes were observed in *E. coli* (Kavenoff and Ryder, 1976) and from sedimentation studies of eukaryotic interphase cell nuclei (Benyajati and Worcel, 1976; Cook and Brazell, 1975). They also highlighted the fact that, in a separate study, they could demonstrate that the scaffold could be isolated as an entity independent of DNA, by treating the chromosomes with micrococcal nuclease before depleting them of histones (Adolph *et al.*, 1977b, 1977a), suggesting that non-histone proteins are responsible for the higher order organization of eukaryotic chromatin.

In 1980, Vogelstein and colleagues first applied the DNA halo technique, which allows to visualize a fluorescent halo made of DNA loops extruded from an insoluble nuclear scaffold, after treating the cells with a non-ionic detergent and dehistonizing the nuclei in the presence of a DNA-intercalating dye (Vogelstein *et al.*, 1980). They measured intact loops with an average size of 90 kb from mouse cells. They concluded that loops were attached to a skeleton kind of nuclear matrix, appearing as an insoluble, structural framework, and could be unwound by nicking the DNA with DNase I or exposing the samples to UV light (Vogelstein *et al.*, 1980). Moreover, they further identified a relationship between DNA loops and replication, as discussed in section 1.4.1.

In 1982, Buongiorno-Nardelli and colleagues observed with the same technique an average loop size of 90 kb (maximum halo radius of 15 μm) for frog cells (Buongiorno-Nardelli *et al.*, 1982). They also plotted the loop sizes for different species versus the respective replicon sizes, as measured by various groups, and hypothesized a relationship between loop and replicon sizes (Buongiorno-Nardelli *et al.*, 1982), which will be further discussed later.

In 1983, Earnshaw and Laemmli developed a method to isolate and deposit intact mitotic chromosomes on electron microscopy grids and measured radial loop sizes of 83 kb \pm 29 kb in human metaphase chromosome preparations (Earnshaw and Laemmli, 1983). They additionally isolated the protein scaffold from where the loops emanated and established their reversible aggregation upon treatment with high levels of Mg^{++} or NaCl (Earnshaw and Laemmli, 1983).

Table 1.1. Sizes of structural chromatin units measured with different methods.

| | Reference | Year | Method | Nomenclature/ Structure | Organism (cell line) | Median/ mean size | Size range |
|------------------------------------|-----------------------------------|---------|--|-----------------------------|--|----------------------|-------------------------|
| Structure | Paulson and Laemmli | 1977 | Histone-depleted metaphase chromosomes | Loop | Human (HeLa) | 70 kb | 30 - 90 kb |
| | Vogelstein, Pardoll & Coffey | 1980 | DNA Halo technique | Loop | Mouse (3T3) | 90 kb | 84 - 96 kb |
| | Buongiorno-Nardelli <i>et al.</i> | 1982 | Halo technique | Loop | Frog (<i>X. laevis</i> erythrocytes and kidney cells) | 90 kb | - |
| | Earnshaw and Laemmli | 1983 | Metaphase chromosome | Loop | Human (HeLa) | 83 kb | +/- 29 kb |
| | Jackson, Dickinson and Cook | 1990 | Nuclease digestion and electrophoresis | Loop | Human (HeLa) | 86 kb | 5 - 200 kb (80 - 90 kb) |
| | Lieberman-Aiden <i>et al.</i> | 2009 | Hi-C | Megadomains | Human (GM06990) | - | 5 Mb - 20 Mb |
| | | | | A/B compartments | | - | 500 kb - 7 Mb |
| | Dixon <i>et al.</i> | 2012 | Hi-C | TADs | Mouse (mESCs) | 880 kb | 100 kb - 5 Mb |
| | Rao <i>et al.</i> | 2014 | Hi-C | Loop domains | Human and mouse cell lines | 185 kb | 40 kb - 3 Mb |
| | Gibcus <i>et al.</i> | 2018 | Hi-C combined with polymer simulation | Inner loops in prophase | Chicken (DT-40) | 60 kb | - |
| | | | | Inner loops in prometaphase | | 80 kb | - |
| Nested outer loops in prometaphase | | | | 400 kb | | - | |
| Hsieh <i>et al.</i> | 2019 | Micro-C | MicroTADs | Mouse (mESCs) | 5.4 kb | 1 - 40 kb | |

After ten years of speculation on the existence of the loop organization of DNA, Jackson and colleagues tackled the issue by isolating chromatin from HeLa cells and embedding it in agarose under physiological buffer conditions to avoid any artifact (Jackson *et al.*, 1990a). They could indeed show that some loops may arise as artifacts from nuclei, nucleoids and scaffolds preparation, but they were also able to show that loops ranged from 5 to 200 kb and averaged on a size of 86 kb throughout the cell cycle (Jackson *et al.*, 1990a). Though not observing any size change between mitosis, G₁ and S-phase, they proposed that loops could still be dynamic structures, which were not detectable by

the assay used. They also fitted the data to a standard curve and obtained an average of 118 kb (Jackson *et al.*, 1990a). In a subsequent work (Jackson *et al.*, 1990b), they investigated loop sizes further with the physiological lysis method and using electroelution after restriction enzyme DNA digestion. Probing different enzymes and levels of detachment, they could reproducibly observe a size range of 80-90 kb (Jackson *et al.*, 1990b). Moreover, they observed that attachment of loops to the nucleoskeleton was very stable and measured that fragments of about 1 kb remained protected from nuclease attack (Jackson *et al.*, 1990b).

1.1.2. A/B compartments

In 2002, Dekker and colleagues developed a technique to unravel the chromatin structure through the frequency of contacts between different genomic sites, by ligation of these sites and following detection by quantitative PCR reactions (Dekker *et al.*, 2002). This technique of capturing chromosome conformation was subsequently subjected to a variety of improvements and modifications (reviewed in: Barutcu *et al.*, 2016).

In particular, the method was further developed into Hi-C or high-throughput chromosome conformation capture in 2009 by Lieberman-Aiden *et al.*, by combining proximity-based ligation with massively parallel sequencing (van Berkum *et al.*, 2010; Lieberman-Aiden *et al.*, 2009). They applied Hi-C at a 1 Mb resolution to identify “megadomains” of 5-20 Mb, which were further subdivided into 500 kb – 7 Mb sized domains corresponding to the “A” or active compartment, enriched for open chromatin, and the “B” or inactive compartment, enriched for closed chromatin, which together created the plaid pattern in the contacts’ matrices (Lieberman-Aiden *et al.*, 2009).

1.1.3. Topologically associated domains

In 2012, Dixon and colleagues introduced the concept of topologically associated domains (TADs) as largely species- and cell type-conserved megabase-sized domains, which correlated with the constraints of heterochromatic regions and whose boundaries are enriched for the insulator protein CTCF, housekeeping genes, transfer RNAs and SINE retrotransposon elements (Dixon *et al.*, 2012). They observed highly self-interacting regions at a bin size of less than 100 kb (Dixon *et al.*, 2012). In mouse embryonic stem cells, they found 2200 TADs with a median size of 880 kb, occupying 91% of the sequenced genome. Most of these TADs were shared across evolution, with more than 50% of genome boundaries that were found in mice, being present also in humans and vice versa (Dixon *et al.*, 2012). They showed that TADs were related to, but independent from, previously described organization structures such as the A/B or active/inactive compartments (Lieberman-Aiden *et al.*, 2009), the LAD/non-LAD or lamina-associated/not associated domains (Guelen *et al.*, 2008; Peric-

Hupkes *et al.*, 2010), and the early/late replicating domains (Ryba *et al.*, 2010). They further reported that CTCF alone is insufficient to determine TADs boundaries, being that the binding of this protein was found enriched at most boundaries but only 15% of its binding sites were located within these boundaries (Dixon *et al.*, 2012).

In 2015, Hsieh and colleagues introduced Micro-C, a novel Hi-C method with nucleosome resolution, in which micrococcal nuclease is used instead of restriction enzymes to fragment chromatin (Hsieh *et al.*, 2015). In 2019, Hsieh and colleagues showed by Micro-C that TADs are segregated further into microTADs by the action of transcription factors, cofactors and chromatin modifiers (Hsieh *et al.*, 2020). Krietenstein and colleagues utilized the same technique to resolve more than 20000 additional looping interactions with single-nucleosome accuracy in comparison to Hi-C (Krietenstein *et al.*, 2020).

1.1.4. Loop domains

In 2014, Rao and colleagues achieved a 1 kb-resolved map of the human genome, made of the so-renamed 10000 loop or contact domains (Rao *et al.*, 2014). These domains were reported to have a median size of 185 kb (ranging from 40 kb to 3 Mb), to be associated with histone marks and often linking promoters and enhancers, with CTCF sites enriched at the loops' anchors in a convergent orientation (Rao *et al.*, 2014). Furthermore, they identified six compartments with distinct patterns of histone modifications, two of which related to early and mid replicating regions of the previously identified "A" compartment, and the remaining four to be related to facultative or constitutive heterochromatin of the "B" compartment. All boundaries observed were associated with either a sub-compartment transition (occurring circa every 300 kb) or with a loop (occurring circa every 200 kb) and many with both (Rao *et al.*, 2014).

1.2. The chromatin architectural proteins CTCF and cohesin

Increasing evidence has established the architectural proteins CTCF and the cohesin complex as major players in genome organization, as extensively reviewed before (see e.g., Merkenschlager and Nora, 2016; Nasmyth and Haering, 2009; Phillips and Corces, 2009). Genome function and its structural organization have indeed coevolved during the branching process of the tree of life. While cohesin-like proteins are found already in prokaryotes (Gligoris and Löwe, 2016; Volkov *et al.*, 2003), CTCF is conserved in most bilaterian metazoan and might have impacted the body patterning across Bilateria by forming the kernel of a gene regulatory network together with the *Hox* genes, through its role in chromatin domain formation (Heger *et al.*, 2012; Vietri Rudan *et al.*, 2015).

CTCF is an eleven-zinc-finger DNA binding protein, which was initially discovered for its transcriptional regulation of the chicken *c-myc* gene (Klenova *et al.*, 1993; Lobanenkov *et al.*, 1990). This protein was shown to mediate the insulation of a chromatin loop by bringing together two distant DNA sites, after binding sequence-specific DNA sites in a convergent orientation (Fudenberg *et al.*, 2016).

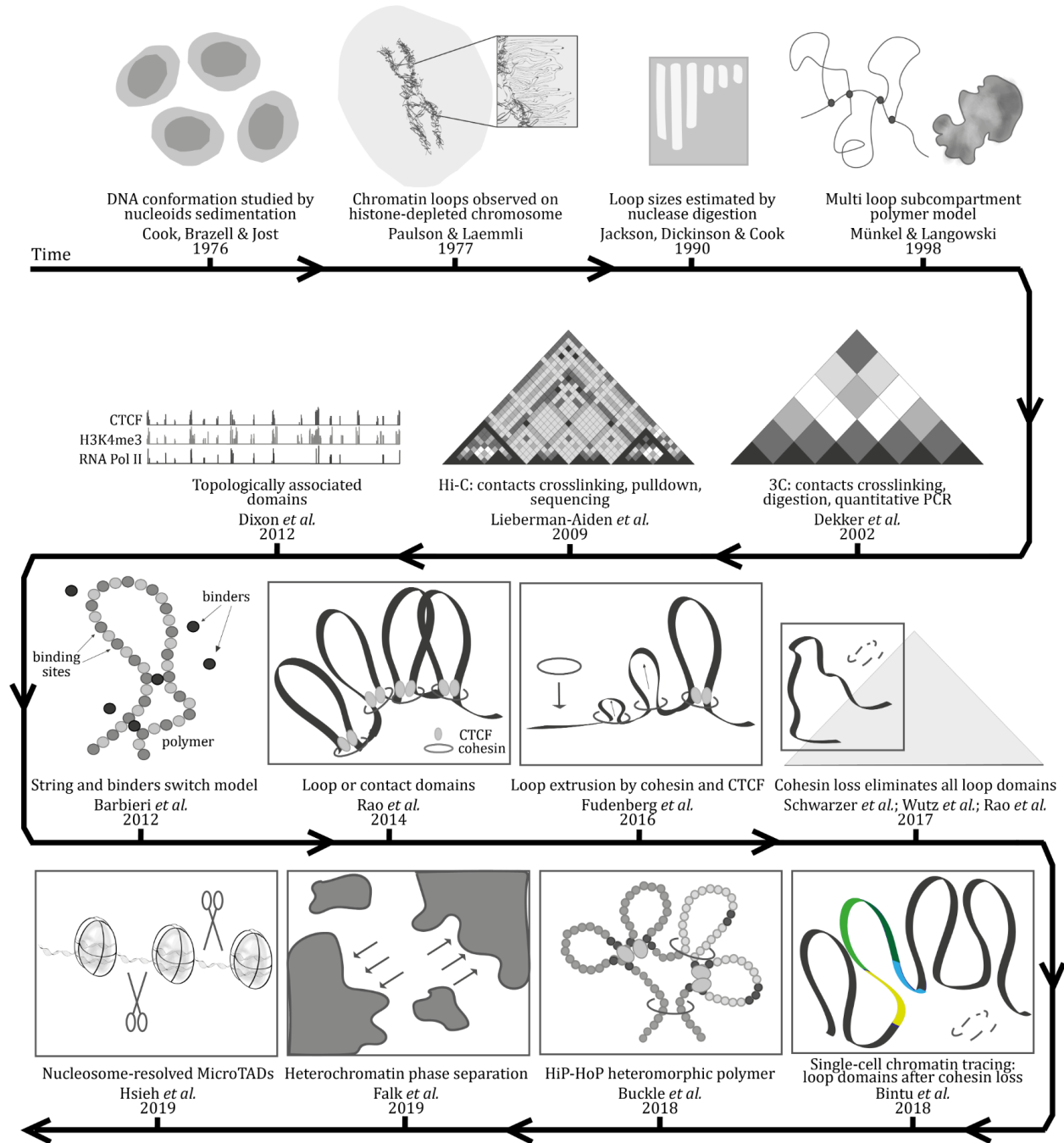


Figure 1.2. Timeline of measurements and modeling of chromatin structures.

Cohesin is a ring-shaped protein complex, which was primarily known to provide cohesion between two sister chromatids after DNA replication (reviewed in: Nasmyth and Haering, 2009). More recently, the complex has been proposed to load on DNA and to extrude a loop until being removed by the release factor WAPL or until encountering an obstacle such as CTCF, as stated in the loop extrusion model (Fudenberg *et al.*, 2016; reviewed in: Mirny *et al.*, 2019; see also below).

1.2.1. Effects of CTCF and cohesin depletion on chromatin

In 2017, Schwarzer *et al.* deleted the cohesin-loading factor Nipbl and observed the disappearance of TADs-associated Hi-C peaks but not of A/B compartments (Schwarzer *et al.*, 2017). Furthermore, no effect on transcription was detected (Schwarzer *et al.*, 2017). Rao *et al.* (2017) similarly reported that cohesin loss eliminated all loop domains, while having only minor effects on transcription (Rao *et al.*, 2017). The loss of the short-range loops did not affect the histone modification patterns nor the A/B compartments (Rao *et al.*, 2017). Moreover, they promoted a fast model of “loop-extrusion” guided by the cooperation between the two architectural proteins CTCF and cohesin, based on the fact that loop domains reform in a few minutes after cohesin recovery (Rao *et al.*, 2017). Similarly, Nora *et al.* (2017) observed only minor global transcriptional effects and no change in A/B compartmentalization upon CTCF depletion (Nora *et al.*, 2017). In the same year, Wutz and colleagues also showed that cohesin is required for TADs and additionally proved that extended loops were formed once the cohesin release factors WAPL and PDS5A/B were removed (Wutz *et al.*, 2017). Hence, CTCF could define the loop boundaries but it would be bypassed if the cohesin unloading factors did not control the length of loops (Wutz *et al.*, 2017). Hansen and colleagues showed by Micro-C that an RNA-binding region in CTCF mediates self-association and that its deletion disrupts half of the CTCF loops, leading to reorganization of TADs (Hansen *et al.*, 2019).

A recent study by Bintu and colleagues in 2018, applied sequential rounds of FISH after partitioning a target genomic region into 30 kb segments, in order to generate high resolution spatial maps of chromatin from single cells (Bintu *et al.*, 2018). They showed that the disappearance of TAD-like structures after cohesin depletion might be in fact an artifact due to averaging at a population level, since single-cell studies revealed that, in the absence of cohesin, the loop boundaries are shifted from cell to cell and, therefore, not detectable as a peak of frequencies at a population level (Bintu *et al.*, 2018). Still in 2018, using Hi-C methods in combination with imaging methods, Gibcus and colleagues (Gibcus *et al.*, 2018) were able to establish using synchronized chicken DT40 cells that, in prophase, consecutive arrays of 60 kb loops are formed followed by, in prometaphase, the formation of 80 kb inner loops nested within 400 kb outer loops in a helical arrangement. They could, furthermore, show

that this arrangement is dependent on the condensin family of proteins and that condensins I and II exerted their effects at different levels (Gibcus *et al.*, 2018).

1.3. Modeling of chromatin organization

Since the earliest discoveries on chromatin folding, a variety of models have been proposed (Figure 1.2.). With the advancement of physics, informatics and machine-learning algorithms, these could be computed in 3D polymer simulations and compared to experimental data.

Already in 1998, Münkkel and Langowski (Münkkel and Langowski, 1998) simulated human chromosomes by polymer modeling of a fiber arranged into loops and subsequently forming subcompartments. They could indeed reproduce the formation of chromosome territories in interphase cells (Münkkel and Langowski, 1998). The year after, Münkkel and colleagues developed the model further by assuming a chromatin fiber folding into 120 kb loops and their arrangement into rosette-like structures (Münkkel *et al.*, 1999). By comparison with experimental data, they found agreement on the overlap, number and size of subcompartments between the model of chromosome 15 and the observed subchromosomal foci of either early or late replicating chromatin. The model also showed expected distances as observed for specific marker loci using FISH at both the sub- and megabase ranges (Münkkel *et al.*, 1999).

In the subsequent years, models describing folding of chromosomes over length scales between 0.5 to 75 Mb based on random loops were proposed by Bohn, Mateos-Langerak and colleagues (Bohn *et al.*, 2007; Mateos-Langerak *et al.*, 2009). The model assumed a self-avoiding polymer and defined the probability of two monomers to interact, creating a loop and extending through the whole chromosome. They also tested the model using experimental data and were able to obtain chromatin folding within a confined space (Mateos-Langerak *et al.*, 2009), which agreed with the evidence that chromosomes occupy distinct territories in interphase nuclei (Bolzer *et al.*, 2005).

More recently, the strings and binders switch model (SBS) (Barbieri *et al.*, 2012) recapitulated well key aspects of chromatin looping, by investigating the interaction between diffusing binders and a free polymer, on which the positions of the binding sites are assigned. These settings allowed investigation of ‘switches’ or conformational changes that the polymer can experience when bound by other proteins (Barbieri *et al.*, 2012). Randomly diffusing binders were shown to be sufficient to dynamically determine TADs, territories and thermodynamic changes (reviewed in: Nicodemi and Pombo, 2014).

Reviving an older concept of loop extrusion dating back to the 1990s (reviewed in: Mirny *et al.*, 2019) and adding new biochemical evidence, Fudenberg and colleagues proposed in 2016 (Fudenberg *et*

al., 2016) that chromatin folding into TADs could result from multiple loops being dynamically extruded. This differs from the models where loops are formed by proteins bringing together the ends of a loop. They also proposed that ring-shaped cohesin complexes would be responsible for the extrusion process. Once loaded onto the DNA, cohesin would start extruding a loop until being removed by the releasing factor WAPL or encountering an obstacle. CTCF bound to DNA sites in a convergent orientation would constitute such an obstacle, stalling the loop extrusion and defining boundaries (Fudenberg *et al.*, 2016).

Nuebler and colleagues (Nuebler *et al.*, 2018) more recently proposed that chromosome organization is shaped by both the affinity-driven compartmentalization and loop extrusion processes, coexisting within the cell nucleus in a nonequilibrium state. Active loop extrusion would counteract and outcompete the compartmental segregation of active and inactive chromatin while enhancing TADs, affecting only compartments sized between 500 kb and 2 Mb (Nuebler *et al.*, 2018). This nonequilibrium model of loop extrusion could be used to explain compartmental mixing and different experimental findings related to chromatin perturbations, namely removal of either CTCF, cohesin's loader NIPBL, or its release factor WAPL (Nuebler *et al.*, 2018).

In the same year, 2018, Buckle and colleagues speculated that the simple bead-and-spring polymers assume a homogeneous chromatin fiber, which is not reflecting the situation *in vivo* (Buckle *et al.*, 2018). Hence, they developed the HiP-HoP or highly predictive heteromorphic polymer model, in which data from epigenetic marks, chromatin accessibility and CTCF/cohesin anchors were added onto a polymer chain to reproduce the variability of the chromatin fiber along its length (Buckle *et al.*, 2018). They integrated this heteromorphic chain with diffusing protein bridges and loop extrusion and were able to reproduce the 3D chromatin organization of genomic loci at both population and single cell level (based on 3C and FISH data, respectively), being able to describe varying levels of transcriptional activity across cell types (Buckle *et al.*, 2018).

In 2019, polymer simulations by Falk *et al.* (Falk *et al.*, 2019) based on both Hi-C and microscopy data could highlight the dominating role of heterochromatin (in particular, constitutive heterochromatin) in inducing phase separation, whereas euchromatin interactions were found to be dispensable for compartmentalization. Heterochromatin-heterochromatin interactions lead to the formation of large (micrometer size) compartments and are likely mediated by affinity between homotypic repetitive elements, modified histones and heterochromatin associated proteins (Falk *et al.*, 2019). In fact, taking constitutive heterochromatin as an example, we could show that increasing the concentration of a single factor (MeCP2, methyl-CpG-binding protein 2) binding DNA by electrostatic as well as modification specific interactions, resulted in coalescence of pericentromeric regions into

increasingly larger clusters (Brero *et al.*, 2005). Accordingly, Solovei and colleagues (Solovei *et al.*, 2009) subsequently demonstrated that, in the absence of attachment to the nuclear periphery in rodent rod cell nuclei, these chromosomal regions completely fuse into a single cluster in the middle of the nucleus.

In 2020, Brackley and Marenduzzo (Brackley and Marenduzzo, 2020) reviewed the string and binders model focusing on the dynamics of multivalent binders, i.e. transcription factors or other proteins, which can bind chromatin at more than one point to form "molecular bridges" that stabilize loops. In the simplest case, interactions can be electrostatic and non-sequence specific and could lead to spontaneous clustering or "bridging-induced attraction", depending on the interaction's strength or on the protein's residence time. This can result in a positive feedback in which protein clusters continue to grow and coarsen in a "phase separation" mode (Brackley and Marenduzzo, 2020). When specific high-affinity binding sites are included in the model, cluster growth is limited due to the looping out of the low affinity (e.g., electrostatic) interaction chromatin stretches. The resulting "clouds of loops" would, in addition, sterically hinder any cluster to merge further, hence stabilizing the microphase separation (Brackley and Marenduzzo, 2020).

To conclude, in living cells, it is highly probable to find a coexistence of different mechanisms variably dictating the chromatin compaction in different subnuclear regions. The various models would contribute differently within each chromatin compartment, with one model being predominant in some compartments but not in others.

1.4. Global genomic processes: function versus structure

A well-known example of functional chromatin loops is given by the insulation of enhancers and promoters, which are distant from each other on the linear DNA sequence. The looping of the DNA between the two sites allows these elements to be brought in close proximity and to affect transcription rates. This very interesting escamotage contributed to the fame of CTCF as an insulator protein influencing the transcription of thousands of genes (reviewed in: Merckenschlager and Nora, 2016). Transcription might indeed be a function locally defining the chromatin architecture. Although the regulation of transcription can locally define the chromatin structure and vice-versa the chromatin looping can influence the transcription rates, transcription can be very differently regulated depending on the cell state and on the environment and only a small percentage of the whole genome is involved in transcription at any given time. This cell-to-cell variability in relation to the regulation of gene expression is exactly the reason why the influence of the transcriptional function on chromatin looping is so relevant. However, we will focus here on those events of DNA

metabolism that are consistent in every cell independently of the cell's developmental state. In this sense, DNA replication and the repair of DNA damage can be considered as more global events: even though these two processes are also spatio-temporally regulated and, hence, not simultaneously involving the whole genome, they have to cover its full length in a defined time in order to ensure cell proliferation and the correct maintenance of the genome. A selection of studies dealing with replication/repair subnuclear structures are presented below and summarized in Table 1.2. and timeline Figure 1.3.

Table 1.2. Sizes of functional chromatin units measured with different methods.

| | Reference | Year | Method | Nomenclature /Structure | Organism (cell line) | Median/mean size | Size range |
|----------------------------|---------------------------|--|---------------------------------------|----------------------------|----------------------|--|--|
| Function | Huberman and Riggs | 1968 | Labeled DNA autoradiography | Replication sections (IOD) | Hamster and Human | 7 - 30 μm (15 - 60 μm) | (up to 160 μm) |
| | Lau and Arrighi | 1981 | Premature chromosome condensation | Replication units | Hamster (CHO) | 0.6 μm | 0.2 - 1.2 μm |
| | Nakamura, Morita and Sato | 1986 | Conventional microscopy foci analysis | Replication domains | Rat (3Y1-B) | 1000 kb | - |
| | Nakayasu and Berezney | 1989 | Conventional microscopy foci analysis | Replication granules | Kangaroo (PtK1) | 0.5 μm | 0.4 - 0.6 μm (late S up to few μm) |
| | Jackson and Pombo | 1998 | Replication labeling on DNA fibers | IOD (eq. to a replicon) | Human (HeLa) | 144 kb | 25 - 325 kb |
| | | | Conventional microscopy foci analysis | Replicon clusters | Human (HeLa) | 0.8 Mb | - |
| | Chagin <i>et al.</i> | 2016 | Replication labeling on DNA fibers | IOD (eq. to a replicon) | Human (HeLa Kyoto) | 189 kb | +/- 121 kb |
| | | | | IOD (eq. to a replicon) | Mouse (C2C12) | 162 kb | +/- 100 kb |
| Natale, Rapp <i>et al.</i> | 2017 | 3D-SIM of γH2AX -labeled chromatin | Repair nano-foci | Human (HeLa) | 75 kb | 34 kb - 159 kb | |

1.4.1. DNA replication units

Interestingly, already in 1982 Buongiorno-Nardelli and colleagues collected measurements from different studies to propose a relationship between the loop length and the replicon size in different animal and plant species (Buongiorno-Nardelli *et al.*, 1982). In DNA halos prepared from radiolabeled frog cells, they observed that radioactivity distributed on a progressively wider area beyond the

nuclear matrix at a rate of 0.47 $\mu\text{m}/\text{minute}$. Taking into account replication bidirectionality and the average loop size of 90 kb in frogs, they estimated that one loop would replicate in 30 minutes and, indeed, they did not observe any increase of the labeled area with a pulse of 60 minutes (Buongiorno-Nardelli *et al.*, 1982). Similarly, Vogelstein and colleagues had already observed that the radiolabeled DNA moved progressively from the matrix to the halo region, either by increasing the pulse or the chase duration after the pulse (Vogelstein *et al.*, 1980). By comparing the loop size estimated with the halo method and the replicon size known from fiber autoradiography studies, Buongiorno-Nardelli and colleagues proposed that the maximum halo radius or loop size is species-specific and that this is directly proportional to the average replicon length in the same species (Buongiorno-Nardelli *et al.*, 1982). In fact, they calculated that all species analyzed had an average replicon length four times longer than the maximum halo, which means twice the loop size. Hence, they speculated that a replicon might consist of two adjacent loops, might be read by two matrix bound replication complexes and have origins and terminations at the anchors of the loops: the newly formed loop would be then released to bind the new matrix (Buongiorno-Nardelli *et al.*, 1982).

This correlation was possible because other groups had already measured the length of newly synthesized DNA on stretched DNA fibers starting with Cairns in 1963 (Cairns, 1963). From DNA autoradiograms of *E. coli* cultured in H^3 -thymidine, he observed that replication progressed from a fork-like growing point by forming what he called theta-structures (looking like the Greek letter θ ; Cairns, 1963). On mammalian DNA fibers he also showed that the newly replicated DNA appeared as tandemly separated sections (Cairns, 1966).

In 1968, Huberman and Riggs confirmed Cairns' experiments in Chinese hamster and HeLa cells, showing that replication proceeded from an origin in each of the tandemly joined replicating sections (Huberman and Riggs, 1968). By exploiting thymidines with two different affinities, they observed a bidirectional synthesis progressing in opposite directions from each origin, leading them to propose the bidirectional model of DNA replication (Huberman and Riggs, 1968). They also proposed the term "replication unit" as the basic unit of replication, meaning that adjacent sections sharing an origin would initiate replication together and hypothesized that replication might proceed until converging with the next growing point (Huberman and Riggs, 1968).

A variety of subsequent studies (Lau and Arrighi, 1981; Nakamura *et al.*, 1986; Nakayasu and Berezney, 1989) using nucleotide pulse labeling and microscopical analysis established the existence of functional units of DNA replication in different rodent and marsupial cell lines and furthermore, described the focal pattern changes throughout S-phase.

Additional analysis of replication labeling performed on stretched DNA fibers determined that the spacing between adjacent origins in mammalian cells varies between 50 and 300 kb (reviewed in: Edenberg and Huberman, 1975; Hand, 1978). This length corresponds to the segment of chromosomal DNA replicated from a single origin of bidirectional DNA replication. This segment is commonly referred to as “replicon”.

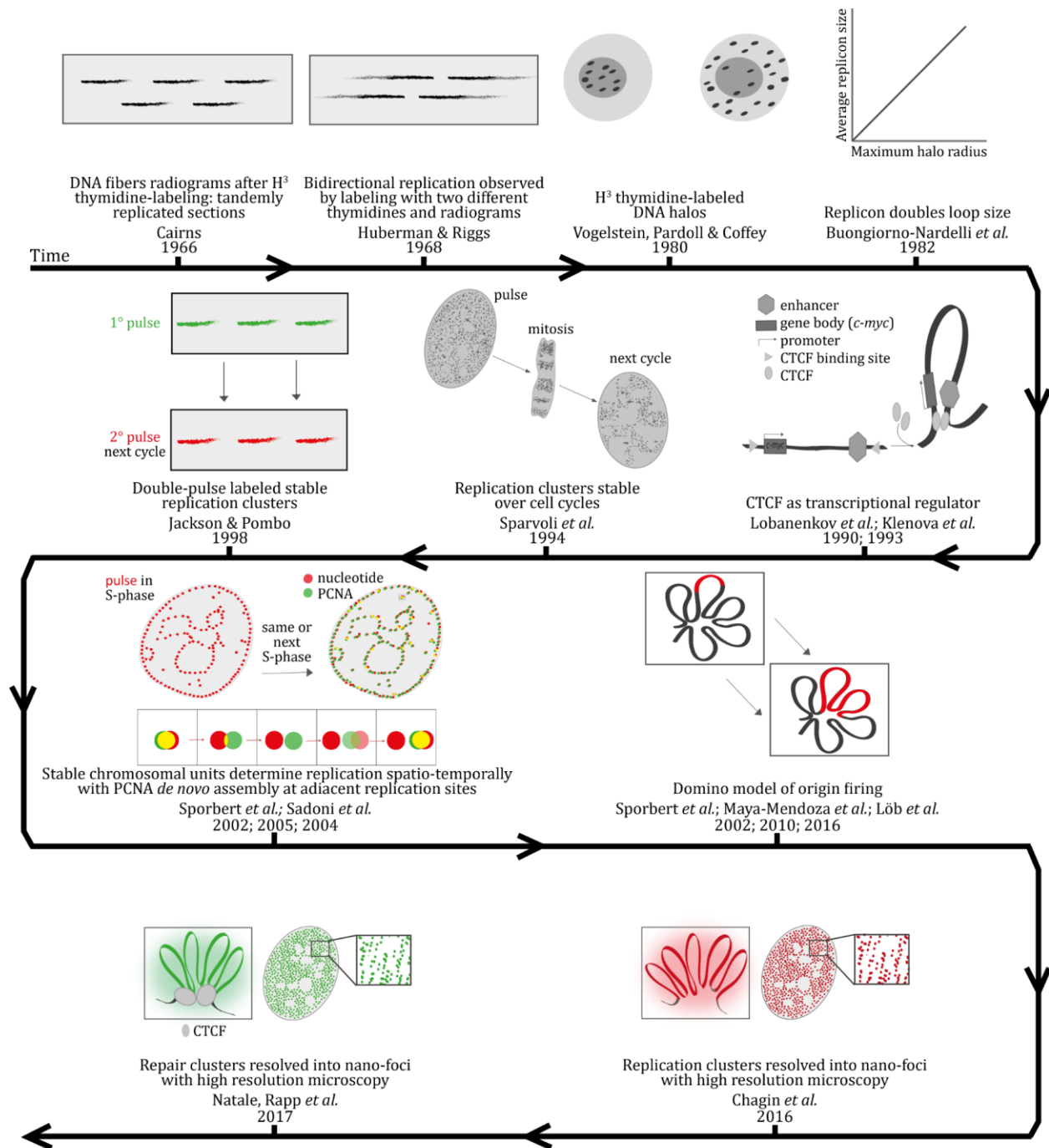


Figure 1.3. Timeline of measurements and concepts of chromatin functions.

In 1998, Jackson and Pombo confirmed such values and, by analyzing numbers of adjacent replicons in DNA fibers, confirmed that they are activated in clusters (Jackson and Pombo, 1998), as already shown by the earlier fibers studies. Based on pulse-chase labeling of replicating DNA in subsequent cell cycles, these authors proposed that such clusters reflect units of chromosome structure and are stable over cell cycles (Jackson and Pombo, 1998).

The fact that loops are dynamic is altogether not incompatible with the hypothesis of a stable structural unit. Loops can dynamically be released and reformed, which gives rise to single-cell variability when taking single snapshots in time (Bintu *et al.*, 2018; Hansen *et al.*, 2018). However, over time, loops or clusters of loops are stable in the sense that both the focal structures and their replication timing are maintained over multiple cell generations (Sadoni *et al.*, 2004; Sparvoli *et al.*, 1994) (see also below).

Making use of several decades of technological developments, our laboratory applied a multi-dimensional approach to perform a comprehensive analysis of replication dynamics in mammalian cells (Baddeley *et al.*, 2010; Chagin *et al.*, 2016). In detail, replication units (each defined as a segment of DNA that is synthesized from a single origin by two opposing forks) were extensively analyzed by live cell microscopy of cells stably expressing fluorescent replication factors and by super-resolution microscopy of fixed cells in combination with molecular characterization of replicons in combed DNA fibers and measurement of S-phase duration (Chagin *et al.*, 2016). In both human and mouse cells, 5000 replication units or nano-foci (RFi) could be counted on average at any sub-stage of S-phase, when imaged at high-resolution by 3D-structured illumination microscopy (3D-SIM) (Chagin *et al.*, 2016). These data showed that the replication structures commonly observed at conventional resolution light microscopy are not the actual units of replication, but higher-order organization clusters comprising on average 4-5 of the basic units (Chagin *et al.*, 2016). These findings on the cluster composition were confirmed with 2D-stochastic optical reconstruction microscopy (STORM) by Xiang and colleagues, which showed that an average cluster consists of four co-replicating regions that are spaced 60 nm apart within a total region of 150 nm (Xiang *et al.*, 2018). Molecular combing of newly replicated DNA fibers showed that the average replicon size estimated as inter-origin distance (IOD) was of 188.7 and 161.7 kb, with an average lifetime of 57 and 33 minutes, respectively in human and mouse cells (Chagin *et al.*, 2016). The replicon sizes obtained in our laboratory are coincidentally within a two-fold larger size to published loop sizes in mammalian cells (see above; Table 1.1.; Buongiorno-Nardelli *et al.*, 1982; Earnshaw and Laemmli, 1983; Jackson *et al.*, 1990b, 1990a).

After measuring the genome size of each cell line used, both, the time to replicate the genome from a single fork as well as the number of replication forks that need to be active in parallel in order to replicate the full genome within the S-phase duration were calculated (Chagin *et al.*, 2016). This calculated number of required replication forks was divided by two assuming that most replication units are bidirectional. This number was subsequently divided by the actual number of replication nano-foci counted at any given time of S-phase and the result was approximately one (0.92 in human cells; Chagin *et al.*, 2016). Bridging these different analyses at different resolutions, it was possible to conclude that most of the replication nano-foci imaged at 3D-SIM represent single (bidirectional) replicons being active in parallel. This indicates that individual replicons could be optically resolved as spatially separated entities, leading to the conclusion that the DNA synthesis machinery should be actually reading structural chromatin units (Chagin *et al.*, 2016).

1.4.2. Modeling of DNA replication

The folding of chromatin would consequently induce the firing of adjacent origins within the 3D nuclear space, as discussed in our proposed domino-like model of S-phase progression (Löb *et al.*, 2016; see also: Maya-Mendoza *et al.*, 2010; Sadoni *et al.*, 2004; Sporbert *et al.*, 2002, 2005). In more detail, whenever an origin is fired, this would increase the probability of firing of the neighboring origins as in the domino game the fall of one bar would lead the neighboring bars to fall down (see Figure 1.3.; Löb *et al.*, 2016). The resolution of chromatin units as replicons thousand times larger than the nucleosomes, in a range of 150-200 kb or bp, respectively (Chagin *et al.*, 2016), led us to propose that these could represent the next level of chromatin organization above the nucleosome level. Furthermore, these chromatin structural units would be read by the DNA replication machinery in a spatio-temporal manner every time the cell needs to duplicate the genome.

1.4.3. DNA repair units

Another global process that involves the whole genome and might help us to unravel the chromatin organization is the chromatin signaling upon DNA damage (DNA damage response or DDR), which starts with the phosphorylation of the histone variant H2AX (γ H2AX) (reviewed in: van Attikum and Gasser, 2009; Turinetto and Giachino, 2015). This modification has been proposed to spread up to several Mb from the original site of damage and it can be detected as a focal structure with conventional microscopy. In a recent analysis of 53BP1 focal structures, Kilic and colleagues proposed that phase separation also plays a role in delimiting the DDR (Kilic *et al.*, 2019).

With the use of 3D-SIM and STED (stimulated emission depletion) microscopy, it was shown in our laboratory that γ H2AX foci are actually clusters of nano-foci with a median DNA size of 75 kb

(spanning from 40 to 160 kb) in human cells (Natale *et al.*, 2017). The nano-focus DNA content was estimated by applying a novel calculation based on the fraction of genomic DNA in the volume of each singularly segmented nano-focus in relation to the overall DNA content within the full nuclear volume. The measurement of distances between the centroid of all the nano-foci allowed us to estimate their clustering. Cluster size distributions had a median DNA size of 921, 623 or 220 kb (ranging from 112 to 938 kb), depending on the time point after irradiation (0.5, 3 or 24 hours post irradiation, respectively) (Natale *et al.*, 2017). The DDR nano-foci are, hence, lower order units of chromatin organization, which appear to be spatially organized in higher-order clusters within the (sub-)megabase size range. When these foci were imaged together with labeled phospho-Ku70 proteins, as one of the first repair factors known to bind the ends of the double strand break, *circa* one focus of phospho-Ku70 was present within every cluster of 3-4 γ H2AX nano-foci (Natale *et al.*, 2017). This indicated that multiple units of γ H2AX-decorated chromatin made up a domain in which one single double strand break was found. Moreover, the signaling of damage and the subsequent DNA repair were both impaired upon depletion of CTCF (Natale *et al.*, 2017), which, as mentioned before, is one of the main architectural proteins involved in chromatin looping together with cohesin. In addition, CTCF could also play a role in recruiting repair factors to double strand breaks (Hilmi *et al.*, 2017).

The impairment of DNA repair after CTCF depletion suggested that the DNA damage response is structured by chromatin loops clustered together by CTCF. In particular, after depleting CTCF to 40% of the control protein levels and upon irradiation, γ H2AX nano-foci decreased in number, clustering and DNA content (Natale *et al.*, 2017). This was consistent with the fact that, in control cells, CTCF was shown to delimit the clusters of γ H2AX-decorated chromatin, both through high-resolution single-cell imaging and ChIP-Seq (chromatin immunoprecipitation-sequencing) data analysis before and during DDR (Natale *et al.*, 2017). According to our findings on the DNA repair nano-foci clustering, each γ H2AX nano-focus would be a single loop within a CTCF-delimited multi-loop cluster. Hence, CTCF influences the spreading of the signal of DNA damage through its role in delimiting clusters of repair units. Colony formation assays and measurements of the residual damage through single-cell comet assay demonstrated also that CTCF depletion resulted in radiosensitization and decreased the cellular ability to repair the damaged DNA, supporting its impact on the DNA repair function by its role in chromatin organization (Natale *et al.*, 2017).

2. Aims

Upon decades of investigations on the physical identity of chromatin loops, nowadays multiple studies are focusing on the frequency of contacts between different genomic sites in matrices generated by population studies through chromosome conformation capture techniques. Given the increasing understanding of genomic functions and the advancements in microscopy, the present study aims at bridging the latest definitions of chromatin domains as computed through contact matrices with microscopically resolved nuclear structures. Since both DNA replication and DNA repair are global genomic events, spatio-temporally regulated and defined by focal structures, their units were chosen as targets for investigating the relationship between genomic functions and chromatin structure. To allow more insights, the role of the main architectural proteins CTCF and cohesin (Figure 2.1.) in the spatio-temporal organization of DNA replication and DNA repair was investigated.

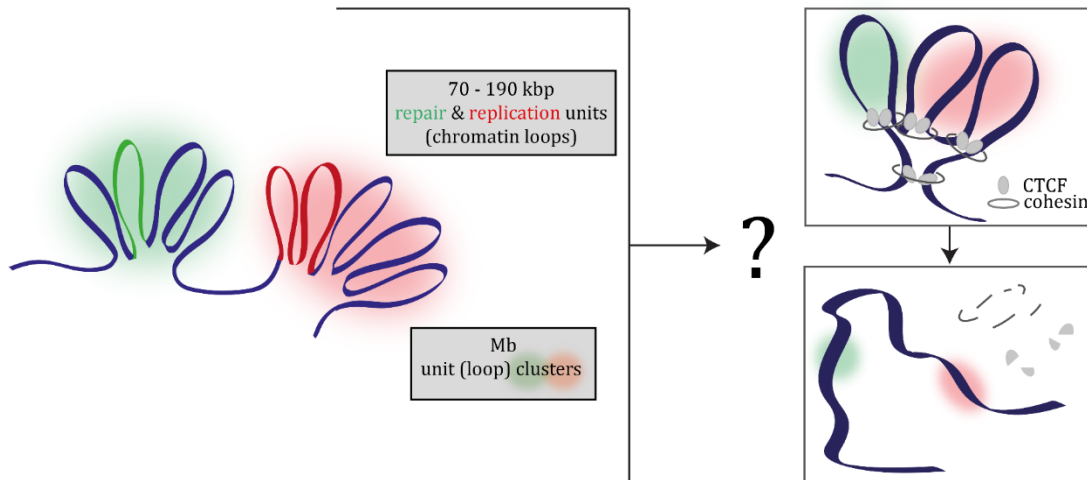


Figure 2.1. Do the chromatin architectural proteins CTCF and cohesin affect genomic functions by structuring chromatin domains?

3. CTCF participates in defining the structural units of DNA repair and replication

3.1. CTCF is critical for cellular survival upon ionizing radiation

3.1.1. Introduction

CTCF (CCCTC-binding factor) is an eleven-zinc finger protein, which was initially described to bind three repeats of the DNA motif CCCTC and thereby to regulate the transcription of the *c-myc* oncogene (Klenova *et al.*, 1993; Lobanenko *et al.*, 1990). The very conserved eleven zinc fingers of CTCF can be combined in different ways to achieve binding of various sequences, as the ones of promoters of the same gene which have diverged during evolution in different species (Filippova *et al.*, 1996). CTCF was hence initially classified as an insulator protein, due to its ability to insulate proximal DNA sequences (as reviewed in: Merckenschlager and Nora, 2016; Phillips and Corces, 2009). By mediating the insulation of enhancers and promoters, CTCF can either act as a transcriptional activator or repressor (Phillips and Corces, 2009). Besides its important role in transcriptional regulation, CTCF has gained major interest for its cooperation with the cohesin complex in chromatin loop formation. According to the loop extrusion model, CTCF would act as a border to the chromatin extruding activity of the ring-shaped cohesin complex, when two CTCF molecules bind two DNA motifs which are convergent in orientation (Fudenberg *et al.*, 2016).

With the introduction of chromosome conformation capture (3C) and related high-throughput techniques (e.g., Hi-C), matrices of contact frequencies between different genomic sites have been calculated. Genome-wide interaction maps of CTCF were thus generated under various cellular conditions (reviewed in: Barutcu *et al.*, 2016). It soon became clear that CTCF binding sites are enriched at the boundaries of different types of chromatin domains, ranging from the loop domains (Rao *et al.*, 2014), through the topologically associated domains (TADs; Dixon *et al.*, 2012), till the A/B compartments (Lieberman-Aiden *et al.*, 2009). The determinants of such domains have been investigated through depletion of main architectural proteins and their cofactors as well as deletion of genomic loci associated to domain boundaries and subsequent modeling. Since the homozygous knock out of the CTCF gene was shown to be lethal (Heath *et al.*, 2008; Moore *et al.*, 2012; Splinter *et al.*, 2006), subsequent studies employed knock down strategies. Zuin and colleagues proposed that CTCF and cohesin shape TADs in non-redundant ways, with CTCF being necessary for the maintenance of their boundaries and cohesin promoting self-association within the domains but not the segregation of neighboring domains (Zuin *et al.*, 2014).

Nora and colleagues engineered mouse embryonic stem cells with an auxin-inducible degron to deplete CTCF (Nishimura *et al.*, 2009; Nora *et al.*, 2017) and showed its requirement for those loops

with CTCF binding sites at their anchors (Nora *et al.*, 2017). CTCF depletion also caused loss of TADs insulation, while A/B compartmentalization was mostly unaffected (Nora *et al.*, 2017). Additionally, they showed that misfolding defects were dose-dependent and that TADs loss required the highest CTCF depletion (Nora *et al.*, 2017). The fact that upon depletion of either cohesin or CTCF, TADs are weakened or lost while the A/B compartments stay unaffected or get even strengthened (Bintu *et al.*, 2018; Cremer *et al.*, 2020; Nora *et al.*, 2017; Rao *et al.*, 2017; Schwarzer *et al.*, 2017; Wutz *et al.*, 2017; Zuin *et al.*, 2014), led the authors of the loop extrusion model to seek for an explanation (Nuebler *et al.*, 2018). Through polymer modeling, they concluded that chromatin organization is the result of a competition between loop extrusion and phase separation-mediated compartmentalization (Nuebler *et al.*, 2018).

CTCF loops were shown to be highly dynamic, based on the very transient and cell cycle-dependent binding time of the protein, as measured by live-cell single molecule microscopy (Agarwal *et al.*, 2017; Hansen *et al.*, 2018). However, as we reviewed recently (Mamberti and Cardoso, 2020), this dynamicity does not interfere with the concept of loops as stable structures over time. Their constant act of releasing and reforming will simply give rise to single-cell and cell cycle-dependent variability, which can anyway be overcome by averaging the single cell snapshots on a population level.

Ionizing radiation is a high-energy radiation able to directly induce DNA breaks (30% - 40% of lesions) and to generate reactive oxygen species (ROS) that oxidize biological molecules (60% - 70% of lesions) (Borrego-Soto *et al.*, 2015; Huang and Zhou, 2020; Santivasi and Xia, 2014). When these free radicals interact with DNA, they can generate abasic sites, base and sugar damage, depolymerization, crosslinking and single strand breaks (SSBs) (Borrego-Soto *et al.*, 2015; Huang and Zhou, 2020; Santivasi and Xia, 2014). Double strand breaks (DSBs) are considered the most important DNA lesion, as they have the highest probability of inducing cell death, mutation, chromosomal aberrations and carcinogenic transformation (Huang and Zhou, 2020; Schipler and Iliakis, 2013; Vignard *et al.*, 2013).

Recently, we identified CTCF as a key regulator of the DNA damage response (DDR) upon DSBs (Natale *et al.*, 2017), which typically starts with a signaling cascade through the phosphorylation of the histone variant H2AX on serine 139 (γ H2AX) (Rogakou *et al.*, 1998, 1999). Per each Gray unit of ionizing radiation, corresponding roughly to 30 DSBs, 1% of the total H2AX amount of the genome gets phosphorylated, which means that 2 Mbp of chromatin are involved in the response to a single DSB in a G1-phase genome of mammalian cells (0.03% of 6×10^9 bp; Rogakou *et al.*, 1998, 1999). H2AX phosphorylation is deposited by the key repair kinases ATM (ataxia telangiectasia mutated), DNA-PKcs (DNA-dependent protein kinase, catalytic subunit) and ATR (ATM and RAD3-related)

(Fernandez-Capetillo *et al.*, 2002; Lees-Miller *et al.*, 1992) and initiates at DSB sites (Karlsson and Stenerlöv, 2004; Leatherbarrow *et al.*, 2006) before spreading further (Bakkenist and Kastan, 2003; Rogakou *et al.*, 1998). ATM, DNA-PKcs and ATR are correspondingly activated by the DNA-binding complexes MRN (MRE11-RAD50-NBS1) (Lee and Paull, 2005; Uziel *et al.*, 2003), Ku70-Ku86 (XRCC6/XRCC5; Ku: first two letters of the prototype Japanese patient's surname, in Mimori *et al.*, 1981) (Blackford and Jackson, 2017; Sibanda *et al.*, 2017; Singleton *et al.*, 1999) and RPA-ATRIP (replication protein A, ATR-interacting protein) (Wang *et al.*, 2017; Zou and Elledge, 2003), which have respectively high affinity for diverse structures including DSBs (Paull, 2015), DSB ends (Blackford and Jackson, 2017; Singleton *et al.*, 1999) and extended ssDNA from resected DSBs (Menolfi and Zha, 2020; Zou and Elledge, 2003). The γ H2AX mark induces the recruitment of the repair factors to the sites of DNA damage, such as 53BP1 (p53-binding protein 1), BRCA1 (breast cancer gene 1) and RAD51 (radiation-sensitive mutant 51) (Bhogal *et al.*, 2009; Paull *et al.*, 2000; Redon *et al.*, 2002; Schultz *et al.*, 2000; Scully *et al.*, 2019). The choice between the two main DSB repair pathways of non-homologous end-joining (NHEJ) or homologous recombination (HR) is determined by the cell cycle phase and the chromatin environment (Scully *et al.*, 2019; Swift *et al.*, 2021).

Through 3D-structured illumination microscopy (3D-SIM), we could resolve the γ H2AX foci into clusters of ~ four 75 kb-sized nano-foci (median size; Natale *et al.*, 2017). Interestingly, this DNA size corresponds to the one of a single chromatin loop (reviewed in: Mamberti and Cardoso, 2020). We measured that single γ H2AX-labeled loops are clustered together by a couple of CTCF molecules at the anchor of this multi-loops domain (Natale *et al.*, 2017). Each cluster of loops contains a single DSB, as shown by the 1:4 ratio of the foci of DSB-binding phospho-Ku70 proteins to γ H2AX nano-foci (Natale *et al.*, 2017). Additionally, we found that CTCF depletion impairs the spreading of H2AX phosphorylation after damage, decreasing the number of γ H2AX nano-foci and their clustering (Natale *et al.*, 2017).

A different study showed that CTCF supports homologous recombination by associating with BRCA2 in a PARylation (poly[ADP-ribosyl]ation) dependent manner, hence enhancing the recruitment of BRCA2 to the sites of DSBs (Hilmi *et al.*, 2017). CTCF accumulated rapidly at DNA lesions following ultraviolet laser micro-irradiation, persisting up to two hours (Hilmi *et al.*, 2017). Its depletion delayed the repair kinetics of γ H2AX foci but not 53BP1, increased the sensitivity to PARP-1 (poly[ADP-ribose] polymerase 1) inhibitors and decreased the survival potential (Hilmi *et al.*, 2017). In this study, the survival ability of different CTCF-depleted cell lines upon exposure to ionizing radiation was assessed through clonogenic assays. CTCF levels were quantified prior to and upon

CTCF depletion. The fine tuning of CTCF dosage revealed a CTCF-dose dependency in survival curves. Through the collaboration with Dr. Michael Scholz (GSI Helmholtzzentrum für Schwerionenforschung, Darmstadt), the experimental data were integrated into a biophysical model on the impact of CTCF on cellular radiosensitivity. We compared the survival rates to predictions of a variant of the Giant-Loop-Binary-Lesion model (GLOBLE) (Friedrich *et al.*, 2012, 2013; Herr *et al.*, 2014), which takes into account the number of giant 2 Mbp domains onto which double strand breaks have the opportunity to distribute and how the clustering of DNA breaks can affect their repair and lethality. Based on our finding that CTCF holds together the anchors of a multi-loop chromatin domain, in which one single DSB is surrounded by on average 4 γ H2AX decorated chromatin loops (Natale *et al.*, 2017), the model could well explain the increased cell lethality in CTCF-depleted cells upon irradiation. In fact, the model can predict the observed cell survival data when chromatin domains are supposed to lose coherence upon CTCF-depletion and, consequently, multiple DSBs are clustered together, leading to decreased survival.

3.1.2. Results

3.1.2.1. Validation of the genome size, CTCF basal levels and binding in different cancer cell lines

In our previous study based on high resolution microscopy, we observed that on average four loop-sized γ H2AX nano-foci cluster around each double strand break and that the DNA damage response is impaired in cells with diminished amounts of CTCF (Natale *et al.*, 2017). We concluded that the ability to signal DNA damage and to repair DSBs relies on CTCF anchoring multi-loop domains (Natale *et al.*, 2017). In order to better understand the relationship between CTCF and radiosensitivity we aimed to design a model able to predict the clonogenic survival potential when a lower number of domains is anchored by CTCF.

Given the increased necessity of a better understanding of cancer cells dynamics and treatment, two different human tumor cell lines were used: cervical carcinoma (HeLa Kyoto; Erfle *et al.*, 2007) and osteosarcoma (U2OS; Pontén and Saksela, 1967; Supplementary Table ST1). In order to measure the impact of CTCF depletion in the two cell lines under study, the differences in genome size and total amount of CTCF were first assessed (Figure 3.1.1.). This is particularly important, as tumor cells are known to be genomically unstable. As a DNA sequence specific binding protein, the amount of CTCF needs to be evaluated relative to the cell's genome size, which would translate to more or less CTCF binding sites. To this aim, both untreated HeLa Kyoto and U2OS cells were immunostained for CTCF and DNA was counterstained with DAPI (Supplementary Table ST2).

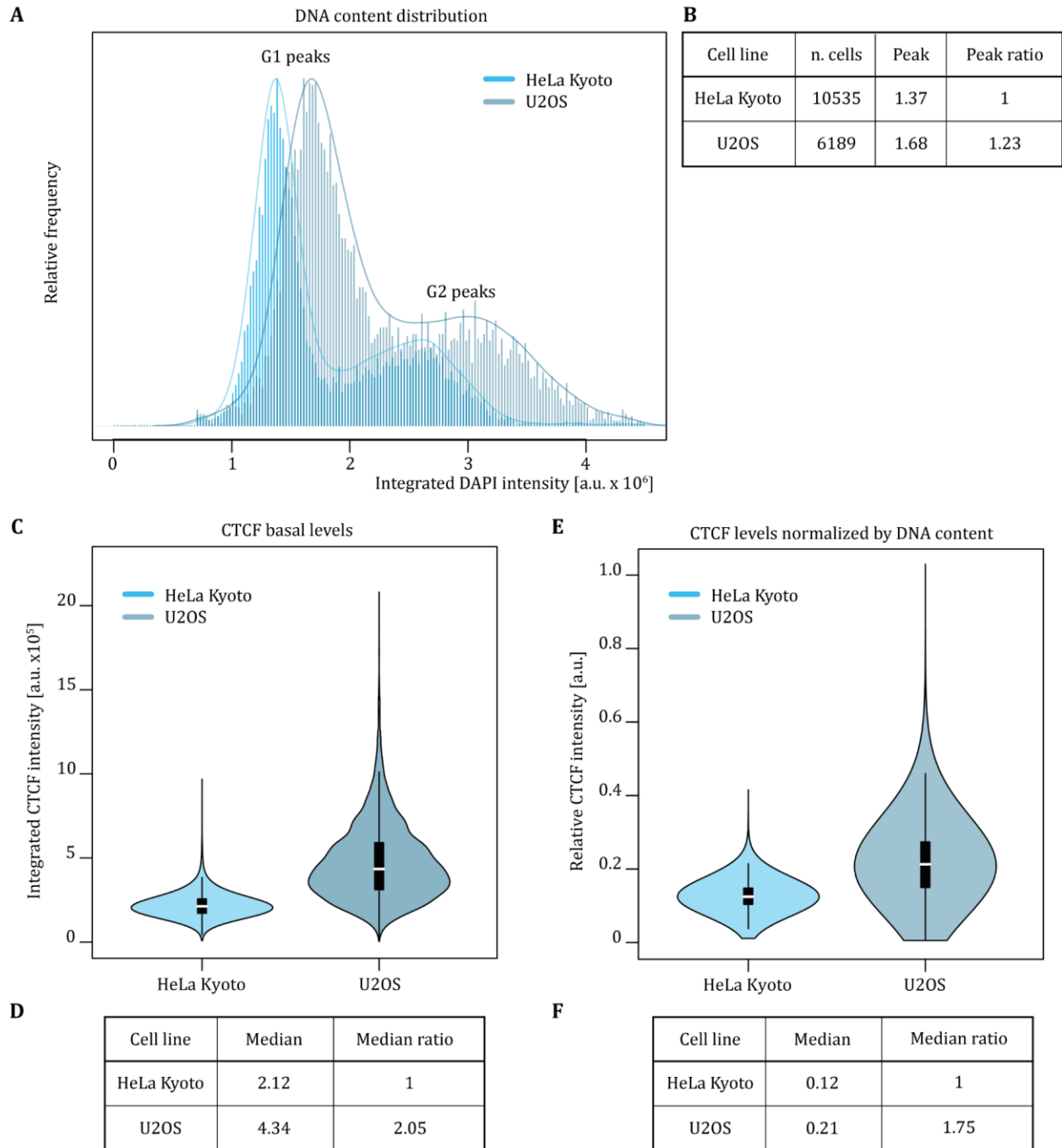


Figure 3.1.1. Genome size and CTCF basal levels differ in HeLa Kyoto and U2OS. A - F Untreated cells from the two different cell lines were grown on coverslips, simultaneously fixed, permeabilized, immunostained for CTCF and DNA counterstained with DAPI (see Supplementary Table ST2 for antibody characteristics). Cells were imaged with high-content wide-field microscopy (see Supplementary Table ST3 for imaging system characteristics) and the total nuclear CTCF and DNA intensities were calculated from the segmented nuclei (see Supplementary Figure SF1 for image analysis pipeline). The number of cells for (A - F) is shown in B, resulting from two biological replicates (see Supplementary Table ST4 for statistics). As HeLa Kyoto showed the lowest values for both DNA content and CTCF amounts, this cell line was chosen to calculate the relative ratios for a

quantitative comparison. **A** DNA content distribution of HeLa Kyoto and U2OS cells showing the respective G1 and G2 peaks. The frequency of integrated nuclear DAPI intensities was plotted together with a density function to visualize and compare the genome size distribution of the two cancer cell lines. **B** The raw G1 peak measurements of the genome distributions shown in A and the ratio of the G1 peak of U2OS to the one of HeLa Kyoto are shown. **C** Violin plots showing CTCF basal levels in HeLa Kyoto and U2OS. Total nuclear CTCF intensities were plotted for each cell line, upon subtraction of the background values. The background values were calculated from the intensity levels of cells stained with the primary antibody being omitted. **D** Median values relative to C and the ratio of U2OS median value to the one of HeLa Kyoto are shown. **E** Violin plots showing total nuclear CTCF intensity upon normalization by DNA content, i.e. divided by total nuclear DAPI intensities. **F** Median values relative to E and the ratio of U2OS median value to the one of HeLa Kyoto are shown.

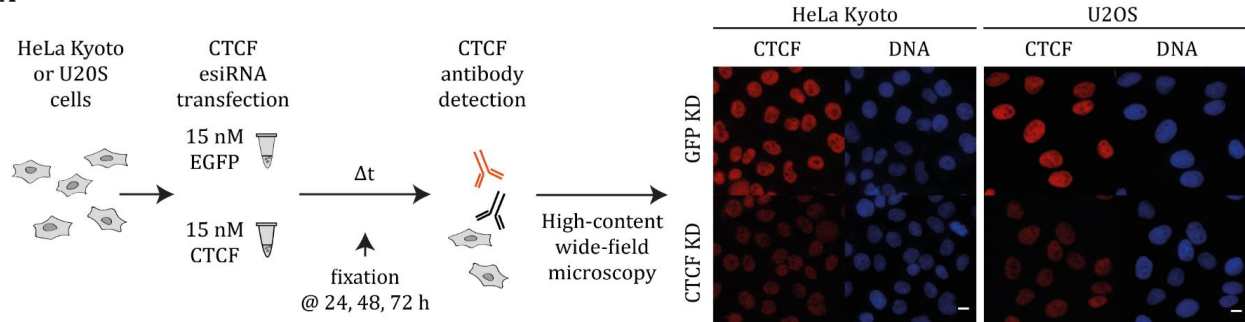
Upon high-content microscopy imaging, nuclei were segmented and analyzed for both DNA content and CTCF basal levels (Figure 3.1.1.; Supplementary Figure SF1; Supplementary Table ST3). By plotting the integrated nuclear DNA intensity distribution, the major G1 and G2 peaks, separated by the population of cells progressing through S-phase, were identified. The G1 peak was utilized to calculate a ratio of the higher genome content of U2OS to the lower one of HeLa Kyoto, which yielded a 1.23-fold larger genome size for the U2OS cells (Figure 3.1.1. A – B). Based on our previous calculations, the genome size of HeLa Kyoto corresponds to 9.7×10^3 Mbp (Chagin *et al.*, 2016) and by multiplying this value by the ratio, we can estimate a genome size of 11.93×10^3 Mbp for U2OS. From the same data set, the integrated nuclear intensity of CTCF was extracted (after background subtraction from samples omitting the primary antibody against CTCF). A median value of 2.12 and 4.34 a. u. was measured in HeLa Kyoto and U2OS, respectively (Figure 3.1.1. C – D; Supplementary Figure SF1; Supplementary Table ST4). Once the median value of U2OS was divided by the one of HeLa Kyoto, the total amount of CTCF in the osteosarcoma cell line resulted to be double the one of cervical cancer cells. These findings are in good correlation with copy number differences (Cancer Cell Line Encyclopedia, DepMap Data Explorer) and relative gene expression levels (The Human Protein Atlas). To understand how this could be impacted by the difference in genome size, CTCF intensities were divided by the respective integrated DNA values, obtaining a normalized ratio of CTCF of 1.75 in U2OS compared to HeLa Kyoto (Figure 3.1.1. E – F; Supplementary Figure SF1; Supplementary Table ST4).

3.1.2.2. CTCF knockdown and validation in different cancer cell lines

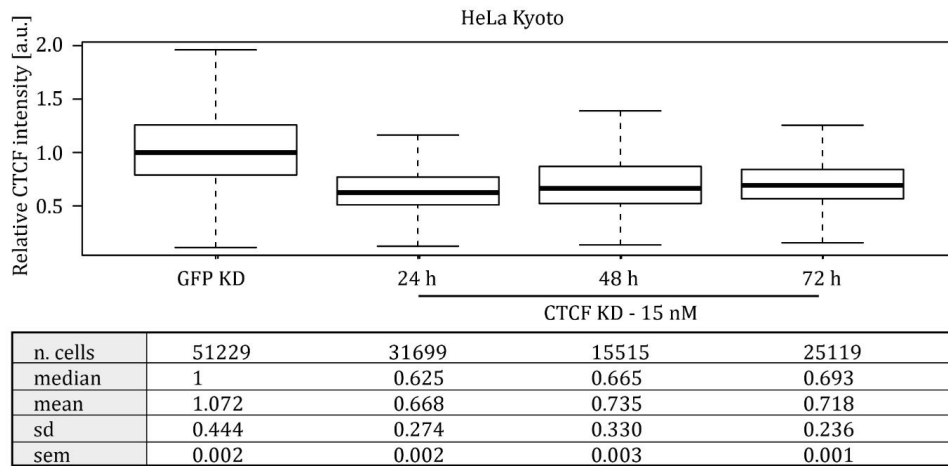
The depletion of CTCF in cancer cells was performed by electroporation mediated delivery of an esiRNA pool targeting the human CTCF transcript (Figure 3.1.2.; Supplementary Table ST5). The knockdown was then confirmed by quantitative immunofluorescence staining *in situ* followed by high-content microscopy analysis (Figure 3.1.2. A; Supplementary Tables ST2 and ST3;

Supplementary Figure SF1). In detail, the nuclear sum CTCF values of each sample were normalized (divided) by the median value of the respective EGFP mock-depleted control (hereafter renamed GFP KD sample).

A



B



C

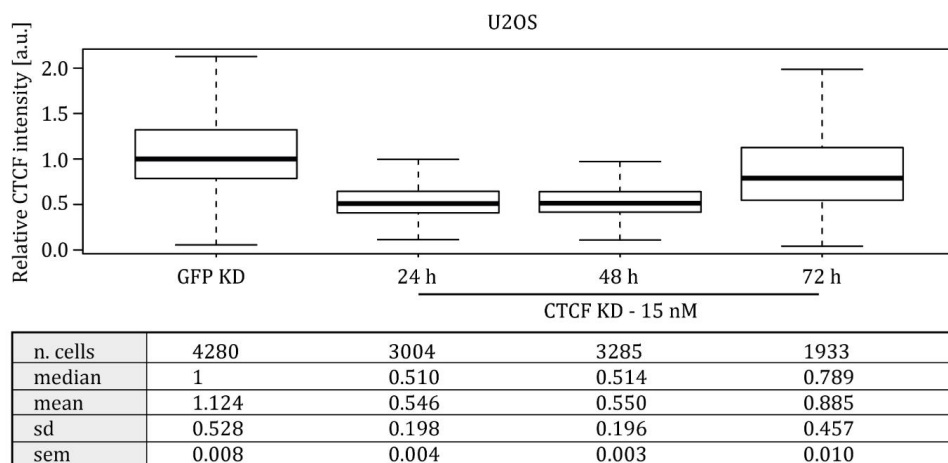


Figure 3.1.2. CTCF knockdown is efficiently achieved in 24 hours in HeLa Kyoto and U2OS. A Experimental settings for the knockdown validation. HeLa Kyoto and U2OS cells were transfected with 15 nM

of esiRNA against either the human CTCF transcript or EGFP through electroporation and seeded on coverslips. Cells were fixed at 24, 48 or 72 hours post transfection and immunostained for CTCF (Supplementary Table ST2). Cells were imaged using a high-content wide-field microscope (scale bar 10 μm ; Supplementary Table ST3). **B – C** Relative CTCF nuclear intensity at different time points upon esiRNA transfection in HeLa Kyoto (**B**) and U2OS (**C**). From the high-content microscopy images, nuclei were masked based on DAPI signal and CTCF nuclear intensities were measured (see Supplementary Figure SF1). The integrated sum intensity values were then normalized to the values of the mock-depleted GFP KD sample and plotted as boxplots (sd = standard deviation; sem = standard error of mean); the results consist of three biological replicates (Supplementary Table ST4). See Supplementary Figure SF2 for boxplot interpretation.

CTCF depletion was reached in both HeLa Kyoto and U2OS already at 24 hours post transfection with 15 nM of esiRNA, with a median depletion of circa 40% and 50% of the control levels, respectively (Figure 3.1.2. B – C). A residual amount of protein corresponding to 60% in HeLa Kyoto and 50% in U2OS could therefore be estimated (Figure 3.1.2. B - C; Supplementary Table ST4). At later time points, the same concentration gave similar results (Figure 3.1.2. B – C), indicating that the depletion was quite stable and that the early time point could be used for the following experiments, i.e. irradiation.

3.1.2.3. CTCF depletion increases the radiosensitivity of cancer cells in a cell line dependent way

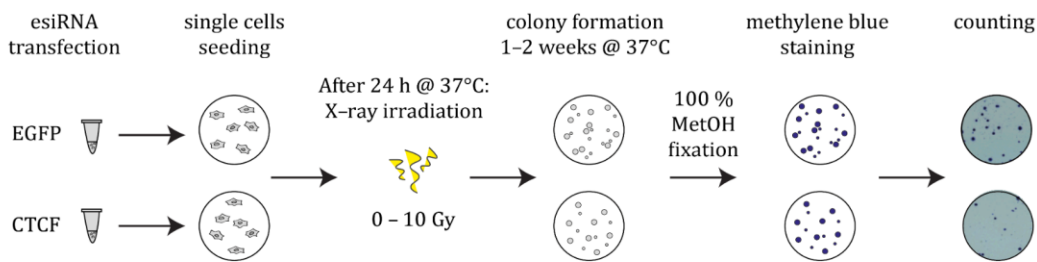
In our previous studies on the DNA damage response units (Natale *et al.*, 2017), we observed that CTCF-depleted cells were unable to properly signal the damage through γH2AX , recruit the repair factors and showed a reduced DSB repair upon irradiation. Based on the architectural role of CTCF, we concluded that this deficiency of repairing DNA double strand breaks was related to the loss of correct chromatin looping.

Therefore, we decided to investigate further this relationship by testing a range of X-ray doses on CTCF-depleted cancer cells and by elaborating the survival data into a model. In particular, cells were first subjected to 40% - 50% depletion of the architectural protein CTCF (Figure 3.1.2.), then exposed to different doses of X-ray irradiation at 24 hours post transfection and allowed to form colonies (Figure 3.1.3. A).

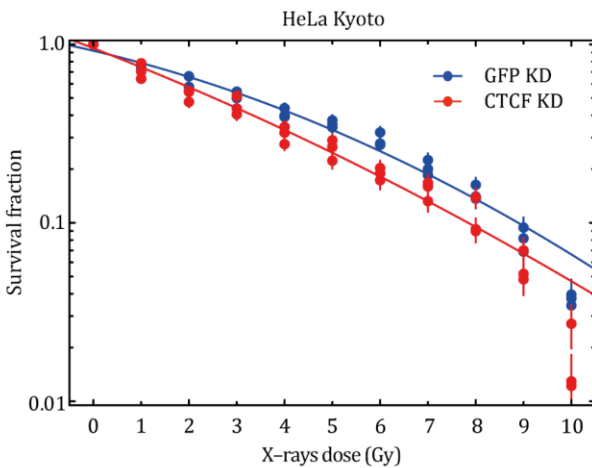
The survival data of each treatment was normalized to the average of the respective unirradiated control to calculate the survival fraction (see Supplementary Table ST6 for survival data statistics). In general, the survival curves follow the typical linear-quadratic behavior, i.e. $S(D) = e^{-(\alpha D + \beta D^2)}$, with α representing the initial slope at low doses and β characterizing the bending of the dose response curve. CTCF-depleted cells of both cell lines had a lower clonogenic potential than mock treated cells at all radiation doses (Figure 3.1.3. B – C; Supplementary Figure SF3; Supplementary Figure SF4 A –

B; Supplementary Table ST6). The hypothesis we formulated together with Dr. M. Scholz (GSI, Darmstadt) is that an effect of CTCF depletion would be more relevant on the high doses part of any survival curve, which is shaped by the β term and related to the increased frequency of clustered DSBs. The less CTCF is present in the nucleus, holding the borders of chromatin domains, the higher the β term would be. This correlation is hypothesized based on the role of CTCF in shaping chromatin domains and the concomitant distribution of DNA damage within the same or different domain(s). In particular, cervical cancer cells are characterized by a survival curve with a very high α/β ratio (Table 3.1.), meaning that the β term is not dominant in shaping the curve of HeLa Kyoto. A modest increase of radiosensitivity of this cervical cancer cell line was observed upon CTCF depletion (Figure 3.1.3. B; Supplementary Figure SF4 A; see Supplementary Table ST6 for survival data statistics and Supplementary Figure SF3 for colony formation images).

A



B



C

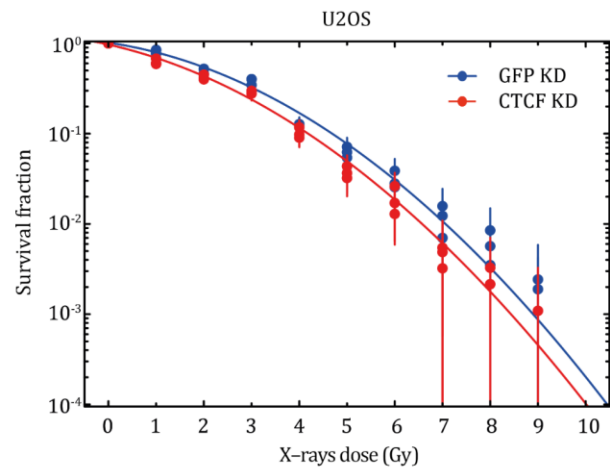


Figure 3.1.3. Radiosensitivity is increased and relative survival is decreased upon CTCF depletion. A Experimental settings for the clonogenic assay. Cells were transfected with 15 nM of an esiRNA pool against either the human CTCF transcript or against EGFP as a mock treatment (Supplementary Table ST5). From each different transfection, single cells were seeded and allowed to attach before irradiation at the respective time point of maximum depletion for each cell line (40% - 50% of CTCF depletion at 24 h for HeLa Kyoto and U2OS; Figure 3.1.2. B - C). Cells were then irradiated with different doses of X-rays and allowed to form colonies for 7 - 10 days under standard culture conditions. Colonies were then fixed with cold 100% methanol and stained

with methylene blue. The colonies with more than 50 cells were microscopically identified and counted by eye. **B – C** Clonogenic assay results of CTCF-depleted HeLa Kyoto (**B**) and U2OS (**C**). The number of colonies of each technical replicate and treatment was normalized to the average of the respective unirradiated control and plotted as relative survival fraction in semi-logarithmic scale. A linear-quadratic dose-response curve fitting weighted by $1/[\text{relative error}]^2$ was applied. The results are based on three biological replicates, each depicted as a dot in the survival graph and composed of technical replicates (whiskers = error bars; Supplementary Table ST6). Color legend: blue = GFP KD, red = CTCF KD. The same experimental data are plotted with equal y axis scaling in Supplementary Figure SF4 A – B for a direct comparison of the two cell lines.

The same treatment was applied to the osteosarcoma cell line, expecting to see a higher impact from the CTCF depletion. U2OS cells are in fact known to have a smaller α/β ratio (Table 3.1.) and hence a more pronounced shoulder in the survival curve compared to HeLa Kyoto (Figure 3.1.3. C; Supplementary Figure SF4 B; Supplementary Table ST6). However, the higher endogenous CTCF levels in U2OS led to a modest difference in survival upon CTCF depletion (Figure 3.1.3. C; Supplementary Figure SF4 B; see Supplementary Table ST6 for survival data statistics and Supplementary Figure SF3 for colony formation images).

3.1.2.4. GLOBLE model investigates the impact of DSB clustering in chromatin domains on cell kill

Through a collaboration with Dr. Michael Scholz (GSI Helmholtzzentrum für Schwerionenforschung, Darmstadt), we applied a modeling approach based on an adaptation of the previously published Giant-Loop-Binary-LEsion (GLOBLE) (see section 3.1.4.6.; Friedrich *et al.*, 2012, 2013), which allows quantitative prediction of several aspects of the cellular response to photon radiation. These comprise e.g. the general linear-quadratic shape of cell survival curves (Friedrich *et al.*, 2012, 2013), the impact of dose rate on radiosensitivity (Herr *et al.*, 2014) and the cell cycle dependence of radiosensitivity (Hufnagl *et al.*, 2015).

The GLOBLE model is based on the premise that the initial clustering properties of primary DNA damages, i.e. DSBs, are predictive for the expected cell killing. Clustering is defined with respect to the multiplicity of DSB within chromatin domains. Based on a given DSB yield and irradiation dose the multiplicity of DSB within the domains can be determined by Poisson statistics, assuming that the DSBs are randomly distributed within the DNA after photon irradiation. Cases where only single DSBs are found in a domain are called “isolated DSBs” (iDSB), cases with two or more DSBs in a domain are called “clustered DSBs” (cDSB).

Since CTCF is considered a key molecule involved in defining higher order chromatin domain structures, it can be expected to also play a dominant role in defining the domain size. We, thus, hypothesize that the average size of chromatin domains is reciprocally proportional to the amount

of CTCF. This leads to the following hypothesis that a CTCF reduction to 50% leads to less binding sites being occupied and correspondingly to an average increase of the domain size by a factor of 2. The GLOBLE model can therefore predict the impact of CTCF depletion by just correspondingly adapting the domain size, but keeping all other parameters constant as for the control cells. The corresponding lethalties are derived from a linear-quadratic fit of the survival curve for GFP KD control cells and using equations (9) and (10) to assign the lethalties (see section 3.1.4.6.). These lethalties are kept constant for both conditions, i.e. control and CTCF-depleted cells, and only the frequency of iDSB and cDSB differs according to the change of the domain size. All relevant input parameters are summarized in Table 3.1.

Table 3.1. Parameters that were used in the GLOBLE model for prediction of the impact of CTCF depletion. The linear-quadratic parameters α and β and the corresponding lethalties ε_i and ε_c were determined by Dr. Michael Scholz (GSI, Darmstadt) from the survival curves for GFP KD conditions, after pooling all biological replicates. The genome size of HeLa Kyoto was taken from (Chagin *et al.*, 2016) and the one of U2OS estimated from that value multiplied by the genome size ratio in Figure 3.1.1. B. The genome size for mouse mESC-AID-CTCF cells was taken from (Guénet, 2005) (see results section 3.1.2.5.). The default domain size was chosen identical for all cell lines.

| Cell Line | HeLa Kyoto | U2OS | mESC-AID-CTCF |
|-------------------------------|-------------------|---------------------|--------------------|
| Genome size [Mbp] | 9.7×10^3 | 11.93×10^3 | 5.2×10^3 |
| Domain size [Mbp] | 2 | 2 | 2 |
| α [Gy^{-1}] | 0.145 ± 0.014 | 0.179 ± 0.034 | 0.111 ± 0.025 |
| β [Gy^{-2}] | 0.012 ± 0.002 | 0.067 ± 0.0067 | 0.013 ± 0.0029 |
| α/β [Gy] | 12.1 | 2.67 | 8.54 |
| ε_i | 0.0030 | 0.0030 | 0.0043 |
| ε_c | 0.0555 | 0.2310 | 0.1085 |

As a consequence of the above-mentioned concept, the α -term as defined by the lethality of iDSB according to eq. (9) should be untouched in the case of CTCF depletion, since the relative change in the number of iDSB at low doses is negligible. In contrast, the increase of the domain size should be connected with an increased β -term of the survival curves according to eq. (10), since due to the constant α -values, a decrease in ND must be compensated by a corresponding increase of β .

Our model predicted that CTCF depletion results in a change of survival curves towards increased sensitivity, as a consequence of the hypothesized increase of the chromatin domain size and the corresponding higher number of more severe cDSB. In general, the order of magnitude of the shift is

in reasonable agreement with the experimental data for both cell lines (CTCF KD: red dots; GFP KD: full blue curve), as shown by the comparison to model predictions in Figure 3.1.4. (model: red curves).

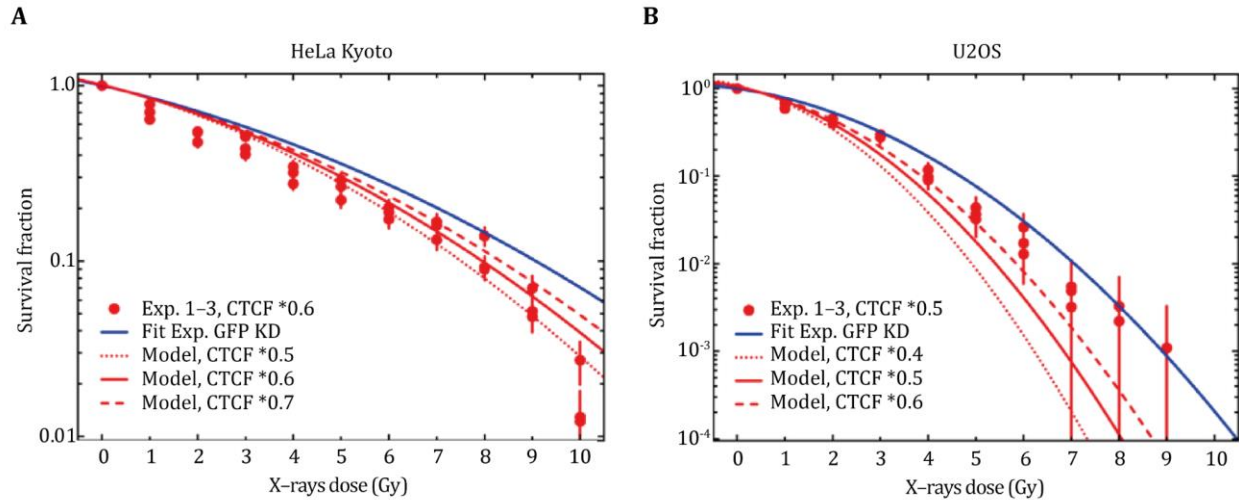


Figure 3.1.4. GLOBLE predictions of clonogenic survival upon different levels of CTCF depletion in HeLa Kyoto and U2OS cells, in comparison to the experimental data. LQ parameters for reference conditions were determined based on the GFP KD control survival (full blue curve, fitting weighted by $1/[\text{relative error}]^2$). Full red lines indicate model predictions for the experimentally determined CTCF depletion level, whose experimental data from three biological replicates is shown as dots for comparison (whiskers = error bars); predictions for other knockdown levels are shown as dashed lines to indicate the expected impact of knockdown efficiency. **A** GLOBLE predictions for HeLa Kyoto. **B** GLOBLE predictions for U2OS. The same predictions are plotted with equal y axis scaling in Supplementary Figure SF4, C – D, for comparison. The modeling was provided by Dr. Michael Scholz (GSI, Darmstadt).

In particular, the expected change in sensitivity as predicted by the model is shown for different levels of CTCF depletion (full and dashed red curves). The predictions for the experimentally determined depletion level (full red curves) agree best with the experimental data of HeLa Kyoto. For U2OS cells the predicted shift is more pronounced as compared to the measured data, likely due to a possible influence of the different genome size on chromatin domains architecture. The same predictions are plotted with equal y axis scaling in Supplementary Figure SF4, C – D, for a direct comparison of the two cell lines.

3.1.2.5. CTCF effect on radiosensitivity is observed in mouse ES cells also and is CTCF dose-dependent

The use of a mouse embryonic stem cell (mESC) line engineered with an auxin-inducible degron (AID) for CTCF, bearing a CTCF-GFP-tag (mESC-AID-CTCF; Nora *et al.*, 2017; Supplementary Table

ST1), allowed to investigate further the effects of depletion in a completely different cell system and with a more synchronous dose regulation (Figure 3.1.5. A). Different auxin concentrations (0, 25, 500, 1000 μM ; Figure 3.1.5. A) were applied for four hours. Differential levels of depletion were obtained (Figure 3.1.5. B), with circa 32% residual CTCF in the 25 μM sample and 28% CTCF in the 500 μM and 1000 μM treated cells, compared to the untreated cells.

After subtracting the background GFP values measured in wild type untagged mESC (ES14 (Hooper *et al.*, 1987); Supplementary Table ST1), a median 4% of CTCF left was obtained in the 25 μM sample and below 1% left in the 500 μM and 1000 μM samples (Figure 3.1.5. B). Besides the similar median values, the 25 μM and 500 μM samples displayed a different CTCF intensity distribution: in the lowest auxin treatment, circa 70% of cells retain a small amount of CTCF, in particular 43% of the population shows a level of at least 10% of CTCF left, while only in 30% of cells CTCF is not detectable; with higher auxin treatments, the opposite is observed, with CTCF being equal to background levels in 60% of the cell population and the remaining 30% having circa 10% residual CTCF (see "Percent of cells in each intensity class" in Figure 3.1.5. B; Figure 3.1.5. C). Next, the survival of the cells with different CTCF levels to irradiation was evaluated (Figure 3.1.6. A). The impact of CTCF on radiosensitivity proved to be dose dependent, as the fitting curves show decreased survival along with decreasing CTCF levels (Figure 3.1.6. B; see Supplementary Table ST6 for survival data statistics and Supplementary Figure SF3 for colony formation images).

As it is reported that near to complete depletion does not allow cells to grow longer than four days (Nora *et al.*, 2017), auxin was washed off one hour after irradiation, in order to validate its impact solely on the DNA repair ability (Figure 3.1.6. A). Although the samples treated with 500 and 1000 μM auxin showed an almost equivalent CTCF values distribution (Figure 3.1.5.), an independent experiment was performed to assess the timing of CTCF depletion and recovery upon auxin wash off (Supplementary Figure SF5; Supplementary Table ST4). In this way, it was observed that the higher the auxin concentration, the faster CTCF is depleted and the slower is its recovery (Supplementary Figure SF5; Supplementary Table ST4). This explains how a slightly lower survival rate could be achieved with 1000 μM auxin (Figure 3.1.6. B) even though the actual CTCF levels in the population were comparable with the 500 μM -treated sample (Figure 3.1.5.). However, the decrease in survival in stem cells was lower than in the tumor cells that retained a higher CTCF level (Figure 3.1.3. B – C), which may indeed be due to the faster recovery of CTCF levels in the first hours upon auxin wash off.

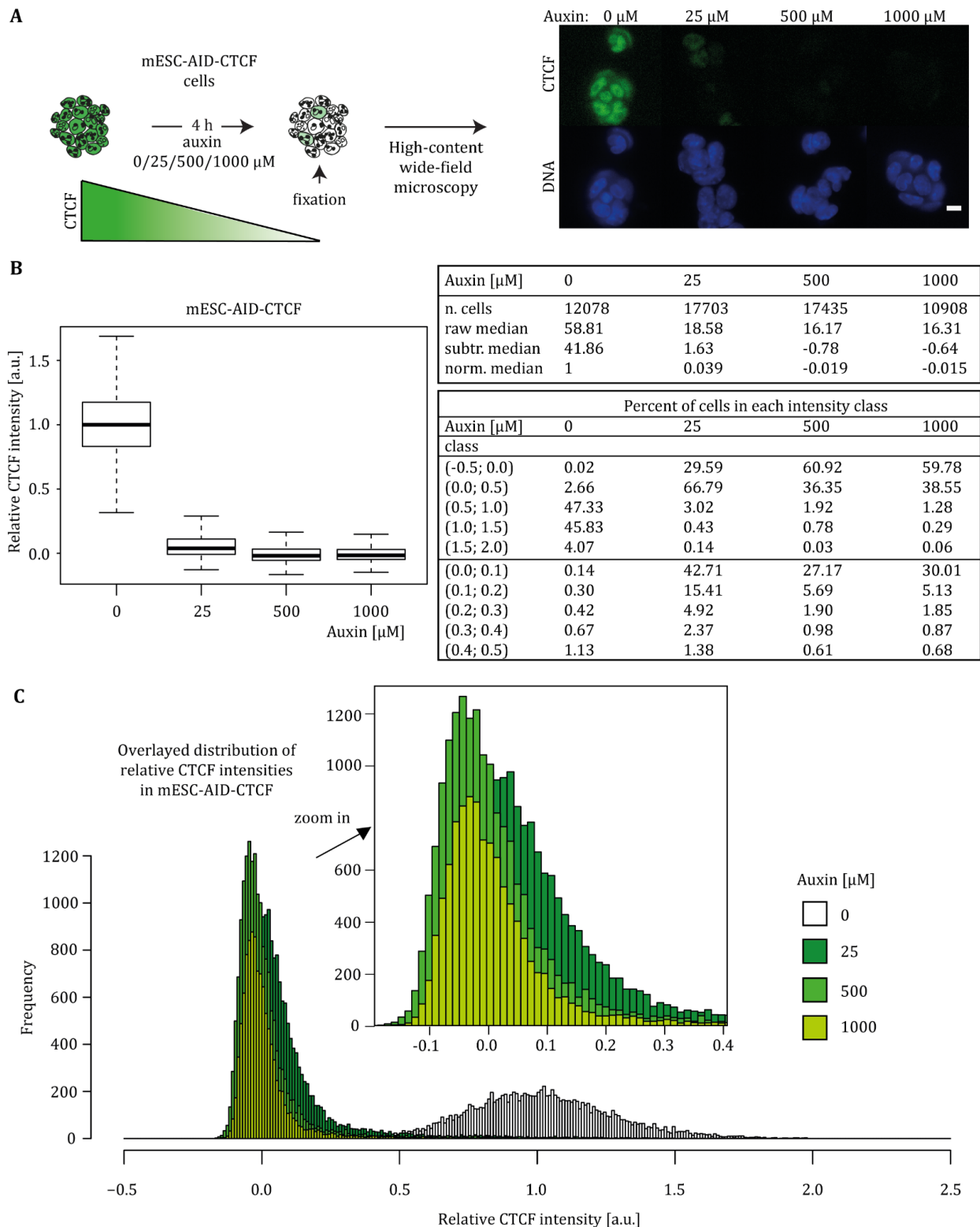


Figure 3.1.5. Degron system validation in mESC-AID-CTCF cells. **A** Cells were subjected to different concentrations (0, 25, 500, 1000 μM) of auxin for 4 hours, fixed and imaged using a high content wide-field microscope (scale bar 10 μm ; Supplementary Figure SF1; Supplementary Table ST3); **B** – **C** Nuclear CTCF-GFP mean intensities were measured, the background as measured in untagged mESC was subtracted and the

resulting data was normalized to the untreated control sample (0 μM); normalized CTCF values are shown as boxplots (**B**) and as frequency distributions (**C**), together with the percent of cells lying within the different classes of CTCF intensities. The results are based on four biological replicates (Supplementary Table ST4). See Supplementary Figure SF2 for boxplot interpretation. In Supplementary Figure SF5 the relative kinetics of auxin-induced CTCF depletion and recovery after auxin wash-off are further investigated in a time course experiment.

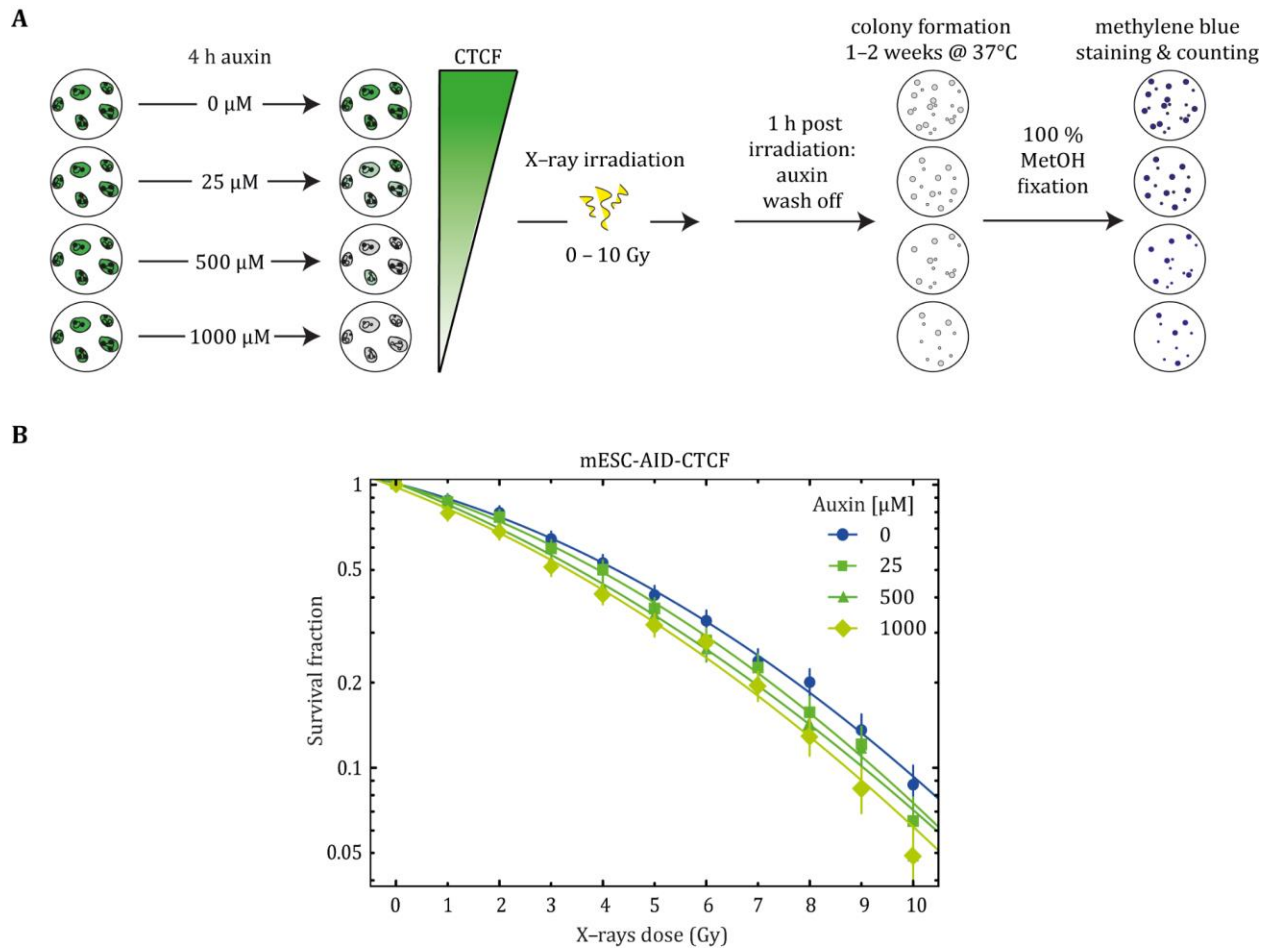


Figure 3.1.6. Clonogenic assay of mESC-AID-CTCF cells upon auxin-induced CTCF depletion and irradiation. **A** Auxin treatment was applied for 4 hours (0, 25, 500, 1000 μM) after single-cells seeding, at which time point cells were irradiated with X-rays (0 – 10 Gy); 1 h after irradiation, auxin was washed off and single cells were allowed to form colonies for 7 – 10 days under standard culture conditions. Colonies were then fixed with cold 100% methanol and stained with methylene blue. The colonies with more than 50 cells were microscopically identified and counted by eye; **B** Each data point was normalized to the average of the respective unirradiated control and plotted as relative survival fractions in semi-logarithmic scale with a linear-quadratic dose-response curve fitting (whiskers = error bars; fit weighted by $1/[\text{relative error}]^2$). The results consist of four biological replicates (Supplementary Table ST6).

The modeling of CTCF depletion in the engineered cell line was performed by Dr. Michael Scholz (GSI, Darmstadt). It was made qualitatively for residual values close to the observed raw CTCF residual values without background subtraction, i.e. 35%, 30% and 25% (see Figure 3.1.7.), for two reasons. On the one hand, the experimental method comes to its limits, since the detected CTCF signal is close to the background value for the higher auxin concentrations, leading to a substantial fraction of negative values in the intensity distribution (Figure 3.1.5. B); therefore, the low values are subject to substantial uncertainties. On the other hand, the near-to-complete depletion imposed mathematical limits to the modeling. The model calculations based on the raw intensity values should therefore be interpreted as a lower limit for the expected impact of the CTCF depletion in this case.

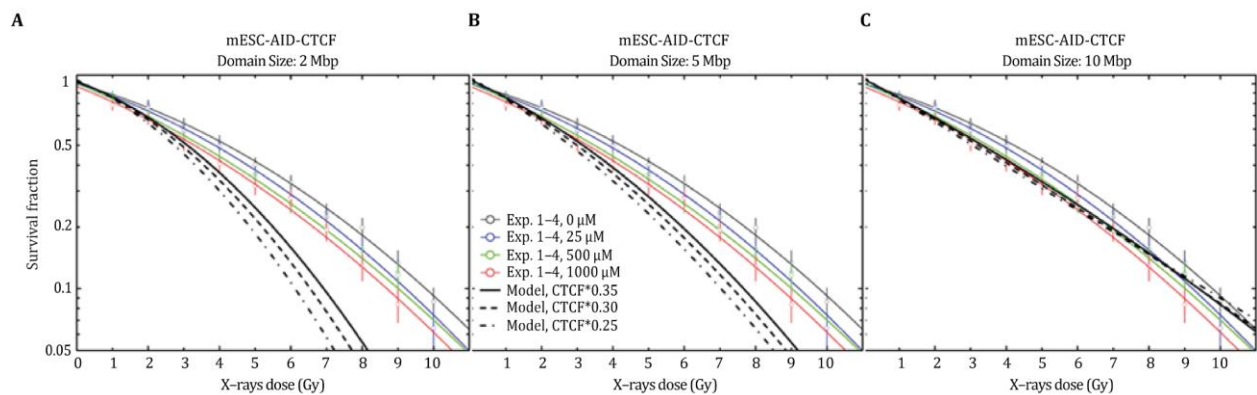


Figure 3.1.7. GLOBLE predictions of clonogenic survival upon different levels of auxin-induced CTCF depletion in mESC-AID-CTCF cells, in comparison to the experimental data. The reference condition (0 μM auxin) is depicted as a full thin black curve. Bold dashed black lines indicate model predictions for the experimentally determined CTCF depletion levels, whose experimental data from four biological replicates is shown as colored fit lines (curve fit weighted by $1/[\text{relative error}]^2$) and dots (mean) for comparison (whiskers = error bars). **A** Predictions modeled based on the standard 2 Mbp domain size. **B – C** Predictions modeled based on a domain size of 5 Mbp (**B**) and 10 Mbp (**C**). The modeling was provided by Dr. Michael Scholz (GSI, Darmstadt).

When the GLOBLE modeling approach was applied based on the standard 2 Mbp domain size, the obtained model predictions deviated from the experimental data (Figure 3.1.7. A), likely due to the higher kinetics of CTCF recovery upon auxin wash off (Supplementary Figure SF5; Supplementary Table ST4). The resulting predictions of survival are therefore lower than the actual experimental data. This is probably due to the much faster CTCF recovery in this degron system compared to the KD systems used earlier. However, when a higher domain size of 5 or 10 Mbp was used, the predictions of survival were nearer to the experimental data (Figure 3.1.7. B – C). This would be consistent with a unique and looser chromatin architecture and correspondingly larger domain sizes in embryonic stem cells (Pękowska *et al.*, 2018).

To investigate this possibility, the domain-size dependency on the impact of CTCF depletion was analyzed by Dr. M. Scholz (GSI, Darmstadt) in a range from 0.2 Mbp up to 10 Mbp (Figure 3.1.8.). A CTCF depletion up to 25% or 50% residual levels, similarly impacts domains of different sizes up to 2 Mbp. However, the outcome changes beyond 2 Mbp: the model predicted a substantially reduced sensitivity to CTCF depletion when the considered domains have a size closer to 5 or 10 Mbp (Figure 3.1.8.). The reduction of the impact of CTCF towards larger reference domain sizes is most pronounced for mESC and HeLa cells, whereas for U2OS the effect is considerably smaller. This can be traced back to the much smaller α/β ratio for this cell line, indicating a larger impact of clustered DSB as compared to isolated DSB and consequently also a larger impact of CTCF depletion. More insights on possible reasons for this deviation are illustrated in the discussion section.

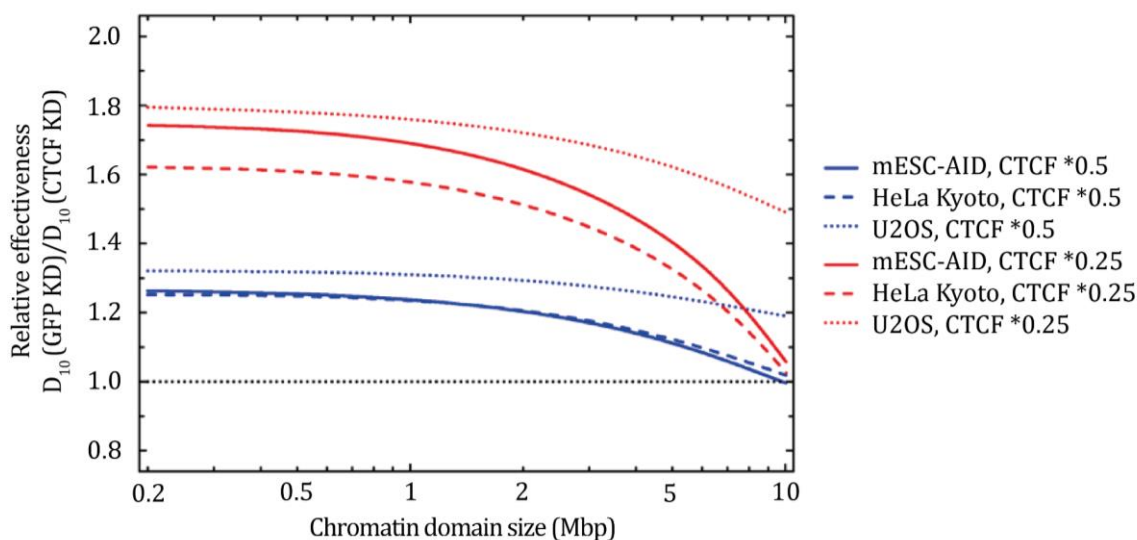


Figure 3.1.8. GLOBLE predictions of radiation sensitivity analyzing the impact of CTCF depletion on differentially sized control chromatin domains. As an indicator of the impact, ratios of D10 (the dose required to achieve 10% survival) under control conditions to the D10 after CTCF depletion are used. CTCF depletion has the most significant impact for control domain sizes below approximately 2 Mbp for all three cell lines, whereas towards larger control domain sizes the impact gets reduced. The black dotted line indicates the reference value, corresponding to no impact of CTCF depletion. The modeling was provided by Dr. Michael Scholz (GSI, Darmstadt).

3.1.3. Discussion

In this study, the survival of CTCF-depleted cells treated with increasing amounts of ionizing radiation was tested, in order to establish a biophysical model on the impact of CTCF on cellular radiosensitivity. The measurements of residual CTCF amounts after esiRNA- or auxin-induced depletion (Figures 3.1.2. and 3.1.5.) were integrated by Dr. Michael Scholz (GSI, Darmstadt) into an adaptation of the Giant-LOop-Binary-LEsion (GLOBLE) model (see methods section 3.1.4.6.;

Friedrich *et al.*, 2012, 2013). This allowed us to qualitatively predict the decreased survival of CTCF-depleted cells, based on the higher probability of DSBs clustering and the related higher lethality (Figures 3.1.4. and 3.1.7.).

We previously demonstrated that CTCF is essential for the correct spreading of the signaling of DNA damage, i.e. phosphorylation of the histone variant H2AX (Natale *et al.*, 2017). Based on our high resolution microscopy measurements, when a single DSB occurs on a multi-loop domain, whose bases are held together by CTCF, on average four chromatin loops within this domain get decorated by γ H2AX (Natale *et al.*, 2017). When this domain-wide signal spreading is not possible due to reduced CTCF amounts, the following repair cascade gets impaired and consequently the survival potential too. Moreover, the reduced CTCF presence translates into diminished bordering of the chromatin domains and hence into more DSBs clustering together. As the GLOBLE model assigns a higher lethality to clustered DSBs, which affect the higher doses part of the survival curve, we could predict a relationship between CTCF depletion and an increased cell lethality upon ionizing radiation (Figures 3.1.4. and 3.1.7.). The lower effect seen in the CTCF-depleted osteosarcoma cells compared to the cervical cancer cells (Figures 3.1.3. and 3.1.4.; Supplementary Figure SF4) was hypothesized to reflect the fact that is often neglected, that the endogenous levels of CTCF are significantly different in the two cell lines (Figure 3.1.1.). As U2OS cells exhibit approximately twice the amount of CTCF compared to HeLa Kyoto cells, residual CTCF levels after depletion in U2OS were still higher, leading to a lower impact on survival, relatively to the other tumor type.

The modeling approach considered the effect of different levels of CTCF depletion on radiosensitivity, assuming an identical impact on all cell cycle phases, as cells were not synchronized and the relative effects would be averaged. The main model parameters, i.e. the lethalties assigned to iDSBs and cDSBs, were determined from fits to survival curves under reference conditions (see methods section 3.1.4.6.). Importantly, uncertainties in these parameters are small and do not substantially affect the model predictions, which means the model settings are robust (data not shown, see: Mamberti *et al.*, 2022). The model predictions were built on the distribution of DSBs as isolated or clustered together within the same chromatin domains defined as “Giant Loops” of 2 Mbp (based on: Johnston *et al.*, 1997; Rogakou *et al.*, 1998; Tommasino *et al.*, 2013, 2015a, 2015b). However, how CTCF depletion could differentially affect chromatin domains of different sizes was also modeled and CTCF-dependent radiosensitivity was predicted not to change in a size range between 0.2 and 2 Mbp (Figure 3.1.8.). In other words, the effects of CTCF depletion on such domains would equally contribute to the enhanced radiosensitivity, independent on the size under reference conditions. Despite these simplistic assumptions that could indeed average different situations *in vivo*, the model

was successful to predict the general trend and the order of magnitude by which different CTCF levels affect clonogenic survival curves in the two tumor cell lines under study (Figure 3.1.4.). To postulate a dependency between the presence of the chromatin domain-anchoring protein CTCF and the tendency of DSBs to cluster within a domain was sufficient to recapitulate the experimental data of both tumor cells. We can hence conclude that the dominating mechanism by which reduced CTCF amounts result in increased radiosensitivity is based on the premise that in the absence of defined domain boundaries, DSBs probabilities to cluster are enhanced (Figure 3.1.9.). As the lethality of cDSBs is higher and related to the β -term of survival functions, this is reflected in the higher impact of CTCF depletion in the high-doses part of survival curves.

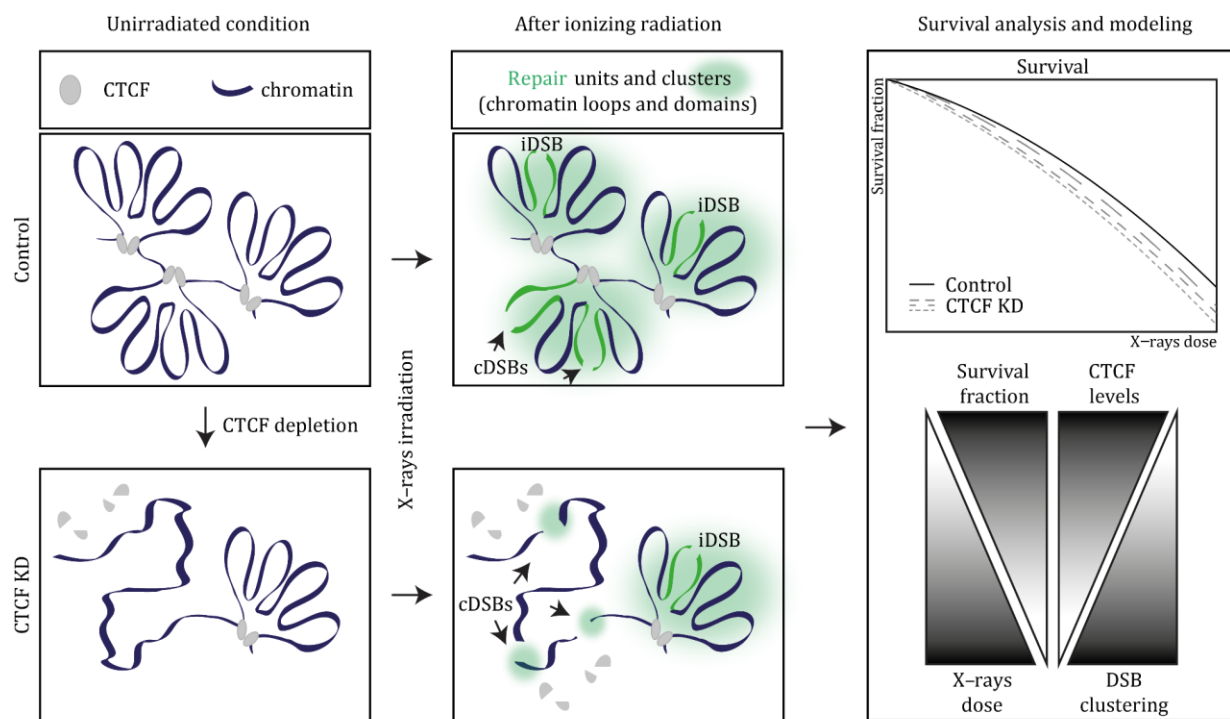


Figure 3.1.9. Lower CTCF levels lead to less chromatin domains and higher probability that DSBs will not be separated into different chromatin domains (cDSBs). The cDSBs have a higher lethality due to the loss of DNA in between and will then result in a decreased survival.

Next, the impact of CTCF depletion was further confirmed by using mouse embryonic stem cells engineered with an auxin-inducible degron system for the depletion of CTCF (Figure 3.1.5.; Supplementary Table ST1; Nora *et al.*, 2017). Embryonic stem cells are characterized by weakly condensed heterochromatin and large nucleosome-free regions (Ricci *et al.*, 2015), which is indicative of their high transcriptional activity (Efroni *et al.*, 2008; Marks *et al.*, 2012). The unique chromatin architecture of stem cells consists of infrequent and primarily short-ranged loop domains,

whose boundaries are more permissive of interactions and will get reinforced only during differentiation (Pękowska *et al.*, 2018). As stem cells have high pan-nuclear γ H2AX levels, associated with global chromatin decondensation (Banáth *et al.*, 2009) but not DSBs, they are expected to have a consistent response to DSBs and were shown to have faster DSB repair rates than somatic cells (Saretzki *et al.*, 2004). Together with suppression of mutagenesis, the elimination of damaged cells through apoptosis appears to be a mechanism to ensure genome integrity in pluripotent embryos (Aladjem *et al.*, 1998; Cervantes *et al.*, 2002; Lin *et al.*, 2005), as also reviewed in Tichy and Stambrook, 2008. It is widely accepted in radiation biology that DSBs are the most genotoxic lesions (as reviewed in: Karagiannis and El-Osta, 2004; Sedelnikova *et al.*, 2003; Valerie and Povirk, 2003). Their repair in somatic mammalian cells preferentially uses the non-homologous end-joining (NHEJ) pathway, which commonly occurs between G1 and early S-phase and can be error prone when the broken ends require processing before religation (Rothkamm *et al.*, 2003; Scully *et al.*, 2019; Swift *et al.*, 2021; Takata *et al.*, 1998; Wang *et al.*, 2001). Since the S-phase is the predominant cell cycle phase in highly proliferative embryonic stem cells (approximately 75% of the time; Savatier *et al.*, 2002), their repair mechanism of choice is likely the homologous recombination (HR) pathway (Francis and Richardson, 2007; Friedberg and Meira, 2006; Yang *et al.*, 2004), which ensures high fidelity through the use of a template and mainly occurs between late S-phase and G2 (as reviewed in: Tichy and Stambrook, 2008). The different chromatin architecture and DDR pathways choice might be a reason why the survival of mESC-AID-CTCF cells upon CTCF depletion does not meet the model predictions (Figure 3.1.7.) and also why the experimental data showed a different sensitivity between tumor and embryonic cells (Figures 3.1.3. and 3.1.6., respectively). Indeed, stem cells are more sensitive to damage, but they readily eliminate the damaged cells and those which do not undergo apoptosis likely have higher survival potential and successfully proliferate into colonies. On the other hand, the tumor cell lines under study would accumulate important damage and show less survival in the long term. Moreover, the lethality of CTCF depletion (Heath *et al.*, 2008; Moore *et al.*, 2012; Splinter *et al.*, 2006) required to timely limit the depletion. This could not be taken into account for the modeling, which therefore predicts what would happen with a longer CTCF depletion (Figure 3.1.7.).

Mechanistic insights into the decreased survival of CTCF depleted cells are found in the assumptions of the GLOBLE model itself and the literature from which it retrieves its basis (see sections 3.1.1. and 3.1.4.6.; Friedrich *et al.*, 2012, 2013; Herr *et al.*, 2014). The modeling approach presented here predicts cell survival based on the reverse proportion between the amounts of CTCF and the domain size, with the latter being instead proportional to the probability of cDSBs to occur (Figure 3.1.9.). More than the induced number of DSBs, previous studies attributed cellular death to the delayed DSB

rejoining and retained persistent damage at later time points (Banáth *et al.*, 2004; Johnston *et al.*, 1997; MacPhail *et al.*, 2003; Mirzayans *et al.*, 2006; Tommasino *et al.*, 2015a, 2015b; Wada *et al.*, 2005), often related to nano- (Nikjoo *et al.*, 2001; Ottolenghi *et al.*, 1995; Sutherland *et al.*, 2000; Ward, 1994) or micrometer (Friedland *et al.*, 2006; Johnston *et al.*, 1998a, 1998b; Tommasino *et al.*, 2013) clustering of the initial lesions. The yields of DSB induction considered in the model implicitly include not only the prompt DSBs but also those originating from clustered non-DSBs lesions (Georgakilas *et al.*, 2013; Singh *et al.*, 2011b, 2013; Stenerlöw *et al.*, 2003; Tommasino *et al.*, 2015a, 2015b).

In previous studies based on filter elution techniques and flow cytometry detection of γ H2AX (Tommasino *et al.*, 2015a, 2015b), the GLOBLE model could well reproduce the gradually slowed-down processing of DSBs after high doses, supporting the higher toxicity of clustered DSBs at the micrometer scale in higher order chromatin structures (extensively discussed in: Hufnagl *et al.*, 2015; Tommasino *et al.*, 2015a, 2015b). The model distinguishes iDSB from cDSB, where a cluster is defined by a domain containing two or more DSBs. Even when the distance between two DSBs within the same chromatin domain is so high that these can be considered as single DSBs in terms of their individual repair, inter-DSBs DNA would anyway become a spatially independent fragment and any stabilization of its ends would be at risk. A further development of the model could make another distinction within the cDSB class, to predict in more detail the impact of DSB density on lethality. On one hand, the more DSBs accumulate within a chromatin domain, the more DNA would be fragmented, leading to a complex task for the repair machinery. On the other hand, two DSBs very close to the bases of a domain would evict a large portion of DNA, and an additional fragmentation would not further enhance the damage severity. This distinction would hence allow us to define what is more critical for repair, the DSB density defined as the ratio between the domain size and the number of DSBs within the domain, or the domain size itself as self-determinant of the length of DNA which can be deleted with two DSBs at its bases. Moreover, the modeling could be additionally refined with differentiation of chromatin states into eu- or heterochromatin and their relative impact on domain sizes, as well as by considering the activity of different proteins and transcription events. As previously mentioned, DSBs are considered the key damage in the field of radiation biology, but ionizing radiation induces various types of DNA lesions other than DSBs (Borrego-Soto *et al.*, 2015; Huang and Zhou, 2020; Santivasi and Xia, 2014). However, these occur both in control as well as in CTCF-depleted cells and it is unlikely that the deviations seen under CTCF depletion conditions could be mainly traced back to these other damages like SSB or crosslinks. Damage to lipids and proteins is also a consequence of ionizing radiation, but the related effects will become visible only at

extremely high doses, due to the high cellular numbers of these molecules. At the dose ranges typically used for cell survival studies (0 – 10 Gy), these effects can be considered negligible as compared to damage to the DNA.

Interestingly, the dose-dependency found here between CTCF and radiosensitivity is consistent with the observation of Nora and colleagues on chromatin folding (Nora *et al.*, 2017). They observed that chromatin changes scaled together with CTCF depletion, with insulation of domains being still more preserved in cells with 15% residual CTCF than in those cells with almost complete depletion (Nora *et al.*, 2017). Nonetheless, it is worth noting that even if TADs are lost upon CTCF depletion, higher order A/B compartments are largely unaffected (Nora *et al.*, 2017). This might partially explain the overall small decrease in survival of depleted cells and points to the fact that our understanding of the chromatin organization and related repair is still incipient.

Overall, this study could confirm that the survival potential after exposure to ionizing radiation of different cell lines is dependent on CTCF. Moreover, it showed that survival is finely tuned proportional to CTCF dosage, which is consistent with the reported CTCF-dose scaling of chromatin domains. The application of the GLOBLE modeling approach by Dr. Michael Scholz (GSI, Darmstadt) to the scenario of CTCF depletion allowed us to gain mechanistic insights relative to the decreased survival. CTCF anchoring activity limits the clustering of multiple DSBs, whose repair often has a dramatic outcome and ends with irreversible domain fractionation. Future research in cancer treatment should take into consideration the relative amount of this architectural protein in the particular tumor cell line under study and apply this model in order to predict the tumor survival to radiation therapy.

3.1.4. Materials and Methods

3.1.4.1. Cell culture

All cells were grown at 37 °C in a humidified atmosphere with 5% CO₂. HeLa Kyoto and U2OS cells (Supplementary Table ST1) were cultured in Dulbecco's modified Eagle's medium (DMEM) high glucose (Cat. No.: D6429) supplemented with 50 µg/ml gentamicin (Cat. No.: G1397), 2 mM L-glutamine (Cat. No.: G7513) and 10% fetal calf serum (FCS; Cat. No.: F7524). mESC-AID-CTCF and wild type ES-E14TG2a cells (Supplementary Table ST1) were cultured in DMEM high glucose (Cat. No.: D6429) supplemented with 15% FCS (Cat. No.: F7524), 1× non-essential amino acids (Cat. No.: M7145), 1× penicillin/streptomycin (Pen/Strep) (Cat. No.: P4333), 1× L-glutamine (Cat. No.: G7513), 0.1 mM beta-mercaptoethanol (Cat. No.: 4227, Carl Roth, Karlsruhe, Germany), 1000 U/ml recombinant mouse LIF (Millipore) and 2i (1 M PD032591 and 3 M CHIR99021, Cat. Nos.: 1408 and

1386 respectively, Axon Medchem, Netherlands) on gelatin-coated culture dishes (0.2% gelatin/ddH₂O; Cat. No.: G2500). Unless otherwise stated, all catalog numbers (Cat. No.) indicated above refer to Sigma-Aldrich Chemie GmbH, Steinheim, Germany.

3.1.4.2. CTCF knockdown

An esiRNA pool against human CTCF (Supplementary Table ST5; Cat. No.: EHU130111, MISSION® esiRNA) was used to deplete HeLa Kyoto and U2OS cells from the protein. The pool targets the region 692–1195 of the human CTCF transcript (NM_006565.3). Both cancer cell lines were transfected with 15 nM of esiRNA against either human CTCF or EGFP as a mock-depleted control (Supplementary Table ST5; Cat. No.: EHUEGFP, MISSION® esiRNA) using the electroporation Neon™ Transfection System (Cat. No.: MPK5000, Thermo Fisher Scientific, Waltham, United States). Voltage, width and pulse for the different cell lines were applied as follows: HeLa Kyoto 1005 V, 35 ms, 2×; U2OS 1230 V, 10 ms, 4×. For the knockdown validation (Figure 3.1.2.), cells were seeded on coverslips immediately after transfection and fixed with 3.7% formaldehyde/1× phosphate-buffered saline PBS (Cat. No.: F8775) at different time points (24 h, 48 h, 72 h). The results shown in Figure 3.1.2. are based on three biological replicates (Supplementary Table ST4). The same HeLa Kyoto and U2OS transfection aliquots were diluted in parallel for single cell seeding to perform the clonogenic assay (Figure 3.1.3.; section 3.1.4.5.). For CTCF depletion and its validation with the degron system (Figure 3.1.5.), mESC-AID-CTCF cells were seeded on gelatinized coverslips (0.2% gelatin/ddH₂O; Cat. No.: G2500) and treated with auxin-supplemented medium (0, 25, 500, 1000 μM; 3-Indoleacetic acid IAA, Cat. No.: I3750) for four hours, then washed and fixed with 3.7% formaldehyde/1× PBS (Cat. No.: F8775). The results shown in Figure 3.1.5. are based on four biological replicates (Supplementary Table ST4). The same auxin-supplemented medium was given in parallel to the single cells seeded for the clonogenic assay (Figure 3.1.6.; section 3.1.4.5.). In an independent time course experiment (three biological replicates; Supplementary Table ST4; Supplementary Figure SF5), stem cells seeded on gelatinized coverslips (0.2% gelatin/ddH₂O; Cat. No.: G2500) were treated with 25, 500, 1000 μM auxin and fixed with 3.7% formaldehyde/1× PBS (Cat. No.: F8775) at different time points of auxin treatment (0.5, 1, 2, 3, 4 h), washed 3× with warm 1× PBS after four hours, replaced with fresh medium and allowed for CTCF recovery until 24 hours, while multiple time points were collected after auxin wash off (0.5, 1, 2, 4, 6, 8, 18, 24 h). Unless otherwise stated, all catalog numbers (Cat. No.) indicated above refer to Sigma-Aldrich Chemie GmbH, Steinheim, Germany.

3.1.4.3. CTCF immunostaining

The previously fixed HeLa Kyoto and U2OS cells were washed with 1× PBS, permeabilized 15' with 0.7% Triton™ X-100 (Cat. No.: T8787, Sigma-Aldrich Chemie GmbH, Steinheim, Germany) and washed again prior to 30' blocking in 1% BSA (bovine serum albumin; Cat. No.: A4503, Sigma-Aldrich Chemie GmbH, Steinheim, Germany). Incubation overnight at 4°C with the primary rabbit anti-CTCF antibody followed. The information on antibodies is listed in Supplementary Table ST2. Cells were then washed 2× with 1× PBS for 5' and 3× with 0.01% Tween® 20 (Cat. No.: 9127.1, Carl Roth, Karlsruhe, Germany). The secondary goat anti-rabbit IgG (H + L) AF594 antibody was incubated 1 h at room temperature, followed by washing as described above. DNA was counterstained with 10 µg/ml DAPI (4',6-diamidino-2-phenylindole; Cat. No.: D27802, Sigma-Aldrich Chemie GmbH, Steinheim, Germany) for 10' at room temperature, cells dipped in ddH₂O and mounted with Vectashield® antifade medium (Cat. No.: NC9265087, Thermo Fisher Scientific, Walham, United States) on coverslips. All dilutions mentioned above were done in 1× PBS, except antibody dilutions in 1% BSA/1× PBS. mESC-AID-CTCF cells and wild type ES-E14TG2a cells were only subjected to permeabilization, DNA counterstaining and mounting as described above.

3.1.4.4. Microscopy imaging and quantification

The samples were imaged at the high-content wide-field microscopy system Operetta® and images were analyzed with the Harmony™ software – Version 3.5.1 – © 09-2013 (both PerkinElmer, see Supplementary Table ST3), as described in the Supplementary Figure SF1. In particular, the DAPI signal was used to create a nuclear mask and select nuclei. The nuclear intensities of both DAPI – DNA and AF594 – CTCF or GFP – CTCF signals were measured and exported. The results tables were analyzed in RStudio (Version 0.99.902 – © 2009-2016 RStudio Inc., Boston, United States) to produce the plots shown in Figures 3.1.1., 3.1.2., 3.1.5. and Supplementary Figures SF5. See Supplementary Figure SF2 for boxplot interpretation.

3.1.4.5. Clonogenic assay

HeLa Kyoto and U2OS cells were irradiated with X-ray doses of 0 – 10 Gy (1 Gy/58 s, 250 kV, 10 mA; Isovolt Titan, GE Sensing & Inspection Technologies, Ahrensburg, Germany) at 24 hours post esiRNA transfection (Figure 3.1.3.), at the respective time point of maximum depletion for each cell line (Figure 3.1.2. B – C). Cells were incubated with 5% CO₂ at 37 °C for 7 - 10 days until colonies were formed. Colonies were then fixed with cold 100% methanol and stained with 0.2% methylene blue in 50% methanol/1× PBS followed by washing in water (Figure 3.1.3. A). The colonies with more than 50 cells were verified by microscopy and counted by eye. The results for both HeLa Kyoto and

U2OS consist of three biological replicates, each composed of technical replicates (Supplementary Table ST6). mESC-AID-CTCF cells were treated with different auxin concentrations (0, 25, 500, 1000 μM ; IAA, Cat. No.: I3750, Sigma-Aldrich Chemie GmbH, Steinheim, Germany) for four hours prior to irradiation (same conditions as above), washed three times with $1\times$ PBS and given fresh medium one hour after irradiation (Figure 3.1.6. A). Cells were then allowed to form colonies and treated as described above for the tumor cell lines. The results for mESC-AID-CTCF cells consist of four biological replicates (Supplementary Table ST6). The number of colonies was plotted as a survival ratio, in which each value is normalized to the average of the respective unirradiated controls.

The homegrown “gd” software (gd online documentation at: <http://bio.gsi.de/DOCS/gd.html>; GSI Helmholtzzentrum für Schwerionenforschung GmbH, Biophysics Department, Darmstadt, Germany) was used for plotting the survival curves in Figure 3.1.3., Figure 3.1.6. and Supplementary Figure SF4. A linear-quadratic dose-response curve fitting weighted by $1/[\text{relative error}]^2$ was applied (dots = mean; whiskers = error bars; see the footer of Supplementary Table ST6 for the calculation of the relative error).

3.1.4.6. Modeling of cell survival using the Giant-Loop Binary Lesion (GLOBLE) model

In Table 3.2. the equations applied by Dr. Michael Scholz (GSI, Darmstadt) to perform the modeling of cell survival to ionizing radiation upon CTCF depletion are listed. A detailed explanation of the equations and their application is found in: Mamberti *et al.*, 2022.

GLOBLE model calculations were applied and the homegrown “gd” software (gd online documentation: <http://bio.gsi.de/DOCS/gd.html>; GSI Helmholtzzentrum für Schwerionenforschung GmbH, Biophysics Department, Darmstadt, Germany) was used by Dr. Michael Scholz (GSI, Darmstadt) to produce the plots in Figures 3.1.4., 3.1.7., 3.1.8. and in Supplementary Figure SF4. GLOBLE parameters are listed in Table 3.1. The linear-quadratic parameters α and β and the corresponding lethalties ϵ_i and ϵ_c were determined from the survival curves for GFP KD conditions (curve fit weighted by $1/[\text{relative error}]^2$), after pooling all respective biological replicates (three biological replicates of HeLa Kyoto and U2OS, four biological replicates of mESC-AID-CTCF cells; Supplementary Table ST6).

Table 3.2. Equations of the GLOBLE model applied to CTCF depletion.

| Equation | n. | Definitions |
|---|------|---|
| $N_D = \frac{G}{g_D}$ | (1) | N_D : number of chromatin domains; G : genome size; g_D : domain genomic content (standard: 2 Mbp) |
| $\overline{N_{DSB}(D)} = Y_{DSB} \cdot D$ | (2) | $\overline{N_{DSB}(D)}$: Mean number of DSBs induced by a dose D in the whole nucleus; Y_{DSB} : yield of 30 DSB/Gy/cell |
| $\overline{n_{DSB}(D)} = \frac{\overline{N_{DSB}(D)}}{N_D}$ | (3) | $\overline{n_{DSB}(D)}$: mean number of DSB induced per domain |
| $P_{DSB}(k, \bar{n}) = \frac{\bar{n}^k}{k!} e^{-\bar{n}}$ | (4) | Poisson statistics for the mean value of DSB induced in a domain at a given dose D (probability to induce iDSB or cDSB) |
| $n_i(D) = P_{DSB}(1, \bar{n}) \cdot N_D = \bar{n} e^{-\bar{n}} \cdot N_D$ | (5) | $n_i(D)$: number of iDSB |
| $n_c(D) = (1 - P_{DSB}(0, \bar{n}) - P_{DSB}(1, \bar{n})) \cdot N_D$ | (6) | $n_c(D)$: number of cDSB |
| $S(D) = e^{-(n_i(D)\varepsilon_i + n_c(D)\varepsilon_c)}$ | (7) | ε_i and ε_c : lethalities assigned to iDSBs and cDSBs; D : dose; n_i and n_c : number of damages for iDSBs and cDSBs; $S(D)$: final effect on survival |
| $S(D) = e^{-(\alpha D + \beta D^2)}$ | (8) | standard LQ-formulation of survival curves |
| $\varepsilon_i = \frac{\alpha}{\alpha_{DSB}}$ | (9) | ε_i : lethality of iDSBs, derived from (8), uniquely linked to the initial slope of the dose response curve as given by the linear term α |
| $\varepsilon_c = 2 \left(\frac{N_D \beta + \alpha_{DSB} \alpha}{\alpha_{DSB}^2} \right)$ | (10) | ε_c : lethality of cDSBs, derived from (8), defined by a mixture of contributions from the linear term α and the quadratic term β ; N_D : number of domains per cell nucleus; α_{DSB} : yield of DSB per Gy |
| $g'_D = \frac{1}{f_{CTCF}} g_D$ | (11) | g'_D : modified domain size; f_{CTCF} : fraction of CTCF remaining after depletion |
| $N'_D = f_{CTCF} \cdot N_D$ | (12) | N'_D : modified number of domains |

3.2. CTCF plays a role in DNA replication: a seXY hypothesis

3.2.1. Introduction

DNA replication is spatio-temporally regulated and appears in mammalian nuclei as focal structures during microscopical observation (Baddeley *et al.*, 2010; Chagin *et al.*, 2016). These foci consist of chromatin units that are stable over different cell cycles (Jackson and Pombo, 1998; Sadoni *et al.*, 2004; Sparvoli *et al.*, 1994) and within which multiple alternate origins fire synchronously (Huberman, 1991; Huberman and Riggs, 1968; Jackson and Pombo, 1998; Leonard and Méchali, 2013; Masai *et al.*, 2010). At each S-phase spatially defined patterns of replication foci appear in a timely consistent sequence (Ma *et al.*, 1998; Nakayasu and Berezney, 1989), during which the replication machinery moves along spatially adjacent chromatin sites (Sadoni *et al.*, 2004). These patterns allow us to discriminate between early, mid and late S-phase substages (Manders *et al.*, 1992; Nakamura *et al.*, 1986; Nakayasu and Berezney, 1989), respectively corresponding to the replication of euchromatin, facultative heterochromatin and constitutive heterochromatin (Kill *et al.*, 1991; Nakayasu and Berezney, 1989; O'Keefe *et al.*, 1992). The precisely timed replication of specific DNA sequences within eukaryotic S-phase was named replication timing, RT (Goldman *et al.*, 1984; Hatton *et al.*, 1988; Rhind and Gilbert, 2013), while clusters of replication units duplicating with similar RT were renamed replication domains, RDs (Desprat *et al.*, 2009; Hiratani *et al.*, 2008). The RT and the related spatial organization of RDs are established in early G1 at the so-called replication timing decision point, RTD (Dimitrova and Gilbert, 1999; Lu *et al.*, 2010). RDs differ between cell types and differentiation states (Gilbert *et al.*, 2010; Hiratani *et al.*, 2010; Ryba *et al.*, 2010). As we highlighted in Mamberti and Cardoso, 2020, the size of mammalian replication units composing such clusters corresponds to twice the one of a chromatin loop (Chagin *et al.*, 2016) and strikingly coincides with the median size of the so-called loop domains (Rao *et al.*, 2014). RDs align with the Hi-C mapped topologically associated domains, TADs (Dixon *et al.*, 2012; Pope *et al.*, 2014). Multiple TADs often replicate with similar RT when clustered at a higher order of organization within the same A/B compartments (Ryba *et al.*, 2010; Takebayashi *et al.*, 2012), which indeed match the RT measured on a genome wide scale (Pope *et al.*, 2014; Ryba *et al.*, 2010; Yaffe *et al.*, 2010). Consistent with the early notion that replication units are stable over cell cycles, it was shown that not only RDs but also TADs, A/B compartments and the relative RT are reestablished at every G1 phase upon being disrupted during mitosis (Dileep *et al.*, 2015). However, TADs often change compartment location and relative RT during developmental changes of chromatin organization (Dixon *et al.*, 2015; Ryba *et al.*, 2010; Takebayashi *et al.*, 2012). It was recently shown by our laboratory that the replication timing changes along with differentiation in mouse embryonic stem cells, where the developmental

compaction of chromocenters matches with a switch in their replication timing from a mid to a late stage of S-phase (Rausch *et al.*, 2020).

Within the spatio-temporal regulation of DNA replication, the organization of replication of the mammalian sex chromosomes occupies a special niche. In particular, the inactive \underline{X} chromosome (X_i) displays the features of facultative heterochromatin and as such replicates during mid S-phase in somatic cells (Heinz *et al.*, 2019; Morishima *et al.*, 1962; Takagi *et al.*, 1982). The Y chromosome is characterized by a late replication timing (Camargo and Cervenka, 1982) and its replication in embryonic stem cells even defines a unique last stage of S-phase, occurring after the whole genome has already replicated (Rausch *et al.*, 2020).

\underline{X} chromosome inactivation (XCI) is a regulatory phenomenon in female mammalian cells, which allows dosage compensation of X-linked genes between XX and XY harboring cells (Gupta *et al.*, 2006; Lyon, 1961; Nguyen and Disteché, 2006). It was reported early on that the transcriptionally inactive X chromosome replicates timely separated from the active \underline{X} homologue (X_a) (Morishima *et al.*, 1962). The X inactivation and related timing switch occurs before cell lineage differentiation (Takagi *et al.*, 1982), is accompanied by chromatin condensation (the so-called “Barr body”; Barr and Bertram, 1949) and maintained in the differentiated progeny (Chadwick and Willard, 2003). In 1983, cytological investigations of metaphase spreads from mouse embryos after X/autosome chromosomes translocations led to propose that the inactivation of a whole X chromosome would start in *cis* from a single \underline{X} -inactivation center locus, *Xic* (Rastan, 1983). Its location and requirement were later confirmed by deletion studies (Rastan and Robertson, 1985). Soon afterwards the *Xist/XIST* (\underline{X} -inactive specific transcript) gene was suggested as a candidate gene for the inactivation due to its unique location within the *Xic* locus and its expression occurring only in inactive X chromosomes in both murine and human cells (Borsani *et al.*, 1991; Brockdorff *et al.*, 1991; Brown *et al.*, 1991). Interestingly, *Xist* is unique to eutherian or placental mammals and allows random inactivation of one of the two X chromosomes, while marsupial and other early mammals exclusively undergo imprinted inactivation of the paternally-inherited \underline{X} (X_p) (Duret *et al.*, 2006). Imprinted X_p inactivation also occurs in eutherian mammals through high expression of the paternal *Xist* allele (Kay *et al.*, 1994) but only in the preimplantation embryo (two-to-four-cells stage, embryonic day E1.5) until the early blastocyst stage (E4.5), at which X_p is reactivated in the inner cell mass (ICM) cells and a second wave of XCI starts under *Xist* regulation (Huynh and Lee, 2003; Mak *et al.*, 2004; Marks *et al.*, 2015; Okamoto *et al.*, 2004; Payer *et al.*, 2011). Only extra-embryonic tissues maintain the imprinted XCI of the paternal X (Takagi and Sasaki, 1975).

Xist long noncoding lncRNA triggers the inactivation by coating (Clemson *et al.*, 1996) and silencing in *cis* of the X chromosome (Marahrens *et al.*, 1997; Penny *et al.*, 1996), followed by recruitment of Polycomb repressive complexes (PRC1/2) and induction of heterochromatin establishment (Disteche, 2016; Payer *et al.*, 2011; Raznahan and Disteche, 2021). From the same *Xist* gene, *Tsix* RNA is transcribed in the antisense orientation (Debrand *et al.*, 1999; Lee *et al.*, 1999; Mise *et al.*, 1999). *Tsix* is initially highly expressed in both X chromosomes, repressing *Xist* expression robustly in pluripotent embryonic stem cells (Lee *et al.*, 1999; Marks *et al.*, 2015; Payer *et al.*, 2011). During development and differentiation *Tsix* expression becomes monoallelic, as it is repressed in one of the two X chromosomes, allowing *Xist* expression and the consequent silencing of that chromosome (Lee *et al.*, 1999; Marks *et al.*, 2015; Payer *et al.*, 2011). *Tsix* indeed influences the X chromosome choice, as its heterozygous deletion leads to inactivation of the X bearing the deletion (Lee and Lu, 1999). The probabilistic choice for *Tsix* monoallelic expression at the onset of XCI and the persistence of *Tsix* on the future active X are promoted in *cis* by *Xite* (X-inactivation intergenic transcription elements) (Ogawa and Lee, 2003; Stavropoulos *et al.*, 2005). Chao and colleagues identified CTCF binding sites in the *Tsix* locus and showed the binding of *Tsix* elements to CTCF *in vitro* and *in vivo* (Chao *et al.*, 2002). By binding *Tsix* on the future Xa, CTCF might insulate and prevent the shared enhancer to contact *Xist* promoter (Chao *et al.*, 2002). They also found that CTCF binding is sensitive to DNA methylation *in vitro* and alternatively proposed CTCF to work as an epigenetic switch in the X choice (Chao *et al.*, 2002). It was later shown that differential methylation domains on *Tsix* regions spanning CTCF binding sites and on its modulator *Xite* mimic X inactivation patterns (Boumil *et al.*, 2006). Together with co-transcription of *Tsix* and *Xite*, CTCF was shown to be essential at *Tsix* and *Xite* sites for the X homologous pairing, which allows in *trans* “communication” of the two chromosomes and is necessary for the exclusive designation of the Xa and Xi (Xu *et al.*, 2007).

More recent investigations on the Xi chromatin architecture showed that the *Xic* locus is bipartited into two topologically associated domains (TADs), which separate *Xist* and *Tsix* promoters and related *cis*-regulators allowing their different regulation during development (Nora *et al.*, 2012). This topological partitioning was found to be critical for the developmental timing of inactivation, as shown by experiments in which the transcriptional units and respective promoters were swapped between the two TADs (van Bommel *et al.*, 2019). Placing the promoter in each other’s TAD led to advanced up-regulation of *Xist* and to abnormally prolonged expression of *Tsix* during differentiation (van Bommel *et al.*, 2019). Two CTCF binding sites (CBSs) within *Xite* were shown to contribute to proper insulation of the two TADs and to promote strong intra-TAD interaction (van Bommel *et al.*, 2019). However, numerous other CBSs within each and at the border between the two TADs were

proposed to redundantly support the partitioning (van Bemmelen *et al.*, 2019). Other than this bipartitioning of the *Xic* locus and few exceptions (e.g. regions escaping inactivation and cell line-specific observations; Bauer *et al.*, 2021b; Deng *et al.*, 2015; Giorgetti *et al.*, 2016; Marks *et al.*, 2015; Minajigi *et al.*, 2015), the inactive X was defined as largely unstructured and either having weak or lacking A/B compartment and TAD boundaries (Darrow *et al.*, 2016; Giorgetti *et al.*, 2016; Wang *et al.*, 2018, 2019). The whole Xi is in fact organized in two superdomains which differ in genomic content between mouse and human, but are similarly separated in both species by a hinge region close to the *Dxz4/DXZ4* locus (Darrow *et al.*, 2016; Deng *et al.*, 2015; Rao *et al.*, 2014). In mouse, this hinge region was found to bind CTCF and to associate with the nucleolus (Deng *et al.*, 2015). By combining datasets of allelic distribution with 3D models, the density of CTCF, RNA PolIII and genes escaping inactivation was found to be enriched on the outer periphery regions of the Xi but not of the Xa (Deng *et al.*, 2015). Regarding DNA replication, the *Xic* locus contains some origins shared between Xa and Xi, whose usage dynamically changes during differentiation and is affected by deletion of XCI regulatory elements (Rowntree and Lee, 2006). The Xi replication was shown by our laboratory to occur highly synchronously, faster and earlier than previously estimated, that is within a frame of 1-2 hours in early-mid S-phase (Casas-Delucchi *et al.*, 2011). Moreover, the same study highlighted that the establishment of a synchronous replication in a *Xist*-inactivated autosome is epigenetically controlled and correlates with a decrease in histone acetylation occurring only upon differentiation (Casas-Delucchi *et al.*, 2011), hence adding another evidence to development-related changes in replication timing. In a subsequent study from our laboratory, histone hypoacetylation and DNA demethylation unveiled as major epigenetic determinants of the X chromosomes in the vole species *Microtus cabrae*, which presents “giant” sex chromosomes with large heterochromatin blocks (Heinz *et al.*, 2019). The induction of histone hyperacetylation led to a faster nucleotide incorporation in early S-phase rather than in mid/late S-phase, a prolongation of the replication of the different X-chromosome associated heterochromatin blocks, alongside with a timing switch of facultative heterochromatin replication from mid to early S-phase (Heinz *et al.*, 2019).

The Y chromosome of mammals is highly degenerated, as it retains only circa 1-5% of the ancestral X-linked genes (Bellott *et al.*, 2014; Soh *et al.*, 2014). The two sex chromosomes currently share a pseudoautosomal region, PAR (Burgoyne, 1982; Otto *et al.*, 2011) (only a single 700 kb-PAR in mouse, two PARs in human that sum up to 2.7 Mb; reviewed in: Raudsepp and Chowdhary, 2015), which still undergoes synapsis and recombination during meiosis (Flaquer *et al.*, 2008; Kauppi *et al.*, 2011; Soriano *et al.*, 1987). The genetic exchange between X and Y was shown to occur in mice through a notable rearrangement of loops along the axes, which allows higher frequency of double

strand breaks in such a short region (Acquaviva *et al.*, 2020; Humphrey and Cole, 2020). The Y chromosome used to be a proper “homolog” of the X as within a common pair of autosomes (Charlesworth, 2021a; Lahn and Page, 1999; Ohno, 1967), before a series of concatenated events occurred over millions of years, such as the evolution of a sex determining locus (harboring the *SRY* gene, sex region Y; Gubbay *et al.*, 1990; Miyawaki *et al.*, 2020; Sinclair *et al.*, 1990), the suppression of meiotic recombination, the loss of euchromatin and the expansion of heterochromatin (Charlesworth, 2021b; Graves, 1995; Griffin *et al.*, 2002; Rice, 1987b, 1987a). The human Y chromosome is indeed considered as mainly heterochromatic and gene-poor, however the male-specific Y (MSY) region in mouse was shown to be euchromatic, ampliconic and containing circa 700 protein-coding genes (Soh *et al.*, 2014). Most of these mouse's MSY genes belong to three massively amplified gene families that have homologs in the mouse X chromosome but not in the MSY of primates (Soh *et al.*, 2014). Although a strong debate is always ongoing on whether or not the human Y chromosome is going to disappear (Graves, 2016; Griffin, 2012; Guo *et al.*, 2020; Larmuseau and Ottoni, 2018), it is noticeable that the present state of the human Y chromosome has been preserved for the last 25 million years (Griffin, 2012). The replication of the Y chromosome occurs late in S-phase (Camargo and Cervenka, 1982; Kałuzewski, 1982; Kikuchi and Sandberg, 1964; Schmid, 1963) and occupies a lonely last stage in mouse embryonic stem cells (Rausch *et al.*, 2020). The role of CTCF in Y architecture was studied in terms of transcriptional regulation (Singh *et al.*, 2011a). It was shown that CTCF associates with different marks of histone and DNA methylation within tandem repeats and within the loci *SRY* and *TSPY* (testis-specific protein Y-encoded, a Y-linked proto-oncogene; Kido and Lau, 2019; Salo *et al.*, 1995; Tsuchiya *et al.*, 1995), suggesting that the epigenetic environment might dictate the architecture-mediated regulation of gene expression (Singh *et al.*, 2011a). While the Xi has been extensively studied and characterized in the past years, both DNA replication and chromatin architecture of the Y chromosome have been otherwise almost ignored and definitely need further investigation.

Despite the extensive past studies on either CTCF or DNA replication, a real understanding of their interrelationship is still missing. Since DNA replication is spatio-temporally regulated and encompassing the whole genome, and CTCF has an important role in structuring the genome, to study their interplay could unveil mechanisms regulating DNA replication. Here, I microscopically investigated whether CTCF presence is related to the structure of DNA replication in mammalian nuclei. The present study was then extended to CTCF and the replication of the sex chromosomes, whose comprehension is also lacking in depth insights.

3.2.2. Results

3.2.2.1. CTCF is enriched at the time and at the sites of DNA replication

The interrelationship between the architectural protein CTCF and DNA replication was first visually investigated in mouse myoblasts (Figure 3.2.1.). C2C12 cells (Supplementary Table ST1) were pulse-labeled with 10 μ M of the thymidine analogue 5-ethynyl-2'-deoxyuridine (EdU; Supplementary Table ST8) for 30' at 37°C, fixed and stained for CTCF and EdU detection (Figure 3.2.1. A). Upon confocal microscopy imaging, a first glance of a possible colocalization between CTCF and DNA replication was obtained by plotting the color profile of the CTCF and EdU signals from cells showing early, mid or late S-phase patterns (Figure 3.2.1. B). Indeed, multiple peaks of EdU intensity coincided with peaks of CTCF intensity, as indicated by the black arrows overlaid on the color profile plots in Figure 3.2.1. B. Given the pan-nuclear appearance of CTCF foci, which is due to its genome-wide role in structuring chromatin domains, the colocalization with DNA replication foci is not complete, nor very evident by simple visual inspection. However, the color profile plots are useful to see that some intensity peaks have a strong overlap in the two channels, especially in the early and late S-phase examples shown in Figure 3.2.1. B. In some cases the peaks from the two channels perfectly match. In other cases, two CTCF peaks confine a single EdU peak in the plot, as it is also visible in the microscopy images where two or more CTCF foci are contouring sites of DNA replication.

In human HeLa Kyoto cells (Supplementary Table ST1) the colocalization of CTCF with DNA replication was further questioned with a pulse chase experiment and confocal microscopy imaging (Figure 3.2.1. C – E). In particular, cells were pulse labeled for 15' at 37°C with EdU (Supplementary Table ST8), which was then washed off and replaced with fresh medium for a 4 hours-chase. Cells were fixed immediately after the pulse and at different time points (0, 2, 4 h) during the chase (Figure 3.2.1. C). After confocal imaging and image deconvolution (Figure 3.2.1. D; Supplementary Table ST3), the replication foci were segmented based on the EdU signal and the mean CTCF intensity within the replication foci was measured (Figure 3.2.1. E). Interestingly, the mean focal CTCF intensity was higher at the time point 0 h, while it decreased with increasing hours of chase (Figure 3.2.1. E). In other words, CTCF intensity within replication foci was the highest in those cells fixed immediately after the pulse, i.e. at the time of EdU incorporation. In those cells fixed at 2 or 4 hours of chase, the EdU-labeled foci indicate sites in which DNA was previously replicated and was not undergoing replication at the time of fixation. Focal CTCF intensity was lower in those EdU foci, which completed replication hours earlier and from which the replication machinery already moved away.

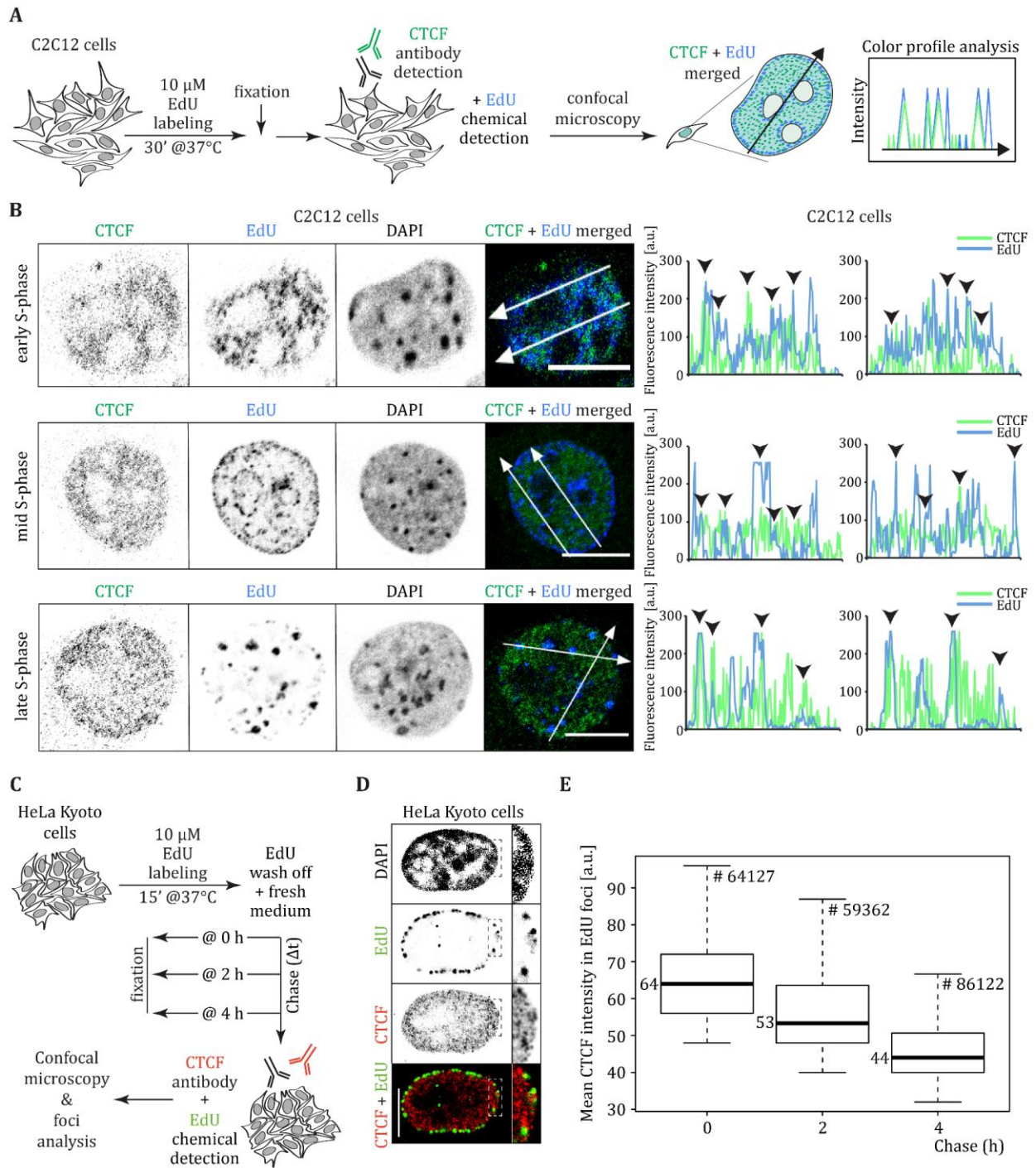


Figure 3.2.1. CTCF is enriched at the time and at the sites of DNA replication. **A - B** Color profile analysis of CTCF and replication foci colocalization. **A** Experimental scheme for the visualization of CTCF and DNA replication colocalization. Mouse C2C12 cells (Supplementary Table ST1) were pulse labeled with 10 μ M EdU for 30' at 37°C and immediately fixed after the pulse. Cells were immunostained against CTCF and chemically treated for EdU detection (Supplementary Table ST2). After confocal microscopy imaging (Supplementary Table ST3), images were processed with the plug-in “Color Profiler” of the Fiji software to visualize EdU (blue) and CTCF (green) colocalization along an overlaid arrowed line. **B** Exemplary confocal images of C2C12 cells in early, mid and late S-phase showing EdU and CTCF detection. For each image panel, a merged image of the EdU

and the CTCF channels was created, and two arrowed lines (white) were overlaid (scale bar: 10 μm). The color line profiles on the right side of each panel indicate the intensity profile of both channels along the respective overlaid arrowed lines. Black arrows in the color profile plots indicate colocalizing intensity peaks. **C - E** Confocal analysis of CTCF enrichment within replication foci over time. **C** Experimental scheme of the pulse-chase experiment. Human HeLa Kyoto cells (Supplementary Table ST1) were pulse labeled with 10 μM EdU for 15' at 37°C, subsequently washed and given fresh medium. Cells were then fixed at 0, 2, 4 hours of chase. After CTCF immunostaining and EdU chemical detection (Supplementary Table ST2), cells were imaged with confocal microscopy (Supplementary Table ST3), images were deconvolved and the replication foci were segmented based on the EdU signal within a DAPI-based nuclear mask. **D** Exemplary cell with mid S-phase pattern (EdU: green; CTCF: red) imaged with confocal microscopy and subjected to image deconvolution. The dashed rectangular overlay indicates the area that is shown as a zoom-in on the right side of each channel (scale bar: 10 μm). **E** Mean CTCF intensity within the EdU-labeled replication foci over time (0, 2, 4 hours of chase), obtained upon segmentation of the EdU foci in deconvolved confocal images with the Volocity software. The median value is indicated next to the corresponding median black line of each boxplot, while the value indicated with a # on top of them is the respective total number of EdU foci analyzed from different cells. A two-sided Wilcoxon test was performed to test significance (0 h - 2 h, 2 h - 4 h, 0 h - 4 h: $p < 0.0001$). See Supplementary Figures SF2 for boxplot explanation and Supplementary Table ST4 for plot statistics.

Moreover, the decrease in intensity progressed in time with a statistically significant difference not only between the cells that were fixed immediately after the replication pulse labeling and those fixed upon a chase (i.e. 0 and 2 hours), but also between the two different time points of chase (i.e. 2 and 4 hours; Figure 3.2.1. E). These results suggest that a temporary enrichment of CTCF occurs at the time and sites of DNA replication, and that this local CTCF accumulation does not get immediately resolved.

3.2.2.2. CTCF depletion affects cell cycle and S-phase progression

An involvement of CTCF in cell cycle progression was investigated by performing CTCF knock down and subsequently addressing the DNA distribution of CTCF-depleted cells (Figure 3.2.2. A). CTCF depletion was obtained through transfection of an esiRNA against the mouse CTCF transcript (Supplementary Table ST5) in mouse myoblasts (C2C12 cells; Supplementary Table ST1). After 72 hours of knock down, cells were fixed and immunostained for CTCF (Figure 3.2.2. A). Cells were imaged with high-content wide-field microscopy and the nuclear CTCF and DNA intensities were measured, in order to validate the knock down and to evaluate the cell cycle progression by means of DNA intensity distributions (Figure 3.2.2. A). The obtained knockdown showed to be heterogeneous within the esiRNA-treated population, compared to the mock control sample, which underwent the same transfection procedure with the esiRNA against CTCF being omitted. While control cells appeared to have a bright pan-nuclear CTCF signal, the knock down sample showed variable levels of lower CTCF intensities (Figure 3.2.2. B). When the two whole populations were compared in terms of mean nuclear CTCF values (control: 117 a.u., CTCF KD: 51 a.u.), the CTCF KD

cells proved to have a median of 44% residual CTCF relative to the control sample (Figure 3.2.2. C; Supplementary Table ST4). Since the CTCF levels appeared to be quite heterogeneous by visual inspection of the knock down sample (Figure 3.2.2. B), the whole population was further subdivided in subpopulations with differential levels of residual CTCF, the lowest of which are plotted in Figure 3.2.2. D (Supplementary Table ST4). From these three subpopulations of the CTCF KD sample, having respectively circa 21%, 30% and 39% residual CTCF levels (Figure 3.2.2. D), the impact of CTCF depletion on cell cycle progression was evaluated. Based on the frequency histogram of the integrated nuclear DNA intensities, it was possible to distinguish the G1 and G2 peaks (respectively with single and double genome content or nuclear DAPI sum intensity), separated by the distribution of cells progressing through S-phase (as depicted in the schematics in Figure 3.2.2. A). The percentage of cells within each stage was hence calculated for the three CTCF KD subpopulations and the control sample (Figure 3.2.2. E). The CTCF KD subpopulation with 21% residual CTCF was the most impacted in terms of cell cycle progression, with the highest percentage of cells stalling in G1 and the least cells proceeding to S-phase and G2 phase. With increasing CTCF amounts, the percentage of cells stalling in G1 decreases in favor of more cells entering S-phase, which however do not fully progress as the respective fraction of cells in G2 is still lower than in the control sample (Figure 3.2.2. E).

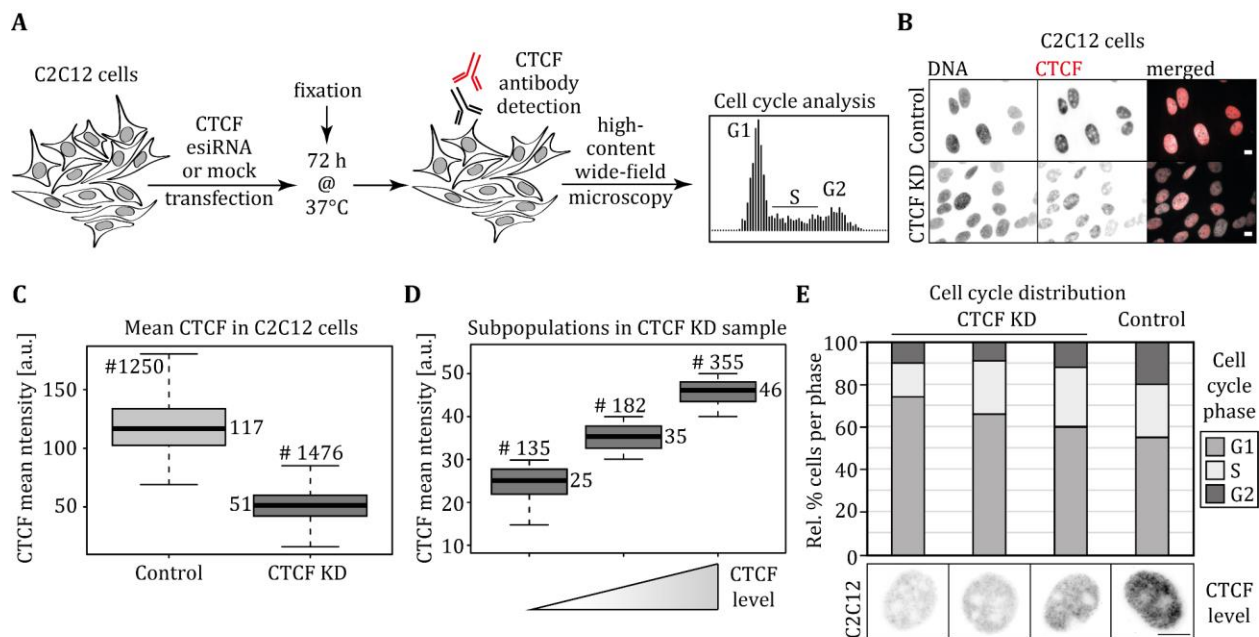


Figure 3.2.2. CTCF depletion impairs cell cycle and S-phase progression in mammalian cells. A Experimental scheme for the evaluation of the cell cycle progression in CTCF depleted cells. C2C12 cells (Supplementary Table ST1) were transfected with an esiRNA against CTCF (Supplementary Table ST5) or mock transfected for 72 hours at 37°C, 5% CO₂. After fixation, cells were immunostained for CTCF detection and imaged with high-content wide-field microscopy (Supplementary Table ST2 and ST3) to measure CTCF and

DNA intensities. The integrated DNA content distribution (histogram of DNA intensities) was used to calculate the percentage of cells in the G1, S and G2 phases. **B** Exemplary wide-field microscopy images of control and CTCF KD cells showing the DNA (DAPI, gray) and CTCF (red) channels (scale bar: 10 μm). **C** Knock down validation by high-content wide-field microscopy measurement. Nuclear CTCF mean intensity in the control (light gray) and CTCF KD (dark gray; median: 44% residual CTCF) samples (Supplementary Table ST4). **D** Boxplots showing the CTCF mean intensity measurements for the three subpopulations of the CTCF KD sample with the lowest CTCF residual levels. The three subpopulations have a residual CTCF amount corresponding respectively to 21, 30 and 39% of the control level. In both C and D, the median value is indicated next to the median black line of each boxplot and the number of cells is indicated with a # on top of each sample (see Supplementary Figures SF2 for boxplot explanation and Supplementary Table ST4 for plot statistics). **E** Evaluation of the impact of CTCF depletion on cell cycle. Based on the integrated DAPI measurements made with high-content microscopy, the DNA content distribution was plotted for the control sample (right side bar) and the three subpopulations with the lowest CTCF amount from the CTCF KD sample (first three bars corresponding in order to the three boxplots shown in D). Each distribution was subdivided in G1, S and G2 phases (see legend on the right side) based on the DNA content values and the respective relative percentage of cells in each phase was calculated for each cell population. Below each bar a representative image of a cell with corresponding CTCF amount is shown (scale bar: 10 μm).

3.2.2.3. CTCF is enriched at the replicating Xi and Y chromosomes and is necessary to maintain the synchrony of Y chromosome replication

As presented in the introduction, a general relationship between chromatin architecture and DNA replication exists and is exquisitely shown by its spatio-temporal regulation into subnuclear patterns. A particular case is found for the DNA replication of the inactive X chromosome and the Y chromosome, which are recognized by microscopy as large synchronously-replicating structures. Being CTCF an important architectural protein, a possible role in the replication of sex chromosomes was investigated. Due to the ease of visualization of the inactive X chromosome in female mouse myoblasts (C2C12 cells) and of the Y chromosome in male mouse embryonic stem cells (J1 mES and mESC-AID-CTCF cells; Supplementary Table ST1), these cells were chosen for the investigation and pulse labeled for 30 minutes with 10 μM EdU at 37°C, 5% CO₂ (Figure 3.2.3.). Upon fixation, cells were processed for EdU and CTCF detection, followed by X or Y chromosome paint probes and fluorescent *in situ* hybridization (FISH; Supplementary Tables ST2, ST7 and ST8). By imaging cells with confocal microscopy (Supplementary Table ST3), it was possible to observe a strong enrichment of CTCF in the replicating Xi in C2C12 and in the replicating Y chromosome in both J1 and mESC-AID-CTCF cells (Figure 3.2.3. A). The enrichment was already evident by simple visual inspection as shown in the montages of confocal images, in which the overlaid black arrows indicate the replicating sex chromosomes. Moreover, the result was confirmed by plotting the color profile along an overlaid arrowed line (as in the experimental scheme in Figure 3.2.1. A). In fact, the intensity peaks from the FISH-labeled Xi or Y signal (in red) which overlap an EdU peak (in blue; meaning that those chromosomes were replicating at the time of fixation) also perfectly match a CTCF intensity peak (in

green), suggesting a strong enrichment of the architectural protein at the replicating Xi and Y chromosomes (Figure 3.2.3. A). In the Supplementary Figure SF6, it is shown that the peaks corresponding to not replicating Xa and Y chromosomes (which do not overlap any EdU peak) do not have any colocalizing peak of CTCF intensity, meaning that the CTCF enrichment occurs only when the Xi and Y chromosomes are replicating.

Another proof of enrichment was shown through segmentation of the sex chromosomes from the confocal microscopy images (Figure 3.2.3. B). As depicted in the schematic next to the boxplot, not only the replicating sex chromosomes, but also the not replicating ones were segmented based on FISH signal intensity. In the X chromosomes analysis, the segmentation of not replicating ones corresponds to the active Xa chromosomes, which are also detected by FISH but whose replication occurs in a different time frame than the Xi and does not appear as a synchronously replicating structure. Additionally, a region of interest (ROI) mask was created for each segmented chromosome and moved to a different random region of the same nucleus, in order to measure intensities elsewhere in an equal volume which had no relationship with the sex chromosomes. The CTCF mean intensity was measured in the above-mentioned segmented structures and plotted in Figure 3.2.3. B. CTCF intensity proved to be the highest in the replicating Xi or Y chromosomes, when compared to not replicating X or Y or to random ROIs, for all the three cell lines measured (C2C12, J1 and mESC-AID-CTCF cells; Figure 3.2.3. B, Supplementary Table ST4). This result further confirmed the specificity of CTCF enrichment in the replicating Xi and Y chromosomes, as significantly higher than the CTCF amount in not replicating sex chromosomes or in random nuclear regions of equal volume. Subsequently, the possibility of the auxin-inducible CTCF degradation in the mESC-AID-CTCF male cell line (Supplementary Table ST1) was exploited to question how CTCF depletion could affect Y chromosome replication (Figure 3.2.3. C – K). mESC-AID-CTCF cells were treated with 0 μ M (control) or 500 μ M (CTCF KD) auxin for 4 hours prior to 30' replication labeling (10 μ M EdU; Supplementary Table ST8; both treatments at 37°C, 5% CO₂). EdU, CTCF and Y chromosome FISH detection followed upon fixation as described above (see respectively Figure 3.2.3. C and D for pipeline and example images). Cells were then imaged with high-content wide-field microscopy to validate the knock down of CTCF (mainly as described in Supplementary Figure SF1). A near to complete degradation was obtained, as visible in the example images in Figure 3.2.3. D, with circa 81% of the auxin-treated cell population having 6% residual CTCF. In fact, a median CTCF mean intensity of 89.57 a.u. and 5.53 a.u. was respectively calculated for the control and the CTCF KD sample (values obtained upon subtraction of the background value measured in untagged ES-E14TG2a cells; Supplementary Figure SF7; Supplementary Table ST1 and ST4).

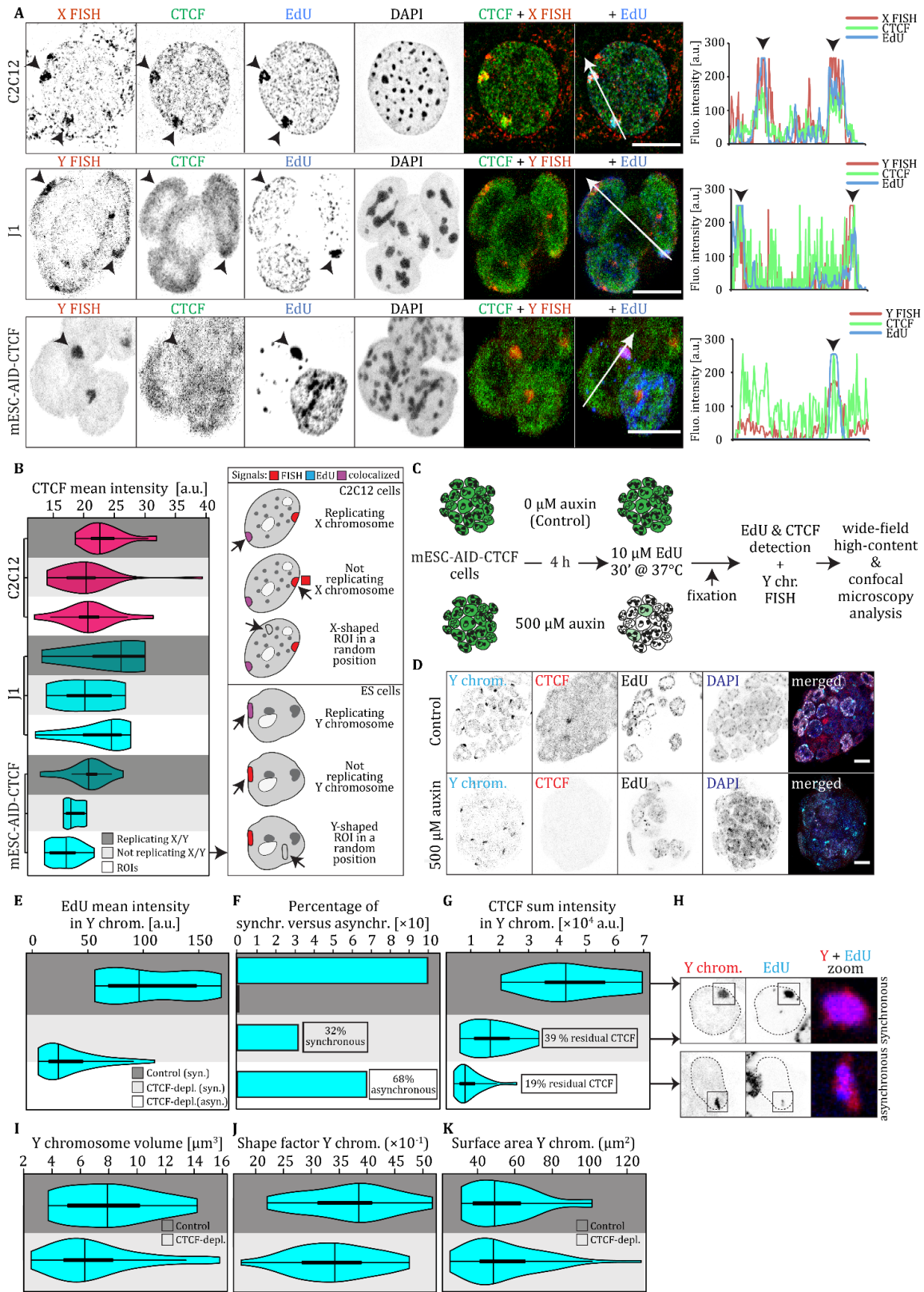


Figure 3.2.3. CTCF [a.u.] is enriched at the replicating Xi and Y chromosomes and its depletion impairs the synchrony of Y replication. A Visualization of CTCF enrichment in replicating Xi and Y chromosomes. Somatic

C2C12, embryonic J1 mES and mESC-AID-CTCF cells (Supplementary Tables ST1) were pulse labeled with 10 μ M EdU at 37°C, 5% CO₂ for 30' prior to fixation. Cells were then processed for EdU and CTCF detection, followed by X or Y chromosome FISH; since the heat denaturation required for FISH degraded the GFP tag, CTCF was detected by immunostaining with antibodies also in mESC-AID-CTCF cells (Supplementary Tables ST2, ST7 and ST8). Cells were imaged with confocal microscopy (Supplementary Tables ST3) and analyzed for colocalization through plotting of the color profile along an overlaid arrowed line. Overlaid black arrows indicate the Xi and Y chromosomes in the confocal images and the corresponding peaks in the color profile plots (scale bar: 10 μ m). **B** CTCF amounts within the Xi and Y chromosomes are higher during DNA replication and in general higher than in a random equal nuclear volume. From the confocal microscopy images (of which examples are shown in A), both the replicating Xi and Y, and the not replicating Xa and Y chromosomes were segmented based on the FISH signal. The chromosome masks were then moved in a random nuclear region to obtain measurements of an equal volume, unrelated to the chromosomes (ROI: region of interest). The CTCF mean intensities measured within such structures were plotted as violin plots (Supplementary Tables ST4). Next to the plot, the structures chosen for segmentation are depicted schematically. **C** Experimental settings for the validation of the relationship between CTCF and Y chromosome replication. mESC-AID-CTCF cells were treated for 4 hours with 0 μ M (control) or 500 μ M (CTCF KD) auxin and pulse labeled with 10 μ M EdU for 30' prior to fixation. Cells were then processed for EdU, CTCF and Y chromosome FISH detection as in A, and imaged with both high-content wide-field and confocal microscopy (Supplementary Tables ST3). **D** Example of confocal images of mESC-AID-CTCF cells processed as in C (scale bar: 10 μ m). **E - H** EdU intensity in CTCF-depleted Y chromosomes is decreased due to the loss of replication synchrony. **E** Mean EdU intensity within the replicating Y chromosome is decreased in CTCF-depleted cells. Cells were processed as in C, the Y chromosome was segmented based on the FISH signal and the mean EdU intensity within the chromosome was plotted as violin plots (Supplementary Tables ST4). **F** The majority of Y chromosomes in CTCF KD cells replicate asynchronously. The replicating Y chromosomes were distinguished based on the replicating fraction into synchronous and asynchronous, and the relative percentage within each sample was plotted. The distinction was based on the comparison between the volume of the chromosome and the volume of the replication labeling. **G** Synchronously replicating Y chromosomes have higher CTCF amounts. CTCF sum intensity was measured in the segmented Y chromosomes, already categorized as synchronously or asynchronously replicating, and plotted as violin plots (Supplementary Tables ST4). **H** Example images of synchronous and asynchronous replication of the Y chromosome in mESC-AID-CTCF cells. The dashed rectangular area corresponds to the zoom-in shown on the right part of the image montage after merging the channels. **I - K** CTCF-depleted Y chromosomes show changes in the general architecture, irrespective of DNA replication. Y chromosomes were segmented based on the FISH signal; both replicating and not replicating Y chromosomes were included in the analysis of chromosome architecture (Supplementary Tables ST4). **I** Volume of the Y chromosome. **J** Shape factor of the Y chromosome (a value of 1 corresponds to a fully round shaped structure). **K** Surface area of the Y chromosome.

Confocal image analysis of the same samples allowed the segmentation of the Y chromosome for further investigations (Figure 3.2.3. E - K). The mean EdU intensity within replicating Y chromosomes was strongly decreased upon CTCF depletion (Figure 3.2.3. E). The EdU decrease might be due to two different options: either the chromosome is still replicating synchronously but less nucleotide is incorporated, meaning the fork speed is slowed down, or replication gets asynchronous and only a portion of the chromosome is replicated at a given time. To ascertain this, the volume of the replicating Y chromosomes was compared with the volume of the replication labeling (EdU) segmented within them. In synchronously replicating Y chromosomes, the volume of

the chromosome and of the replication labeling thereof would mainly coincide. In asynchronously replicating Y, only fractions of the chromosome would have the replication labeling, which would hence not cover the whole Y volume.

A co-existence of the two hypothesized populations was observed and the frequency of both was counted. This proved that 68% of replicating Y chromosomes were asynchronous while only 32% was unaffected within the CTCF KD sample (Figure 3.2.3. F). In order to check whether these unaffected chromosomes belonged to those few cells that escaped the auxin-induced CTCF depletion, the CTCF sum intensity within the replicating Y chromosomes was measured. Indeed, the synchronously replicating Y chromosomes retained 39% of CTCF levels, while the asynchronous ones only retained 19% residual CTCF (percentages are relative to the control median value; Figure 3.2.3. G, see Supplementary Table ST4 for statistics). In Figure 3.2.3. H, example images of synchronous versus asynchronous replication of the Y chromosome are shown.

Furthermore, different parameters could be measured through segmentation of the Y chromosome from confocal images. These proved a general change in the architecture of the Y chromosome in the absence of CTCF, irrespective of DNA replication. The CTCF-depleted cells showed a lower median volume, but a wider range of volume values compared to control cells (Figure 3.2.3. I). The shape factor also showed a substantial decrease, indicating that the shape of the Y chromosome in CTCF-depleted cells is more irregular (Figure 3.2.3. K). In fact, a shape factor value of 1 would correspond to fully round shaping. Regarding the surface area, the untreated and CTCF-depleted cells showed non-significant differences (Figure 3.2.3. J).

3.2.3. Discussion

CTCF is one of the main chromatin architectural proteins, widely studied for its cooperation with the cohesin complex in loop extrusion. Past studies often focused on its role as a transcriptional regulator, which in the simplest case is achieved by insulation of enhancers and promoters. The role of CTCF in the regulation of other genomic functions such as DNA replication is poorly understood. Here I exploited DNA replication labeling and CTCF immunostaining to microscopically characterize the reciprocal distribution within mammalian nuclei. The results in different mammalian cell lines indicate a higher intensity of CTCF at the sites of DNA replication, in comparison with the non-replicating DNA fractions (Figure 3.2.1.). By applying a time chase after a nucleotide pulse, I could further observe that not only CTCF is enriched at the sites but also at the time of replication. In fact, the intensity of CTCF signal in EdU foci in human cells was highest at the time of the nucleotide pulse and decreased over time during the chase (Figure 3.2.1. E; Supplementary Table ST4). This indicates

that CTCF accumulation was specific to the replication event. Future investigation should aim at answering the question on how this enrichment mechanistically occurs and also on how it gets resolved over time, since the pulse-chase experiment showed that CTCF intensity in replication foci was still decreasing between the two time points of chase (2 and 4 hours; Figure 3.2.1. E). It will be important to understand whether CTCF is actively recruited at the sites of replication and what is the interplay of this protein with the different players of the replication machinery. Since a successful DNA replication contributes to a normal cell cycle progression, the impact of CTCF depletion on cell cycle stages was questioned (Figure 3.2.1.). Through the analysis of DNA content distributions, an impairment in the progression of CTCF-depleted cells from G1 to S-phase was observed. The impact of CTCF depletion on cell cycle progression appeared to be dose-dependent. The CTCF-depleted sample was in fact subdivided into different classes of knock down and those cells with the lowest CTCF levels were the most impacted, having the highest percentage of cells stalling in G1 (Figure 3.2.1. E).

Through replication labeling, subsequent detection and sex chromosomes FISH, CTCF was found to be enriched at the inactive X chromosome and Y chromosome during their replication in somatic and embryonic mouse cells, respectively. CTCF chromosomal levels were higher during replication compared to the same not replicating chromosomes and to different nuclear regions of equal volume (Figure 3.2.3. A – B; Supplementary Figure SF6). Upon CTCF depletion (Figure 3.2.3. C – D; Supplementary Figure SF7), the replicating Y chromosomes showed a decrease in EdU intensity (Figure 3.2.3. E). The reduction proved to be due to both less nucleotide incorporation and impaired synchrony of replication. In fact, Y chromosome replication synchrony was mainly lost, with 68% of Y chromosomes showing only partial asynchronous replication (Figure 3.2.3. F, H). This is in line with results on metaphase spreads by our colleague Maruthi Pabba Kumar (TU Darmstadt), who further proved through a pulse-chase experiment that the replication banding on the Y chromosome lost synchrony in CTCF-depleted mouse ES cells (unpublished data, not shown). To further prove that the loss of synchrony was related to CTCF depletion, the CTCF sum intensity within the synchronous and asynchronous Y chromosomes was measured (Figure 3.2.3. G). The results indicated that indeed the fraction of synchronously replicating Y chromosomes within the CTCF-depleted sample retained higher CTCF levels than the asynchronous ones, although still lower than the control sample. The respective cells probably partially escaped the auxin treatment. However, the correlation is supporting a dose-dependent role of CTCF in sustaining the DNA replication synchrony through chromosome architecture (Figure 3.2.3. G). Moreover, the general architecture of the chromosome is affected irrespectively of DNA replication, as shown by the analysis of chromosome architectural

parameters in both replicating and not replicating Y chromosomes (Figure 3.2.3. I – K). Upon CTCF depletion, the Y chromosome decreased in volume and acquired a more irregular shape (Figure 3.2.3. I, J), although maintaining a similar surface area (Figure 3.2.3. K).

Mechanistically, CTCF might act as a limiting factor for origin firing on the Y. A full understanding of the eukaryotic limiting factors for replication initiation is still missing (Mantiero *et al.*, 2011). A correlation with chromatin accessibility and the timing origin firing was observed (Bell *et al.*, 2010; Heinz *et al.*, 2019; Méchali, 2010), suggesting that the order in which limiting factors are recruited could at least partially depend on a dynamic chromatin environment (Mantiero *et al.*, 2011). The synchronous replication of the whole chromosome might then occur when the limiting factor, in this case CTCF, is recruited at high rates, allowing simultaneous firing of multiple origins in different replication domains. Alternatively, the recruitment of CTCF might contribute to the removal of an inhibitory modification, thereby leading to the concomitant activation of pre-replication complexes. Similar hypotheses on limiting factors were in fact previously postulated for the Xi synchronous replication (Aladjem and Fu, 2014; Martin *et al.*, 2011). Aladjem and colleagues suggest a model in which essential limiting factors might be diffused within the nucleus during early S-phase and then get trapped by the late replicating structures in high concentrations, once the majority of the genome has already been duplicated (Aladjem and Fu, 2014). Our colleague Dr. Paulina Prorok (TU Darmstadt) analyzed existing datasets from sequencing-based origin mapping and ChIP-seq studies in mouse embryonic stem cells. The results of Dr. P. Prorok analysis indicate a significant enrichment of both CTCF and cohesin at mapped origins of DNA replication (unpublished data, not shown). Additionally, Dr. P. Prorok measured a genome-wide correlation between convergent CTCF binding sites and replication origins, with the median distance between convergent CTCF sites being in the range of the calculated inter origin distance (IOD) on the X chromosome (unpublished data, not shown). Future analysis will aim to investigate a possible disruption of replication origins in the absence of CTCF.

The possible role of CTCF as a mediator between the chromatin structure and replication function finds a parallel on the discoveries on the RIF1 protein (Rap1-interacting-factor-1), initially found as a telomere-binding protein (Hardy *et al.*, 1992). RIF1 regulates chromatin loop sizes, replication domains architecture and induces the simultaneous firing of different replication domains (Cornacchia *et al.*, 2012; Yamazaki *et al.*, 2012, 2013). In other words, RIF1 bridges the structural regulation of chromatin domains with the functional control of DNA replication timing. It binds mid-S-phase domains to the insoluble nuclear lamina and nucleolar peripheries in early G1 and “sequesters” these RIF1-associated domains (RADs) until mid S-phase, thereby preventing an earlier

unorganized duplication of such domains and overall organizing the replication timing genome-wide (Cornacchia *et al.*, 2012; Foti *et al.*, 2016; Yamazaki *et al.*, 2012, 2013). Our laboratory recently contributed to unveil that both nuclear architecture and replication timing depend on the conserved interaction of RIF1 with Protein phosphatase 1 (PP1; Song *et al.*, 1993) (Gnan *et al.*, 2021), which is critical in the regulation of late origins firing (Alver *et al.*, 2017; Davé *et al.*, 2014; Hiraga *et al.*, 2014, 2017). However, they show a different degree of dependency, with chromatin compartmentalization being already sensitive to RIF1 dosage and replication timing being affected only by a full lack of functional RIF1 (*Rif1-KO* and *Rif1-ΔPP1*; Gnan *et al.*, 2021). It was recently shown by our colleague Dr. Cathia Rausch (TU Darmstadt) that both the chromosome architecture in terms of volume and compaction and the replication timing of the Y chromosome are clearly altered in the absence of RIF1 (unpublished data, not shown).

Overall, the present work highlights a role of CTCF in the synchrony of Y chromosome replication, based on the great enrichment of CTCF within the replicating Y chromosome and the observed Y replication asynchrony in the absence of CTCF in male mouse embryonic stem cells (Figure 3.2.3.). A notable degree of CTCF enrichment is also observed within the inactive X chromosome (Xi) during its replication, while none is observed in not replicating Xi, nor in the active Xa (Figure 3.2.3.; Supplementary Figure SF6). This leads to the hypothesis that CTCF may structurally regulate the replication not only of the Y chromosome but of the inactive X chromosome too. However, robust CTCF depletion should be performed in female somatic cells to confirm this hypothesis, since the present observations were derived from untreated female mouse myoblasts. Another outlook for future studies is to investigate possible contributions of cohesin to the regulation of sex chromosomes replication and the interplay thereof with CTCF. Different studies tried to unveil the level of cohesin involvement in Xi organization, which might help us in directioning future hypotheses on the regulation of replication. Through isolation and characterization of the protein interactome of the *Xist* RNA, it was observed that cohesin gets evicted *in cis* by *Xist* RNA during Xi coating and that cohesin depletion destabilizes *Xist*-mediated repression (Minajigi *et al.*, 2015). *Xist* deletion leads instead to cohesin binding at Xa-specific sites and to the establishment of an Xa conformation (Minajigi *et al.*, 2015). In the same experiments of *Xist* deletion, a positive shift in CTCF peaks was also observed but in a locus-specific rather than chromosome-broad manner, suggesting that the two architectural proteins do not completely overlap in occupancy on the Xi chromosome (Minajigi *et al.*, 2015). However, being cohesin and CTCF binding sites found not only at TADs border but also within TADs, it was suggested that these proteins might not be the only determinant of loci expression regulation (van Bommel *et al.*, 2019). In a different depletion study in embryonic stem

cells, X inactivation was shown to rely on a subtle balance between cohesin retention and eviction (Kriz *et al.*, 2021). The Xi silencing was attenuated by forced cohesin retention (obtained through depletion of cohesin's releasing factor WAPL) (Kriz *et al.*, 2021). Cohesin depletion instead only minimally affected gene silencing, as *Xist* RNA-Polycomb complexes would sustain superloops in response to disrupted higher chromosome organization (Kriz *et al.*, 2021). In fact, Polycomb-targeted genes got even more robustly repressed in the absence of cohesin through reinforced interaction between Polycomb domains (Kriz *et al.*, 2021). Another study showed that while TADs are attenuated on the Xi, both Xa and Xi have TAD-like single-cell domains with similar features which are not affected when major epigenetic components are perturbed (Cheng *et al.*, 2021). Additionally it was shown that X inactivation-related chromatin compaction relies on a level higher than TADs and the observed single-cell domains (Cheng *et al.*, 2021).

In conclusion, a correlation was observed between CTCF and DNA replication of the whole genome in general and of the sex chromosomes in particular. The enrichment of CTCF suggests that this architectural protein might mediate the structural arrangement of chromatin loops in relation to the replication machinery. In support of this hypothesis, previous studies found a correlation between chromatin loops and replication units, and postulated that the size of a replicon would be double the one of a loop (Buongiorno-Nardelli *et al.*, 1982). Subsequent studies better defined the replicons as functional units that are stable over cell cycles (Jackson and Pombo, 1998; Nakayasu and Berezney, 1989), suggesting that DNA replication relies on an underlying chromatin structure. Additionally, our laboratory measured a median inter origin distance (Chagin *et al.*, 2016), which is double the size of chromatin loops (Buongiorno-Nardelli *et al.*, 1982; Earnshaw and Laemmli, 1983; Jackson *et al.*, 1990b, 1990a) and equal to the size of convergently-bound CTCF-anchored "loop domains" (Rao *et al.*, 2014) in mammalian cells.

The altered cell cycle progression (Figure 3.2.2. E) and the impaired synchrony of nucleotide incorporation in the Y chromosome (Figure 3.2.3. E – H) of CTCF-depleted cells further point to the fact that the chromatin architectural contribution by CTCF sustains a correct temporal regulation of DNA replication. Future studies could investigate this correlation deeper in terms of altered replication foci structure and distribution within mammalian nuclei. The timing of DNA replication could also be further addressed and the influence of CTCF depletion on different players of the replication machinery could be questioned in order to ultimately understand the mechanisms regulating this relationship.

3.2.4. Material and methods

3.2.4.1. Cell culture

All cells were grown at 37 °C in a humidified atmosphere with 5% CO₂. Human HeLa Kyoto and mouse C2C12 cells (Supplementary Table ST1) were cultured in DMEM high glucose (Cat. No.: D6429) supplemented with 50 µg/ml gentamicin (Cat. No.: G1397), 2 mM L-glutamine (Cat. No.: G7513) and respectively 10% and 20% FCS (Cat. No.: F7524). mESC-AID-CTCF, ES-E14TG2a and J1 mouse embryonic stem cells (Supplementary Table ST1) were cultured in DMEM high glucose (Cat. No.: D6429) supplemented with 15% FCS, 1× non-essential amino acids (Cat. No.: M7145), 1× penicillin/streptomycin (Pen/Strep) (Cat. No.: P4333), 1× L-glutamine (Cat. No.: G7513), 0.1 mM beta-mercaptoethanol (Cat. No.: 4227, Carl Roth, Karlsruhe, Germany), 1000 U/ml recombinant mouse LIF (Millipore) and 2i (1 M PD032591 and 3 M CHIR99021, Cat. Nos.: 1408 and 1386 respectively, Axon Medchem, Netherlands) on gelatin-coated culture dishes (0.2% gelatin; Cat. No.: G2500) or on gelatinized coverslips for immunostaining. Unless otherwise stated, all catalog numbers (Cat. No.) indicated above refer to Sigma-Aldrich Chemie GmbH, Steinheim, Germany.

3.2.4.2. CTCF knock down

For the experiments in Figure 3.2.2., C2C12 were transfected with 15 nM of an esiRNA pool against the mouse CTCF transcript (Supplementary Table ST5; Cat. No.: EMU044061, MISSION® esiRNA, Sigma-Aldrich Chemie GmbH, Steinheim, Germany) or mock transfected without any esiRNA as a control. Transfection was performed with the HiPerFect Transfection Reagent following the manufacturer instructions (Cat. No.: 301704, QIAGEN, Hilden, Germany). Cells were seeded on coverslips 3 h prior to transfection and fixed at 72 h post transfection with 3.7% formaldehyde/1× PBS (Cat. No.: F8775, Sigma-Aldrich Chemie GmbH, Steinheim, Germany) for the subsequent immunostaining. For the experiments in Figure 3.2.3. C – K and Supplementary Figure SF7, mESC-AID-CTCF and ES-E14TG2a cells were seeded on gelatinized coverslips and treated in parallel with 0 - 500 µM auxin (IAA; Cat. No.: I3750, Sigma-Aldrich Chemie GmbH, Steinheim, Germany) for 4 h. mESC-AID-CTCF cells were subsequently pulse labeled as indicated in section 3.2.4.3. and both mES cell lines were fixed with 3.7% formaldehyde/1× PBS. During the incubation time for any treatment before the time point of fixation, cells were cultured as indicated in the section 3.2.4.1. See Supplementary Table ST4 for statistics.

3.2.4.3. EdU pulse labeling

All cell lines were pulse labeled in their respective conditioned medium with 10 µM EdU (Cat. No.: 61135-33-9, Carl Roth, Karlsruhe, Germany) at 37 °C with 5% CO₂. HeLa Kyoto cells shown in Figure

3.2.1. C – E were labeled for 15'. C2C12, mESC-AID-CTCF and J1 cells (Figure 3.2.1., Figure 3.2.3. and Supplementary Figure SF6) were labeled for 30'. After 3× washing with 1× PBS, cells were fixed with 3.7% formaldehyde/1× PBS. All cells were fixed immediately after the EdU pulse, except HeLa Kyoto cells in Figure 3.2.1. C – E, which were washed 3× with warm 1× PBS and given fresh medium for the subsequent chase for 0, 2 or 4 hours at 37 °C with 5% CO₂ before fixation as above.

3.2.4.4. EdU detection, CTCF immunostaining and sex chromosomes FISH

All previously fixed cells were washed with 1× PBS, permeabilized 15' with 0.7% Triton™ X-100 (Cat. No.: T8787, Sigma-Aldrich Chemie GmbH, Steinheim, Germany) and washed again prior to blocking. C2C12 and HeLa Kyoto cells (Figure 3.2.1.) were blocked for 30' in 1% BSA (Cat. No.: A4503, Sigma-Aldrich Chemie GmbH, Steinheim, Germany) and chemically treated with the EdU “Click-it” reaction, performed as instructed by the manufacturer (EdU Click-488 ROTI®Kit für Imaging, Cat. No.: 7773, Carl Roth, Karlsruhe, Germany) for 45' at room temperature. Upon EdU detection, cells were washed 2× 5' with PBS and 3× 10' with 0.02% Tween® 20 (Cat. No.: 9127.1, Carl Roth, Karlsruhe, Germany). C2C12 cells in Figure 3.2.2. were blocked for 30' in 1% BSA and immunostained for CTCF without any EdU detection. For the immunostaining of CTCF, cells were incubated overnight at 4°C with the primary rabbit anti-CTCF antibody (see Supplementary Table ST2 for information on antibodies). After washing 2× with 1× PBS for 5' and 3× 10' with 0.02% Tween® 20, cells were incubated with the secondary goat anti-rabbit IgG (H + L) AF594 antibody for 1 h at room temperature. Washing followed as described above. All dilutions mentioned above were done in 1× PBS, except antibody dilutions in 1% BSA/1× PBS. DNA was counterstained with 10 µg/ml DAPI (Cat. No.: D27802, Sigma-Aldrich Chemie GmbH, Steinheim, Germany) for 10' at room temperature, cells dipped in ddH₂O and mounted with Vectashield® antifade medium (Cat. No.: NC9265087, Thermo Fisher Scientific, Walham, United States) on coverslips.

C2C12, mESC-AID-CTCF and J1 cells processed for sex chromosomes FISH detection (Figure 3.2.3. and Supplementary Figure SF6) were blocked 5' in 1% BSA, 0.2% fish skin gelatin (FSG), 0.02% Tween® 20 in 1× PBS (see (Weber *et al.*, 2018) for the original Repli-FISH protocol, which couples the detection of replication labeling with the FISH procedure). The EdU “Click-it” reaction and the immunostaining of CTCF were performed as described above. The GFP tag gets degraded by the heat denaturation used for the FISH procedure (Cremer *et al.*, 2008), therefore the antibody detection of CTCF was required also in the GFP-tagged mESC-AID-CTCF cell line. A mild 1% formaldehyde fixation was applied after CTCF immunostaining. After 2' in 2× saline-sodium citrate (SSC) to equilibrate, cells were incubated for 30' with 50% formamide/2× SSC and combined with the mouse X or Y probe

(home made and provided by Dr. Cathia Rausch, TU Darmstadt; Supplementary Tables ST7 and ST8) that was previously denatured at 80°C for 5'. The slides were sealed in a metal chamber and heated at 80°C for 5', followed by overnight incubation at 37°C for annealing. After 2 hours of washing in 2× SSC, cells were blocked in 2% BSA/4× SSC for 30' and incubated with Cy5-Streptavidin (Supplementary Table ST2) for 1 h at room temperature. After washing, DNA was counterstained with DAPI and cells were mounted on coverslides as described above.

The mESC-AID-CTCF and wild type ES-E14TG2a cells used for the knock down validation were only subjected to permeabilization, DNA counterstaining and mounting as described above (Supplementary Figure SF7).

3.2.4.5. Microscopy imaging and analysis

For the Figure 3.2.1., 3.2.3. and Supplementary Figure SF6, the C2C12, HeLa Kyoto, J1 and mESC-AID-CTCF samples were imaged at the confocal point scanner microscope Leica TCS SP5 II (software Leica Application Suite X (LAS X), © 2022 Leica Microsystems, Wetzlar, Germany; Supplementary Table ST3) with a 63× oil objective (63×/1.40-0.60 HCX PL APO oil lambda blue objective). Confocal images were analyzed with the softwares Fiji (Fiji Is Just ImageJ, Version 1.53c; Schindelin *et al.*, 2012) and Volocity (Version 6.3 – © 1998 – 2022 PerkinElmer Inc., Waltham, Massachusetts, United States).

For the Figure 3.2.1., 3.2.3. A – B and Supplementary Figure SF6, the confocal images were deconvolved prior to further processing. First, a point spread function (PSF) was created for each channel based on microscopy specifications (i.e. media refraction index, numerical aperture, wavelength, image size, slice spacing, etc.) by running the Fiji software plug-in “Diffraction PSF 3D” (© 2005, OptiNav, Inc.; 2005, B. Dougherty). Each image channel from the confocal images was then separately deconvolved with the appositely created PSF of the respective channel by running the Fiji software plug-in “Iterative Deconvolve 3D” (© 2005, OptiNav, Inc.; 2005 b, B. Dougherty).

To obtain the intensity profile shown in the plots in 3.2.1. B, 3.2.3. A and Supplementary Figure SF6, images were processed with the plug-in “Color Profiler” (2005, D. Prodanov) of the Fiji software. First, a composite image of the desired channels was produced from the deconvolved confocal image and saved as RGB. For C2C12, the maximum projection of the full z-stack (made of the series of z-planes) was used, in order to visualize all four X chromosomes simultaneously. For embryonic stem cells (J1 and mESC-AID-CTCF cells), a maximum projection of the z-stack could not be used due to the presence of different cells in multiple planes, therefore the z-plane allowing the best visualization of the Y chromosomes was chosen to create the composite RGB image. An arrowed line was then overlaid over the region of interest and the plug-in was run to obtain the color profile with the

intensity peaks of each channel along the overlaid line. The overlap of different peaks in the color profile plot indicates sites of colocalization of the signal from the different channels in the corresponding image.

For the Figure 3.2.1. C – E, the deconvolved confocal images of HeLa Kyoto were further processed with the Volocity software. The DAPI – DNA signal was used to create nuclear masks (pipeline: find objects in DAPI channel, automatic threshold, dilate and erode, fill holes). Within these nuclear masks, the AF488 – EdU intensities were used to segment the replication foci (pipeline: find objects in AF488 channel, constant threshold using standard deviation, separate touching objects). The AF594 – CTCF mean intensities within the replication foci were then measured and exported as text tables to produce the plot in Figure 3.2.1. E.

To obtain the measurements shown in Figure 3.2.3. B, E – G and I – K, the confocal images of C2C12, J1 and mESC-AID-CTCF cells were analyzed with the Volocity software. A nuclear mask was segmented as above, based on DAPI. Within each nuclear mask, the Cy5 – X (in C2C12) or Cy5 – Y (in J1 and mESC-AID-CTCF) intensities were used to segment the sex chromosomes (pipeline: find objects in Cy5 channel, constant threshold using standard deviation, separate touching objects). To produce the plot shown in Figure 3.2.3. B, the replicating and not replicating chromosomes were categorized based on the presence of the EdU signal within each chromosome. Each chromosome mask was subsequently used to create a ROI and the ROI was moved to a different nuclear position within the same nucleus. The AF594 – CTCF mean intensities were then measured within the X/Y chromosomes and ROI masks. For the Figure 3.2.3. E, the AF488 – EdU mean intensities were measured within the Y chromosomes. The same Y chromosomes were subdivided into synchronously and asynchronously replicating based on the replicating fraction of the chromosomal volume, in order to calculate the relative percentages as plotted in Figure 3.2.3. F. After this subdivision into categories, the AF594 – CTCF sum intensities within the synchronously and asynchronously replicating Y chromosomes were also exported (Figure 3.2.3. G). For the Figure 3.2.3. I – K, the parameters concerning chromosome architecture were measured and exported without making any further distinction, for both replicating and not replicating Y chromosomes (parameters: volume in I, shape factor in J and surface area in K).

For the analysis of the DNA distribution shown in Figure 3.2.2. E and for the quantification of CTCF shown in Figure 3.2.2. C – D, and Supplementary Figure SF7, the samples were imaged at the high-content wide-field microscopy system Operetta® and images were analyzed with the Harmony™ software – Version 3.5.1 – © 09-2013 (both PerkinElmer, see Supplementary Table ST3), mainly as described in the Supplementary Figure SF1. In particular, the DAPI signal was used to create a nuclear

mask and select nuclei. The nuclear intensities of both DAPI – DNA and AF594 – CTCF or GFP – CTCF signals were measured and exported. In Figure 3.2.2. C the whole population from the CTCF KD sample was plotted together with the control. The CTCF KD sample was then subdivided in different subpopulations based on ranges of CTCF mean intensities and the three subgroups within the lowest ranges were plotted in Figure 3.2.2. D. The integrated DNA intensities were plotted as frequency distribution in order to distinguish the G1 and G2 peaks, separated by the progression of cells in S-phase. The DNA content distribution was then utilized to subdivide the control sample and the three CTCF KD subpopulations in cell cycle phases. The percentages of cells for each phase were subsequently calculated and plotted in Figure 3.2.2. E. To obtain the plots in Supplementary Figure SF7, the median level measured in the GFP channel in the untagged ES-E14TG2a cells was used to subtract the background from the measurements obtained for the mESC-AID-CTCF cells.

For all experiments, the results tables were analyzed in RStudio (Version 0.99.902 – © 2009-2016 RStudio Inc., Boston, United States) to produce the plots shown. See Supplementary Figure SF2 for boxplot interpretation and Supplementary Table ST4 for all the statistics.

4. Cohesin is required to organize chromatin and DNA repair units

4.1. Introduction

Cohesin is a ring-shaped protein complex which is essential for sister chromatid cohesion, hence its name. The isolation of cohesion-deficient mutants and the screenings for synthetic lethality in *Saccharomyces cerevisiae* allowed the identification of the cohesin components (namely Smc1, Smc3, Scc1 and Scc3; see Figure 4.1.1.) and associated regulatory proteins (Guacci *et al.*, 1997; Hartman *et al.*, 2000; Michaelis *et al.*, 1997; Strunnikov *et al.*, 1993; Tóth *et al.*, 1999; see Table 4.1. for protein nomenclature in budding yeast and human).

Smc1 and Smc3 are two members of the structural maintenance of chromosomes (SMC) protein family of ATPases (Michaelis *et al.*, 1997; Strunnikov *et al.*, 1993), which comprises also the Smc2 and Smc4 subunits of the condensin complex and the Smc5 and Smc6 components of the Smc5/6 complex (Higashi and Uhlmann, 2022; Hirano *et al.*, 1995; Oldenkamp and Rowland, 2022; Pradhan *et al.*, 2022; Saitoh *et al.*, 1995).

The α -kleisin winged-helix domain (WHD) subunit was discovered in parallel by two different groups, which named it sister chromatid cohesion 1 (Scc1; Michaelis *et al.*, 1997) and mitotic chromosome determinant 1 (Mcd1; Guacci *et al.*, 1997). The human ortholog was first identified by sequence homology to *S. pombe rad21* (radiation-sensitive mutant 21; McKay *et al.*, 1996), which was already under study for its involvement in DNA repair (Birkenbihl and Subramani, 1992), and subsequently cloned together with the murine gene (McKay *et al.*, 1996).

A tandem HEAT repeat characterizes the fourth cohesin component, whose two mammalian isoforms STAG1 and STAG2 (or SA1/2, stromal antigen) got identified with an immunoscreening of a murine cDNA library with an antibody raised against stromal cells (Carramolino *et al.*, 1997). Improved screenings for cohesion mutants allowed the identification of the yeast STAG ortholog Scc3 (sister chromatid cohesion 3, Tóth *et al.*, 1999; previously Irr1, irregular cell behavior 1, Kurlandzka *et al.*, 1995, 1999). Smc1, Smc3, Scc1 and Scc3 were finally proven to form a stable “cohesin” complex (Tóth *et al.*, 1999).

Smc1 and Smc3 heterotypically interact through their “hinge” domains to build up a V-shaped heterodimer (Figure 4.1.1., left side; Haering *et al.*, 2002). Both topological and non-topological DNA entrapment by cohesin depend on its hinge domain (Srinivasan *et al.*, 2018), which is critical for chromosomal association (Mishra *et al.*, 2010), cohesion (Kurze *et al.*, 2011), and loop-mediated gene regulation (Carico *et al.*, 2021). The hinge interacts with both Smc heads and the kleisin-bound Scc3 and Pds5 (Haering *et al.*, 2004; McIntyre *et al.*, 2007; Xu *et al.*, 2018). Each hinge lays in the middle of a 50 nm-long intramolecular antiparallel coiling, at whose end the N- and C-terminal globular

domains are brought together to form a nucleotide-binding “head” domain (NBD) (Haering *et al.*, 2002; Hirano *et al.*, 1997; Melby *et al.*, 1998). A composite ATPase domain of the ATP binding cassette (ABC) family is thereby assembled with two ATP molecules “sandwiched” between the two Smc heads, as the ATP binding site (Walker A motif) within Smc1 N-terminal meets the DA box (Walker B motif) within Smc3 C-terminal and vice versa (see Figure 4.1.1., middle; Arumugam *et al.*, 2003; Haering *et al.*, 2002; Hopfner *et al.*, 2000; Lammens *et al.*, 2004; Löwe *et al.*, 2001).

Table 4.1. Protein subunits of the cohesin complex and its regulators in human and budding yeast. Alternative protein names are indicated in brackets, e.g. Scc3 = (Irr1); in the “Original references” column the first papers identifying that particular subunit/protein or investigating its role in cohesin regulation are quoted; see the Protein Ontology “PRO” database and main text for further references.

| Cohesin component or regulator | | <i>Homo sapiens</i> | <i>Saccharomyces cerevisiae</i> | Original references |
|---|--|---|--|---|
| κ-SMC subunit | | SMC1α* (SMC1A) | Smc1*** (structural maintenance of chromosomes 1) | (Michaelis <i>et al.</i> , 1997; Schmiesing <i>et al.</i> , 1998; Strunnikov <i>et al.</i> , 1993) |
| | | SMC1β** (SMC1B) | | |
| v-SMC subunit | | SMC3*** (CSPG6, Bamacan) | Smc3*** | (Michaelis <i>et al.</i> , 1997; Schmiesing <i>et al.</i> , 1998) |
| α-Kleisin WHD subunit | | RAD21* (radiation-sensitive mutant 21, SCC1) | Scc1* (sister chromatid cohesion 1, Mcd1, mitotic chromosome determinant 1) | (Birkenbihl and Subramani, 1992; McKay <i>et al.</i> , 1996; Guacci <i>et al.</i> , 1997; Michaelis <i>et al.</i> , 1997) |
| | | REC8**, RAD21L** | | |
| HEAT repeat subunit (HEAT-B) | | STAG1* (stromal antigen 1, SA1) | Scc3*** (structural maintenance of chromosomes 3, Irr1, irregular cell behavior 1) | (Carramolino <i>et al.</i> , 1997; Tóth <i>et al.</i> , 1999) |
| | | STAG2* (SA2) | | |
| | | STAG3** (SA3) | | |
| Kollerin: loading and loop extrusion | HEAT repeat subunit | NIPBL (nipped-B-like protein, delangin, SCC2, NIPBLA) | Scc2 | (Ciosk <i>et al.</i> , 2000; Tóth <i>et al.</i> , 1999) |
| | TPR repeat subunit | MAU2 (maternal-effect uncoordinated 2, SCC4, NIPBLB) | Scc4 | |
| α-kleisin and HEAT repeat subunits interactors: | HEAT repeat associated (HEAT-A), dual role | PDS5A | Pds5 (precocious dissociation of sisters 5) | (Hartman <i>et al.</i> , 2000) |
| | | PDS5B (APRIN, AS3) | | |

| | | | | |
|--|---|---|--|--|
| balance between cohesion establishment and release | Destabilization, dissociation | WAPL (<u>w</u> ings <u>a</u> part-like, WAPAL) | Rad61 (Wpl1, Wapl) | (Game <i>et al.</i> , 2003; Gandhi <i>et al.</i> , 2006; Kueng <i>et al.</i> , 2006; Oikawa <i>et al.</i> , 2004; Rolef Ben-Shahar <i>et al.</i> , 2008) |
| | Stabilization, establishment | sororin (CDCA5, <u>c</u> ell <u>d</u> ivision <u>c</u> ycle-associated protein <u>5</u>) | orthologue is unknown | (Nishiyama <i>et al.</i> , 2010; Rankin <i>et al.</i> , 2005; Schmitz <i>et al.</i> , 2007) |
| Cohesin N-acetyl transferase (CoAT): cohesion establishment through Smc3 acetylation | ESCO1 | ESCO2 | Eco1 (<u>e</u> stablishment of sister <u>c</u> ohesion <u>1</u> , Ctf7, <u>c</u> hromosome <u>t</u> ransmission <u>f</u> idelity <u>2</u>) | (Skibbens <i>et al.</i> , 1999; Tóth <i>et al.</i> , 1999) |
| | ESCO2 | | | |
| Cohesin deacetylase (CoDAC): cohesin recycling through Smc3 deacetylation | HDAC8 (<u>h</u> istone <u>d</u> eacetylase <u>8</u>) | Hos1 | (Beckouët <i>et al.</i> , 2010; Borges <i>et al.</i> , 2010; Xiong <i>et al.</i> , 2010) | |
| Separase: anaphase triggering through cleavage of Scc1 | ESPL1 (<u>e</u> xtra <u>s</u> pindle <u>p</u> oles-like <u>1</u> protein, separin, separase) | Esp1 | (Ciosk <i>et al.</i> , 1998) | |
| Securin: anaphase inhibition through binding of separin | PTTG1 (<u>p</u> ituitary <u>t</u> umor-transforming gene <u>1</u> protein, securin) | Pds1 (<u>p</u> recocious <u>d</u> issociation of <u>s</u> isters <u>1</u>) | | |
| Shugoshin phosphatase complex: protection of centromeric cohesin | SGO1 (<u>s</u> hugoshin <u>1</u> , guardian spirit) | Sgo1 | (Kitajima <i>et al.</i> , 2004; Marston <i>et al.</i> , 2004; Rabitsch <i>et al.</i> , 2004) | |
| | PP2A (serine/threonine protein phosphatase <u>2A</u>) | PP2A | (Kitajima <i>et al.</i> , 2006; Riedel <i>et al.</i> , 2006; Rivera and Losada, 2006; Tang <i>et al.</i> , 2006) | |

* mitotic; ** meiotic; *** both mitotic and meiotic.

ATP hydrolysis drives heads disengagement (Arumugam *et al.*, 2003; Lammens *et al.*, 2004; Marcos-Alcalde *et al.*, 2017) and is required for cohesin chromosomal association, loading, translocation, cohesion and loop extrusion (Davidson *et al.*, 2019; Kim *et al.*, 2019; Vian *et al.*, 2018). Smc1 and Smc3 coiled coils “arms” interact widely and can zip up in a closed “rod” conformation (Bürmann *et al.*, 2019; Chapard *et al.*, 2019; Diebold-Durand *et al.*, 2017; Soh *et al.*, 2015), leading to juxtaposition of the two rotated heads in the absence of ATP (Chapard *et al.*, 2019; Diebold-Durand *et al.*, 2017). Moreover, the folding of coiled coils around their “elbow” leads to a hinge-head interaction and allows cohesin to transition between extended and folded conformations (Bürmann *et al.*, 2019). The

“clamped” state is achieved when Scc2/NIPBL induces such folding and Scc3/SA clamps DNA on top of the engaged ATP-bound Smc heads (Figure 4.1.1., right side; Oldenkamp and Rowland, 2022).

The kleisin subunit Scc1 closes the tripartite ring by connecting the two NBD domains (Figure 4.1.1., left side; Haering *et al.*, 2002). The two α -helices in the N-terminal of Scc1 establish a four-helix bundle with the “neck” of Smc3 (the part of coiled coil emerging from the head; Gligoris *et al.*, 2014). Scc1 C-terminal winged helical domain binds to the “cap” of Smc1 ATPase head (Haering *et al.*, 2004).

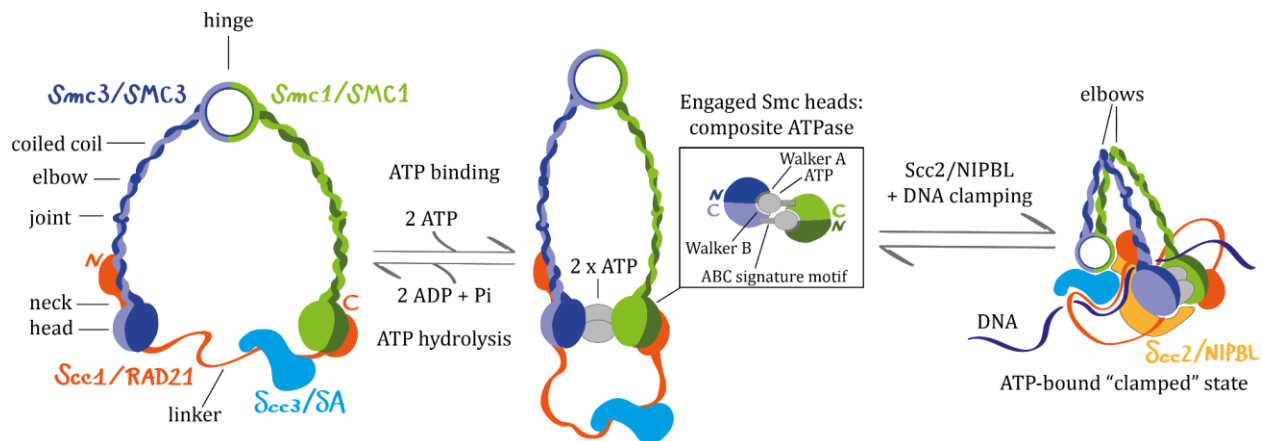


Figure 4.1.1. Cohesin components and conformations within the ATP cycle. Smc heads engage by binding two ATP molecules and build up a composite ATPase, which hydrolyzes ATP and leads to heads disengagement; a particular ATP-bound conformation is the “clamped” state, in which the cohesin regulator Scc2/NIPBL folds the Smc coiled coils on their elbows by bringing the hinge close to the heads (hinge “swinging” or coiled coils “zipping”) and clamps DNA into a channel on top of Smc heads (Bauer *et al.*, 2021a; Collier *et al.*, 2020; Higashi *et al.*, 2020; Petela *et al.*, 2021; Shi *et al.*, 2020b); Scc3/SA folds the flexible Scc1/RAD21 linker region like a “safety belt” (Kschonsak *et al.*, 2017) that wraps around a second segment of DNA, which might represent the second anchor of a loop (Collier *et al.*, 2020; Lee *et al.*, 2022; Shaltiel *et al.*, 2021). Figure adapted from: Arumugam *et al.*, 2003; Oldenkamp and Rowland, 2022.

The dynamic modulation of cohesin activity depends on several regulators. The trimeric protein complexes of the SMC-kleisin family indeed also interact with large hook-shaped regulatory proteins, belonging to the Kite (kleisin interacting winged-helix tandem elements) family, in the case of bacterial and archeal complexes, or of the mammalian Smc5/6 complex (Oldenkamp and Rowland, 2022; Palecek and Gruber, 2015), or to the Hawk (HEAAT proteins assoiated with kleisins) family in the case of eukaryotic condensins and cohesins (Oldenkamp and Rowland, 2022; Wells *et al.*, 2017). The Hawk family comprises Scc2/NIPBL, Pds5/PDS5A-B and Scc3/SA1-2, and evolved from the Kite protein family (Wells *et al.*, 2017). The SMC, kleisin and HEAT repeat subunits may all interact with DNA (Gligoris *et al.*, 2014; Li *et al.*, 2018; Shi *et al.*, 2020b).

Scc1 is responsible for the recruitment of the Hawk proteins as well as of Wapl, another cohesin regulator, to the ring complex (Roig *et al.*, 2014). Scc3/SA binds to two sections of Scc1 through its C-

terminal (Haering *et al.*, 2002; Roig *et al.*, 2014). It is involved in the loading of cohesin on chromosome through interaction with the loading complex Scc2-Scc4 (Hu *et al.*, 2011; Murayama and Uhlmann, 2014), in maintaining sister chromatid cohesion (Roig *et al.*, 2014) and in cohesin release modulated by Scc3/SA phosphorylation (Hauf *et al.*, 2005) and by Smc3 acetylation (Roig *et al.*, 2014; Rowland *et al.*, 2009).

Cohesin loading on chromosomes at the end of G1 or mitosis (in yeast and metazoan respectively; Wendt, 2017; Woodman *et al.*, 2014) depends on the “adherin” (Dorsett, 2004) or “kollerin” (Nasmyth, 2011) heterodimer formed by the yeast proteins Scc2 and Scc4 (Ciosk *et al.*, 2000; Tóth *et al.*, 1999). DNA entry within cohesin’s ring occurs through a transient opening at the Smc hinge interface, driven by ATP hydrolysis and the kollerin complex (Arumugam *et al.*, 2003, 2006; Gruber *et al.*, 2006; Hu *et al.*, 2011; Weitzer *et al.*, 2003). Scc2 is sufficient and essential to activate ATP hydrolysis in the absence of Pds5 and to promote cohesin loading (Petela *et al.*, 2018). Scc2 is also necessary to maintain chromosomal association during G1 (but not G2; Srinivasan *et al.*, 2019) and for loop extrusion (Davidson *et al.*, 2019; Kim *et al.*, 2019). Scc2-Scc4 loading activity is temporally regulated by Scc2 cleavage, which is induced by its dephosphorylation and leads to its disengagement from Scc4 (Woodman *et al.*, 2014). Scc2 and Scc4 correspond to NIPBL (nipped-B-like protein; Krantz *et al.*, 2004; Tonkin *et al.*, 2004) and MAU2 (maternal-effect uncoordinated 2; Seitan *et al.*, 2006; Watrin *et al.*, 2006) in human. Cohesin somatic mutations can lead to cancer (Carico *et al.*, 2021; Fisher *et al.*, 2017; Hill *et al.*, 2016; Katainen *et al.*, 2015), while germline ones cause a range of developmental disorders named “cohesinopathies” (Liu *et al.*, 2009). Mutations in the human *NIPBL* gene are the most frequent cause (up to 60%) of the cohesinopathy “Cornelia de Lange sndrome” (CdLS OMIM Entry # 122470; Avagliano *et al.*, 2020; Barbero, 2013; Deardorff and Krantz, 2014; Horsfield *et al.*, 2012; Parenti *et al.*, 2020; Piché *et al.*, 2019). In yeast, Scc2 gets recruited also by the remodels the structure of chromatin (RSC) complex (Lopez-Serra *et al.*, 2014), which is a member of the switch/sucrose non-fermentable (SWI/SNF) family of ATP-dependent chromatin-remodelers (Wagner *et al.*, 2020; Wang, 2003; Xue *et al.*, 2000). RSC would dually act as a chromatin platform for Scc2 to land and as a provider of a nucleosome-free region for cohesin to load (Lopez-Serra *et al.*, 2014), thereby collaborating in gene transcriptional regulation (Lopez-Serra *et al.*, 2014; Muñoz *et al.*, 2019, 2020). By fluorescence recovery after photobleaching (FRAP) and single molecule tracking (Rhodes *et al.*, 2017), NIPBL was observed to “hop” dynamically on chromatin between different cohesin rings, suggesting that NIPBL stimulation of cohesin’s ATPase might not only drive loading but also loop extrusion (Rhodes *et al.*, 2017).

The interaction of either Scc2/NIPBL or Pds5 with cohesin is mutually exclusive (Petela *et al.*, 2018). Pds5 (precocious dissociation of sisters 5) is recruited in G1 by Scc1, is essential for establishment and maintenance of cohesion and dissociates from chromosomes upon cleavage at the metaphase-to-anaphase transition (Hartman *et al.*, 2000; Panizza *et al.*, 2000). Pds5 has a dual role of cohesin (de)stabilization (Beckouët *et al.*, 2016; Chan *et al.*, 2012, 2013), facilitated by its binding close to Scc1 N-terminal (Chan *et al.*, 2013; Lee *et al.*, 2016; Ouyang *et al.*, 2016). Pds5 inhibits Scc2/NIPBL activity, leading to an arrest of ATP hydrolysis and cohesin translocation (Petela *et al.*, 2018). It promotes chromosomal dissociation through Wapl recruitment, ensuring a high rate of turnover through destabilization (Gandhi *et al.*, 2006; Kanke *et al.*, 2016; Kueng *et al.*, 2006; Nishiyama *et al.*, 2010). Additionally, Pds5 also promotes Smc3 *de novo* acetylation by EcoI/ESCO1-2 during S-phase and prevents subsequent deacetylation by Hos1/HDAC8 deacetylase during G2 and M phases, thereby blocking dissociation and stabilizing cohesin to hold sister chromatids (Beckouët *et al.*, 2016; Chan *et al.*, 2012, 2013).

Rad61 (or Wpl1, Wapl in yeast (Game *et al.*, 2003; Rolef Ben-Shahar *et al.*, 2008); WAPL in human, wings apart-like; Oikawa *et al.*, 2004) interacts with Scc1 and Scc3/SA through its N-terminal, destabilizes unacetylated chromosome-bound cohesin and induces its release from chromatin (Gandhi *et al.*, 2006; Kueng *et al.*, 2006; Lopez-Serra *et al.*, 2013). Its activity negatively regulates the maintenance of cohesion in G2 and facilitates the resolution of sister chromatids from mitotic prophase until telophase (Gandhi *et al.*, 2006; Kueng *et al.*, 2006; Lopez-Serra *et al.*, 2013). Moreover, WAPL forms a subcomplex with PDS5A (Kueng *et al.*, 2006) and together they co-regulate the size of chromatin loops by restricting cohesin activity (Wutz *et al.*, 2017). Additionally, WAPL creates a pool of free cohesin to maintain a dynamic turnover that is important for enhancer-promoter loop regulation (Liu *et al.*, 2021).

Sororin (CDCA5, cell division cycle-associated protein 5) is a WAPL antagonist (Nishiyama *et al.*, 2010), which actively and dynamically interacts with cohesin (Ladurner *et al.*, 2016). It is not necessary for cohesin chromosomal association, but essential for the establishment of sister chromatid cohesion during S-phase and its stabilization in G2 (hence its name from the Latin *soror*, “sister”) (Rankin *et al.*, 2005; Schmitz *et al.*, 2007). Its action is cell-cycle dependent and it gets degraded in G1 through ubiquitination mediated by the anaphase promoting complex (APC) (Rankin *et al.*, 2005). Its binding to cohesin is promoted by Smc3 acetylation and DNA replication (Ladurner *et al.*, 2016; Nishiyama *et al.*, 2010). It inhibits cohesin dissociation by sequestering WAPL’s targets PDS5A-B until mitosis, when it gets phosphorylated and loses this antagonizing ability (Nishiyama *et al.*, 2010). No orthologue of sororin was found outside vertebrates (Rankin *et al.*, 2005), but sororin-

related proteins were identified in many invertebrates (e.g. dalmatian protein in the fruit fly; Nishiyama *et al.*, 2010).

The yeast protein establishment of cohesion 1 (Eco1) (Tóth *et al.*, 1999), also named chromosome transmission fidelity 7 (Ctf7) (Skibbens *et al.*, 1999), is a N-acetyltransferase able to acetylate cohesin (Ivanov *et al.*, 2002; Rowland *et al.*, 2009). Acetylation of two residues of Smc3 by Eco1/Ctf7 promotes tethering of sister chromatids by chromatin-bound cohesin, hence stabilization of the complex on chromosomes and cohesion establishment (Ladurner *et al.*, 2016; Rolef Ben-Shahar *et al.*, 2008; Unal *et al.*, 2008; Zhang *et al.*, 2008). However Eco1/Ctf7 is not necessary for either cohesin loading onto chromosomes, nor for the maintenance of cohesion during G2 phase and mitosis (Skibbens *et al.*, 1999; Tóth *et al.*, 1999). Of the two mammalian orthologs ESCO1 and -2, ESCO2 is the one mainly responsible for cohesion establishment during S-phase, while ESCO1 is largely acetylating Smc3 throughout interphase, likely with different regulatory purposes (Alomer *et al.*, 2017). Smc3 acetylation blocks the opening of a DNA exit gate at the Smc3-kleisin interface (Beckouët *et al.*, 2010, 2016; Chan *et al.*, 2012; Gligoris *et al.*, 2014; Sakata *et al.*, 2021). This gate would support the hypothesis that cohesin must encircle two DNA strands to entrap them together, likely between the juxtaposed Smc heads and kleisin (Chapard *et al.*, 2019; Gligoris *et al.*, 2014; Huis in 't Veld *et al.*, 2014; Ouyang *et al.*, 2016).

Deacetylation of Smc3 is triggered by Scc1 cleavage and promoted by Scc3/SA to remove cohesin from chromosomes (both in prophase and anaphase pathways, see later in text) (Li *et al.*, 2017; Roig *et al.*, 2014). Deacetylation by Hos1 (Borges *et al.*, 2010) (HDAC8 in mammals, histone deacetylase 8; Deardorff *et al.*, 2012) allows to dissolve pro-cohesive elements and to regenerate recyclable cohesin for the next cell cycle (Deardorff *et al.*, 2012).

Sister chromatid cohesion consists in the physical tethering of sister DNA molecules along their chromosome arms and more strongly at centromeres (Figure 4.1.2. A) (Morales and Losada, 2018; Nasmyth and Haering, 2009). Cohesion must be established during S-phase to ensure proper segregation of the duplicated DNA into daughter cells by preventing their premature separation during G2/M (Losada *et al.*, 1998; Michaelis *et al.*, 1997; Uhlmann and Nasmyth, 1998; Zuilkoski and Skibbens, 2022). Cohesion is in fact what allows sister chromatids to establish an amphitelic or bipolar attachment between their kinetochores and the microtubules of the mitotic spindle, such that each chromatid is pulled in opposite directions (reviewed in: Losada, 2008; Nasmyth and Haering, 2009; Nasmyth and Schleiffer, 2004; Peters *et al.*, 2008). In a process of error correction, the correct poleward-directed “bi-orientation” would only be stabilized when tension between the centromeres is generated, that is when the sister molecules are pulled in opposite direction and cohesin opposes

resistance (Nasmyth and Schleiffer, 2004; Nicklas, 1967, 1997). The separation of sister chromatids will then occur, unless lagging and/or incorrectly bioriented chromatids inhibit cohesion resolution at the spindle assembly checkpoint (SAC) (Corbett, 2017; Garcia *et al.*, 2021; Manic *et al.*, 2017; Nasmyth and Schleiffer, 2004; Pidoux *et al.*, 2000; Sane *et al.*, 2021).

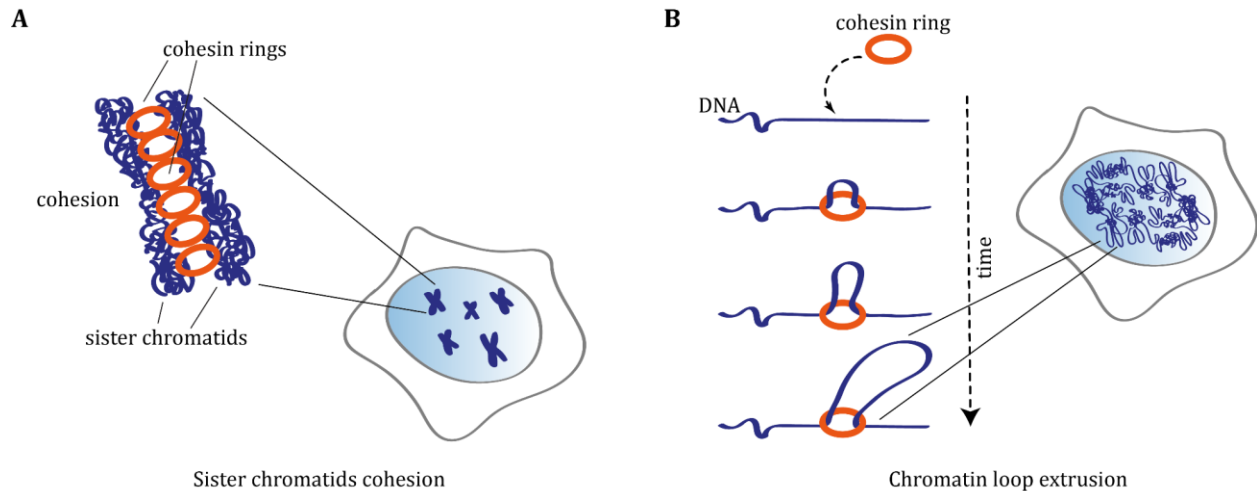


Figure 4.1.2. Cohesin major functions. **A** Sister chromatid cohesion: cohesin holds together sister chromatids from S-phase until mitosis to allow proper segregation. **B** Chromatin loop extrusion: cohesin loads on chromatin and extrudes loops to shape genome architecture in interphase nuclei. Figure adapted from: Oldenkamp and Rowland, 2022.

Cohesin binding to chromosomes is necessary but not sufficient for cohesion (Tóth *et al.*, 1999). Both the cohesin complexes that were already chromosome-associated and those that get *de novo*-loaded by Scc2-Scc4/NIPBL-MAU2 onto nascent strands participate in cohesion establishment (Srinivasan *et al.*, 2020). Eco1/Ctf7 ensures a faithful cohesion establishment by binding PCNA and other DNA replication factors and activating cohesin as a “tethering-competent” complex in a post-fork context during S-phase (reviewed in: Zuilkoski and Skibbens, 2022). Cohesion likely occurs through dimerization or clustering of the ring-shaped complex (Cattoglio *et al.*, 2019; Eng *et al.*, 2015; Kulemzina *et al.*, 2012; Shi *et al.*, 2020a; Skibbens *et al.*, 1999; Tong and Skibbens, 2014, 2015; Xiang and Koshland, 2021; Zhang *et al.*, 2008). Eco1/Ctf7, Wpl1 and Hos1 would control dimerization in S-phase and monomerization in mitosis (Shi *et al.*, 2020a).

A correct timing of anaphase inhibition and triggering, respectively corresponding to cohesion maintenance and resolution, is mediated by a complex made of the two proteins separin (Esp1/ESPL1, extra spindle poles-like 1; Ciosk *et al.*, 1998; McGrew *et al.*, 1992; Nagase *et al.*, 1996) and securin (Pds1/PTTG1, pituitary tumor-transforming gene 1; Guacci *et al.*, 1993; Yamamoto *et al.*, 1996a; Zou *et al.*, 1999; as reviewed in: Yanagida, 2000).

In *S. cerevisiae*, cohesin remains bound until Scc1 gets cleaved at two sites by the clan CD cysteine peptidase “separin” or “separase” at the metaphase-anaphase transition (anaphase pathway; Uhlmann *et al.*, 1999, 2000). In vertebrates most of cohesin (95%) dissociates already in prophase and only a small fraction keeps holding sister chromatids till anaphase (prophase pathway; Losada and Hirano, 2000). Cohesion dissolution in vertebrate prophase is induced by phosphorylation by polo-like kinase 1 (Plk1; Holtrich *et al.*, 1994) and Aurora kinase B (AKB; Bischoff *et al.*, 1998) (Hauf *et al.*, 2005; Losada *et al.*, 1998, 2002; Sumara *et al.*, 2000, 2002; Waizenegger *et al.*, 2000). Sororin acts as a docking protein on cohesin and recruits Plk1 to SA2 (Zhang *et al.*, 2011). Human SCC1 is also phosphorylated by the Plk1 homolog cell division control 5 (CDC5) *in vitro*, however this only enhances its cleavability by separase in anaphase (Hauf *et al.*, 2005). At the onset of anaphase in vertebrates also the tighter cohesion of centromeres gets resolved through proteolytic cleavage of the Scc1/RAD21 subunit by separin (Hauf *et al.*, 2001; Rivera and Losada, 2006; Waizenegger *et al.*, 2000).

The anaphase promoting complex/cyclosome (APC/C) is a ubiquitin protein ligase involved in the destruction of cyclins at the end of mitosis (Barford, 2020; King *et al.*, 1995; Sudakin *et al.*, 1995; Zachariae and Nasmyth, 1996; Zachariae *et al.*, 1996). APC/C mediates the proteolysis of Pds1 (Ciosk *et al.*, 1998; Cohen-Fix *et al.*, 1996), which is essential for cohesin dissociation (Cohen-Fix *et al.*, 1996; Funabiki *et al.*, 1996; Guacci *et al.*, 1993; Yamamoto *et al.*, 1996b, 1996a). Pds1 in fact forms a complex with and inhibits the protein Esp1 (Ciosk *et al.*, 1998). APC/C liberates Esp1 from the Esp1-Pds1 complex, allowing it to release cohesin from the chromatids through Scc1 cleavage at anaphase onset in yeast (Amon, 2001; Ciosk *et al.*, 1998; Uhlmann *et al.*, 1999; Yamamoto *et al.*, 1996b).

An additional complex formed by Shugoshin 1 (Sgo1; from the Japanese *shugoshin*, “guardian spirit”; Kitajima *et al.*, 2004; Marston *et al.*, 2004; Rabitsch *et al.*, 2004; Sane *et al.*, 2021; Watanabe, 2005) and the serine/threonine protein phosphatase PP2A (Janssens and Goris, 2001) shields centromeric cohesin from Wapl dissociation in early mitosis and from separase cleavage in meiosis I (Hara *et al.*, 2014; Kitajima *et al.*, 2006; Riedel *et al.*, 2006; Rivera and Losada, 2006; Tang *et al.*, 2006). Sgo1 gets localized on centromeres by the checkpoint kinase budding uninhibited by benzimidazole 1 (Bub1; Bernard *et al.*, 2001; Kim and Gartner, 2021; Kitajima *et al.*, 2004) and it recruits PP2A (Kitajima *et al.*, 2006; Riedel *et al.*, 2006; Rivera and Losada, 2006; Tang *et al.*, 2006).

Besides sister chromatids cohesion, a novel role of cohesin in chromatin loop formation emerged (Figure 4.1.2. B). In 2008 several pioneer papers found that cohesin colocalizes at many CTCF sites and that CTCF was responsible for such localization (Parelho *et al.*, 2008; Rubio *et al.*, 2008; Stedman *et al.*, 2008; Wendt *et al.*, 2008). Their architectural activity at the base of chromatin loops became

evident with the first studies on their co-mediated gene expression regulation within specific loci (Hadjur *et al.*, 2009; Marsman *et al.*, 2014; Nativio *et al.*, 2009; Rhodes *et al.*, 2010; Wendt and Peters, 2009). Cohesin and CTCF co-enrichment was confirmed by many chromosome conformation capture and chromatin immunoprecipitation-related studies at different resolutions and loci (Deng *et al.*, 2012; Dixon *et al.*, 2015; Zuin *et al.*, 2014). These studies enabled to newly define different orders of chromatin organization such as TADs and A/B compartments (see section 1.1. of the General Introduction; Dixon *et al.*, 2012; Lieberman-Aiden *et al.*, 2009; Rao *et al.*, 2014) and the convergent orientation of CTCF binding sites as a prerequisite for loop formation (Gómez-Marín *et al.*, 2015; Rao *et al.*, 2014; Vietri Rudan *et al.*, 2015; de Wit *et al.*, 2015).

Based on these discoveries, the loop extrusion model was postulated: the cohesin ring complex extrudes chromatin loops until encountering an obstacle such as convergently oriented CTCF molecules or being released by Wapl (Fudenberg *et al.*, 2016, 2017; Nuebler *et al.*, 2018; Vian *et al.*, 2018). CTCF N-terminal interacts with SCC1 and SA2 (Li *et al.*, 2020) and its cohesin-halting activity might be a multi-step process made of pausing and stabilization (Hansen, 2020). Cohesin is likely assuming different conformational states at CTCF-bound domain borders and non-CTCF intra-domain loop anchors, as shown by differences in cleavage sensitivity in experiments involving an engineered cleavable RAD21 (Liu and Dekker, 2021). Various cohesin compartments with a DNA-entrapment potential can form through interactions between its subunits (Chapard *et al.*, 2019). Different cryo-EM (electron microscopy) studies investigated cohesin conformation in its “clamped” state (Collier *et al.*, 2020; Higashi *et al.*, 2020; Petela *et al.*, 2021; Shi *et al.*, 2020b). A “butterfly” conformation with multiple foldings of Smc arms was also observed (Xiang and Koshland, 2021). Two of the various up-to-date models for chromatin loop enlargement are summarized in Figure 4.1.3. (reviewed in: Higashi and Uhlmann, 2022; Oldenkamp and Rowland, 2022).

Live imaging of condensin (Ganji *et al.*, 2018) and cohesin (Davidson *et al.*, 2019; Kim *et al.*, 2019) mediated loop extrusion confirmed the ability of these complexes to work as fast ATP-dependent molecular motors. Condensin-mediated loop extrusion in metaphase is asymmetric, while cohesin one in interphase is bidirectional and symmetric (Banigan and Mirny, 2020; Davidson *et al.*, 2019; Ganji *et al.*, 2018; Golfier *et al.*, 2020; Kim *et al.*, 2019). The average observed speed of cohesin extrusion was 0.5 kb/s (Kim *et al.*, 2019) - 1 kb/s (Davidson *et al.*, 2019), which means that cohesin could potentially fold the whole human genome in a few minutes. Cohesin molecular motor was shown to depend on NIPBL-MAU2 and once formed, loops did not require ATP to be maintained (Davidson *et al.*, 2019; Kim *et al.*, 2019).

on naked DNA, can hardly pass over nucleosomes and is constrained by DNA-bound CTCF (Davidson *et al.*, 2016; Stigler *et al.*, 2016). The fact that cohesin was observed to extrude both naked and nucleosome-bound DNA suggested that the complex works via non- or pseudo-topological binding (Kim *et al.*, 2019). This is consistent with experiments using a recombinant single-chain cohesin that would prevent topological DNA entrapment (Davidson *et al.*, 2019).

In this work, I aimed at unraveling how the architectural role of cohesin affects chromatin organization and function. First, I investigated the effects of RAD21 depletion on chromatin loop size through direct visualization by the use of the DNA halo method (sections 4.2.1. – 4.2.2.; data published in: Cremer *et al.*, 2020). Subsequently, I observed the effects of SA1 knock out on genomic functions by microscopical characterization of functional repair foci (sections 4.2.3. – 4.2.4.).

4.2. Results

4.2.1. RAD21 depletion and quantitation in HCT116-RAD21-mAC cells.

The use of an auxin-inducible degron system in human HCT116-RAD21-mAC cells allowed a rapid and efficient depletion of the cohesin RAD21 subunit (a schematic for the RAD21 degron system is shown in Figure 4.2.1. A and a scheme for the targeting of RAD21 to proteasomal degradation is shown in Figure 4.2.1. B; HCT116-RAD21-mAID-mClover cells were kindly provided by Masato Kanemaki, National Institute of Genetics, Japan; see Supplementary Table ST1 for cell line characteristics). Cells were treated with 500 μ M auxin for 6 hours, fixed and imaged with high content wide-field microscopy to quantify nuclear mean mClover-RAD21 intensities (Figure 4.2.1. C; see Supplementary Figure SF8 for high content image analysis pipeline and Supplementary Table ST3 for imaging system characteristics). RAD21 was efficiently and homogeneously depleted, with only a few cells escaping the auxin treatment (Figure 4.2.1. D). The median background level measured in untagged HCT116 wild type cells was subtracted from the mean mClover intensities measured in HCT116-RAD21-mAC cells to accurately calculate the actual protein depletion. RAD21-depleted cells showed a median value of 2.62 a.u., corresponding to 10% of RAD21 levels in untreated cells (the results obtained from three biological replicates are shown in Figure 4.2.1. D; plot statistics in Supplementary Table ST4; single replicates for both wild type and engineered HCT116 cells are separately plotted in Supplementary Figure SF9).

4.2.2. RAD21-depleted HCT116 cells display up to ten fold larger DNA loops

Once validated the RAD21-degron settings, the structure of chromatin loops upon cohesin depletion was investigated by applying the DNA halo approach (Figure 4.2.2. A).

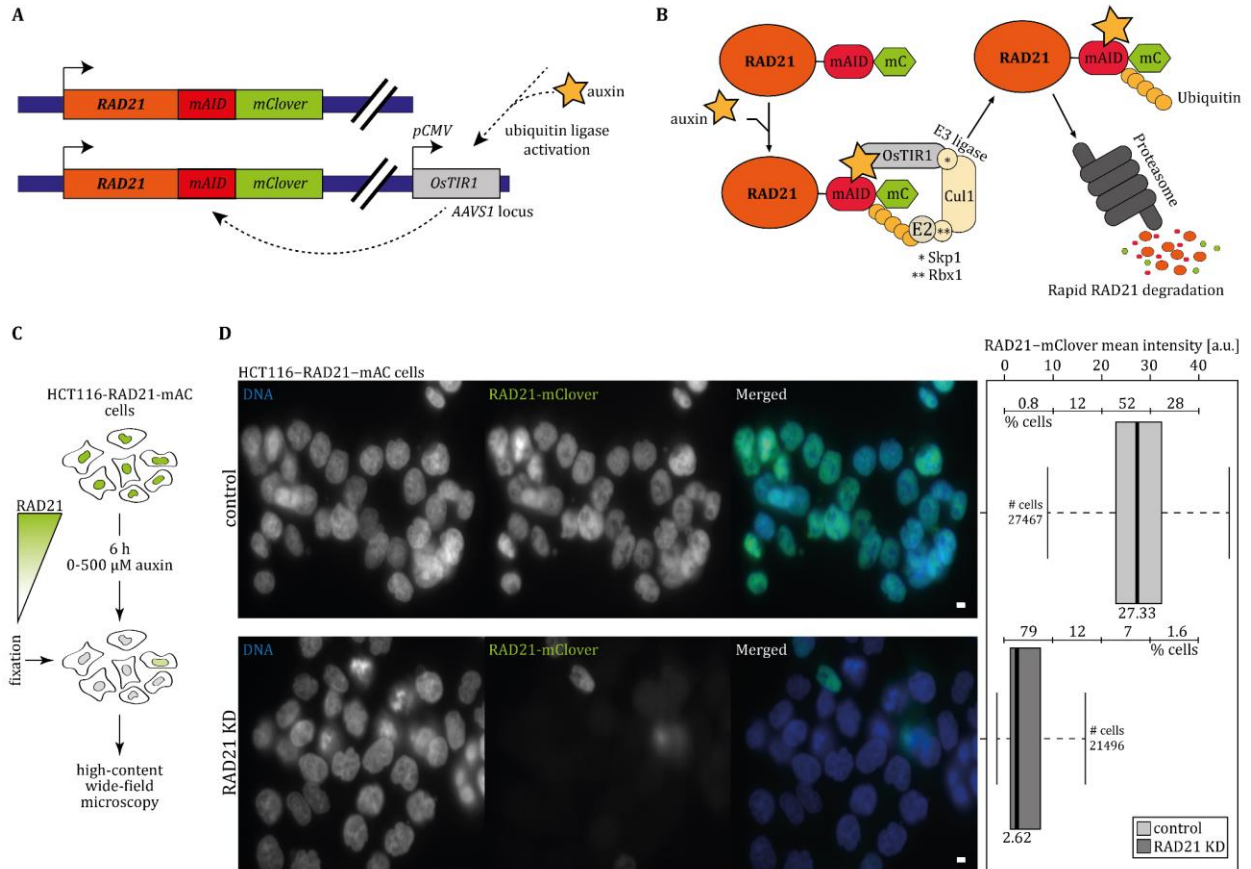


Figure 4.2.1. Cohesin major component RAD21 is efficiently depleted up to 10% in HCT116-RAD21-mAC cells. **A** Scheme of the auxin-inducible degron (AID) system in HCT116-RAD21-mAC cells. An AID cassette and an mClover reporter are fused to both *RAD21* endogenous alleles. At the *AAVS1* locus, the cell line harbors the *OsTIR1* gene, under control of the pCMV promoter. **B** Schematic of the auxin-induced targeting of RAD21 to proteasomal degradation. The auxin-responsive *OsTIR1* (F-box protein *TIR1*, derived from *Oryza sativa*) forms a functional SCF-*OsTIR1* E3 ligase complex (*Skp1*, *Cullin* and *E-box*) by interaction with the endogenous human components (conserved in all eukaryotes). When added to the cell culture, auxin binds to the *OsTIR1*-containing ubiquitin ligase and promotes its interaction with the AID-fused RAD21. The ligase polyubiquitinates the RAD21-degron, leading to its proteolysis by the proteasome. Panels A and B adapted from (Natsume *et al.*, 2016; Nishimura *et al.*, 2009; Rao *et al.*, 2017). **C** Experimental settings for the validation of RAD21 depletion in HCT116-RAD21-mAC cells. Cells grown on microscope slide coverslips were treated with 0-500 μ M auxin for 6 hours, fixed, DAPI-stained and imaged with a high-content wide-field microscope. **D** Mean RAD21-mClover intensities of untreated (median = 27.33 a.u.) and 500 μ M auxin-treated cells (median = 2.62 a.u.). Single cells were imaged with a high-content wide-field microscope, nuclei were segmented based on the DNA signal and nuclear RAD21-mClover intensities measured; the background measured in untagged HCT116 cells treated with the same conditions was also measured and subtracted from the values obtained in the mClover-tagged cell line to precisely quantitate RAD21 levels. A two-sided Wilcoxon test was performed to test significance ($p < 0.0001$). Percentages of cells in the different ranges of intensities, corresponding to different RAD21 nuclear amounts, are shown along the boxplots. A small percentage of cells escaped the auxin treatment, as shown by the small overlap between untreated and auxin-treated samples boxplots and by the exemplary images shown on the left side (scale bar: 5 μ m). # cells: number of cells of the sample (composed of three biological replicates, each made of technical duplicates). The data shown in D was published in: Cremer *et al.*,

2020. See Supplementary Figures SF2 for boxplot explanation, SF8 for image analysis pipeline and background calculation, SF9 for plotting of the single replicates, Supplementary Table ST4 for plot statistics.

This technique allows to investigate changes in chromatin organization at the level of DNA loops (Buongiorno-Nardelli *et al.*, 1982; Vogelstein *et al.*, 1980). Briefly, the cells were permeabilized by detergents, the soluble fraction of nuclear proteins was extracted with high salt buffers and distension of loops was achieved with high salt concentration and a DNA-intercalating dye. DNA loops were allowed to span out of an insoluble nuclear scaffold, thus providing a measure of their size (Figure 4.2.2. A). Histone extraction in interphase nuclei by high-salt incubation in fact triggers the extrusion of chromatin loops from a densely stained central chromatin core. After DAPI staining, a very bright and structured scaffold could be distinguished from a more faded halo, which corresponded to the extruded loops (Figure 4.2.2. B, C). RAD21 depleted cells exhibited larger DNA loops (500 μM auxin for 6 h; Figure 4.2.2. C) than untreated one (0 μM auxin for 6 h; Figure 4.2.2. B), reflecting a local loss of chromatin structural organization. Additionally, they often exhibited bundles of fibers departing from jagged halo borders (Figure 4.2.2. C), reflecting the loss of the structural organization for which cohesin is responsible, as confirmed by the very conserved, defined and tightly wrapped halos observed in the untreated cells (Figure 4.2.2. B). Based on the DAPI signal, the halo area around the insoluble scaffolds was manually segmented and plotted in Figure 4.2.2. D. The DNA halos displayed upon RAD21 degradation were more variable in shape and reached up to ten times larger areas in comparison to the control, with the median and the mean value being respectively two and three fold higher than those of untreated cells (the results of four biological replicates is shown in Figure 4.2.2. D; see Supplementary Figure SF10 for plotting of the single replicates and the Supplementary Table ST4 for plot statistics). The largest DNA halo measured was of 190.01 μm^2 and of 971.53 μm^2 in the untreated and cohesin depleted cells, respectively. From the manually segmented DNA halo areas, the DNA halo radiuses were mathematically calculated and plotted as frequency distribution in Figure 4.2.2. E. The radiuses of the untreated control cells laid in a short and defined range of values, whereas the radiuses of cohesin depleted cells spanned further and more variably (Figure 4.2.2. E).

4.2.3. Validation of SA1 KO in iMEF cells

The cohesin component of the Hawk family, namely Scc3 in budding yeast, exists as two isoforms in mammals: SA1 and SA2 (or STAG1, STAG2; in mouse and human respectively; Carramolino *et al.*, 1997; Tóth *et al.*, 1999). In this work, a possible role of the subunit SA1 in DNA repair was investigated through the use of a SA1 KO iMEF cell line (immortalized mouse embryonic fibroblasts, Supplementary Table ST1).

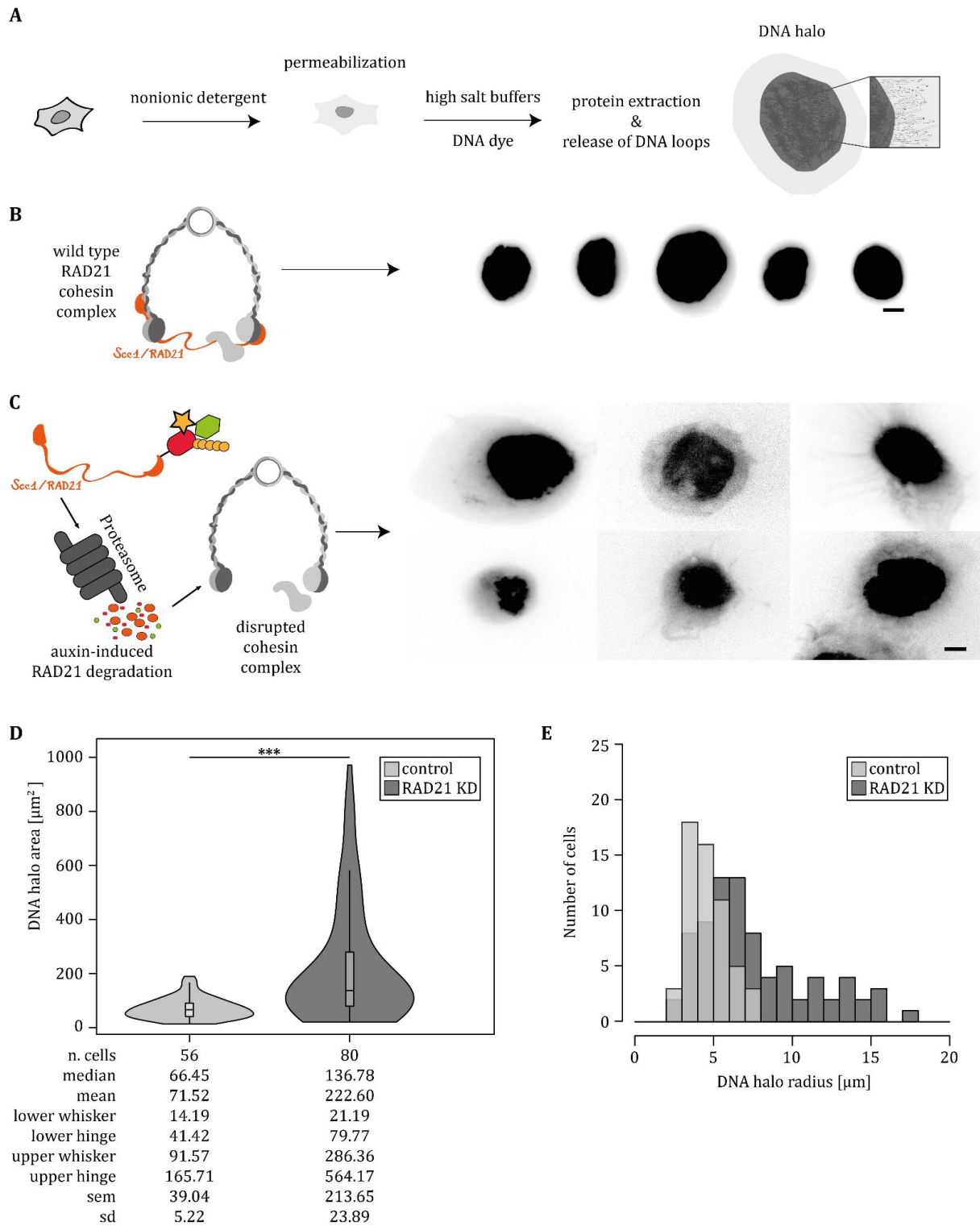


Figure 4.2.2. Cohesin is essential to regulate chromatin loop sizes. **A** Schematic of the DNA halo method. Upon permeabilization by the use of nonionic detergents, deproteinization by high salt buffers and the use of a

DNA-intercalating dye, DNA loops are extruded and appear as a faded halo around a bright insoluble scaffold. **B – C** Schematics of WT versus RAD21-depleted cohesin and representative images of DNA halos stained with DAPI. The faded DNA halo surrounding a brighter insoluble nuclear scaffold corresponds to the DNA loops, whose extent reflects the degree of structural organization of chromatin. **B** Schematic of wild type cohesin complex with RAD21 and images of typical nuclei from control cells with small, rather uniform, and well delimited halos. **C** Schematic of disrupted cohesin complex depleted of RAD21 and exemplary images of DNA halos of cohesin depleted cells, showing variable shapes and size, often ending up in extruded bundles of DNA fibers. Scale bar in B-C: 5 μm . **D** Violin plots showing the differences in area of the DNA halo between control and RAD21 depleted cells (6 h of 0-500 μM auxin treatment), determined as described in Methods ($A_h = A_t - A_s$). The violin plots show the whole data points distribution and harbor a boxplot, whose statistics are explained in Supplementary Figure SF2. The results represent four biological replicates (see Supplementary Figure SF10 for plotting of the single replicates and the Supplementary Table ST4 for plot statistics) A two-sided Wilcoxon test was performed to test significance ($p < 0.0001$). **E** Distribution of radial values of DNA halos for the two populations shown in D. The radius was calculated as in the methods: $R = \sqrt{(A_h/\pi)}$. The data in D-E and the representative images shown in B-C were published in: Cremer *et al.*, 2020.

First, the knock out of SA1 in iMEF cells was validated through SA1 immunostaining (Supplementary Table ST2; both the cell lines and the anti-SA1 antibody were provided by Dr. Ana Losada, Centro Nacional de Investigaciones Oncológicas (CNIO), Madrid, Spain; published in: Remeseiro *et al.*, 2012a) and subsequent microscopy imaging (Figure 4.2.3. A). The cohesin complex with or without the SA1 subunit is drawn in Figure 4.2.3. B. Upon high-content wide-field microscopy, the SA1 nuclear mean intensities were quantified (Figure 4.2.3. C). A median value of 85.5 and 32.4 a.u. was respectively measured in SA1 WT and KO iMEF cells. The intensities observed in the KO cell line clearly belong to background levels, as supported by the fact that they mostly do not overlap the range of intensities in the WT cells (Figure 4.2.3. C; Supplementary Table ST4). Confocal imaging of both cell lines further confirmed the complete absence of SA1 in the nuclei of the KO iMEF cells (Figure 4.2.3. D).

4.2.4. DNA damage signaling after ionizing radiation is impaired in SA1 KO iMEF cells

Cohesin is since long known to have a role in the repair of DNA damage, as the name itself of the main RAD21 subunit tells, in which “rad” stands for radiation-sensitive mutant (Birkenbihl and Subramani, 1992). However, the precise mechanisms through which cohesin is required for a proper DNA repair are not yet fully elucidated. Additionally, how the single subunits of the complex contribute to this role is not clear.

Here, the contribution of the cohesin subunit SA1 in DNA damage repair is investigated. To this aim, SA1 WT and KO iMEF cells were subjected to different doses of ionizing radiation (0, 2, 5, 10 Gy, X-rays; Figure 4.2.4. A). Cells were fixed half an hour after the induction of DNA damage and immunostained to detect γH2AX (Supplementary Table ST2).

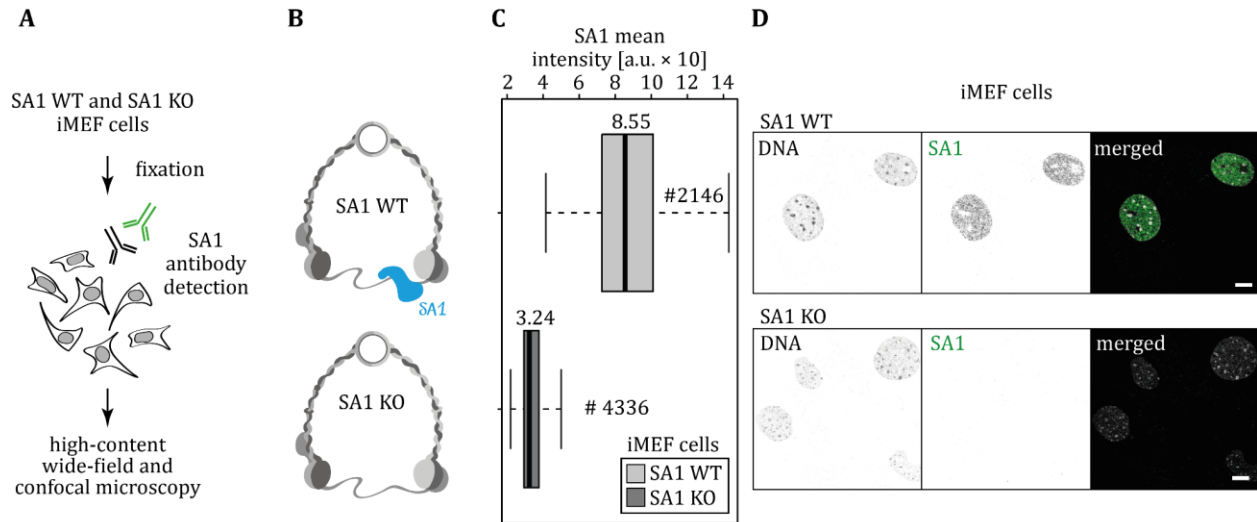


Figure 4.2.3. SA1 KO validation in iMEF SA1 KO cells. **A** Schematic of the experimental procedure for SA1 KO validation. SA1 WT and KO iMEF cells (Supplementary Table ST1) grown on microscope slide coverslips were fixed, immunostained for SA1 detection and imaged with a high-content wide-field microscope (Supplementary Table ST3). **B** Schematic of the cohesin complex in the wild type state with SA1 (depicted in light blue) and without SA1, knock out state. **C** SA1 mean intensity in SA1 WT (light gray) and KO (dark gray) iMEF cells. After imaging with high-content wide-field microscopy the cells treated as in A, the DNA signal was used to segment nuclear masks (mainly as in Supplementary Figure SF8 A). The SA1 nuclear mean intensities were then measured and plotted as boxplots. The median value is indicated on the top of each black median line of the boxplots, while the value indicated with a # corresponds to the total number of cells analyzed. The results consist of three biological replicates (two-sided Wilcoxon test for significance: $p < 0.0001$). See Supplementary Figures SF2 for boxplot explanation and Supplementary Table ST4 for plot statistics. **D** Example montages of confocal microscopy images of SA1 WT and KO iMEF cells (SA1 in green; scale bar: 10 μm).

The phosphorylation of the histone variant H2AX (on serine 139; Rogakou *et al.*, 1998, 1999) is in fact a mark for the signaling of DNA damage. Its deposition by key kinases starts at the sites of double strand breaks and spreads for megabases (Fernandez-Capetillo *et al.*, 2002; Rogakou *et al.*, 1999), thereby inducing the recruitment of DNA repair factors (reviewed in (Blackford and Jackson, 2017; Scully *et al.*, 2019); see section 3.1.1. for more details on the DNA damage response). Upon high-content wide-field microscopy, the γH2AX nuclear mean intensities were quantified. A significant difference was observed between SA1 WT and KO iMEF cells for all the radiation doses, indicating an impairment in the signaling of DNA damage in the absence of SA1 (Figure 4.2.4. B; Supplementary Table ST4). The cells were subsequently imaged with a confocal microscope (Supplementary Table ST3; see Supplementary Figure SF11 for example images at all radiation doses) and the ones irradiated with 2 Gy X-rays (Figure 4.2.4. C) were analyzed with the aim to characterize the γH2AX repair foci. Upon nuclear masking, the repair foci were segmented based on the γH2AX antibody signal and their focal characteristics were quantified.

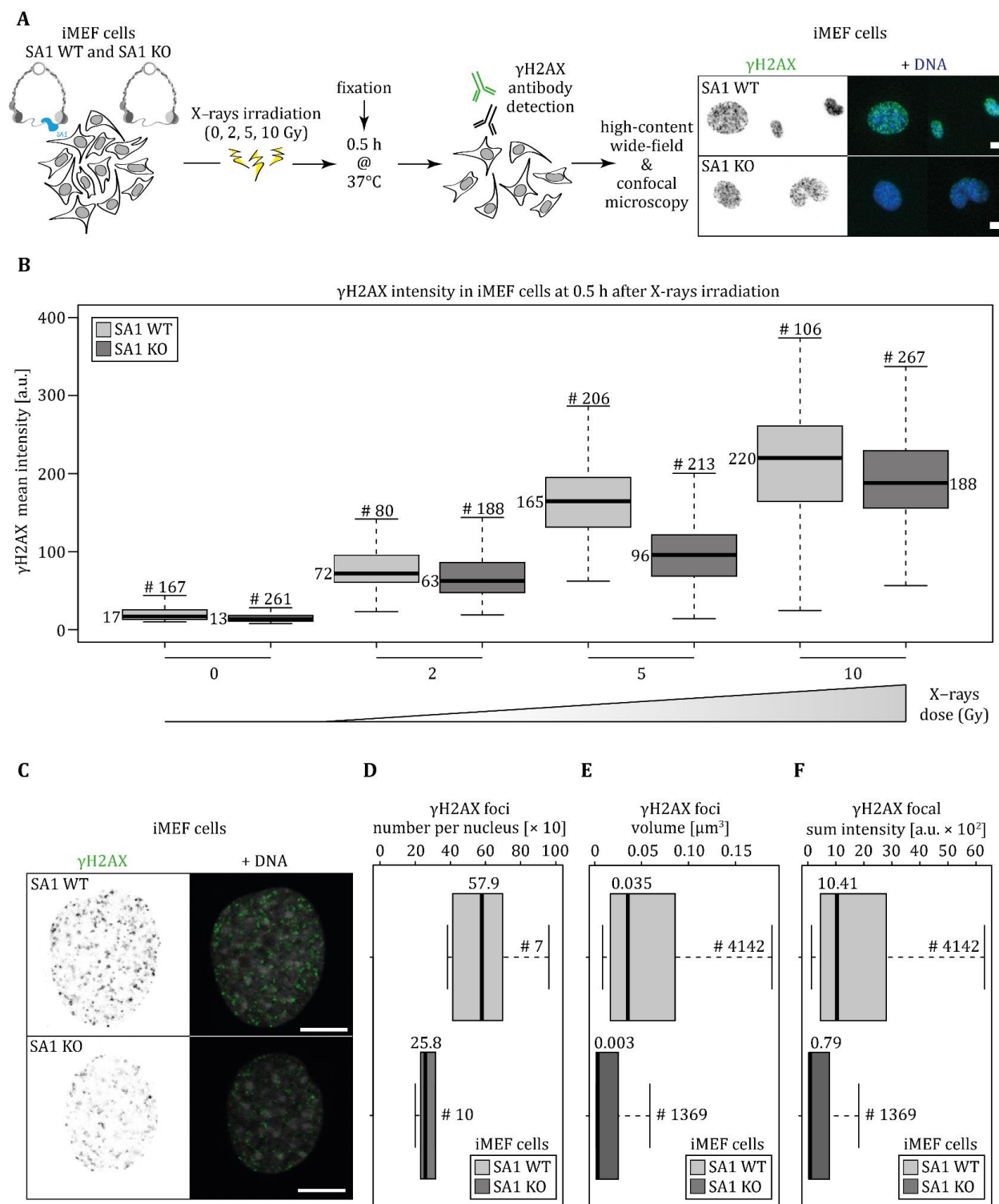


Figure 4.2.4. The signaling of DNA damage is impaired in iMEF SA1 KO cells. **A** Experimental scheme for the evaluation of the DNA damage signaling ability in SA1 KO cells. SA1 WT and KO iMEF cells (Supplementary Table ST1) grown on microscope slide coverslips were irradiated with different X-ray doses (0, 2, 5, 10 Gy) and fixed 30' after DNA damage induction. Cells were then immunostained for γH2AX detection and imaged with

high-content wide-field and confocal microscopy (Supplementary Tables ST2, ST3). On the right, an example of SA1 WT and KO iMEF cells showing the γ H2AX signal at 30' after 5 Gy X-rays is presented (scale bar: 10 μ m; for more representative images at the different X-ray doses, see Supplementary Figure SF11). **B** γ H2AX mean intensity in SA1 WT (light gray) and KO (dark gray) iMEF cells at 30' post X-rays irradiation. Cells were treated as in A and analyzed upon imaging with high-content wide-field microscopy (mainly as in Supplementary Figure SF8). Nuclear masks were segmented based on the DNA signal and the γ H2AX nuclear mean intensities were exported. The median values are shown next to each median line and the number of cells indicated with a # on top of the respective boxplots. A two-sided Wilcoxon test was performed to test significance between WT and KO samples for each X-ray dose (0 Gy: $p < 0.0001$; 2 Gy: $p = 0.0021$; 5 Gy: $p < 0.0001$; 10 Gy: $p = 0.0025$). **C – F** Confocal microscopy image analysis of SA1 WT and KO iMEF cells at 30' upon 2 Gy X-rays irradiation. **C** Example of confocal images of SA1 WT and KO iMEF cells irradiated with 2 Gy X-rays, fixed after 30' and immunostained for γ H2AX detection (as schematically depicted in A; scale bar: 10 μ m). From the confocal images, the nuclei of both SA1 WT and KO iMEF cells were masked based on DAPI – DNA. The γ H2AX foci were segmented within the nuclear masks based on the AF488 – γ H2AX signal. γ H2AX foci characteristics were then analyzed and the results were plotted as boxplots. **D** Number of γ H2AX foci per nucleus. **E** Volume of γ H2AX foci. **F** γ H2AX sum intensity within γ H2AX foci. In D – F, the median values are written on top of each boxplot, while the value indicated with a # corresponds to the number of analyzed cells in D and to the total number of γ H2AX foci from all cells in E and F. A two-sided Wilcoxon test was performed for each parameter (D: $p = 0.0031$; E and F: $p < 0.0001$). For both B and D – F, see Supplementary Figures SF2 for boxplot explanation and Supplementary Table ST4 for plot statistics.

The SA1 KO iMEF cells showed a significant reduction in the total number of γ H2AX foci per nucleus (Figure 4.2.4. D). Moreover, both the volume of γ H2AX foci (Figure 4.2.4. E) and the γ H2AX focal sum intensity measured within the segmented foci (Figure 4.2.4. F) were significantly decreased in the absence of SA1 (see Supplementary Table ST4 for statistics). The results from the confocal microscopy analysis proved that the lower γ H2AX nuclear mean intensities quantified by high-content microscopy (Figure 4.2.4. B) were also due to a decrease in the number and in the volume of the repair foci, and not only due to a general decrease in foci intensity (Figure 4.2.4. D – F).

4.3. Discussion

The ring-shaped cohesin complex gained the fame of being a chromatin-loop ATP-dependent extruding machine (Davidson *et al.*, 2019; Kim *et al.*, 2019). In this work I investigated the influence of cohesin on genome structural and functional units with microscopy techniques. To address cohesin-mediated structuring of chromatin loops, I utilized the HCT116-RAD21-mAC cell line (Natsume *et al.*, 2016), which has been previously used to observe the changes in Hi-C maps in the absence of cohesin (Rao *et al.*, 2017). By the means of auxin-induced ubiquitination, degradation of RAD21 can be achieved and this can be measured by quantifying the fused mClover reporter (see Figure 4.2.1. A-B for a schematic of the functioning of RAD21-fused auxin degron; Natsume *et al.*, 2016; Nishimura *et al.*, 2009).

I validated the knockdown with high content microscopy upon 6 hours of auxin-induced RAD21 depletion (experimental scheme in Figure 4.2.1. C). Upon nuclei segmentation based on the DNA signal, the nuclear intensities of RAD21-mClover were calculated and the background level measured in not engineered WT HCT116 cells was subtracted in order to precisely quantify the actual residual amount of protein (Supplementary Figure SF8). The median of nuclear RAD21 intensities was reduced by ten fold in the auxin-treated sample, meaning that a protein depletion of 90% compared to the untreated sample was reached (Figure 4.2.1. D; Supplementary Table ST4; Supplementary Figure SF9).

Once validated the knockdown efficiency, the DNA loop sizes were observed directly by applying the DNA halo assay (Figure 4.2.2. A). The technique allowed me to obtain a DNA halo made of loops released from an insoluble nuclear scaffold. By manual segmentation of the area between the insoluble bright scaffold and the external border of the halo, it was possible to calculate the DNA halo area and to derive the related radius. While the untreated cells showed a short and homogenous halo (Figure 4.2.2. B), the DNA halo of RAD21-depleted cells showed a striking heterogeneity in shape and size (500 μ M auxin treatment for 6 h; Figure 4.2.2. C). DNA halo preparations provided consistent evidence for an increase in the sizes of chromatin loops in the absence of cohesin. After its depletion, a certain degree of structure in the chromatin organization was indeed lost, loops were extruded further and heterogeneously from the nuclear scaffold, often resulting in unusual shapes of DNA halos, with jagged and fibrous borders.

The DNA loops in the absence of cohesin showed a double median value, extended up to 10 fold in size and distributed in multiple populations (Figure 4.2.2. D; Supplementary Table ST4; Supplementary Figure SF10), as also nicely shown by the distribution of radius frequencies (Figure 4.2.2. E). The increase of DNA loop sizes upon auxin-induced RAD21 degradation in HCT116-RAD21-mAC cells shown here is consistent with similar results obtained in HeLa cells after esiRNA-mediated RAD21 depletion (Guillou *et al.*, 2010) and with the observations that cohesin-mediated loop extrusion compacts the DNA (Davidson *et al.*, 2019; Kim *et al.*, 2019).

The chromatin loop extension might in turn locally influence the number and the volume of replication domains due to the lack of subdivision into smaller functional loops. This hypothesis would be in line with early findings showing a correlation between the size of DNA loops and the length of replication units (Buongiorno-Nardelli *et al.*, 1982; Lemaitre *et al.*, 2005; Vogelstein *et al.*, 1980). The possibility of a functional-structural relationship between DNA replication and chromatin loops is further supported by the observation that the median DNA content of replication units measured in our laboratory (Chagin *et al.*, 2016) corresponds to the average size of chromatin loop

domains measured by Hi-C (Rao *et al.*, 2014), as widely discussed in (Mamberti and Cardoso, 2020). Cohesin is enriched at replication origins and interacts with MCM proteins, as shown by bioinformatics analysis and by immunoprecipitation, respectively (Guillou *et al.*, 2010). Cohesin depletion reduces the density of active origins while not affecting the fork speed, thereby causing a delay in S-phase (Guillou *et al.*, 2010). It was therefore suggested that cohesin is required for the formation and/or stabilization of loops at replication foci, mediating those long-range interactions which bring together a cluster of origins (Guillou *et al.*, 2010).

In the same work to which I contributed with my RAD21 quantification of depletion and DNA halo measurements, our colleagues analyzed DNA replication nano-foci with high resolution microscopy upon RAD21 depletion and measured a modest increase in focal volume and foci numbers (Cremer *et al.*, 2020). However the replication patterns and the replication timing were maintained, suggesting that chromatin structure was unaffected at a higher global genomic level (Cremer *et al.*, 2020). Additional features representative of the higher order of chromatin organization were also maintained in the absence of cohesin, such as chromosome territories and the distribution of both chromatin density and functional chromatin markers (SC35 for splicing speckles, H3K27me3 for heterochromatin and RNA Pol II for actively transcribed chromatin) (Cremer *et al.*, 2020). The most evident deficiency observed in RAD21-depleted cells was the inability to divide properly, leading to the formation of multilobulated nuclei through endomitosis, which however still conserved the various global chromatin architectural features mentioned above (Cremer *et al.*, 2020). This result might reconcile both the cohesive and the loop forming roles of cohesin. The telophase was in fact identified as a critical transition state when the mitotic condensin-mediated loops are lost and leave the stage to the interphase cohesin-mediated chromatin folding that emerges together with TADs positioning already at cytokinesis (Abramo *et al.*, 2019).

The present work additionally addressed the question of a possible role of the SA1 subunit in the response to DNA damage (Figure 4.2.4.). SA1 is one of the alternative cohesin subunits from the Hawk protein family (Wells *et al.*, 2017). The authors of the SA1 KO iMEF cell line used in this study showed that the homozygous knockout of SA1 results in embryonic lethality, while a heterozygous ablation leads to early development of tumors in adult mice (Remeseiro *et al.*, 2012a). They showed that the decreased proliferation and aneuploidy of SA1 KO mouse embryonic fibroblasts is due to the SA1-specific role in telomeres cohesion and replication (Cuadrado *et al.*, 2012; Remeseiro *et al.*, 2012a). The alternative subunit SA2 was shown to be instead specific for centromeric cohesion (Canudas and Smith, 2009; Remeseiro *et al.*, 2012a). SA1-containing cohesin complexes were shown to accumulate at promoters and at CTCF-bound sites, while SA1 knock out led to transcriptional dysregulation of

clusters of genes (Remeseiro *et al.*, 2012b). Subsequent studies showed that both SA1 and SA2 can colocalize with CTCF sites, while only SA2-containing cohesin is found at non-CTCF enhancer-promoter contacts (Kojic *et al.*, 2018). While SA1 was suggested to robustly organize TADs together with CTCF, SA2 was linked to tissue-specific transcriptional regulation (Cuadrado and Losada, 2020; De Koninck *et al.*, 2020; Kojic *et al.*, 2018).

In this work, upon validation of the SA1 KO in iMEF cells (Figure 4.2.3.; Supplementary Table ST1 and ST4), a decrease in γ H2AX nuclear mean intensities was observed after irradiation with different X-ray doses in the absence of SA1 (Figure 4.2.4. A – B; Supplementary Figure SF11; Supplementary Table ST4). Repair foci characterization by analysis of confocal microscopy images further proved that γ H2AX foci were reduced in number in the nuclei of 2 Gy-irradiated SA1 KO cells (Figure 4.2.4. C – D; Supplementary Table ST4). Moreover, the volume and the focal intensity of γ H2AX foci were also significantly decreased in SA1 KO cells (Figure 4.2.4. E – F; Supplementary Table ST4). Overall, the Hawk subunit proved to be involved in the signaling of DNA damage at different irradiation doses. In particular, the results from confocal microscopy suggest that the impairment lies in a deficiency of proper structuring of the γ H2AX repair domains. An interesting outlook would be to define different contributions of the cohesin complex to the repair of euchromatin versus heterochromatin. The Scc1 subunit was proven to constrain the movements of Rad52 repair foci upon damage in yeast (Dion *et al.*, 2013). The degree of chromatin mobility at sites of DSBs in the presence or absence of the different cohesin subunits in mammalian cells could be an additional outlook. Future perspective should also focus on clarifying the repair function of the alternative subunit SA2. Previous studies reported that the SA2-containing cohesin would be the main complex to be corecruited with NIPBL at sites of DNA lesions during S/G2 phases, preventing transcription from DSBs (Kong *et al.*, 2014; Meisenberg *et al.*, 2019). However, the results presented here clearly indicate that SA1 contributes to efficient signaling of DNA damage, hence the respective roles of the two alternative subunits require deeper investigation. Moreover, further characterization would require the concomitant knock down of CTCF, in order to precisely assess the interplay of the two architectural proteins in the definition of the chromatin domains that underlie the response to DNA damage.

Beyond the importance of the chromatin context (Scully *et al.*, 2019), the hierarchical organization into domains indeed poses a space constraint that is likely regulating the repair of DNA damage through homologous recombination (HR), as this requires the proximity of a template (Bordelet and Dubrana, 2019). The cohesive role of the cohesin complex is thought to facilitate the homology search for the repair of DSBs and hence to promote HR between sister chromatids (reviewed in: Litwin *et al.*, 2018; Phipps and Dubrana, 2022). Simultaneously, cohesin would safeguard the genome from

instability by preventing ectopic repair events. However, other findings suggested an involvement of cohesin also in the non-homologous end joining (NHEJ) pathway, although with unknown mechanisms (Gelot *et al.*, 2016; Schär *et al.*, 2004).

Early on, DNA damage was shown in human cells to stimulate the binding of cohesin SMC1 and SA1 subunits to chromatin, an event which required cohesin to interact with the MRX repair complex component MRE11 during S/G2 phase (Kim *et al.*, 2002a). Moreover, SMC1 was shown to be phosphorylated by ATM upon ionizing irradiation (Kim *et al.*, 2002b). The cohesin Smc1 and Scc1 subunits were found by ChIP to be recruited at DSB sites in budding yeast, with the formation of a 100 kb cohesin domain around a single DSB for post-replicative repair (Unal *et al.*, 2004). In particular, H2AX phosphorylation by Mec1 and Tel1 kinases (corresponding to ATR and ATM in mammals) enabled a large domain to become permissive of cohesin binding, which was then promoted by Scc2 (NIPBL) and the MRX repair complex component Mre11 (Unal *et al.*, 2004). NIPBL requirement for the accumulation of cohesin at DSBs (Ström *et al.*, 2004; Unal *et al.*, 2004) might suggest both *de novo* loading and enrichment through NIPBL-mediated loop extrusion (Arnould *et al.*, 2021; Davidson *et al.*, 2019). Eco1 was also shown to be triggered by DSBs (Unal *et al.*, 2007). Subsequently, more protein regulators and cohesin post-translational modifications were shown to participate in the DNA damage response (reviewed in: Litwin *et al.*, 2018; Phipps and Dubrana, 2022). For example, SUMOylation (small ubiquitin-like modifier; reviewed in: Ulrich, 2012) of cohesin by the SMC5/6 complex was proven necessary for cohesion upon DNA damage (Andrews *et al.*, 2005; De Piccoli *et al.*, 2006; McAleenan *et al.*, 2012). The SMC5/6 complex might sense DNA damage through recognition of resected DSB ends by its ssDNA-binding motifs (Alt *et al.*, 2017) or it might accumulate at DSB sites through interaction with the γ H2AX-binding protein Rtt107 (Leung *et al.*, 2016). The work presented here is in line with recent findings showing that the γ H2AX repair domains largely reflect and depend on the chromatin interactome of the DSB site (Collins *et al.*, 2020). Inducing a DSB at a CTCF-bordered TAD anchor would lead to leaking of the γ H2AX deposition to the neighboring TADs, confirming the role of chromatin architectural proteins in shaping DNA repair domains (Collins *et al.*, 2020). Another work based on Hi-C and ChIP-seq highlighted the enrichment of “stripes” in the maps of contact frequencies on both sides of each DSB (Arnould *et al.*, 2021), stripes which were previously correlated with cohesin stopping at CTCF-bound sites and accumulating upon loop extrusion (Fudenberg *et al.*, 2016; Mirny *et al.*, 2019; Vian *et al.*, 2018). Depletion of SCC1 abolished the stripes pattern and also decreased γ H2AX spreading (Arnould *et al.*, 2021), in line with the results achieved here by microscopy analysis for the SA1 subunit (Figure 4.2.4.). It was proposed that cohesin would extrude chromatin loops away from both sides of the DSB site and that the histone

variant H2AX would get phosphorylated along with this one-sided extrusion (Arnaud *et al.*, 2021). Cohesin mediated loop extrusion of γ H2AX repair units would also be consistent with previous findings from our laboratory (Natale *et al.*, 2017). Through high-resolution 3D-SIM microscopy characterization, the size of γ H2AX nano-foci was in fact assessed to agree with reported sizes of chromatin loops (median DNA content of a γ H2AX nano-focus: 75 kb, see Natale *et al.*, 2017; average size of a chromatin loop: 90 kb, see Buongiorno-Nardelli *et al.*, 1982). Additionally, the impaired signaling of DNA damage (Natale *et al.*, 2017) and the decreased survival (Mamberti *et al.*, 2022) after ionizing radiation in CTCF-depleted cells are compatible with a model in which cohesin and CTCF cooperate to define chromatin functional domains for the signaling of DNA damage and its subsequent repair.

Emerging evidences found the cause of several types of cancer in the mutations of different cohesin subunits (Guo *et al.*, 2013; Lawrence *et al.*, 2014; Thol *et al.*, 2014; Tothova *et al.*, 2021). Moreover, cells derived from patients with mutations in *SMC1*, *SMC3* or *NIPBL* were proven to be more sensitive to genotoxic agents (Mannini *et al.*, 2012; Revenkova *et al.*, 2009; Vrouwe *et al.*, 2007). However, it has not yet been fully clarified whether this correlation is due to their role in cohesion and hence driven by chromosome segregation defects, or rather connected to their role in loop formation and related potential of transcriptional regulation (reviewed in Litwin *et al.*, 2018; Losada, 2014).

Hi-C data indicates that in the absence of cohesin both loop domains and topologically associated domains are lost, however the higher order A/B compartments are maintained in both pre- and post-mitotic RAD21-depleted cells (Cremer *et al.*, 2020; Rao *et al.*, 2017). Another study mapping genomic contacts in single cells indicated that in the absence of cohesin the borders of TADs are shifted in nearby positions, rather than being completely lost as indicated from population studies (Bintu *et al.*, 2018). Not only CTCF but also housekeeping genes, transfer RNAs and short interspersed element (SINE) retrotransposons are enriched at TADs boundaries (Dixon *et al.*, 2012). These findings together could suggest that TADs are rather “flexible” domains, whose emergence might be the outcome of concurrent factors and cohesin would act as the cherry on top of a cake, stabilizing the borders of such domains at their most favorable position. A/B compartments are mainly defined as active or inactive chromatin by their epigenetic composition (Lieberman-Aiden *et al.*, 2009). The fact that they and the histone marks thereof are unaffected by cohesin depletion (Cremer *et al.*, 2020; Rao *et al.*, 2017) hints to the presence of different mechanisms of compartmentalization, possibly co-driven by phase separation. Indeed different studies addressed the role of phase-separation into genome folding and the modeling of its coexistence with loop-extrusion could well explain different maps of contact frequencies obtained experimentally (Armaos *et al.*, 2021; Birnie and Dekker, 2021;

Conte *et al.*, 2022; Falk *et al.*, 2019; Nuebler *et al.*, 2018; Ryu *et al.*, 2021). In conclusion, cohesin has a differential impact on chromatin structure at the higher and lower orders of organization. While the cohesin complex is essential in determining the structure and the size of DNA loops and local functional units such as the foci of DNA replication and DNA repair, the global genome architecture relies on the concomitant action of multiple different players.

4.4. Material and Methods

4.4.1. Cell culture

HCT-116 wild type and HCT116-RAD21-mAID-mClover cells (referred to as HCT116-RAD21-mAC cells in the main text; Natsume *et al.*, 2016; Supplementary Table ST1) were grown at 37 °C in a humidified atmosphere with 5% CO₂ and cultured in DMEM high glucose (Cat. No.: D6429) supplemented with 50 µg/ml gentamicin (Cat. No.: G1397), 2 mM L-glutamine (Cat. No.: G7513) and 10% FCS (Cat. No.: F7524). SA1 WT and SA1 KO iMEF cells (Supplementary Table ST1; provided by Dr. Ana Losada, Centro Nacional de Investigaciones Oncológicas (CNIO), Madrid, Spain; published in: Remeseiro *et al.*, 2012a) were grown on microscopy slide coverslips and cultured in the same conditions, except 20% FCS (Cat. No.: F7524), before fixation with 3.7% formaldehyde/1× PBS (Cat. No.: F8775; all catalog numbers above refer to Sigma-Aldrich Chemie GmbH, Steinheim, Germany).

4.4.2. RAD21 depletion in HCT116-RAD21-mAC cells

Both HCT-116 RAD21-mAC and HCT-116 wild type cells were seeded on 15 mm ø coverslips and cultured as described above. Once the cells attached, the medium was supplemented with 500 µM auxin (IAA; #15148-2G, Sigma-Aldrich Chemie GmbH, Steinheim, Germany; 500 mM stock solutions in ddH₂O) to induce RAD21 degradation (Figure 4.2.1.). After 6 h, cells were fixed for 15' in 3.7% formaldehyde/1× PBS at room temperature.

4.4.3. DNA halo preparation

HCT116-RAD21-mAC cells were incubated for 6 h in 500 µM auxin for cohesin depletion. DNA halo preparation was largely performed according to (Guillou *et al.*, 2010), see Figure 4.2.2. A for an experimental scheme. After washing the cells in 1× PBS they were incubated for 10' in a buffer at 4°C containing 10 mM Tris pH 8, 3 mM MgCl₂, 0.1 M NaCl, 0.3 M sucrose, protease inhibitors (freshly added to the buffer prior to use) 1 µM pepstatin A, 10 µM E64, 1 mM AEBSF and 0.5 % Nonidet P40. All the following procedures were performed at room temperature. Subsequently DNA was stained for 4' with 2 µg/ml DAPI. After 1' in a second extraction buffer (25 mM Tris pH 8, 0.5 M NaCl, 0.2 mM MgCl₂; protease inhibitors as in nuclei buffer and 1 mM PMSF were added fresh prior to use), cells

were incubated 4' in halo buffer (10 mM Tris pH 8, 2 M NaCl, 10 mM EDTA; protease inhibitors as in nuclei buffer and 1 mM DTT were added fresh prior to use). Eventually cells were washed 1' each in two washing buffers (25 mM Tris pH 8, 0.2 mM MgCl₂; the first buffer with and the second without 0.2 M NaCl). After 10' fixation in 4 % formaldehyde/1× PBS, cells were washed twice in 1× PBS, mounted on slides with Vectashield® antifade medium (Cat. No.: NC9265087, Thermo Fisher Scientific, Walham, United States) and sealed with nail polish.

4.4.4. X-rays irradiation of SA1 WT and SA1 KO iMEF cells.

SA1 WT and KO iMEF cells grown on microscopy slide coverslips were irradiated with 0, 2, 5 or 10 Gy X-ray (1 Gy/58 s, 250 kV, 10 mA; Isovolt Titan, GE Sensing & Inspection Technologies, Ahrensburg, Germany). After 30' at 37 °C in a humidified atmosphere with 5% CO₂, cells were fixed with 3.7% formaldehyde/1× PBS (experimental scheme in Figure 4.2.4. A).

4.4.5. RAD21 detection, SA1 and γ H2AX immunostaining

All previously fixed cells were washed with 1× PBS, permeabilized 15' with 0.7% Triton™ X-100 (Cat. No.: T8787, Sigma-Aldrich Chemie GmbH, Steinheim, Germany) and washed again prior to the subsequent steps. Both HCT116-RAD21-mAC and HCT116 wild type cells (Figure 4.2.1.; Supplementary Figures SF8 and SF9) were counterstained with 1 μ g/ml DAPI for 10', dipped in ddH₂O, mounted with Vectashield® antifade medium (Cat. No.: NC9265087, Thermo Fisher Scientific, Walham, United States) and sealed on microscopy coverslips with nail polish. SA1 WT and KO iMEF cells (Figures 4.2.3., 4.2.4. and Supplementary Figure SF11) were blocked for 30' in 1% BSA (Cat. No.: A4503, Sigma-Aldrich Chemie GmbH, Steinheim, Germany). For the immunostaining of SA1 (Figure 4.2.3.), cells were incubated overnight at 4°C with the primary rabbit anti-SA1 antibody (published in (Remeseiro *et al.*, 2012a); see Supplementary Table ST2 for information on all antibodies). After washing 2× with 1× PBS for 5' and 3× 10' with 0.02% Tween® 20, cells were incubated with the secondary goat anti-rabbit IgG (H + L) AF488 antibody for 1 h at room temperature. Washing followed as described above. DNA was counterstained and cells were mounted as described above. For the immunostaining of γ H2AX (Figure 4.2.4. and Supplementary Figure SF11), cells were incubated overnight at 4°C with the primary mouse anti-phospho-histone H2A.X (Ser139) antibody. Subsequently, cells were incubated with the secondary donkey anti-mouse IgG (H + L) AF488 antibody for 1 h at room temperature. All dilutions mentioned above were done in 1× PBS, except antibody dilutions in 1% BSA/1× PBS. Washing was performed after each antibody incubation, DNA was counterstained and cells mounted on microscopy coverslips as described above.

4.4.6. Microscopy imaging and analysis

For the quantification of RAD21 in HCT-116 RAD21-mAC cells (Figure 4.2.1. D; Supplementary Figure SF9), for the validation of SA1 KO in iMEF cells shown in Figure 4.2.3. C and for the quantification of γ H2AX shown in Figure 4.2.4. B, the samples were imaged at the high-content wide-field microscopy system Operetta® (40×/0.95 NA air objective; Jenoptik firecamj203 camera) and the images were analyzed on batch through a pipeline created with the Harmony™ software – Version 3.5.1 – © 09-2013 (both PerkinElmer, see Supplementary Table ST3), mainly as described in the Supplementary Figure SF8. In particular, nuclei were identified based on the DNA – DAPI signal. The nuclei found on the border of each field were removed and the remaining nuclei were selected based on morphology parameters, such as size and roundness. The RAD21 – mClover (Figure 4.2.1. D; Supplementary Figure SF9), SA1 – AF488 (Figure 4.2.3. C) or γ H2AX – AF488 (Figure 4.2.4. B) intensities were then measured within the nuclear mask of the selected nuclei. For Figure 4.2.1. D, the background level of 10 a.u. measured in the mClover channel for the untagged wild type HCT-116 (not engineered with any fluorescent tag; 10.23 and 10.56 a.u. in the untreated and auxin-treated WT cells, respectively; see Supplementary Figure SF9) was subtracted from all values measured of the untreated and auxin-treated HCT116-RAD21-mAC cells. The percentages of cells with different amounts of residual RAD21 (shown along the boxplots in Figure 4.2.1. D) were calculated by subdividing the whole population of each sample into different ranges of intensities, exporting the number of cells included within each range and calculating the corresponding fraction in relation to the total number of cells imaged for that sample. Exemplary high-content images of WT HCT-116 and HCT116-RAD21-mAC cells are shown in Supplementary Figure SF8 B.

HCT-116 RAD21-mAC cells were additionally imaged at the wide-field microscope Zeiss Axiovert 200 (63×/1.4 NA Plan-Apochromat Oil Ph3 objective; Supplementary Table ST3; Axiovision software (version 4.8.2.0 SP3); AxioCam mRM camera) to produce the montages shown in Figure 4.2.1. D (left side) with the Fiji software (Fiji Is Just ImageJ, Version 1.53c; Schindelin *et al.*, 2012).

For the measurements of chromatin loop sizes in HCT116-RAD21-mAC cells (Figure 4.2.2.; Supplementary Figure SF10), the nuclear scaffolds and the faded DNA halos were imaged at a widefield microscope (Zeiss AxioPlan 2, Supplementary Table ST3; 100×/1.30 NA Plan-Neofluar Oil Ph3 objective; Axiovision software (version 4.8.2.0 SP3); AxioCam mRM camera). Exemplary images of DNA halos are shown in Figure 4.2.2. B-C. Both the total area (A_t) and the scaffold area (A_s) of each cell were manually segmented using the software Fiji (Version 1.53c; Schindelin *et al.*, 2012) and the DNA halo area (A_h) calculated as a subtraction of the two ($A_h = A_t - A_s$). The DNA halo radius was

subsequently derived with the formula $R = \sqrt{(Ah/\pi)}$. Four biological replicates were prepared and measured (Figure 4.2.2. D-E; Supplementary Table ST4; Supplementary Figure SF10).

For the Figures 4.2.3. D, 4.2.4. C – F and Supplementary Figure SF11, the SA1 WT and SA1 KO iMEF samples were imaged at the confocal point scanner microscope Leica TCS SPE-II (mounted on a Leica DMi8 stand; software Leica Application Suite X (LAS X), © 2022 Leica Microsystems, Wetzlar, Germany; Supplementary Table ST3) with a 63× oil objective (63×/1.30 ACS APO Oil CS 0.17/E 0.16). The confocal microscopy images were processed with the Fiji software (Version 1.53c; Schindelin *et al.*, 2012) to produce all shown image montages, and analyzed with the Volocity software (Version 6.3 – © 1998 – 2022 PerkinElmer Inc., Waltham, Massachusetts, United States) to extract the parameters plotted in Figures 4.2.4. D – F. With the Volocity software, the DAPI – DNA signal was used to create nuclear masks (pipeline: find objects in DAPI channel, automatic threshold, dilate and erode, fill holes). Within these nuclear masks, the AF488 – γ H2AX intensities were used to segment the repair foci (pipeline: find objects in AF488 channel, constant threshold using standard deviation, separate touching objects). The number of repair foci, the focal volume and the focal AF488 – γ H2AX sum intensities were then measured and exported as text tables to produce the plot in Figures 4.2.4. D – F. For all experiments, the results tables were analyzed in RStudio (Version 0.99.902 – © 2009-2016 RStudio Inc., Boston, United States) to produce the plots shown. See Supplementary Figure SF2 for boxplot interpretation and Supplementary Table ST4 for all the statistics.

5. General discussion

It has not escaped our notice that replicons have an average size double than that of repair nano-foci, leading us to speculate that a replicon corresponds to two adjacent loops while the DNA damage signaling relies on one single loop (Chagin *et al.*, 2016; Natale *et al.*, 2017). This would nicely correlate with the fact that in most species, the replicon has twice the size of a loop, as reported by Buongiorno-Nardelli and colleagues (Buongiorno-Nardelli *et al.*, 1982). Additionally, one could further hypothesize that each single loop in the double-loop replicon corresponds to a single fork being part of the bidirectional process of DNA replication.

Moreover, in both investigations by our laboratory it was shown that replication and repair foci as seen at conventional microscopy actually consist of clusters of 4-5 nano-foci when observed with super resolution microscopy, suggesting that the two consisted of multiple loops nested together into a domain (Chagin *et al.*, 2016; Natale *et al.*, 2017). Remarkably, the individual replication and damage repair nano-foci are extraordinarily similar at the superresolution light microscopy level and it is, in fact, very difficult to distinguish them when seen side-by-side, as depicted in Figure 5.1.

Buongiorno-Nardelli and colleagues (Buongiorno-Nardelli *et al.*, 1982) predicted that replication would faithfully reproduce the chromosome structure at each cell cycle. This can easily be seen by labeling the cells with nucleotides and observing them with live cell microscopy: the replication pattern corresponding to the S-phase stage in which the cells were labeled is stably visible also in subsequent cell cycles, confirming that the structure determining replication units (a.k.a. replicons) is maintained over different generations, as already shown in 1994 by Sparvoli and colleagues in pea root cells using BrdU pulse labeling (Sparvoli *et al.*, 1994). Jackson and Pombo also highlighted how individual replicon clusters could be stably detected in HeLa cell nuclei throughout successive cell cycles after BrdU pulse labeling (Jackson and Pombo, 1998). They made similar observations on stretched DNA fibers, where 95% of replicons labeled in one S-phase could again be detected in the next cycle (Jackson and Pombo, 1998).

In 2004, using directly labeled nascent DNA and time-lapse microscopy analysis over subsequent cell cycles it was shown in our laboratory that the replication units are stable sub-chromosomal foci, which are read in a defined temporal and spatial order during DNA synthesis in successive cell cycles (Sadoni *et al.*, 2004). In particular, not only a given replication pattern was maintained through different cell generations, but it also colocalized with the replication machinery during the next phase of DNA synthesis, as detected by simultaneously imaging the Cy3-labeled nucleotides incorporated into newly synthesized DNA and their colocalization with replication machinery components in subsequent cell cycles (Sadoni *et al.*, 2004).

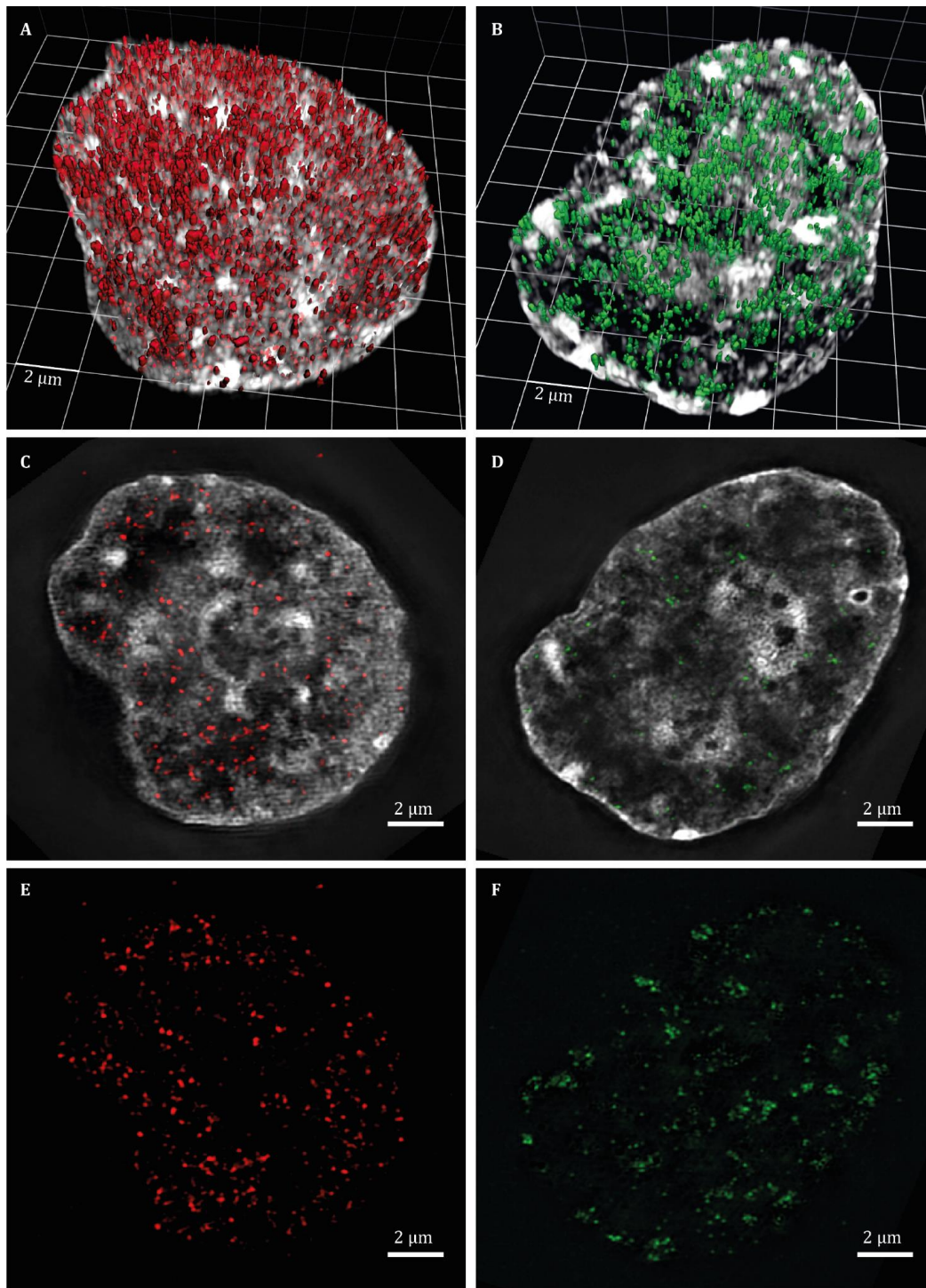


Figure 5.1. DNA replication and repair units in human HeLa Kyoto cells using 3D-structured illumination microscopy. **A** 3D rendering of DNA replication units (red) in a cell labeled during early S-phase by a 10' pulse of the thymidine analogue CldU (10 μ M) followed by detection using immunostaining. **B** 3D rendering of DNA damage response units (green) in a cell irradiated with 5 Gy X-rays, fixed half an hour later and immunostained for phosphorylated H2AX. **C - D** Central sections of the same cells as in (A - B), shown overlaid with the DNA stained with DAPI. **E - F** Central sections of the same cells as in (A - B), shown without DNA overlay.

Moreover, during the same S-phase, the replication machinery dissociated from one Cy3-labeled focus and reassembled at an adjacent new site (Sadoni *et al.*, 2004). This suggested that the replication machinery reads the sub-chromosomal structures that are spatially next to each other. This concept was further developed into a model of domino-like progression of DNA replication, whereby the replication fork induces the firing of nearby origins (Löb *et al.*, 2016; see also: Maya-Mendoza *et al.*, 2010; Sadoni *et al.*, 2004; Sporbert *et al.*, 2002, 2005). Based on this proximity induced firing and taking into account the 3D folding of chromatin, the model was able to reproduce the spatio-temporal distribution of replication units that is commonly observed during S-phase progression (Löb *et al.*, 2016).

Another striking similarity is found between the mean size of 185 kb for the so called “contact domains” measured by Rao and colleagues using Hi-C (Rao *et al.*, 2014) and the mean inter-origin distance, equivalent to one replicon – 189 kb that we measured on stretched DNA fibers after replication labeling (Chagin *et al.*, 2016).

If a replicon, sized as a (double) loop domain (as shown across multiple species and in multiple studies), is made up of two symmetrical forks, each of which has *circa* the same size of a repair nanofocus, we propose that DNA replication and DNA repair, being both global genomic processes, do indeed function by reading a basic chromatin loop unit maintained over cell generations and, hence, genome structure determines its function.

The agreement between the size of a loop, a repair nanofocus and a replication fork is even more striking when we consider that these measurements were achieved with different techniques. Loop sizes were achieved by DNA halo technique (Buongiorno-Nardelli *et al.*, 1982), fork sizes were obtained on stretched DNA fibers (Chagin *et al.*, 2016) and repair units by analysis of focal structures *in situ* (Natale *et al.*, 2017). Hence, no matter which technique is utilized, the replication and the repair functions rely on the same structural unit, which is a DNA loop of *circa* 70 - 90 kb (Table 1.1.). Consequentially, two forks of a bidirectional replicon label a length of DNA that corresponds to a pair of loops, *circa* 160 - 190 kb (Table 1.2.). This is also supported by the observations of Buongiorno-Nardelli and colleagues, which showed that, on average, the replicon size is double the loop size in different species (Buongiorno-Nardelli *et al.*, 1982).

This relationship is further supported by similarities in the kinetics of the two processes. Both replication and repair follow a spatio-temporal order, which is dictated by the fact that euchromatin gets processed earlier than heterochromatin. In both processes, we observe a pan-nuclear pattern of numerous fine foci at earlier stages, whereas focal structures get increasingly clustered at later time points (Chagin *et al.*, 2016; Natale *et al.*, 2017).

We and others have shown that depletion of cohesin increased loop size and replicon size (Cremer *et al.*, 2020; Guillou *et al.*, 2010) and, in addition, we showed that CTCF brings together single repair nano-foci into a cluster and that its absence impairs the spreading of these nano-foci (Natale *et al.*, 2017). As these nano-foci correspond to single loops in size, we hypothesized that CTCF is bringing different loops together in a multi-loop cluster and that this clustering is required for the spreading of the histone modification on the single loops that are brought in proximity. Based on these observations, we can hypothesize that the loops extruded by the cooperation of CTCF and cohesin can have a functional significance in terms of DNA replication and repair. However, future investigations on loop dynamics and the presence and absence of these and other proteins will help us to better elucidate how the structural units of replication and repair are dynamically maintained in living cells.

A reduced nuclear level of CTCF was previously shown to impact the signaling of DNA damage and the subsequent DNA repair (Natale *et al.*, 2017). Here these studies were expanded to two different human tumor cell lines through RNA interference and a mouse embryonic cell line engineered with an auxin inducible degron for the depletion of CTCF. By exploiting these different cellular systems and by applying different degrees of CTCF depletion and radiation damage, it was confirmed that the absence of this architectural protein impairs the cellular survival to ionizing radiation, in a dose dependent way (Figures 3.1.3. and 3.1.6.). Through a collaboration with Dr. M. Scholz (GSI, Darmstadt), we could define a model in which the amount of CTCF is sufficient to predict cellular radioresistance simply by assuming a reverse relationship between the nuclear level of CTCF and the size of chromatin domains (Figures 3.1.4., 3.1.7. and 3.1.8.).

A partial CTCF depletion itself caused a general impairment of cell cycle progression, with an increasing percentage of mouse cells stalling in G1 and a diminished progression through S-phase (Figure 3.2.2.). This is in line with the knowledge that a complete KO of this protein results in early embryonic lethality in mice and that a nearly full depletion also leads to cell death upon a few days of cell culture in mouse embryonic stem cells. CTCF might also play a role in DNA replication, as this study highlighted a partial colocalization of CTCF foci with DNA replication units, during ongoing replication, while the colocalization with the previously replication-labeled DNA vanishes with increasing chase of time (Figure 3.2.1.). This indicates two possible scenarios. In the first one, DNA would reel through the loop border defined by CTCF while getting replicated, hence the incorporated nucleotides would always be found in the same position of CTCF at the time of incorporation. The alternative is that CTCF gets recruited to DNA replication sites or it is even necessary for the replication machinery to load on the DNA that has to be duplicated. From the point of view that the

replication machinery is probably not a fixed so-called “replication factory” through which the DNA is moving, but instead rather soluble and dynamic, the idea that CTCF might serve as a platform or as the director of an orchestra fits better. If the DNA would reel through bound CTCF, there would only be colocalization without changes of intensity, but at confocal resolution, we could appreciate that the intensity of CTCF in the replication foci is higher than elsewhere in the nucleus. This suggests a temporal enrichment of CTCF at the sites where DNA gets duplicated. A much higher accumulation of CTCF at DNA replication sites was observed when FISH was coupled with EdU labeling to detect the replicating Xi and Y sex chromosomes. Given the high compaction of the inactive X and Y chromosomes, one could argue that such enrichment is only due to more CTCF bound to keep the inactive chromatin highly wrapped. This argument fails because CTCF is present at the inactive X and Y chromosomes at the time of their replication, but is simultaneously absent on the not replicating Xa and Y chromosomes (Figure 3.2.3.).

On the other hand, the cohesin complex was also shown to impact chromatin structure, DNA repair (in this study) and DNA replication (see e.g.: Cremer *et al.*, 2020; Guillou *et al.*, 2010; Remeseiro *et al.*, 2012a). Upon degradation of RAD21 in an AID-engineered human colorectal cancer cell line and extraction of chromatin with anionic detergent, the sizes of DNA loops showed a double median value and increased up to ten fold compared to untreated cells with wild type RAD21 levels (Figure 4.2.2.). These DNA halo results suggest that in the absence of cohesin-mediated loop extrusion, the structure of DNA loops gets misregulated in length, abnormally large and irregularly shaped (see Figure 4.2.2. B – C for representative images). This loss of structure might of course lead to the impairment of those genomic functions that rely on a loop-scaffold to work properly.

Our collaborators showed with live-cell microscopy that RAD21-depleted cells went through a mitotic catastrophe ending up in multilobulated nuclei, in which, however, chromosome territories were unaffected (Cremer *et al.*, 2020). Furthermore, they could observe that DNA replication patterns were also maintained, however a slight difference in the volume and in the number of replication foci was observed (Cremer *et al.*, 2020).

In this study, SA1 KO mouse embryonic fibroblast cells exhibited a decreased signaling of DNA damage at half an hour post X-rays irradiation for any tested dose (Figure 4.2.4. B). Nuclear γ H2AX intensities in SA1 KO cells were in fact lower than in wild type cells, as measured with high-content wide-field microscopy. The analysis of confocal microscopy images revealed that not only the γ H2AX focal intensity is diminished but also the number and the volume of repair foci is decreased in knock out cells (Figure 4.2.4. C – F). These results suggest a role for the cohesin subunit SA1 in structuring the chromatin loops for the correct deposition of H2AX phosphorylation. In future studies, the

impairment of γ H2AX spreading in SA1 KO cells could be further investigated in terms of dynamics over time, recruitment of repair factors and survival studies. Furthermore, these DNA repair studies should be applied in parallel to SA2 knock out cells, to assess the precise involvement of each of the two mammalian isoforms and ultimately clarify their respective responsibilities in shaping genomic functions. Given the previous results from our laboratory on the impairment of γ H2AX signaling upon CTCF knock down (Natale *et al.*, 2017) and the results shown in this study on the decreased survival of CTCF-depleted cells, a very important step would be to compare the reported results with research on cells in which a double knock down of both CTCF and cohesin is achieved.

6. Conclusions and outlook

DNA replication and DNA repair were chosen as representative markers of essential genomic functions, in order to investigate the relationship between chromatin structure and genome function. Both of them are global genomic processes that involve the whole genome with a precise spatio-temporal progression, which reflects chromatin organization into eu- and hetero-chromatin. Overall, we can affirm that genomic functions such as DNA replication and the repair of DNA damage are closely related to the chromatin organization within the nucleus of mammalian cells. In particular, both genomic processes appear as nano focal structures and clusters thereof when observed with high resolution microscopy and these resulted to have a DNA content that is in the range of DNA loops (70 – 200 kbp), as measured with different techniques.

The chromatin architectural proteins CTCF and cohesin are the major players of chromatin loop extrusion and work together to define chromatin domain boundaries. Although the mechanistic insights are not yet fully elucidated, the results presented in this work could prove that these loop-extruding proteins do affect both genomic processes of DNA replication and DNA repair (see Figure 6.1. for a schematic summarizing all major results presented here). The lack of CTCF anchoring was proven to lead to an increased clustering of double strand breaks, which dramatically impact cellular survival to damage. CTCF was shown to be also involved in DNA replication, to be especially enriched in the replicating inactive X and Y chromosomes, and to sustain the synchrony of Y chromosome replication. The cohesin subunit RAD21 proved to be required for an ordered structure of chromatin loops. The cohesin subunit SA1 showed to be necessary for the functional spreading of γ H2AX repair foci upon ionizing radiation. Overall, the results of this thesis highlight the impact of chromatin structure over global genomic functions. The depletion of chromatin architectural proteins impaired different features of the DNA replication and repair units. Genomic functions were hence proven to rely on the underlying chromatin structure, with each functional unit being interrelated with the structure provided by CTCF and cohesin.

Future studies will need to clarify the precise mechanisms and dynamics behind this interrelationship. The weight of the contribution of each cohesin subunit and CTCF has to be defined in more detail. The interaction of these two architectural proteins with the major players of DNA replication and DNA repair has to be elucidated. Lastly, all findings should be put in frame with other nuclear processes, such as phase separation and transcription. Ultimately, filling these gaps will help us to achieve a full sight of the nuclear drawing that is hidden within our cells.

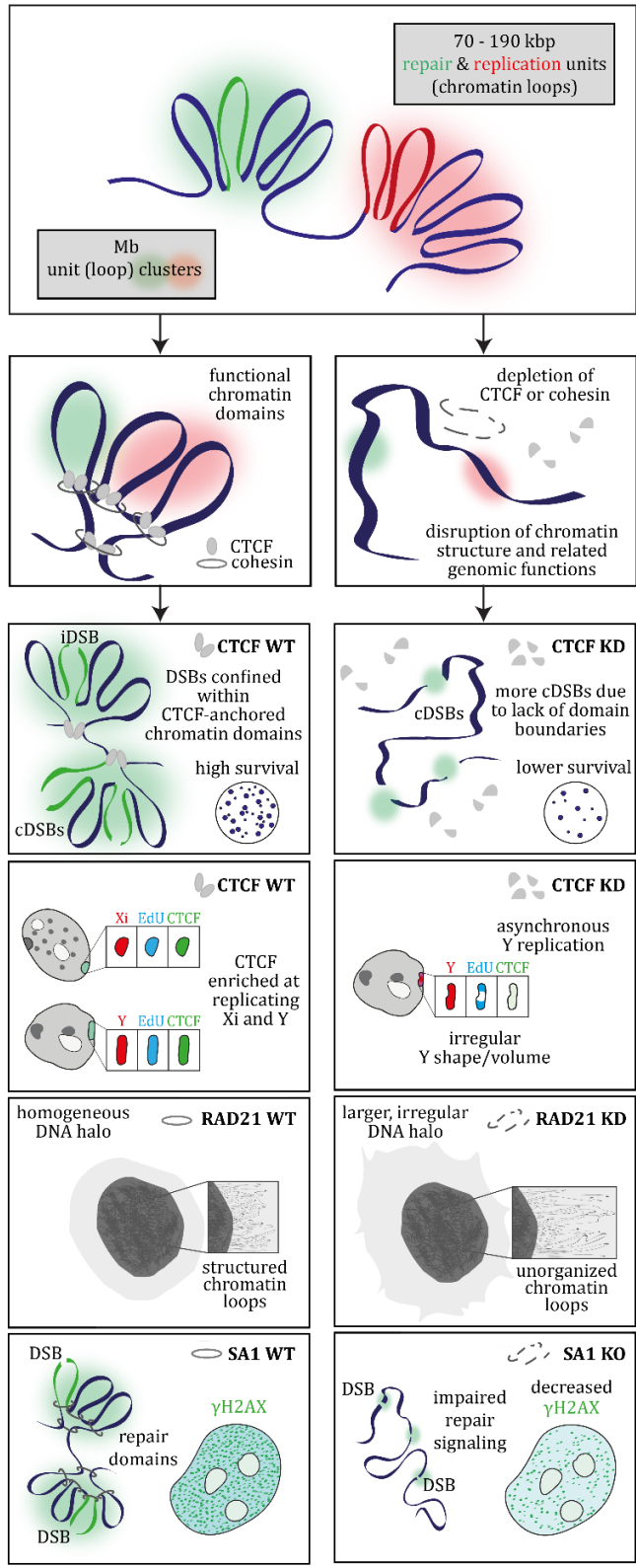


Figure 6.1. CTCF and cohesin orchestrate the spatio-temporal regulation of global genomic functions by structuring chromatin into functional loops and domains.

7. References

- Abramo, K., Valton, A.-L., Venev, S.V., Ozadam, H., Fox, A.N., and Dekker, J. (2019). A chromosome folding intermediate at the condensin-to-cohesin transition during telophase. *Nat. Cell Biol.* *21*, 1393–1402. <https://doi.org/10.1038/s41556-019-0406-2>.
- Acquaviva, L., Boekhout, M., Karasu, M.E., Brick, K., Pratto, F., Li, T., van Overbeek, M., Kauppi, L., Camerini-Otero, R.D., Jasin, M., *et al.* (2020). Ensuring meiotic DNA break formation in the mouse pseudoautosomal region. *Nature* *582*, 426–431. <https://doi.org/10.1038/s41586-020-2327-4>.
- Adolph, K.W., Cheng, S.M., and Laemmli, U.K. (1977a). Role of nonhistone proteins in metaphase chromosome structure. *Cell* *12*, 805–816. [https://doi.org/10.1016/0092-8674\(77\)90279-3](https://doi.org/10.1016/0092-8674(77)90279-3).
- Adolph, K.W., Cheng, S.M., Paulson, J.R., and Laemmli, U.K. (1977b). Isolation of a protein scaffold from mitotic HeLa cell chromosomes. *Proc Natl Acad Sci USA* *74*, 4937–4941. <https://doi.org/10.1073/pnas.74.11.4937>.
- Agarwal, H., Reisser, M., Wortmann, C., and Gebhardt, J.C.M. (2017). Direct Observation of Cell-Cycle-Dependent Interactions between CTCF and Chromatin. *Biophys. J.* *112*, 2051–2055. <https://doi.org/10.1016/j.bpj.2017.04.018>.
- Aladjem, M.I., and Fu, H. (2014). A new light on DNA replication from the inactive X chromosome. *Bioessays* *36*, 591–597. <https://doi.org/10.1002/bies.201400021>.
- Aladjem, M.I., Spike, B.T., Rodewald, L.W., Hope, T.J., Klemm, M., Jaenisch, R., and Wahl, G.M. (1998). ES cells do not activate p53-dependent stress responses and undergo p53-independent apoptosis in response to DNA damage. *Curr. Biol.* *8*, 145–155. [https://doi.org/10.1016/s0960-9822\(98\)70061-2](https://doi.org/10.1016/s0960-9822(98)70061-2).
- Alomer, R.M., da Silva, E.M.L., Chen, J., Piekarczyk, K.M., McDonald, K., Sansam, C.G., Sansam, C.L., and Rankin, S. (2017). Esco1 and Esco2 regulate distinct cohesin functions during cell cycle progression. *Proc Natl Acad Sci USA* *114*, 9906–9911. <https://doi.org/10.1073/pnas.1708291114>.
- Alt, A., Dang, H.Q., Wells, O.S., Polo, L.M., Smith, M.A., McGregor, G.A., Welte, T., Lehmann, A.R., Pearl, L.H., Murray, J.M., *et al.* (2017). Specialized interfaces of Smc5/6 control hinge stability and DNA association. *Nat. Commun.* *8*, 14011. <https://doi.org/10.1038/ncomms14011>.
- Alver, R.C., Chadha, G.S., Gillespie, P.J., and Blow, J.J. (2017). Reversal of DDK-Mediated MCM Phosphorylation by Rif1-PP1 Regulates Replication Initiation and Replisome Stability Independently of ATR/Chk1. *Cell Rep.* *18*, 2508–2520. <https://doi.org/10.1016/j.celrep.2017.02.042>.
- Amon, A. (2001). Together until separin do us part. *Nat. Cell Biol.* *3*, E12–4. <https://doi.org/10.1038/35050642>.
- Andrews, E.A., Palecek, J., Sergeant, J., Taylor, E., Lehmann, A.R., and Watts, F.Z. (2005). Nse2, a component of the Smc5-6 complex, is a SUMO ligase required for the response to DNA damage. *Mol. Cell. Biol.* *25*, 185–196. <https://doi.org/10.1128/MCB.25.1.185-196.2005>.
- Armaos, A., Zacco, E., Sanchez de Groot, N., and Tartaglia, G.G. (2021). RNA-protein interactions: Central players in coordination of regulatory networks. *Bioessays* *43*, e2000118. <https://doi.org/10.1002/bies.202000118>.
- Arnould, C., Rocher, V., Finoux, A.-L., Clouaire, T., Li, K., Zhou, F., Caron, P., Mangeot, P.E., Ricci, E.P., Mourad, R., *et al.* (2021). Loop extrusion as a mechanism for formation of DNA damage repair foci. *Nature* *590*, 660–665. <https://doi.org/10.1038/s41586-021-03193-z>.
- Arumugam, P., Gruber, S., Tanaka, K., Haering, C.H., Mechtler, K., and Nasmyth, K. (2003). ATP hydrolysis is required for cohesin's association with chromosomes. *Curr. Biol.* *13*, 1941–1953. <https://doi.org/10.1016/j.cub.2003.10.036>.
- Arumugam, P., Nishino, T., Haering, C.H., Gruber, S., and Nasmyth, K. (2006). Cohesin's ATPase activity is stimulated by the C-terminal Winged-Helix domain of its kleisin subunit. *Curr. Biol.* *16*, 1998–2008. <https://doi.org/10.1016/j.cub.2006.09.002>.
- van Attikum, H., and Gasser, S.M. (2009). Crosstalk between histone modifications during the DNA damage response. *Trends Cell Biol.* *19*, 207–217. <https://doi.org/10.1016/j.tcb.2009.03.001>.
- Avagliano, L., Parenti, I., Grazioli, P., Di Fede, E., Parodi, C., Mariani, M., Kaiser, F.J., Selicorni, A., Gervasini, C., and Massa, V. (2020). Chromatinopathies: A focus on Cornelia de Lange syndrome. *Clin. Genet.* *97*, 3–11.

<https://doi.org/10.1111/cge.13674>.

Baddeley, D., Chagin, V.O., Schermelleh, L., Martin, S., Pombo, A., Carlton, P.M., Gahl, A., Domaing, P., Birk, U., Leonhardt, H., *et al.* (2010). Measurement of replication structures at the nanometer scale using super-resolution light microscopy. *Nucleic Acids Res.* *38*, e8. <https://doi.org/10.1093/nar/gkp901>.

Bakkenist, C.J., and Kastan, M.B. (2003). DNA damage activates ATM through intermolecular autophosphorylation and dimer dissociation. *Nature* *421*, 499–506. <https://doi.org/10.1038/nature01368>.

Ban ath, J.P., Macphail, S.H., and Olive, P.L. (2004). Radiation sensitivity, H2AX phosphorylation, and kinetics of repair of DNA strand breaks in irradiated cervical cancer cell lines. *Cancer Res.* *64*, 7144–7149. <https://doi.org/10.1158/0008-5472.CAN-04-1433>.

Ban ath, J.P., Ba uelos, C.A., Klovov, D., MacPhail, S.M., Lansdorp, P.M., and Olive, P.L. (2009). Explanation for excessive DNA single-strand breaks and endogenous repair foci in pluripotent mouse embryonic stem cells. *Exp. Cell Res.* *315*, 1505–1520. <https://doi.org/10.1016/j.yexcr.2008.12.007>.

Banigan, E.J., and Mirny, L.A. (2020). The interplay between asymmetric and symmetric DNA loop extrusion. *ELife* *9*. <https://doi.org/10.7554/eLife.63528>.

Barbero, J.L. (2013). Genetic basis of cohesinopathies. *Appl. Clin. Genet.* *6*, 15–23. <https://doi.org/10.2147/TACG.S34457>.

Barbieri, M., Chotalia, M., Fraser, J., Lavitas, L.-M., Dostie, J., Pombo, A., and Nicodemi, M. (2012). Complexity of chromatin folding is captured by the strings and binders switch model. *Proc Natl Acad Sci USA* *109*, 16173–16178. <https://doi.org/10.1073/pnas.1204799109>.

Barford, D. (2020). Structural interconversions of the anaphase-promoting complex/cyclosome (APC/C) regulate cell cycle transitions. *Curr. Opin. Struct. Biol.* *61*, 86–97. <https://doi.org/10.1016/j.sbi.2019.11.010>.

Barr, M.L., and Bertram, E.G. (1949). A morphological distinction between neurones of the male and female, and the behaviour of the nucleolar satellite during accelerated nucleoprotein synthesis. *Nature* *163*, 676. <https://doi.org/10.1038/163676a0>.

Barutcu, A.R., Fritz, A.J., Zaidi, S.K., van Wijnen, A.J., Lian, J.B., Stein, J.L., Nickerson, J.A., Imbalzano, A.N., and Stein, G.S. (2016). C-ing the Genome: A Compendium of Chromosome Conformation Capture Methods to Study Higher-Order Chromatin Organization. *J. Cell. Physiol.* *231*, 31–35. <https://doi.org/10.1002/jcp.25062>.

Bauer, B.W., Davidson, I.F., Canena, D., Wutz, G., Tang, W., Litos, G., Horn, S., Hinterdorfer, P., and Peters, J.-M. (2021a). Cohesin mediates DNA loop extrusion by a “swing and clamp” mechanism. *Cell* *184*, 5448–5464.e22. <https://doi.org/10.1016/j.cell.2021.09.016>.

Bauer, M., Vidal, E., Zorita, E.,  resin, N., Pinter, S.F., Filion, G.J., and Payer, B. (2021b). Chromosome compartments on the inactive X guide TAD formation independently of transcription during X-reactivation. *Nat. Commun.* *12*, 3499. <https://doi.org/10.1038/s41467-021-23610-1>.

Beckou t, F., Hu, B., Roig, M.B., Sutani, T., Komata, M., Uluocak, P., Katis, V.L., Shirahige, K., and Nasmyth, K. (2010). An Smc3 acetylation cycle is essential for establishment of sister chromatid cohesion. *Mol. Cell* *39*, 689–699. <https://doi.org/10.1016/j.molcel.2010.08.008>.

Beckou t, F., Srinivasan, M., Roig, M.B., Chan, K.-L., Scheinost, J.C., Batty, P., Hu, B., Petela, N., Gligoris, T., Smith, A.C., *et al.* (2016). Releasing activity disengages cohesin’s smc3/scc1 interface in a process blocked by acetylation. *Mol. Cell* *61*, 563–574. <https://doi.org/10.1016/j.molcel.2016.01.026>.

Bellott, D.W., Hughes, J.F., Skaletsky, H., Brown, L.G., Pyntikova, T., Cho, T.-J., Koutseva, N., Zaghul, S., Graves, T., Rock, S., *et al.* (2014). Mammalian Y chromosomes retain widely expressed dosage-sensitive regulators. *Nature* *508*, 494–499. <https://doi.org/10.1038/nature13206>.

Bell, O., Schwaiger, M., Oakeley, E.J., Lienert, F., Beisel, C., Stadler, M.B., and Sch ubeler, D. (2010). Accessibility of the *Drosophila* genome discriminates PcG repression, H4K16 acetylation and replication timing. *Nat. Struct. Mol. Biol.* *17*, 894–900. <https://doi.org/10.1038/nsmb.1825>.

van Bommel, J.G., Galupa, R., Gard, C., Servant, N., Picard, C., Davies, J., Szempruch, A.J., Zhan, Y.,  ylicz, J.J., Nora, E.P., *et al.* (2019). The bipartite TAD organization of the X-inactivation center ensures opposing developmental

- regulation of Tsix and Xist. *Nat. Genet.* *51*, 1024–1034. <https://doi.org/10.1038/s41588-019-0412-0>.
- Benyajati, C., and Worcel, A. (1976). Isolation, characterization, and structure of the folded interphase genome of *Drosophila melanogaster*. *Cell* *9*, 393–407. [https://doi.org/10.1016/0092-8674\(76\)90084-2](https://doi.org/10.1016/0092-8674(76)90084-2).
- van Berkum, N.L., Lieberman-Aiden, E., Williams, L., Imakaev, M., Gnirke, A., Mirny, L.A., Dekker, J., and Lander, E.S. (2010). Hi-C: a method to study the three-dimensional architecture of genomes. *J. Vis. Exp.* <https://doi.org/10.3791/1869>.
- Bernard, P., Maure, J.F., and Javerzat, J.P. (2001). Fission yeast Bub1 is essential in setting up the meiotic pattern of chromosome segregation. *Nat. Cell Biol.* *3*, 522–526. <https://doi.org/10.1038/35074598>.
- Bhogal, N., Jalali, F., and Bristow, R.G. (2009). Microscopic imaging of DNA repair foci in irradiated normal tissues. *Int. J. Radiat. Biol.* *85*, 732–746. <https://doi.org/10.1080/09553000902785791>.
- Bintu, B., Mateo, L.J., Su, J.-H., Sinnott-Armstrong, N.A., Parker, M., Kinrot, S., Yamaya, K., Boettiger, A.N., and Zhuang, X. (2018). Super-resolution chromatin tracing reveals domains and cooperative interactions in single cells. *Science* *362*. <https://doi.org/10.1126/science.aau1783>.
- Birkenbihl, R.P., and Subramani, S. (1992). Cloning and characterization of rad21 an essential gene of *Schizosaccharomyces pombe* involved in DNA double-strand-break repair. *Nucleic Acids Res.* *20*, 6605–6611. <https://doi.org/10.1093/nar/20.24.6605>.
- Birnie, A., and Dekker, C. (2021). Genome-in-a-Box: Building a Chromosome from the Bottom Up. *ACS Nano* *15*, 111–124. <https://doi.org/10.1021/acsnano.0c07397>.
- Bischoff, J.R., Anderson, L., Zhu, Y., Mossie, K., Ng, L., Souza, B., Schryver, B., Flanagan, P., Clairvoyant, F., Ginther, C., *et al.* (1998). A homologue of *Drosophila aurora* kinase is oncogenic and amplified in human colorectal cancers. *EMBO J.* *17*, 3052–3065. <https://doi.org/10.1093/emboj/17.11.3052>.
- Blackford, A.N., and Jackson, S.P. (2017). ATM, ATR, and DNA-PK: The Trinity at the Heart of the DNA Damage Response. *Mol. Cell* *66*, 801–817. <https://doi.org/10.1016/j.molcel.2017.05.015>.
- Bohn, M., Heermann, D.W., and van Driel, R. (2007). Random loop model for long polymers. *Phys. Rev. E Stat. Nonlin. Soft Matter Phys.* *76*, 051805. <https://doi.org/10.1103/PhysRevE.76.051805>.
- Bolzer, A., Kreth, G., Solovei, I., Koehler, D., Saracoglu, K., Fauth, C., Müller, S., Eils, R., Cremer, C., Speicher, M.R., *et al.* (2005). Three-dimensional maps of all chromosomes in human male fibroblast nuclei and prometaphase rosettes. *PLoS Biol.* *3*, e157. <https://doi.org/10.1371/journal.pbio.0030157>.
- Bordelet, H., and Dubrana, K. (2019). Keep moving and stay in a good shape to find your homologous recombination partner. *Curr. Genet.* *65*, 29–39. <https://doi.org/10.1007/s00294-018-0873-1>.
- Borges, V., Lehane, C., Lopez-Serra, L., Flynn, H., Skehel, M., Rolef Ben-Shahar, T., and Uhlmann, F. (2010). Hos1 deacetylates Smc3 to close the cohesin acetylation cycle. *Mol. Cell* *39*, 677–688. <https://doi.org/10.1016/j.molcel.2010.08.009>.
- Borrego-Soto, G., Ortiz-López, R., and Rojas-Martínez, A. (2015). Ionizing radiation-induced DNA injury and damage detection in patients with breast cancer. *Genet. Mol. Biol.* *38*, 420–432. <https://doi.org/10.1590/S1415-475738420150019>.
- Borsani, G., Tonlorenzi, R., Simmler, M.C., Dandolo, L., Arnaud, D., Capra, V., Grompe, M., Pizzuti, A., Muzny, D., Lawrence, C., *et al.* (1991). Characterization of a murine gene expressed from the inactive X chromosome. *Nature* *351*, 325–329. <https://doi.org/10.1038/351325a0>.
- Boumil, R.M., Ogawa, Y., Sun, B.K., Huynh, K.D., and Lee, J.T. (2006). Differential methylation of Xite and CTCF sites in Tsix mirrors the pattern of X-inactivation choice in mice. *Mol. Cell. Biol.* *26*, 2109–2117. <https://doi.org/10.1128/MCB.26.6.2109-2117.2006>.
- Brackley, C.A., and Marenduzzo, D. (2020). Bridging-induced microphase separation: photobleaching experiments, chromatin domains and the need for active reactions. *Brief. Funct. Genomics* *19*, 111–118. <https://doi.org/10.1093/bfgp/elz032>.
- Brattain, M.G., Fine, W.D., Khaled, F.M., Thompson, J., and Brattain, D.E. (1981). Heterogeneity of malignant cells

from a human colonic carcinoma. *Cancer Res.* *41*, 1751–1756.

Brero, A., Easwaran, H.P., Nowak, D., Grunewald, I., Cremer, T., Leonhardt, H., and Cardoso, M.C. (2005). Methyl CpG-binding proteins induce large-scale chromatin reorganization during terminal differentiation. *J. Cell Biol.* *169*, 733–743. <https://doi.org/10.1083/jcb.200502062>.

Brockdorff, N., Ashworth, A., Kay, G.F., Cooper, P., Smith, S., McCabe, V.M., Norris, D.P., Penny, G.D., Patel, D., and Rastan, S. (1991). Conservation of position and exclusive expression of mouse Xist from the inactive X chromosome. *Nature* *351*, 329–331. <https://doi.org/10.1038/351329a0>.

Brown, C.J., Ballabio, A., Rupert, J.L., Lafreniere, R.G., Grompe, M., Tonlorenzi, R., and Willard, H.F. (1991). A gene from the region of the human X inactivation centre is expressed exclusively from the inactive X chromosome. *Nature* *349*, 38–44. <https://doi.org/10.1038/349038a0>.

Buckle, A., Brackley, C.A., Boyle, S., Marenduzzo, D., and Gilbert, N. (2018). Polymer simulations of heteromorphic chromatin predict the 3D folding of complex genomic loci. *Mol. Cell* *72*, 786–797.e11. <https://doi.org/10.1016/j.molcel.2018.09.016>.

Buongiorno-Nardelli, M., Micheli, G., Carri, M.T., and Marilley, M. (1982). A relationship between replicon size and supercoiled loop domains in the eukaryotic genome. *Nature* *298*, 100–102. <https://doi.org/10.1038/298100a0>.

Burgoyne, P.S. (1982). Genetic homology and crossing over in the X and Y chromosomes of Mammals. *Hum. Genet.* *61*, 85–90. <https://doi.org/10.1007/BF00274192>.

Bürmann, F., Lee, B.-G., Than, T., Sinn, L., O'Reilly, F.J., Yatskevich, S., Rappsilber, J., Hu, B., Nasmyth, K., and Löwe, J. (2019). A folded conformation of MukBEF and cohesin. *Nat. Struct. Mol. Biol.* *26*, 227–236. <https://doi.org/10.1038/s41594-019-0196-z>.

Cairns, J. (1963). The bacterial chromosome and its manner of replication as seen by autoradiography. *J. Mol. Biol.* *6*, 208–213. [https://doi.org/10.1016/S0022-2836\(63\)80070-4](https://doi.org/10.1016/S0022-2836(63)80070-4).

Cairns, J. (1966). Autoradiography of HeLa cell DNA. *J. Mol. Biol.* *15*, 372–373. [https://doi.org/10.1016/S0022-2836\(66\)80233-4](https://doi.org/10.1016/S0022-2836(66)80233-4).

Camargo, M., and Cervenka, J. (1982). Patterns of DNA replication of human chromosomes. II. Replication map and replication model. *Am. J. Hum. Genet.* *34*, 757–780.

Canudas, S., and Smith, S. (2009). Differential regulation of telomere and centromere cohesion by the Scc3 homologues SA1 and SA2, respectively, in human cells. *J. Cell Biol.* *187*, 165–173. <https://doi.org/10.1083/jcb.200903096>.

Carico, Z.M., Stefan, H.C., Justice, M., Yimit, A., and Downen, J.M. (2021). A cohesin cancer mutation reveals a role for the hinge domain in genome organization and gene expression. *PLoS Genet.* *17*, e1009435. <https://doi.org/10.1371/journal.pgen.1009435>.

Carramolino, L., Lee, B.C., Zaballos, A., Peled, A., Barthelemy, I., Shav-Tal, Y., Prieto, I., Carmi, P., Gothelf, Y., González de Buitrago, G., *et al.* (1997). SA-1, a nuclear protein encoded by one member of a novel gene family: molecular cloning and detection in hemopoietic organs. *Gene* *195*, 151–159. [https://doi.org/10.1016/S0378-1119\(97\)00121-2](https://doi.org/10.1016/S0378-1119(97)00121-2).

Casas-Delucchi, C.S., Brero, A., Rahn, H.-P., Solovei, I., Wutz, A., Cremer, T., Leonhardt, H., and Cardoso, M.C. (2011). Histone acetylation controls the inactive X chromosome replication dynamics. *Nat. Commun.* *2*, 222. <https://doi.org/10.1038/ncomms1218>.

Cattoglio, C., Pustova, I., Walther, N., Ho, J.J., Hantsche-Grininger, M., Inouye, C.J., Hossain, M.J., Dailey, G.M., Ellenberg, J., Darzacq, X., *et al.* (2019). Determining cellular CTCF and cohesin abundances to constrain 3D genome models. *ELife* *8*. <https://doi.org/10.7554/eLife.40164>.

Cervantes, R.B., Stringer, J.R., Shao, C., Tischfield, J.A., and Stambrook, P.J. (2002). Embryonic stem cells and somatic cells differ in mutation frequency and type. *Proc Natl Acad Sci USA* *99*, 3586–3590. <https://doi.org/10.1073/pnas.062527199>.

Chadwick, B.P., and Willard, H.F. (2003). Barring gene expression after XIST: maintaining facultative

- heterochromatin on the inactive X. *Semin. Cell Dev. Biol.* *14*, 359–367. <https://doi.org/10.1016/j.semcdb.2003.09.016>.
- Chagin, V.O., Casas-Delucchi, C.S., Reinhart, M., Schermelleh, L., Markaki, Y., Maiser, A., Bolius, J.J., Bensimon, A., Fillies, M., Domaing, P., *et al.* (2016). 4D Visualization of replication foci in mammalian cells corresponding to individual replicons. *Nat. Commun.* *7*, 11231. <https://doi.org/10.1038/ncomms11231>.
- Chan, K.-L., Roig, M.B., Hu, B., Beckouët, F., Metson, J., and Nasmyth, K. (2012). Cohesin's DNA exit gate is distinct from its entrance gate and is regulated by acetylation. *Cell* *150*, 961–974. <https://doi.org/10.1016/j.cell.2012.07.028>.
- Chan, K.-L., Gligoris, T., Upcher, W., Kato, Y., Shirahige, K., Nasmyth, K., and Beckouët, F. (2013). Pds5 promotes and protects cohesin acetylation. *Proc Natl Acad Sci USA* *110*, 13020–13025. <https://doi.org/10.1073/pnas.1306900110>.
- Chao, W., Huynh, K.D., Spencer, R.J., Davidow, L.S., and Lee, J.T. (2002). CTCF, a candidate trans-acting factor for X-inactivation choice. *Science* *295*, 345–347. <https://doi.org/10.1126/science.1065982>.
- Chapard, C., Jones, R., van Oepen, T., Scheinost, J.C., and Nasmyth, K. (2019). Sister DNA Entrapment between Juxtaposed Smc Heads and Kleisin of the Cohesin Complex. *Mol. Cell* *75*, 224–237.e5. <https://doi.org/10.1016/j.molcel.2019.05.023>.
- Charlesworth, D. (2021a). When and how do sex-linked regions become sex chromosomes? *Evolution* *75*, 569–581. <https://doi.org/10.1111/evo.14196>.
- Charlesworth, D. (2021b). The timing of genetic degeneration of sex chromosomes. *Philos. Trans. R. Soc. Lond. B Biol. Sci.* *376*, 20200093. <https://doi.org/10.1098/rstb.2020.0093>.
- Cheng, Y., Liu, M., Hu, M., and Wang, S. (2021). TAD-like single-cell domain structures exist on both active and inactive X chromosomes and persist under epigenetic perturbations. *Genome Biol.* *22*, 309. <https://doi.org/10.1186/s13059-021-02523-8>.
- Chow, L.T., Scott, J.M., and Broker, T.R. (1975). *Electron microscopy of nucleic acids* (Cold Spring Harbor Laboratory, Cold Spring Harbor, New York).
- Ciosk, R., Zachariae, W., Michaelis, C., Shevchenko, A., Mann, M., and Nasmyth, K. (1998). An ESP1/PDS1 complex regulates loss of sister chromatid cohesion at the metaphase to anaphase transition in yeast. *Cell* *93*, 1067–1076. [https://doi.org/10.1016/s0092-8674\(00\)81211-8](https://doi.org/10.1016/s0092-8674(00)81211-8).
- Ciosk, R., Shirayama, M., Shevchenko, A., Tanaka, T., Toth, A., Shevchenko, A., and Nasmyth, K. (2000). Cohesin's binding to chromosomes depends on a separate complex consisting of Scc2 and Scc4 proteins. *Mol. Cell* *5*, 243–254. [https://doi.org/10.1016/s1097-2765\(00\)80420-7](https://doi.org/10.1016/s1097-2765(00)80420-7).
- Clemson, C.M., McNeil, J.A., Willard, H.F., and Lawrence, J.B. (1996). XIST RNA paints the inactive X chromosome at interphase: evidence for a novel RNA involved in nuclear/chromosome structure. *J. Cell Biol.* *132*, 259–275. <https://doi.org/10.1083/jcb.132.3.259>.
- Cohen-Fix, O., Peters, J.M., Kirschner, M.W., and Koshland, D. (1996). Anaphase initiation in *Saccharomyces cerevisiae* is controlled by the APC-dependent degradation of the anaphase inhibitor Pds1p. *Genes Dev.* *10*, 3081–3093. <https://doi.org/10.1101/gad.10.24.3081>.
- Collier, J.E., Lee, B.-G., Roig, M.B., Yatskevich, S., Petela, N.J., Metson, J., Voulgaris, M., Gonzalez Llamazares, A., Löwe, J., and Nasmyth, K.A. (2020). Transport of DNA within cohesin involves clamping on top of engaged heads by Scc2 and entrapment within the ring by Scc3. *ELife* *9*. <https://doi.org/10.7554/eLife.59560>.
- Collins, P.L., Purman, C., Porter, S.I., Nganga, V., Saini, A., Hayer, K.E., Gurewitz, G.L., Sleckman, B.P., Bednarski, J.J., Bassing, C.H., *et al.* (2020). DNA double-strand breaks induce H2Ax phosphorylation domains in a contact-dependent manner. *Nat. Commun.* *11*, 3158. <https://doi.org/10.1038/s41467-020-16926-x>.
- Conte, M., Irani, E., Chiariello, A.M., Abraham, A., Bianco, S., Esposito, A., and Nicodemi, M. (2022). Loop-extrusion and polymer phase-separation can co-exist at the single-molecule level to shape chromatin folding. *Nat. Commun.* *13*, 4070. <https://doi.org/10.1038/s41467-022-31856-6>.
- Cook, P.R., and Brazell, I.A. (1975). Supercoils in human DNA. *J. Cell Sci.* *19*, 261–279.

<https://doi.org/10.1242/jcs.19.2.261>.

Cook, P.R., Brazell, I.A., and Jost, E. (1976). Characterization of nuclear structures containing superhelical DNA. *J. Cell Sci.* *22*, 303–324. <https://doi.org/10.1242/jcs.22.2.303>.

Corbett, K.D. (2017). Molecular mechanisms of spindle assembly checkpoint activation and silencing. *Prog. Mol. Subcell. Biol.* *56*, 429–455. https://doi.org/10.1007/978-3-319-58592-5_18.

Cornacchia, D., Dileep, V., Quivy, J.-P., Foti, R., Tili, F., Santarella-Mellig, R., Antony, C., Almouzni, G., Gilbert, D.M., and Buonomo, S.B.C. (2012). Mouse Rif1 is a key regulator of the replication-timing programme in mammalian cells. *EMBO J.* *31*, 3678–3690. <https://doi.org/10.1038/emboj.2012.214>.

Cremer, M., Grasser, F., Lanctôt, C., Müller, S., Neusser, M., Zinner, R., Solovei, I., and Cremer, T. (2008). Multicolor 3D fluorescence *in situ* hybridization for imaging interphase chromosomes. *Methods Mol. Biol.* *463*, 205–239. https://doi.org/10.1007/978-1-59745-406-3_15.

Cremer, M., Brandstetter, K., Maiser, A., Rao, S.S.P., Schmid, V.J., Guirao-Ortiz, M., Mitra, N., Mamberti, S., Klein, K.N., Gilbert, D.M., *et al.* (2020). Cohesin depleted cells rebuild functional nuclear compartments after endomitosis. *Nat. Commun.* *11*, 6146. <https://doi.org/10.1038/s41467-020-19876-6>.

Cuadrado, A., and Losada, A. (2020). Specialized functions of cohesins STAG1 and STAG2 in 3D genome architecture. *Curr. Opin. Genet. Dev.* *61*, 9–16. <https://doi.org/10.1016/j.gde.2020.02.024>.

Cuadrado, A., Remeseiro, S., Gómez-López, G., Pisano, D.G., and Losada, A. (2012). The specific contributions of cohesin-SA1 to cohesion and gene expression: implications for cancer and development. *Cell Cycle* *11*, 2233–2238. <https://doi.org/10.4161/cc.20318>.

Darrow, E.M., Huntley, M.H., Dudchenko, O., Stamenova, E.K., Durand, N.C., Sun, Z., Huang, S.-C., Sanborn, A.L., Machol, I., Shamim, M., *et al.* (2016). Deletion of DXZ4 on the human inactive X chromosome alters higher-order genome architecture. *Proc Natl Acad Sci USA* *113*, E4504–12. <https://doi.org/10.1073/pnas.1609643113>.

Davé, A., Cooley, C., Garg, M., and Bianchi, A. (2014). Protein phosphatase 1 recruitment by Rif1 regulates DNA replication origin firing by counteracting DDK activity. *Cell Rep.* *7*, 53–61. <https://doi.org/10.1016/j.celrep.2014.02.019>.

Davidson, I.F., Goetz, D., Zaczek, M.P., Molodtsov, M.I., Huis In 't Veld, P.J., Weissmann, F., Litos, G., Cisneros, D.A., Ocampo-Hafalla, M., Ladurner, R., *et al.* (2016). Rapid movement and transcriptional re-localization of human cohesin on DNA. *EMBO J.* *35*, 2671–2685. <https://doi.org/10.15252/embj.201695402>.

Davidson, I.F., Bauer, B., Goetz, D., Tang, W., Wutz, G., and Peters, J.-M. (2019). DNA loop extrusion by human cohesin. *Science* *366*, 1338–1345. <https://doi.org/10.1126/science.aaz3418>.

Deardorff, M.A., and Krantz, I.D. (2014). Pathways—Cohesinopathies. In *Reference module in biomedical sciences* (Elsevier), p.

Deardorff, M.A., Bando, M., Nakato, R., Watrin, E., Itoh, T., Minamino, M., Saitoh, K., Komata, M., Katou, Y., Clark, D., *et al.* (2012). HDAC8 mutations in Cornelia de Lange syndrome affect the cohesin acetylation cycle. *Nature* *489*, 313–317. <https://doi.org/10.1038/nature11316>.

Debrand, E., Chureau, C., Arnaud, D., Avner, P., and Heard, E. (1999). Functional analysis of the DXPas34 locus, a 3' regulator of Xist expression. *Mol. Cell. Biol.* *19*, 8513–8525. <https://doi.org/10.1128/MCB.19.12.8513>.

Dekker, J., Rippe, K., Dekker, M., and Kleckner, N. (2002). Capturing chromosome conformation. *Science* *295*, 1306–1311. <https://doi.org/10.1126/science.1067799>.

Deng, X., Ma, W., Ramani, V., Hill, A., Yang, F., Ay, F., Berletch, J.B., Blau, C.A., Shendure, J., Duan, Z., *et al.* (2015). Bipartite structure of the inactive mouse X chromosome. *Genome Biol.* *16*, 152. <https://doi.org/10.1186/s13059-015-0728-8>.

Deng, Z., Wang, Z., Stong, N., Plasschaert, R., Moczan, A., Chen, H.-S., Hu, S., Wikramasinghe, P., Davuluri, R.V., Bartolomei, M.S., *et al.* (2012). A role for CTCF and cohesin in subtelomere chromatin organization, TERRA transcription, and telomere end protection. *EMBO J.* *31*, 4165–4178. <https://doi.org/10.1038/emboj.2012.266>.

Desprat, R., Thierry-Mieg, D., Lailler, N., Lajugie, J., Schildkraut, C., Thierry-Mieg, J., and Bouhassira, E.E. (2009).

Predictable dynamic program of timing of DNA replication in human cells. *Genome Res.* 19, 2288–2299. <https://doi.org/10.1101/gr.094060.109>.

De Koninck, M., Lapi, E., Badía-Careaga, C., Cossío, I., Giménez-Llorente, D., Rodríguez-Corsino, M., Andrada, E., Hidalgo, A., Manzanares, M., Real, F.X., *et al.* (2020). Essential roles of cohesin STAG2 in mouse embryonic development and adult tissue homeostasis. *Cell Rep.* 32, 108014. <https://doi.org/10.1016/j.celrep.2020.108014>.

De Piccoli, G., Cortes-Ledesma, F., Ira, G., Torres-Rosell, J., Uhle, S., Farmer, S., Hwang, J.-Y., Machin, F., Ceschia, A., McAleenan, A., *et al.* (2006). Smc5-Smc6 mediate DNA double-strand-break repair by promoting sister-chromatid recombination. *Nat. Cell Biol.* 8, 1032–1034. <https://doi.org/10.1038/ncb1466>.

Diebold-Durand, M.-L., Lee, H., Ruiz Avila, L.B., Noh, H., Shin, H.-C., Im, H., Bock, F.P., Bürmann, F., Durand, A., Basfeld, A., *et al.* (2017). Structure of Full-Length SMC and Rearrangements Required for Chromosome Organization. *Mol. Cell* 67, 334–347.e5. <https://doi.org/10.1016/j.molcel.2017.06.010>.

Dileep, V., Ay, F., Sima, J., Vera, D.L., Noble, W.S., and Gilbert, D.M. (2015). Topologically associating domains and their long-range contacts are established during early G1 coincident with the establishment of the replication-timing program. *Genome Res.* 25, 1104–1113. <https://doi.org/10.1101/gr.183699.114>.

Dimitrova, D.S., and Gilbert, D.M. (1999). The spatial position and replication timing of chromosomal domains are both established in early G1 phase. *Mol. Cell* 4, 983–993. [https://doi.org/10.1016/s1097-2765\(00\)80227-0](https://doi.org/10.1016/s1097-2765(00)80227-0).

Dion, V., Kalck, V., Seeber, A., Schleker, T., and Gasser, S.M. (2013). Cohesin and the nucleolus constrain the mobility of spontaneous repair foci. *EMBO Rep.* 14, 984–991. <https://doi.org/10.1038/embor.2013.142>.

Disteche, C.M. (2016). Dosage compensation of the sex chromosomes and autosomes. *Semin. Cell Dev. Biol.* 56, 9–18. <https://doi.org/10.1016/j.semcdb.2016.04.013>.

Dixon, J.R., Selvaraj, S., Yue, F., Kim, A., Li, Y., Shen, Y., Hu, M., Liu, J.S., and Ren, B. (2012). Topological domains in mammalian genomes identified by analysis of chromatin interactions. *Nature* 485, 376–380. <https://doi.org/10.1038/nature11082>.

Dixon, J.R., Jung, I., Selvaraj, S., Shen, Y., Antosiewicz-Bourget, J.E., Lee, A.Y., Ye, Z., Kim, A., Rajagopal, N., Xie, W., *et al.* (2015). Chromatin architecture reorganization during stem cell differentiation. *Nature* 518, 331–336. <https://doi.org/10.1038/nature14222>.

Dorsett, D. (2004). Adherin: key to the cohesin ring and cornelia de Lange syndrome. *Curr. Biol.* 14, R834–6. <https://doi.org/10.1016/j.cub.2004.09.035>.

Duret, L., Chureau, C., Samain, S., Weissenbach, J., and Avner, P. (2006). The Xist RNA gene evolved in eutherians by pseudogenization of a protein-coding gene. *Science* 312, 1653–1655. <https://doi.org/10.1126/science.1126316>.

Earnshaw, W.C., and Laemmli, U.K. (1983). Architecture of metaphase chromosomes and chromosome scaffolds. *J. Cell Biol.* 96, 84–93. <https://doi.org/10.1083/jcb.96.1.84>.

Edenberg, H.J., and Huberman, J.A. (1975). Eukaryotic chromosome replication. *Annu. Rev. Genet.* 9, 245–284. <https://doi.org/10.1146/annurev.ge.09.120175.001333>.

Efroni, S., Duttagupta, R., Cheng, J., Dehghani, H., Hoepfner, D.J., Dash, C., Bazett-Jones, D.P., Le Grice, S., McKay, R.D.G., Buetow, K.H., *et al.* (2008). Global transcription in pluripotent embryonic stem cells. *Cell Stem Cell* 2, 437–447. <https://doi.org/10.1016/j.stem.2008.03.021>.

Eng, T., Guacci, V., and Koshland, D. (2015). Interallelic complementation provides functional evidence for cohesin-cohesin interactions on DNA. *Mol. Biol. Cell* 26, 4224–4235. <https://doi.org/10.1091/mbc.E15-06-0331>.

Erfle, H., Neumann, B., Liebel, U., Rogers, P., Held, M., Walter, T., Ellenberg, J., and Pepperkok, R. (2007). Reverse transfection on cell arrays for high content screening microscopy. *Nat. Protoc.* 2, 392–399. <https://doi.org/10.1038/nprot.2006.483>.

Falk, M., Feodorova, Y., Naumova, N., Imakaev, M., Lajoie, B.R., Leonhardt, H., Joffe, B., Dekker, J., Fudenberg, G.,

- Solovei, I., *et al.* (2019). Heterochromatin drives compartmentalization of inverted and conventional nuclei. *Nature* 570, 395–399. <https://doi.org/10.1038/s41586-019-1275-3>.
- Fernandez-Capetillo, O., Chen, H.-T., Celeste, A., Ward, I., Romanienko, P.J., Morales, J.C., Naka, K., Xia, Z., Camerini-Otero, R.D., Motoyama, N., *et al.* (2002). DNA damage-induced G2-M checkpoint activation by histone H2AX and 53BP1. *Nat. Cell Biol.* 4, 993–997. <https://doi.org/10.1038/ncb884>.
- Filippova, G.N., Fagerlie, S., Klenova, E.M., Myers, C., Dehner, Y., Goodwin, G., Neiman, P.E., Collins, S.J., and Lobanenkov, V.V. (1996). An exceptionally conserved transcriptional repressor, CTCF, employs different combinations of zinc fingers to bind diverged promoter sequences of avian and mammalian c-myc oncogenes. *Mol. Cell. Biol.* 16, 2802–2813. <https://doi.org/10.1128/MCB.16.6.2802>.
- Fisher, J.B., McNulty, M., Burke, M.J., Crispino, J.D., and Rao, S. (2017). Cohesin mutations in myeloid malignancies. *Trends Cancer* 3, 282–293. <https://doi.org/10.1016/j.trecan.2017.02.006>.
- Flaquer, A., Rappold, G.A., Wienker, T.F., and Fischer, C. (2008). The human pseudoautosomal regions: a review for genetic epidemiologists. *Eur. J. Hum. Genet.* 16, 771–779. <https://doi.org/10.1038/ejhg.2008.63>.
- Foti, R., Gnan, S., Cornacchia, D., Dileep, V., Bulut-Karslioglu, A., Diehl, S., Buness, A., Klein, F.A., Huber, W., Johnstone, E., *et al.* (2016). Nuclear Architecture Organized by Rif1 Underpins the Replication-Timing Program. *Mol. Cell* 61, 260–273. <https://doi.org/10.1016/j.molcel.2015.12.001>.
- Francis, R., and Richardson, C. (2007). Multipotent hematopoietic cells susceptible to alternative double-strand break repair pathways that promote genome rearrangements. *Genes Dev.* 21, 1064–1074. <https://doi.org/10.1101/gad.1522807>.
- Friedberg, E.C., and Meira, L.B. (2006). Database of mouse strains carrying targeted mutations in genes affecting biological responses to DNA damage Version 7. *DNA Repair (Amst)* 5, 189–209. <https://doi.org/10.1016/j.dnarep.2005.09.009>.
- Friedland, W., Jacob, P., Paretzke, H.G., Ottolenghi, A., Ballarini, F., and Liotta, M. (2006). Simulation of light ion induced DNA damage patterns. *Radiat. Prot. Dosimetry* 122, 116–120. <https://doi.org/10.1093/rpd/ncl451>.
- Friedrich, T., Durante, M., and Scholz, M. (2012). Modeling cell survival after photon irradiation based on double-strand break clustering in megabase pair chromatin loops. *Radiat. Res.* 178, 385–394. <https://doi.org/10.1667/RR2964.1>.
- Friedrich, T., Scholz, U., Elsässer, T., Durante, M., and Scholz, M. (2013). Systematic analysis of RBE and related quantities using a database of cell survival experiments with ion beam irradiation. *J. Radiat. Res.* 54, 494–514. <https://doi.org/10.1093/jrr/rrs114>.
- Fudenberg, G., Imakaev, M., Lu, C., Goloborodko, A., Abdennur, N., and Mirny, L.A. (2016). Formation of chromosomal domains by loop extrusion. *Cell Rep.* 15, 2038–2049. <https://doi.org/10.1016/j.celrep.2016.04.085>.
- Fudenberg, G., Abdennur, N., Imakaev, M., Goloborodko, A., and Mirny, L.A. (2017). Emerging evidence of chromosome folding by loop extrusion. *Cold Spring Harb. Symp. Quant. Biol.* 82, 45–55. <https://doi.org/10.1101/sqb.2017.82.034710>.
- Funabiki, H., Yamano, H., Kumada, K., Nagao, K., Hunt, T., and Yanagida, M. (1996). Cut2 proteolysis required for sister-chromatid separation in fission yeast. *Nature* 381, 438–441. <https://doi.org/10.1038/381438a0>.
- Game, J.C., Birrell, G.W., Brown, J.A., Shibata, T., Baccari, C., Chu, A.M., Williamson, M.S., and Brown, J.M. (2003). Use of a genome-wide approach to identify new genes that control resistance of *Saccharomyces cerevisiae* to ionizing radiation. *Radiat. Res.* 160, 14–24. <https://doi.org/10.1667/rr3019>.
- Gandhi, R., Gillespie, P.J., and Hirano, T. (2006). Human Wapl is a cohesin-binding protein that promotes sister-chromatid resolution in mitotic prophase. *Curr. Biol.* 16, 2406–2417. <https://doi.org/10.1016/j.cub.2006.10.061>.
- Ganji, M., Shaltiel, I.A., Bisht, S., Kim, E., Kalichava, A., Haering, C.H., and Dekker, C. (2018). Real-time imaging of DNA loop extrusion by condensin. *Science* 360, 102–105. <https://doi.org/10.1126/science.aar7831>.
- Garcia, Y.A., Velasquez, E.F., Gao, L.W., Gholkar, A.A., Clutario, K.M., Cheung, K., Williams-Hamilton, T.,

- Whitelegge, J.P., and Torres, J.Z. (2021). Mapping proximity associations of core spindle assembly checkpoint proteins. *J. Proteome Res.* *20*, 3414–3427. <https://doi.org/10.1021/acs.jproteome.0c00941>.
- Gelot, C., Guirouilh-Barbat, J., and Lopez, B.S. (2016). The cohesin complex prevents the end-joining of distant DNA double-strand ends in S phase: Consequences on genome stability maintenance. *Nucleus* *7*, 339–345. <https://doi.org/10.1080/19491034.2016.1194159>.
- Georgakilas, A.G., O'Neill, P., and Stewart, R.D. (2013). Induction and repair of clustered DNA lesions: what do we know so far? *Radiat. Res.* *180*, 100–109. <https://doi.org/10.1667/RR3041.1>.
- Gibcus, J.H., Samejima, K., Goloborodko, A., Samejima, I., Naumova, N., Nuebler, J., Kanemaki, M.T., Xie, L., Paulson, J.R., Earnshaw, W.C., *et al.* (2018). A pathway for mitotic chromosome formation. *Science* *359*. <https://doi.org/10.1126/science.aao6135>.
- Gilbert, D.M., Takebayashi, S.I., Ryba, T., Lu, J., Pope, B.D., Wilson, K.A., and Hiratani, I. (2010). Space and time in the nucleus: developmental control of replication timing and chromosome architecture. *Cold Spring Harb. Symp. Quant. Biol.* *75*, 143–153. <https://doi.org/10.1101/sqb.2010.75.011>.
- Giorgetti, L., Lajoie, B.R., Carter, A.C., Attia, M., Zhan, Y., Xu, J., Chen, C.J., Kaplan, N., Chang, H.Y., Heard, E., *et al.* (2016). Structural organization of the inactive X chromosome in the mouse. *Nature* *535*, 575–579. <https://doi.org/10.1038/nature18589>.
- Gligoris, T., and Löwe, J. (2016). Structural Insights into Ring Formation of Cohesin and Related Smc Complexes. *Trends Cell Biol.* *26*, 680–693. <https://doi.org/10.1016/j.tcb.2016.04.002>.
- Gligoris, T.G., Scheinost, J.C., Bürmann, F., Petela, N., Chan, K.-L., Uluocak, P., Beckouët, F., Gruber, S., Nasmyth, K., and Löwe, J. (2014). Closing the cohesin ring: structure and function of its Smc3-kleisin interface. *Science* *346*, 963–967. <https://doi.org/10.1126/science.1256917>.
- Gnan, S., Flyamer, I.M., Klein, K.N., Castelli, E., Rapp, A., Maiser, A., Chen, N., Weber, P., Enverald, E., Cardoso, M.C., *et al.* (2021). Nuclear organisation and replication timing are coupled through RIF1-PP1 interaction. *Nat. Commun.* *12*, 2910. <https://doi.org/10.1038/s41467-021-22899-2>.
- Goldman, M.A., Holmquist, G.P., Gray, M.C., Caston, L.A., and Nag, A. (1984). Replication timing of genes and middle repetitive sequences. *Science* *224*, 686–692. <https://doi.org/10.1126/science.6719109>.
- Golfier, S., Quail, T., Kimura, H., and Brugués, J. (2020). Cohesin and condensin extrude DNA loops in a cell cycle-dependent manner. *ELife* *9*. <https://doi.org/10.7554/eLife.53885>.
- Gómez-Marín, C., Tena, J.J., Acemel, R.D., López-Mayorga, M., Naranjo, S., de la Calle-Mustienes, E., Maeso, I., Beccari, L., Aneas, I., Vielmas, E., *et al.* (2015). Evolutionary comparison reveals that diverging CTCF sites are signatures of ancestral topological associating domains borders. *Proc Natl Acad Sci USA* *112*, 7542–7547. <https://doi.org/10.1073/pnas.1505463112>.
- Graves, J.A.M. (2016). Evolution of vertebrate sex chromosomes and dosage compensation. *Nat. Rev. Genet.* *17*, 33–46. <https://doi.org/10.1038/nrg.2015.2>.
- Graves, J.A. (1995). The origin and function of the mammalian Y chromosome and Y-borne genes--an evolving understanding. *Bioessays* *17*, 311–320. <https://doi.org/10.1002/bies.950170407>.
- Griffin, D.K. (2012). Is the Y chromosome disappearing?--both sides of the argument. *Chromosome Res.* *20*, 35–45. <https://doi.org/10.1007/s10577-011-9252-1>.
- Griffin, D.K., Harvey, S.C., Campos-Ramos, R., Ayling, L.J., Bromage, N.R., Masabanda, J.S., and Penman, D.J. (2002). Early origins of the X and Y chromosomes: lessons from tilapia. *Cytogenet. Genome Res.* *99*, 157–163. <https://doi.org/10.1159/000071588>.
- Gruber, S., Arumugam, P., Katou, Y., Kuglitsch, D., Helmhart, W., Shirahige, K., and Nasmyth, K. (2006). Evidence that loading of cohesin onto chromosomes involves opening of its SMC hinge. *Cell* *127*, 523–537. <https://doi.org/10.1016/j.cell.2006.08.048>.
- Guacci, V., Yamamoto, A., Strunnikov, A., Kingsbury, J., Hogan, E., Meluh, P., and Koshland, D. (1993). Structure and function of chromosomes in mitosis of budding yeast. *Cold Spring Harb. Symp. Quant. Biol.* *58*, 677–685. <https://doi.org/10.1101/sqb.1993.058.01.075>.

- Guacci, V., Koshland, D., and Strunnikov, A. (1997). A direct link between sister chromatid cohesion and chromosome condensation revealed through the analysis of MCD1 in *S. cerevisiae*. *Cell* 91, 47–57. [https://doi.org/10.1016/s0092-8674\(01\)80008-8](https://doi.org/10.1016/s0092-8674(01)80008-8).
- Gubbay, J., Collignon, J., Koopman, P., Capel, B., Economou, A., Münsterberg, A., Vivian, N., Goodfellow, P., and Lovell-Badge, R. (1990). A gene mapping to the sex-determining region of the mouse Y chromosome is a member of a novel family of embryonically expressed genes. *Nature* 346, 245–250. <https://doi.org/10.1038/346245a0>.
- Guelen, L., Pagie, L., Brasset, E., Meuleman, W., Faza, M.B., Talhout, W., Eussen, B.H., de Klein, A., Wessels, L., de Laat, W., *et al.* (2008). Domain organization of human chromosomes revealed by mapping of nuclear lamina interactions. *Nature* 453, 948–951. <https://doi.org/10.1038/nature06947>.
- Guénet, J.L. (2005). The mouse genome. *Genome Res.* 15, 1729–1740. <https://doi.org/10.1101/gr.3728305>.
- Guillou, E., Ibarra, A., Coulon, V., Casado-Vela, J., Rico, D., Casal, I., Schwob, E., Losada, A., and Méndez, J. (2010). Cohesin organizes chromatin loops at DNA replication factories. *Genes Dev.* 24, 2812–2822. <https://doi.org/10.1101/gad.608210>.
- Guo, G., Sun, X., Chen, C., Wu, S., Huang, P., Li, Z., Dean, M., Huang, Y., Jia, W., Zhou, Q., *et al.* (2013). Whole-genome and whole-exome sequencing of bladder cancer identifies frequent alterations in genes involved in sister chromatid cohesion and segregation. *Nat. Genet.* 45, 1459–1463. <https://doi.org/10.1038/ng.2798>.
- Guo, X., Dai, X., Zhou, T., Wang, H., Ni, J., Xue, J., and Wang, X. (2020). Mosaic loss of human Y chromosome: what, how and why. *Hum. Genet.* 139, 421–446. <https://doi.org/10.1007/s00439-020-02114-w>.
- Gupta, V., Parisi, M., Sturgill, D., Nuttall, R., Doctolero, M., Dudko, O.K., Malley, J.D., Eastman, P.S., and Oliver, B. (2006). Global analysis of X-chromosome dosage compensation. *J. Biol.* 5, 3. <https://doi.org/10.1186/jbiol30>.
- Hadjur, S., Williams, L.M., Ryan, N.K., Cobb, B.S., Sexton, T., Fraser, P., Fisher, A.G., and Merckenschlager, M. (2009). Cohesins form chromosomal cis-interactions at the developmentally regulated IFNG locus. *Nature* 460, 410–413. <https://doi.org/10.1038/nature08079>.
- Haering, C.H., Löwe, J., Hochwagen, A., and Nasmyth, K. (2002). Molecular architecture of SMC proteins and the yeast cohesin complex. *Mol. Cell* 9, 773–788. [https://doi.org/10.1016/s1097-2765\(02\)00515-4](https://doi.org/10.1016/s1097-2765(02)00515-4).
- Haering, C.H., Schoffnegger, D., Nishino, T., Helmhart, W., Nasmyth, K., and Löwe, J. (2004). Structure and stability of cohesin's Smc1-kleisin interaction. *Mol. Cell* 15, 951–964. <https://doi.org/10.1016/j.molcel.2004.08.030>.
- Hand, R. (1978). Eucaryotic DNA: organization of the genome for replication. *Cell* 15, 317–325. [https://doi.org/10.1016/0092-8674\(78\)90001-6](https://doi.org/10.1016/0092-8674(78)90001-6).
- Hansen, A.S. (2020). CTCF as a boundary factor for cohesin-mediated loop extrusion: evidence for a multi-step mechanism. *Nucleus* 11, 132–148. <https://doi.org/10.1080/19491034.2020.1782024>.
- Hansen, A.S., Cattoglio, C., Darzacq, X., and Tjian, R. (2018). Recent evidence that TADs and chromatin loops are dynamic structures. *Nucleus* 9, 20–32. <https://doi.org/10.1080/19491034.2017.1389365>.
- Hansen, A.S., Hsieh, T.-H.S., Cattoglio, C., Pustova, I., Saldaña-Meyer, R., Reinberg, D., Darzacq, X., and Tjian, R. (2019). Distinct Classes of Chromatin Loops Revealed by Deletion of an RNA-Binding Region in CTCF. *Mol. Cell* 76, 395–411.e13. <https://doi.org/10.1016/j.molcel.2019.07.039>.
- Hara, K., Zheng, G., Qu, Q., Liu, H., Ouyang, Z., Chen, Z., Tomchick, D.R., and Yu, H. (2014). Structure of cohesin subcomplex pinpoints direct shugoshin-Wapl antagonism in centromeric cohesion. *Nat. Struct. Mol. Biol.* 21, 864–870. <https://doi.org/10.1038/nsmb.2880>.
- Hardy, C.F., Sussel, L., and Shore, D. (1992). A RAP1-interacting protein involved in transcriptional silencing and telomere length regulation. *Genes Dev.* 6, 801–814. <https://doi.org/10.1101/gad.6.5.801>.
- Hartman, T., Stead, K., Koshland, D., and Guacci, V. (2000). Pds5p is an essential chromosomal protein required for both sister chromatid cohesion and condensation in *Saccharomyces cerevisiae*. *J. Cell Biol.* 151, 613–626. <https://doi.org/10.1083/jcb.151.3.613>.

- Hatton, K.S., Dhar, V., Brown, E.H., Iqbal, M.A., Stuart, S., Didamo, V.T., and Schildkraut, C.L. (1988). Replication program of active and inactive multigene families in mammalian cells. *Mol. Cell. Biol.* *8*, 2149–2158. <https://doi.org/10.1128/mcb.8.5.2149-2158.1988>.
- Hauf, S., Waizenegger, I.C., and Peters, J.M. (2001). Cohesin cleavage by separase required for anaphase and cytokinesis in human cells. *Science* *293*, 1320–1323. <https://doi.org/10.1126/science.1061376>.
- Hauf, S., Roitinger, E., Koch, B., Dittrich, C.M., Mechtler, K., and Peters, J.-M. (2005). Dissociation of cohesin from chromosome arms and loss of arm cohesion during early mitosis depends on phosphorylation of SA2. *PLoS Biol.* *3*, e69. <https://doi.org/10.1371/journal.pbio.0030069>.
- Heath, H., Ribeiro de Almeida, C., Sleutels, F., Dingjan, G., van de Nobelen, S., Jonkers, I., Ling, K.-W., Gribnau, J., Renkawitz, R., Grosveld, F., *et al.* (2008). CTCF regulates cell cycle progression of alphabeta T cells in the thymus. *EMBO J.* *27*, 2839–2850. <https://doi.org/10.1038/emboj.2008.214>.
- Heger, P., Marin, B., Bartkuhn, M., Schierenberg, E., and Wiehe, T. (2012). The chromatin insulator CTCF and the emergence of metazoan diversity. *Proc Natl Acad Sci USA* *109*, 17507–17512. <https://doi.org/10.1073/pnas.1111941109>.
- Heinz, K.S., Rapp, A., Casas-Delucchi, C.S., Lehmkuhl, A., Romero-Fernández, I., Sánchez, A., Krämer, O.H., Marchal, J.A., and Cardoso, M.C. (2019). DNA replication dynamics of vole genome and its epigenetic regulation. *Epigenetics Chromatin* *12*, 18. <https://doi.org/10.1186/s13072-019-0262-0>.
- Herr, L., Friedrich, T., Durante, M., and Scholz, M. (2014). A model of photon cell killing based on the spatio-temporal clustering of DNA damage in higher order chromatin structures. *PLoS ONE* *9*, e83923. <https://doi.org/10.1371/journal.pone.0083923>.
- Higashi, T.L., and Uhlmann, F. (2022). SMC complexes: Lifting the lid on loop extrusion. *Curr. Opin. Cell Biol.* *74*, 13–22. <https://doi.org/10.1016/j.ceb.2021.12.003>.
- Higashi, T.L., Eickhoff, P., Sousa, J.S., Locke, J., Nans, A., Flynn, H.R., Snijders, A.P., Papageorgiou, G., O'Reilly, N., Chen, Z.A., *et al.* (2020). A Structure-Based Mechanism for DNA Entry into the Cohesin Ring. *Mol. Cell* *79*, 917–933.e9. <https://doi.org/10.1016/j.molcel.2020.07.013>.
- Hill, V.K., Kim, J.-S., and Waldman, T. (2016). Cohesin mutations in human cancer. *Biochim. Biophys. Acta* *1866*, 1–11. <https://doi.org/10.1016/j.bbcan.2016.05.002>.
- Hilmi, K., Jangal, M., Marques, M., Zhao, T., Saad, A., Zhang, C., Luo, V.M., Syme, A., Rejon, C., Yu, Z., *et al.* (2017). CTCF facilitates DNA double-strand break repair by enhancing homologous recombination repair. *Sci. Adv.* *3*, e1601898. <https://doi.org/10.1126/sciadv.1601898>.
- Hiraga, S.-I., Alvino, G.M., Chang, F., Lian, H.-Y., Sridhar, A., Kubota, T., Brewer, B.J., Weinreich, M., Raghuraman, M.K., and Donaldson, A.D. (2014). Rif1 controls DNA replication by directing Protein Phosphatase 1 to reverse Cdc7-mediated phosphorylation of the MCM complex. *Genes Dev.* *28*, 372–383. <https://doi.org/10.1101/gad.231258.113>.
- Hiraga, S.-I., Ly, T., Garzón, J., Hořejší, Z., Ohkubo, Y.-N., Endo, A., Obuse, C., Boulton, S.J., Lamond, A.I., and Donaldson, A.D. (2017). Human RIF1 and protein phosphatase 1 stimulate DNA replication origin licensing but suppress origin activation. *EMBO Rep.* *18*, 403–419. <https://doi.org/10.15252/embr.201641983>.
- Hirano, T., Mitchison, T.J., and Swedlow, J.R. (1995). The SMC family: from chromosome condensation to dosage compensation. *Curr. Opin. Cell Biol.* *7*, 329–336. [https://doi.org/10.1016/0955-0674\(95\)80087-5](https://doi.org/10.1016/0955-0674(95)80087-5).
- Hirano, T., Kobayashi, R., and Hirano, M. (1997). Condensins, chromosome condensation protein complexes containing XCAP-C, XCAP-E and a *Xenopus* homolog of the *Drosophila* Barren protein. *Cell* *89*, 511–521. [https://doi.org/10.1016/s0092-8674\(00\)80233-0](https://doi.org/10.1016/s0092-8674(00)80233-0).
- Hiratani, I., Ryba, T., Itoh, M., Yokochi, T., Schwaiger, M., Chang, C.-W., Lyou, Y., Townes, T.M., Schübeler, D., and Gilbert, D.M. (2008). Global reorganization of replication domains during embryonic stem cell differentiation. *PLoS Biol.* *6*, e245. <https://doi.org/10.1371/journal.pbio.0060245>.
- Hiratani, I., Ryba, T., Itoh, M., Rathjen, J., Kulik, M., Papp, B., Fussner, E., Bazett-Jones, D.P., Plath, K., Dalton, S., *et al.* (2010). Genome-wide dynamics of replication timing revealed by in vitro models of mouse embryogenesis.

- Genome Res. 20, 155–169. <https://doi.org/10.1101/gr.099796.109>.
- Holtrich, U., Wolf, G., Bräuninger, A., Karn, T., Böhme, B., Rübsamen-Waigmann, H., and Strebhardt, K. (1994). Induction and down-regulation of PLK, a human serine/threonine kinase expressed in proliferating cells and tumors. *Proc Natl Acad Sci USA* 91, 1736–1740. <https://doi.org/10.1073/pnas.91.5.1736>.
- Hooper, M., Hardy, K., Handyside, A., Hunter, S., and Monk, M. (1987). HPRT-deficient (Lesch-Nyhan) mouse embryos derived from germline colonization by cultured cells. *Nature* 326, 292–295. <https://doi.org/10.1038/326292a0>.
- Hopfner, K.P., Karcher, A., Shin, D.S., Craig, L., Arthur, L.M., Carney, J.P., and Tainer, J.A. (2000). Structural biology of Rad50 ATPase: ATP-driven conformational control in DNA double-strand break repair and the ABC-ATPase superfamily. *Cell* 101, 789–800. [https://doi.org/10.1016/s0092-8674\(00\)80890-9](https://doi.org/10.1016/s0092-8674(00)80890-9).
- Horsfield, J.A., Print, C.G., and Mönnich, M. (2012). Diverse developmental disorders from the one ring: distinct molecular pathways underlie the cohesinopathies. *Front. Genet.* 3, 171. <https://doi.org/10.3389/fgene.2012.00171>.
- Hsieh, T.-H.S., Weiner, A., Lajoie, B., Dekker, J., Friedman, N., and Rando, O.J. (2015). Mapping Nucleosome Resolution Chromosome Folding in Yeast by Micro-C. *Cell* 162, 108–119. <https://doi.org/10.1016/j.cell.2015.05.048>.
- Hsieh, T.-H.S., Cattoglio, C., Slobodyanyuk, E., Hansen, A.S., Rando, O.J., Tjian, R., and Darzacq, X. (2020). Resolving the 3D Landscape of Transcription-Linked Mammalian Chromatin Folding. *Mol. Cell* 78, 539–553.e8. <https://doi.org/10.1016/j.molcel.2020.03.002>.
- Huang, R.-X., and Zhou, P.-K. (2020). DNA damage response signaling pathways and targets for radiotherapy sensitization in cancer. *Signal Transduct. Target. Ther.* 5, 60. <https://doi.org/10.1038/s41392-020-0150-x>.
- Huberman, J.A. (1991). Cell cycle control of initiation of eukaryotic DNA replication. *Chromosoma* 100, 419–423. <https://doi.org/10.1007/BF00364551>.
- Huberman, J.A., and Riggs, A.D. (1968). On the mechanism of DNA replication in mammalian chromosomes. *J. Mol. Biol.* 32, 327–341. [https://doi.org/10.1016/0022-2836\(68\)90013-2](https://doi.org/10.1016/0022-2836(68)90013-2).
- Hufnagl, A., Herr, L., Friedrich, T., Durante, M., Taucher-Scholz, G., and Scholz, M. (2015). The link between cell-cycle dependent radiosensitivity and repair pathways: a model based on the local, sister-chromatid conformation dependent switch between NHEJ and HR. *DNA Repair (Amst)* 27, 28–39. <https://doi.org/10.1016/j.dnarep.2015.01.002>.
- Huis in 't Veld, P.J., Herzog, F., Ladurner, R., Davidson, I.F., Piric, S., Kreidl, E., Bhaskara, V., Aebersold, R., and Peters, J.-M. (2014). Characterization of a DNA exit gate in the human cohesin ring. *Science* 346, 968–972. <https://doi.org/10.1126/science.1256904>.
- Humphrey, E., and Cole, F. (2020). How sex chromosomes break up to get together. *Nature* 582, 346–347. <https://doi.org/10.1038/d41586-020-01483-6>.
- Huynh, K.D., and Lee, J.T. (2003). Inheritance of a pre-inactivated paternal X chromosome in early mouse embryos. *Nature* 426, 857–862. <https://doi.org/10.1038/nature02222>.
- Hu, B., Itoh, T., Mishra, A., Katoh, Y., Chan, K.-L., Upcher, W., Godlee, C., Roig, M.B., Shirahige, K., and Nasmyth, K. (2011). ATP hydrolysis is required for relocating cohesin from sites occupied by its Scc2/4 loading complex. *Curr. Biol.* 21, 12–24. <https://doi.org/10.1016/j.cub.2010.12.004>.
- Ivanov, D., Schleiffer, A., Eisenhaber, F., Mechtler, K., Haering, C.H., and Nasmyth, K. (2002). Eco1 is a novel acetyltransferase that can acetylate proteins involved in cohesion. *Curr. Biol.* 12, 323–328. [https://doi.org/10.1016/s0960-9822\(02\)00681-4](https://doi.org/10.1016/s0960-9822(02)00681-4).
- Jackson, D.A., and Pombo, A. (1998). Replicon clusters are stable units of chromosome structure: evidence that nuclear organization contributes to the efficient activation and propagation of S phase in human cells. *J. Cell Biol.* 140, 1285–1295. <https://doi.org/10.1083/jcb.140.6.1285>.
- Jackson, D.A., Dickinson, P., and Cook, P.R. (1990a). The size of chromatin loops in HeLa cells. *EMBO J.* 9, 567–571.

- Jackson, D.A., Dickinson, P., and Cook, P.R. (1990b). Attachment of DNA to the nucleoskeleton of HeLa cells examined using physiological conditions. *Nucleic Acids Res.* *18*, 4385–4393. <https://doi.org/10.1093/nar/18.15.4385>.
- Janssens, V., and Goris, J. (2001). Protein phosphatase 2A: a highly regulated family of serine/threonine phosphatases implicated in cell growth and signalling. *Biochem. J.* *353*, 417–439. <https://doi.org/10.1042/0264-6021:3530417>.
- Jentsch, I., Adler, I.D., Carter, N.P., and Speicher, M.R. (2001). Karyotyping mouse chromosomes by multiplex-FISH (M-FISH). *Chromosome Res.* *9*, 211–214. <https://doi.org/10.1023/a:1016696303479>.
- Johnston, P.J., Olive, P.L., and Bryant, P.E. (1997). Higher-order chromatin structure-dependent repair of DNA double-strand breaks: modeling the elution of DNA from nucleoids. *Radiat. Res.* *148*, 561–567.
- Johnston, P.J., MacPhail, S.H., Banáth, J.P., and Olive, P.L. (1998a). Higher-order chromatin structure-dependent repair of DNA double-strand breaks: factors affecting elution of DNA from nucleoids. *Radiat. Res.* *149*, 533–542.
- Johnston, P.J., MacPhail, S.H., Stamato, T.D., Kirchgessner, C.U., and Olive, P.L. (1998b). Higher-order chromatin structure-dependent repair of DNA double-strand breaks: involvement of the V(D)J recombination double-strand break repair pathway. *Radiat. Res.* *149*, 455–462.
- Kałużewski, B. (1982). BrdU-Hoechst-Giemsa analysis of DNA replication in synchronized lymphocyte cultures. Study of human X and Y chromosomes. *Chromosoma* *85*, 553–569. <https://doi.org/10.1007/BF00327350>.
- Kanke, M., Tahara, E., Huis In't Veld, P.J., and Nishiyama, T. (2016). Cohesin acetylation and Wapl-Pds5 oppositely regulate translocation of cohesin along DNA. *EMBO J.* *35*, 2686–2698. <https://doi.org/10.15252/embj.201695756>.
- Karagiannis, T.C., and El-Osta, A. (2004). Double-strand breaks: signaling pathways and repair mechanisms. *Cell. Mol. Life Sci.* *61*, 2137–2147. <https://doi.org/10.1007/s00018-004-4174-0>.
- Karlsson, K.H., and Stenerlöw, B. (2004). Focus formation of DNA repair proteins in normal and repair-deficient cells irradiated with high-LET ions. *Radiat. Res.* *161*, 517–527. <https://doi.org/10.1667/rr3171>.
- Katainen, R., Dave, K., Pitkänen, E., Palin, K., Kivioja, T., Välimäki, N., Gylfe, A.E., Ristolainen, H., Hänninen, U.A., Cajuso, T., *et al.* (2015). CTCF/cohesin-binding sites are frequently mutated in cancer. *Nat. Genet.* *47*, 818–821. <https://doi.org/10.1038/ng.3335>.
- Kauppi, L., Barchi, M., Baudat, F., Romanienko, P.J., Keeney, S., and Jasin, M. (2011). Distinct properties of the XY pseudoautosomal region crucial for male meiosis. *Science* *331*, 916–920. <https://doi.org/10.1126/science.1195774>.
- Kavenoff, R., and Ryder, O.A. (1976). Electron microscopy of membrane-associated folded chromosomes of *Escherichia coli*. *Chromosoma* *55*, 13–25. <https://doi.org/10.1007/BF00288323>.
- Kay, G.F., Barton, S.C., Surani, M.A., and Rastan, S. (1994). Imprinting and X chromosome counting mechanisms determine Xist expression in early mouse development. *Cell* *77*, 639–650. [https://doi.org/10.1016/0092-8674\(94\)90049-3](https://doi.org/10.1016/0092-8674(94)90049-3).
- Kido, T., and Lau, Y.-F.C. (2019). The Y-linked proto-oncogene TSPY contributes to poor prognosis of the male hepatocellular carcinoma patients by promoting the pro-oncogenic and suppressing the anti-oncogenic gene expression. *Cell Biosci.* *9*, 22. <https://doi.org/10.1186/s13578-019-0287-x>.
- Kikuchi, Y., and Sandberg, A.A. (1964). Chronology and pattern of human chromosome replication. i. blood leukocytes of normal subjects. *J Natl Cancer Inst* *32*, 1109–1143.
- Kilic, S., Lezaja, A., Gatti, M., Bianco, E., Michelena, J., Imhof, R., and Altmeyer, M. (2019). Phase separation of 53BP1 determines liquid-like behavior of DNA repair compartments. *EMBO J.* *38*, e101379. <https://doi.org/10.15252/embj.2018101379>.
- Kill, I.R., Bridger, J.M., Campbell, K.H., Maldonado-Codina, G., and Hutchison, C.J. (1991). The timing of the formation and usage of replicase clusters in S-phase nuclei of human diploid fibroblasts. *J. Cell Sci.* *100 (Pt 4)*, 869–876. <https://doi.org/10.1242/jcs.100.4.869>.

- Kim, T., and Gartner, A. (2021). Bub1 kinase in the regulation of mitosis. *Animal Cells Syst (Seoul)* 25, 1–10. <https://doi.org/10.1080/19768354.2021.1884599>.
- Kim, J.-S., Krasieva, T.B., LaMorte, V., Taylor, A.M.R., and Yokomori, K. (2002a). Specific recruitment of human cohesin to laser-induced DNA damage. *J. Biol. Chem.* 277, 45149–45153. <https://doi.org/10.1074/jbc.M209123200>.
- Kim, S.-T., Xu, B., and Kastan, M.B. (2002b). Involvement of the cohesin protein, Smc1, in Atm-dependent and independent responses to DNA damage. *Genes Dev.* 16, 560–570. <https://doi.org/10.1101/gad.970602>.
- Kim, Y., Shi, Z., Zhang, H., Finkelstein, I.J., and Yu, H. (2019). Human cohesin compacts DNA by loop extrusion. *Science* 366, 1345–1349. <https://doi.org/10.1126/science.aaz4475>.
- King, R.W., Peters, J.M., Tugendreich, S., Rolfe, M., Hieter, P., and Kirschner, M.W. (1995). A 20S complex containing CDC27 and CDC16 catalyzes the mitosis-specific conjugation of ubiquitin to cyclin B. *Cell* 81, 279–288. [https://doi.org/10.1016/0092-8674\(95\)90338-0](https://doi.org/10.1016/0092-8674(95)90338-0).
- Kitajima, T.S., Kawashima, S.A., and Watanabe, Y. (2004). The conserved kinetochore protein shugoshin protects centromeric cohesion during meiosis. *Nature* 427, 510–517. <https://doi.org/10.1038/nature02312>.
- Kitajima, T.S., Sakuno, T., Ishiguro, K., Iemura, S., Natsume, T., Kawashima, S.A., and Watanabe, Y. (2006). Shugoshin collaborates with protein phosphatase 2A to protect cohesin. *Nature* 441, 46–52. <https://doi.org/10.1038/nature04663>.
- Klenova, E.M., Nicolas, R.H., Paterson, H.F., Carne, A.F., Heath, C.M., Goodwin, G.H., Neiman, P.E., and Lobanenko, V.V. (1993). CTCF, a conserved nuclear factor required for optimal transcriptional activity of the chicken c-myc gene, is an 11-Zn-finger protein differentially expressed in multiple forms. *Mol. Cell. Biol.* 13, 7612–7624. <https://doi.org/10.1128/mcb.13.12.7612-7624.1993>.
- Kojic, A., Cuadrado, A., De Koninck, M., Giménez-Llorente, D., Rodríguez-Corsino, M., Gómez-López, G., Le Dily, F., Marti-Renom, M.A., and Losada, A. (2018). Distinct roles of cohesin-SA1 and cohesin-SA2 in 3D chromosome organization. *Nat. Struct. Mol. Biol.* 25, 496–504. <https://doi.org/10.1038/s41594-018-0070-4>.
- Kong, X., Ball, A.R., Pham, H.X., Zeng, W., Chen, H.-Y., Schmiesing, J.A., Kim, J.-S., Berns, M., and Yokomori, K. (2014). Distinct functions of human cohesin-SA1 and cohesin-SA2 in double-strand break repair. *Mol. Cell. Biol.* 34, 685–698. <https://doi.org/10.1128/MCB.01503-13>.
- Krantz, I.D., McCallum, J., DeScipio, C., Kaur, M., Gillis, L.A., Yaeger, D., Jukofsky, L., Wasserman, N., Bottani, A., Morris, C.A., *et al.* (2004). Cornelia de Lange syndrome is caused by mutations in NIPBL, the human homolog of *Drosophila melanogaster* Nipped-B. *Nat. Genet.* 36, 631–635. <https://doi.org/10.1038/ng1364>.
- Krietenstein, N., Abraham, S., Venev, S.V., Abdennur, N., Gibcus, J., Hsieh, T.-H.S., Parsi, K.M., Yang, L., Maehr, R., Mirny, L.A., *et al.* (2020). Ultrastructural details of mammalian chromosome architecture. *Mol. Cell* 78, 554–565.e7. <https://doi.org/10.1016/j.molcel.2020.03.003>.
- Kriz, A.J., Colognori, D., Sunwoo, H., Nabet, B., and Lee, J.T. (2021). Balancing cohesin eviction and retention prevents aberrant chromosomal interactions, Polycomb-mediated repression, and X-inactivation. *Mol. Cell* 81, 1970–1987.e9. <https://doi.org/10.1016/j.molcel.2021.02.031>.
- Kschonsak, M., Merkel, F., Bisht, S., Metz, J., Rybin, V., Hassler, M., and Haering, C.H. (2017). Structural Basis for a Safety-Belt Mechanism That Anchors Condensin to Chromosomes. *Cell* 171, 588–600.e24. <https://doi.org/10.1016/j.cell.2017.09.008>.
- Kueng, S., Hegemann, B., Peters, B.H., Lipp, J.J., Schleiffer, A., Mechtler, K., and Peters, J.-M. (2006). Wapl controls the dynamic association of cohesin with chromatin. *Cell* 127, 955–967. <https://doi.org/10.1016/j.cell.2006.09.040>.
- Kulemzina, I., Schumacher, M.R., Verma, V., Reiter, J., Metzler, J., Failla, A.V., Lanz, C., Sreedharan, V.T., Rättsch, G., and Ivanov, D. (2012). Cohesin rings devoid of Scc3 and Pds5 maintain their stable association with the DNA. *PLoS Genet.* 8, e1002856. <https://doi.org/10.1371/journal.pgen.1002856>.
- Kurlandzka, A., Rytka, J., Gromadka, R., and Murawski, M. (1995). A new essential gene located on *Saccharomyces cerevisiae* chromosome IX. *Yeast* 11, 885–890. <https://doi.org/10.1002/yea.320110910>.

- Kurlandzka, A., Rytka, J., Rózska, B., and Wysocka, M. (1999). *Saccharomyces cerevisiae* IRR1 protein is indirectly involved in colony formation. *Yeast* 15, 23–33. [https://doi.org/10.1002/\(SICI\)1097-0061\(19990115\)15:1<23::AID-YEA337>3.0.CO;2-E](https://doi.org/10.1002/(SICI)1097-0061(19990115)15:1<23::AID-YEA337>3.0.CO;2-E).
- Kurze, A., Michie, K.A., Dixon, S.E., Mishra, A., Itoh, T., Khalid, S., Strmecki, L., Shirahige, K., Haering, C.H., Löwe, J., *et al.* (2011). A positively charged channel within the Smc1/Smc3 hinge required for sister chromatid cohesion. *EMBO J.* 30, 364–378. <https://doi.org/10.1038/emboj.2010.315>.
- Ladurner, R., Kreidl, E., Ivanov, M.P., Ekker, H., Idarraga-Amado, M.H., Busslinger, G.A., Wutz, G., Cisneros, D.A., and Peters, J.-M. (2016). Sororin actively maintains sister chromatid cohesion. *EMBO J.* 35, 635–653. <https://doi.org/10.15252/embj.201592532>.
- Lahn, B.T., and Page, D.C. (1999). Four evolutionary strata on the human X chromosome. *Science* 286, 964–967. <https://doi.org/10.1126/science.286.5441.964>.
- Lammens, A., Schele, A., and Hopfner, K.-P. (2004). Structural biochemistry of ATP-driven dimerization and DNA-stimulated activation of SMC ATPases. *Curr. Biol.* 14, 1778–1782. <https://doi.org/10.1016/j.cub.2004.09.044>.
- Larmuseau, M.H.D., and Ottoni, C. (2018). Mediterranean Y-chromosome 2.0-why the Y in the Mediterranean is still relevant in the postgenomic era. *Ann. Hum. Biol.* 45, 20–33. <https://doi.org/10.1080/03014460.2017.1402956>.
- Lau, Y.F., and Arrighi, F.E. (1981). Studies of mammalian chromosome replication. II. Evidence for the existence of defined chromosome replicating units. *Chromosoma* 83, 721–741. <https://doi.org/10.1007/BF00328530>.
- Lawrence, M.S., Stojanov, P., Mermel, C.H., Robinson, J.T., Garraway, L.A., Golub, T.R., Meyerson, M., Gabriel, S.B., Lander, E.S., and Getz, G. (2014). Discovery and saturation analysis of cancer genes across 21 tumour types. *Nature* 505, 495–501. <https://doi.org/10.1038/nature12912>.
- Leatherbarrow, E.L., Harper, J.V., Cucinotta, F.A., and O'Neill, P. (2006). Induction and quantification of gamma-H2AX foci following low and high LET-irradiation. *Int. J. Radiat. Biol.* 82, 111–118. <https://doi.org/10.1080/09553000600599783>.
- Lees-Miller, S.P., Sakaguchi, K., Ullrich, S.J., Appella, E., and Anderson, C.W. (1992). Human DNA-activated protein kinase phosphorylates serines 15 and 37 in the amino-terminal transactivation domain of human p53. *Mol. Cell. Biol.* 12, 5041–5049. <https://doi.org/10.1128/mcb.12.11.5041-5049.1992>.
- Lee, J.-H., and Paull, T.T. (2005). ATM activation by DNA double-strand breaks through the Mre11-Rad50-Nbs1 complex. *Science* 308, 551–554. <https://doi.org/10.1126/science.1108297>.
- Lee, J.T., and Lu, N. (1999). Targeted mutagenesis of Tsix leads to nonrandom X inactivation. *Cell* 99, 47–57. [https://doi.org/10.1016/s0092-8674\(00\)80061-6](https://doi.org/10.1016/s0092-8674(00)80061-6).
- Lee, B.-G., Roig, M.B., Jansma, M., Petela, N., Metson, J., Nasmyth, K., and Löwe, J. (2016). Crystal Structure of the Cohesin Gatekeeper Pds5 and in Complex with Kleisin Scc1. *Cell Rep.* 14, 2108–2115. <https://doi.org/10.1016/j.celrep.2016.02.020>.
- Lee, B.-G., Rhodes, J., and Löwe, J. (2022). Clamping of DNA shuts the condensin neck gate. *Proc Natl Acad Sci USA* 119, e2120006119. <https://doi.org/10.1073/pnas.2120006119>.
- Lee, J.T., Davidow, L.S., and Warshawsky, D. (1999). Tsix, a gene antisense to Xist at the X-inactivation centre. *Nat. Genet.* 21, 400–404. <https://doi.org/10.1038/7734>.
- Lemaitre, J.-M., Danis, E., Pasero, P., Vassetzky, Y., and Méchali, M. (2005). Mitotic remodeling of the replicon and chromosome structure. *Cell* 123, 787–801. <https://doi.org/10.1016/j.cell.2005.08.045>.
- Leonard, A.C., and Méchali, M. (2013). DNA replication origins. *Cold Spring Harb. Perspect. Biol.* 5, a010116. <https://doi.org/10.1101/cshperspect.a010116>.
- Leung, G.P., Brown, J.A.R., Glover, J.N.M., and Kobor, M.S. (2016). Rtt107 BRCT domains act as a targeting module in the DNA damage response. *DNA Repair (Amst)* 37, 22–32. <https://doi.org/10.1016/j.dnarep.2015.10.007>.
- Lieberman-Aiden, E., van Berkum, N.L., Williams, L., Imakaev, M., Ragoczy, T., Telling, A., Amit, I., Lajoie, B.R.,

- Sabo, P.J., Dorschner, M.O., *et al.* (2009). Comprehensive mapping of long-range interactions reveals folding principles of the human genome. *Science* 326, 289–293. <https://doi.org/10.1126/science.1181369>.
- Lin, T., Chao, C., Saito, S., Mazur, S.J., Murphy, M.E., Appella, E., and Xu, Y. (2005). p53 induces differentiation of mouse embryonic stem cells by suppressing Nanog expression. *Nat. Cell Biol.* 7, 165–171. <https://doi.org/10.1038/ncb1211>.
- Litwin, I., Pilarczyk, E., and Wysocki, R. (2018). The emerging role of cohesin in the DNA damage response. *Genes (Basel)* 9. <https://doi.org/10.3390/genes9120581>.
- Liu, Y., and Dekker, J. (2021). Biochemically distinct cohesin complexes mediate positioned loops between CTCF sites and dynamic loops within chromatin domains. *BioRxiv* <https://doi.org/10.1101/2021.08.24.457555>.
- Liu, J., Zhang, Z., Bando, M., Itoh, T., Deardorff, M.A., Clark, D., Kaur, M., Tandy, S., Kondoh, T., Rappaport, E., *et al.* (2009). Transcriptional dysregulation in NIPBL and cohesin mutant human cells. *PLoS Biol.* 7, e1000119. <https://doi.org/10.1371/journal.pbio.1000119>.
- Liu, N.Q., Maresca, M., van den Brand, T., Braccioli, L., Schijns, M.M.G.A., Teunissen, H., Bruneau, B.G., Nora, E.P., and de Wit, E. (2021). WAPL maintains a cohesin loading cycle to preserve cell-type-specific distal gene regulation. *Nat. Genet.* 53, 100–109. <https://doi.org/10.1038/s41588-020-00744-4>.
- Li, E., Bestor, T.H., and Jaenisch, R. (1992). Targeted mutation of the DNA methyltransferase gene results in embryonic lethality. *Cell* 69, 915–926. [https://doi.org/10.1016/0092-8674\(92\)90611-f](https://doi.org/10.1016/0092-8674(92)90611-f).
- Li, S., Yue, Z., and Tanaka, T.U. (2017). Smc3 Deacetylation by Hos1 Facilitates Efficient Dissolution of Sister Chromatid Cohesion during Early Anaphase. *Mol. Cell* 68, 605–614.e4. <https://doi.org/10.1016/j.molcel.2017.10.009>.
- Li, Y., Muir, K.W., Bowler, M.W., Metz, J., Haering, C.H., and Panne, D. (2018). Structural basis for Scc3-dependent cohesin recruitment to chromatin. *ELife* 7. <https://doi.org/10.7554/eLife.38356>.
- Li, Y., Haarhuis, J.H.I., Sedeño Cacciatore, Á., Oldenkamp, R., van Ruiten, M.S., Willems, L., Teunissen, H., Muir, K.W., de Wit, E., Rowland, B.D., *et al.* (2020). The structural basis for cohesin-CTCF-anchored loops. *Nature* 578, 472–476. <https://doi.org/10.1038/s41586-019-1910-z>.
- Löb, D., Lengert, N., Chagin, V.O., Reinhart, M., Casas-Delucchi, C.S., Cardoso, M.C., and Drossel, B. (2016). 3D replicon distributions arise from stochastic initiation and domino-like DNA replication progression. *Nat. Commun.* 7, 11207. <https://doi.org/10.1038/ncomms11207>.
- Lobanenkov, V.V., Nicolas, R.H., Adler, V.V., Paterson, H., Klenova, E.M., Polotskaja, A.V., and Goodwin, G.H. (1990). A novel sequence-specific DNA binding protein which interacts with three regularly spaced direct repeats of the CCCTC-motif in the 5'-flanking sequence of the chicken c-myc gene. *Oncogene* 5, 1743–1753.
- Lopez-Serra, L., Lengronne, A., Borges, V., Kelly, G., and Uhlmann, F. (2013). Budding yeast Wapl controls sister chromatid cohesion maintenance and chromosome condensation. *Curr. Biol.* 23, 64–69. <https://doi.org/10.1016/j.cub.2012.11.030>.
- Lopez-Serra, L., Kelly, G., Patel, H., Stewart, A., and Uhlmann, F. (2014). The Scc2-Scc4 complex acts in sister chromatid cohesion and transcriptional regulation by maintaining nucleosome-free regions. *Nat. Genet.* 46, 1147–1151. <https://doi.org/10.1038/ng.3080>.
- Losada, A. (2008). The regulation of sister chromatid cohesion. *Biochim. Biophys. Acta* 1786, 41–48. <https://doi.org/10.1016/j.bbcan.2008.04.003>.
- Losada, A. (2014). Cohesin in cancer: chromosome segregation and beyond. *Nat. Rev. Cancer* 14, 389–393. <https://doi.org/10.1038/nrc3743>.
- Losada, A., and Hirano, T. (2000). Biology in pictures. New light on sticky sisters. *Curr. Biol.* 10, R615. [https://doi.org/10.1016/s0960-9822\(00\)00670-9](https://doi.org/10.1016/s0960-9822(00)00670-9).
- Losada, A., Hirano, M., and Hirano, T. (1998). Identification of Xenopus SMC protein complexes required for sister chromatid cohesion. *Genes Dev.* 12, 1986–1997. <https://doi.org/10.1101/gad.12.13.1986>.
- Losada, A., Hirano, M., and Hirano, T. (2002). Cohesin release is required for sister chromatid resolution, but

not for condensin-mediated compaction, at the onset of mitosis. *Genes Dev.* *16*, 3004–3016. <https://doi.org/10.1101/gad.249202>.

Löwe, J., Cordell, S.C., and van den Ent, F. (2001). Crystal structure of the SMC head domain: an ABC ATPase with 900 residues antiparallel coiled-coil inserted. *J. Mol. Biol.* *306*, 25–35. <https://doi.org/10.1006/jmbi.2000.4379>.

Lu, J., Li, F., Murphy, C.S., Davidson, M.W., and Gilbert, D.M. (2010). G2 phase chromatin lacks determinants of replication timing. *J. Cell Biol.* *189*, 967–980. <https://doi.org/10.1083/jcb.201002002>.

Lyon, M.F. (1961). Gene action in the X-chromosome of the mouse (*Mus musculus* L.). *Nature* *190*, 372–373. <https://doi.org/10.1038/190372a0>.

MacPhail, S.H., Banáth, J.P., Yu, T.Y., Chu, E.H.M., Lambur, H., and Olive, P.L. (2003). Expression of phosphorylated histone H2AX in cultured cell lines following exposure to X-rays. *Int. J. Radiat. Biol.* *79*, 351–358.

Mak, W., Nesterova, T.B., de Napoles, M., Appanah, R., Yamanaka, S., Otte, A.P., and Brockdorff, N. (2004). Reactivation of the paternal X chromosome in early mouse embryos. *Science* *303*, 666–669. <https://doi.org/10.1126/science.1092674>.

Mamberti, S., and Cardoso, M.C. (2020). Are the processes of DNA replication and DNA repair reading a common structural chromatin unit? *Nucleus* *11*, 66–82. <https://doi.org/10.1080/19491034.2020.1744415>.

Mamberti, S., Pabba, M.K., Rapp, A., Cardoso, M.C., and Scholz, M. (2022). The Chromatin Architectural Protein CTCF Is Critical for Cell Survival upon Irradiation-Induced DNA Damage. *Int. J. Mol. Sci.* *23*. <https://doi.org/10.3390/ijms23073896>.

Manders, E.M., Stap, J., Brakenhoff, G.J., van Driel, R., and Aten, J.A. (1992). Dynamics of three-dimensional replication patterns during the S-phase, analysed by double labelling of DNA and confocal microscopy. *J. Cell Sci.* *103* (Pt 3), 857–862. <https://doi.org/10.1242/jcs.103.3.857>.

Manic, G., Corradi, F., Sistigu, A., Siteni, S., and Vitale, I. (2017). Molecular regulation of the spindle assembly checkpoint by kinases and phosphatases. *Int. Rev. Cell Mol. Biol.* *328*, 105–161. <https://doi.org/10.1016/bs.ircmb.2016.08.004>.

Mannini, L., Menga, S., Tonelli, A., Zanotti, S., Bassi, M.T., Magnani, C., and Musio, A. (2012). SMC1A codon 496 mutations affect the cellular response to genotoxic treatments. *Am. J. Med. Genet. A* *158A*, 224–228. <https://doi.org/10.1002/ajmg.a.34384>.

Mantiero, D., Mackenzie, A., Donaldson, A., and Zegerman, P. (2011). Limiting replication initiation factors execute the temporal programme of origin firing in budding yeast. *EMBO J.* *30*, 4805–4814. <https://doi.org/10.1038/emboj.2011.404>.

Marahrens, Y., Panning, B., Dausman, J., Strauss, W., and Jaenisch, R. (1997). Xist-deficient mice are defective in dosage compensation but not spermatogenesis. *Genes Dev.* *11*, 156–166. <https://doi.org/10.1101/gad.11.2.156>.

Marcos-Alcalde, Í., Mendieta-Moreno, J.I., Puisac, B., Gil-Rodríguez, M.C., Hernández-Marcos, M., Soler-Polo, D., Ramos, F.J., Ortega, J., Pié, J., Mendieta, J., *et al.* (2017). Two-step ATP-driven opening of cohesin head. *Sci. Rep.* *7*, 3266. <https://doi.org/10.1038/s41598-017-03118-9>.

Marks, H., Kalkan, T., Menafra, R., Denissov, S., Jones, K., Hofemeister, H., Nichols, J., Kranz, A., Stewart, A.F., Smith, A., *et al.* (2012). The transcriptional and epigenomic foundations of ground state pluripotency. *Cell* *149*, 590–604. <https://doi.org/10.1016/j.cell.2012.03.026>.

Marks, H., Kerstens, H.H.D., Barakat, T.S., Splinter, E., Dirks, R.A.M., van Mierlo, G., Joshi, O., Wang, S.-Y., Babak, T., Albers, C.A., *et al.* (2015). Dynamics of gene silencing during X inactivation using allele-specific RNA-seq. *Genome Biol.* *16*, 149. <https://doi.org/10.1186/s13059-015-0698-x>.

Marsman, J., O'Neill, A.C., Kao, B.R.-Y., Rhodes, J.M., Meier, M., Antony, J., Mönnich, M., and Horsfield, J.A. (2014). Cohesin and CTCF differentially regulate spatiotemporal runx1 expression during zebrafish development. *Biochim. Biophys. Acta* *1839*, 50–61. <https://doi.org/10.1016/j.bbagr.2013.11.007>.

- Marston, A.L., Tham, W.-H., Shah, H., and Amon, A. (2004). A genome-wide screen identifies genes required for centromeric cohesion. *Science* 303, 1367–1370. <https://doi.org/10.1126/science.1094220>.
- Marti-Renom, M.A., Almouzni, G., Bickmore, W.A., Bystricky, K., Cavalli, G., Fraser, P., Gasser, S.M., Giorgetti, L., Heard, E., Nicodemi, M., *et al.* (2018). Challenges and guidelines toward 4D nucleome data and model standards. *Nat. Genet.* 50, 1352–1358. <https://doi.org/10.1038/s41588-018-0236-3>.
- Martin, M.M., Ryan, M., Kim, R., Zakas, A.L., Fu, H., Lin, C.M., Reinhold, W.C., Davis, S.R., Bilke, S., Liu, H., *et al.* (2011). Genome-wide depletion of replication initiation events in highly transcribed regions. *Genome Res.* 21, 1822–1832. <https://doi.org/10.1101/gr.124644.111>.
- Masai, H., Matsumoto, S., You, Z., Yoshizawa-Sugata, N., and Oda, M. (2010). Eukaryotic chromosome DNA replication: where, when, and how? *Annu. Rev. Biochem.* 79, 89–130. <https://doi.org/10.1146/annurev.biochem.052308.103205>.
- Mateos-Langerak, J., Bohn, M., de Leeuw, W., Giromus, O., Manders, E.M.M., Verschure, P.J., Indemans, M.H.G., Gierman, H.J., Heermann, D.W., van Driel, R., *et al.* (2009). Spatially confined folding of chromatin in the interphase nucleus. *Proc Natl Acad Sci USA* 106, 3812–3817. <https://doi.org/10.1073/pnas.0809501106>.
- Maya-Mendoza, A., Olivares-Chauvet, P., Shaw, A., and Jackson, D.A. (2010). S phase progression in human cells is dictated by the genetic continuity of DNA foci. *PLoS Genet.* 6, e1000900. <https://doi.org/10.1371/journal.pgen.1000900>.
- Ma, H., Samarabandu, J., Devdhar, R.S., Acharya, R., Cheng, P.C., Meng, C., and Berezney, R. (1998). Spatial and temporal dynamics of DNA replication sites in mammalian cells. *J. Cell Biol.* 143, 1415–1425. <https://doi.org/10.1083/jcb.143.6.1415>.
- McAleenan, A., Cordon-Preciado, V., Clemente-Blanco, A., Liu, I.-C., Sen, N., Leonard, J., Jarmuz, A., and Aragón, L. (2012). SUMOylation of the α -kleisin subunit of cohesin is required for DNA damage-induced cohesion. *Curr. Biol.* 22, 1564–1575. <https://doi.org/10.1016/j.cub.2012.06.045>.
- McGrew, J.T., Goetsch, L., Byers, B., and Baum, P. (1992). Requirement for ESP1 in the nuclear division of *Saccharomyces cerevisiae*. *Mol. Biol. Cell* 3, 1443–1454. <https://doi.org/10.1091/mbc.3.12.1443>.
- McKay, M.J., Troelstra, C., van der Spek, P., Kanaar, R., Smit, B., Hagemeyer, A., Bootsma, D., and Hoeijmakers, J.H. (1996). Sequence conservation of the rad21 *Schizosaccharomyces pombe* DNA double-strand break repair gene in human and mouse. *Genomics* 36, 305–315. <https://doi.org/10.1006/geno.1996.0466>.
- McIntyre, J., Muller, E.G.D., Weitzer, S., Snydsman, B.E., Davis, T.N., and Uhlmann, F. (2007). *In vivo* analysis of cohesin architecture using FRET in the budding yeast *Saccharomyces cerevisiae*. *EMBO J.* 26, 3783–3793. <https://doi.org/10.1038/sj.emboj.7601793>.
- Méchal, M. (2010). Eukaryotic DNA replication origins: many choices for appropriate answers. *Nat. Rev. Mol. Cell Biol.* 11, 728–738. <https://doi.org/10.1038/nrm2976>.
- Meisenberg, C., Pinder, S.I., Hopkins, S.R., Wooller, S.K., Benstead-Hume, G., Pearl, F.M.G., Jeggo, P.A., and Downs, J.A. (2019). Repression of Transcription at DNA Breaks Requires Cohesin throughout Interphase and Prevents Genome Instability. *Mol. Cell* 73, 212–223.e7. <https://doi.org/10.1016/j.molcel.2018.11.001>.
- Melby, T.E., Ciampaglio, C.N., Briscoe, G., and Erickson, H.P. (1998). The symmetrical structure of structural maintenance of chromosomes (SMC) and MukB proteins: long, antiparallel coiled coils, folded at a flexible hinge. *J. Cell Biol.* 142, 1595–1604. <https://doi.org/10.1083/jcb.142.6.1595>.
- Menolfi, D., and Zha, S. (2020). ATM, ATR and DNA-PKcs kinases—the lessons from the mouse models: inhibition \neq deletion. *Cell Biosci.* 10, 8. <https://doi.org/10.1186/s13578-020-0376-x>.
- Merkenschlager, M., and Nora, E.P. (2016). CTCF and cohesin in genome folding and transcriptional gene regulation. *Annu. Rev. Genomics Hum. Genet.* 17, 17–43. <https://doi.org/10.1146/annurev-genom-083115-022339>.
- Michaelis, C., Ciosk, R., and Nasmyth, K. (1997). Cohesins: chromosomal proteins that prevent premature separation of sister chromatids. *Cell* 91, 35–45. [https://doi.org/10.1016/s0092-8674\(01\)80007-6](https://doi.org/10.1016/s0092-8674(01)80007-6).
- Mimori, T., Akizuki, M., Yamagata, H., Inada, S., Yoshida, S., and Homma, M. (1981). Characterization of a high

molecular weight acidic nuclear protein recognized by autoantibodies in sera from patients with polymyositis-scleroderma overlap. *J. Clin. Invest.* 68, 611–620. <https://doi.org/10.1172/JCI110295>.

Minajigi, A., Froberg, J., Wei, C., Sunwoo, H., Kesner, B., Colognori, D., Lessing, D., Payer, B., Boukhali, M., Haas, W., *et al.* (2015). Chromosomes. A comprehensive Xist interactome reveals cohesin repulsion and an RNA-directed chromosome conformation. *Science* 349. <https://doi.org/10.1126/science.aab2276>.

Mirny, L.A., Imakaev, M., and Abdennur, N. (2019). Two major mechanisms of chromosome organization. *Curr. Opin. Cell Biol.* 58, 142–152. <https://doi.org/10.1016/j.ceb.2019.05.001>.

Miron, E., Innocent, C., Heyde, S., and Schermelleh, L. (2016). *In Vivo* and *In Situ* Replication Labeling Methods for Super-resolution Structured Illumination Microscopy of Chromosome Territories and Chromatin Domains. *Methods Mol. Biol.* 1431, 127–140. https://doi.org/10.1007/978-1-4939-3631-1_10.

Mirzayans, R., Severin, D., and Murray, D. (2006). Relationship between DNA double-strand break rejoining and cell survival after exposure to ionizing radiation in human fibroblast strains with differing ATM/p53 status: implications for evaluation of clinical radiosensitivity. *Int. J. Radiat. Oncol. Biol. Phys.* 66, 1498–1505. <https://doi.org/10.1016/j.ijrobp.2006.08.064>.

Mise, N., Goto, Y., Nakajima, N., and Takagi, N. (1999). Molecular cloning of antisense transcripts of the mouse Xist gene. *Biochem. Biophys. Res. Commun.* 258, 537–541. <https://doi.org/10.1006/bbrc.1999.0681>.

Mishra, A., Hu, B., Kurze, A., Beckouët, F., Farcas, A.-M., Dixon, S.E., Katou, Y., Khalid, S., Shirahige, K., and Nasmyth, K. (2010). Both interaction surfaces within cohesin's hinge domain are essential for its stable chromosomal association. *Curr. Biol.* 20, 279–289. <https://doi.org/10.1016/j.cub.2009.12.059>.

Miyawaki, S., Kuroki, S., Maeda, R., Okashita, N., Koopman, P., and Tachibana, M. (2020). The mouse Sry locus harbors a cryptic exon that is essential for male sex determination. *Science* 370, 121–124. <https://doi.org/10.1126/science.abb6430>.

Moore, J.M., Rabaia, N.A., Smith, L.E., Fagerlie, S., Gurley, K., Loukinov, D., Distèche, C.M., Collins, S.J., Kemp, C.J., Lobanenkov, V.V., *et al.* (2012). Loss of maternal CTCF is associated with peri-implantation lethality of Ctf null embryos. *PLoS ONE* 7, e34915. <https://doi.org/10.1371/journal.pone.0034915>.

Morales, C., and Losada, A. (2018). Establishing and dissolving cohesion during the vertebrate cell cycle. *Curr. Opin. Cell Biol.* 52, 51–57. <https://doi.org/10.1016/j.ceb.2018.01.010>.

Morishima, A., Grumbach, M.M., and Taylor, J.H. (1962). Asynchronous duplication of human chromosomes and the origin of sex chromatin. *Proc Natl Acad Sci USA* 48, 756–763. <https://doi.org/10.1073/pnas.48.5.756>.

Münkel, C., and Langowski, J. (1998). Chromosome structure predicted by a polymer model. *Phys. Rev. E* 57, 5888–5896. <https://doi.org/10.1103/PhysRevE.57.5888>.

Münkel, C., Eils, R., Dietzel, S., Zink, D., Mehring, C., Wedemann, G., Cremer, T., and Langowski, J. (1999). Compartmentalization of interphase chromosomes observed in simulation and experiment. *J. Mol. Biol.* 285, 1053–1065. <https://doi.org/10.1006/jmbi.1998.2361>.

Muñoz, S., Minamino, M., Casas-Delucchi, C.S., Patel, H., and Uhlmann, F. (2019). A Role for Chromatin Remodeling in Cohesin Loading onto Chromosomes. *Mol. Cell* 74, 664–673.e5. <https://doi.org/10.1016/j.molcel.2019.02.027>.

Muñoz, S., Passarelli, F., and Uhlmann, F. (2020). Conserved roles of chromatin remodellers in cohesin loading onto chromatin. *Curr. Genet.* 66, 951–956. <https://doi.org/10.1007/s00294-020-01075-x>.

Murayama, Y., and Uhlmann, F. (2014). Biochemical reconstitution of topological DNA binding by the cohesin ring. *Nature* 505, 367–371. <https://doi.org/10.1038/nature12867>.

Nagase, T., Seki, N., Ishikawa, K., Tanaka, A., and Nomura, N. (1996). Prediction of the coding sequences of unidentified human genes. V. The coding sequences of 40 new genes (KIAA0161-KIAA0200) deduced by analysis of cDNA clones from human cell line KG-1. *DNA Res.* 3, 17–24. <https://doi.org/10.1093/dnares/3.1.17>.

Nakamura, H., Morita, T., and Sato, C. (1986). Structural organizations of replicon domains during DNA synthetic phase in the mammalian nucleus. *Exp. Cell Res.* 165, 291–297. [https://doi.org/10.1016/0014-4827\(86\)90583-5](https://doi.org/10.1016/0014-4827(86)90583-5).

- Nakayasu, H., and Berezney, R. (1989). Mapping replicational sites in the eucaryotic cell nucleus. *J. Cell Biol.* *108*, 1–11. <https://doi.org/10.1083/jcb.108.1.1>.
- Nasmyth, K. (2011). Cohesin: a catenase with separate entry and exit gates? *Nat. Cell Biol.* *13*, 1170–1177. <https://doi.org/10.1038/ncb2349>.
- Nasmyth, K., and Haering, C.H. (2009). Cohesin: its roles and mechanisms. *Annu. Rev. Genet.* *43*, 525–558. <https://doi.org/10.1146/annurev-genet-102108-134233>.
- Nasmyth, K., and Schleiffer, A. (2004). From a single double helix to paired double helices and back. *Philos. Trans. R. Soc. Lond. B Biol. Sci.* *359*, 99–108. <https://doi.org/10.1098/rstb.2003.1417>.
- Natale, F., Rapp, A., Yu, W., Maiser, A., Harz, H., Scholl, A., Grulich, S., Anton, T., Hörl, D., Chen, W., *et al.* (2017). Identification of the elementary structural units of the DNA damage response. *Nat. Commun.* *8*, 15760. <https://doi.org/10.1038/ncomms15760>.
- Nativio, R., Wendt, K.S., Ito, Y., Huddleston, J.E., Uribe-Lewis, S., Woodfine, K., Krueger, C., Reik, W., Peters, J.-M., and Murrell, A. (2009). Cohesin is required for higher-order chromatin conformation at the imprinted IGF2-H19 locus. *PLoS Genet.* *5*, e1000739. <https://doi.org/10.1371/journal.pgen.1000739>.
- Natsume, T., Kiyomitsu, T., Saga, Y., and Kanemaki, M.T. (2016). Rapid Protein Depletion in Human Cells by Auxin-Inducible Degron Tagging with Short Homology Donors. *Cell Rep.* *15*, 210–218. <https://doi.org/10.1016/j.celrep.2016.03.001>.
- Nguyen, D.K., and Disteche, C.M. (2006). Dosage compensation of the active X chromosome in mammals. *Nat. Genet.* *38*, 47–53. <https://doi.org/10.1038/ng1705>.
- Nichols, M.H., and Corces, V.G. (2018). A tethered-inchworm model of SMC DNA translocation. *Nat. Struct. Mol. Biol.* *25*, 906–910. <https://doi.org/10.1038/s41594-018-0135-4>.
- Nicklas, R.B. (1967). Chromosome micromanipulation. II. Induced reorientation and the experimental control of segregation in meiosis. *Chromosoma* *21*, 17–50. <https://doi.org/10.1007/BF00330545>.
- Nicklas, R.B. (1997). How cells get the right chromosomes. *Science* *275*, 632–637. <https://doi.org/10.1126/science.275.5300.632>.
- Nicodemi, M., and Pombo, A. (2014). Models of chromosome structure. *Curr. Opin. Cell Biol.* *28*, 90–95. <https://doi.org/10.1016/j.ceb.2014.04.004>.
- Nijkoo, H., O'Neill, P., Wilson, W.E., and Goodhead, D.T. (2001). Computational approach for determining the spectrum of DNA damage induced by ionizing radiation. *Radiat. Res.* *156*, 577–583. [https://doi.org/10.1667/0033-7587\(2001\)156\[0577:cafdfs\]2.0.co;2](https://doi.org/10.1667/0033-7587(2001)156[0577:cafdfs]2.0.co;2).
- Nishimura, K., Fukagawa, T., Takisawa, H., Kakimoto, T., and Kanemaki, M. (2009). An auxin-based degron system for the rapid depletion of proteins in nonplant cells. *Nat. Methods* *6*, 917–922. <https://doi.org/10.1038/nmeth.1401>.
- Nishino, Y., Eltsov, M., Joti, Y., Ito, K., Takata, H., Takahashi, Y., Hihara, S., Frangakis, A.S., Imamoto, N., Ishikawa, T., *et al.* (2012). Human mitotic chromosomes consist predominantly of irregularly folded nucleosome fibres without a 30-nm chromatin structure. *EMBO J.* *31*, 1644–1653. <https://doi.org/10.1038/emboj.2012.35>.
- Nishiyama, T., Ladurner, R., Schmitz, J., Kreidl, E., Schleiffer, A., Bhaskara, V., Bando, M., Shirahige, K., Hyman, A.A., Mechtler, K., *et al.* (2010). Sororin mediates sister chromatid cohesion by antagonizing Wapl. *Cell* *143*, 737–749. <https://doi.org/10.1016/j.cell.2010.10.031>.
- Nora, E.P., Lajoie, B.R., Schulz, E.G., Giorgetti, L., Okamoto, I., Servant, N., Piolot, T., van Berkum, N.L., Meisig, J., Sedat, J., *et al.* (2012). Spatial partitioning of the regulatory landscape of the X-inactivation centre. *Nature* *485*, 381–385. <https://doi.org/10.1038/nature11049>.
- Nora, E.P., Goloborodko, A., Valton, A.-L., Gibcus, J.H., Uebersohn, A., Abdennur, N., Dekker, J., Mirny, L.A., and Bruneau, B.G. (2017). Targeted Degradation of CTCF Decouples Local Insulation of Chromosome Domains from Genomic Compartmentalization. *Cell* *169*, 930–944.e22. <https://doi.org/10.1016/j.cell.2017.05.004>.
- Nuebler, J., Fudenberg, G., Imakaev, M., Abdennur, N., and Mirny, L.A. (2018). Chromatin organization by an

interplay of loop extrusion and compartmental segregation. *Proc Natl Acad Sci USA* *115*, E6697–E6706. <https://doi.org/10.1073/pnas.1717730115>.

O’Keefe, R.T., Henderson, S.C., and Spector, D.L. (1992). Dynamic organization of DNA replication in mammalian cell nuclei: spatially and temporally defined replication of chromosome-specific alpha-satellite DNA sequences. *J. Cell Biol.* *116*, 1095–1110. <https://doi.org/10.1083/jcb.116.5.1095>.

Ogawa, Y., and Lee, J.T. (2003). Xite, X-inactivation intergenic transcription elements that regulate the probability of choice. *Mol. Cell* *11*, 731–743. [https://doi.org/10.1016/s1097-2765\(03\)00063-7](https://doi.org/10.1016/s1097-2765(03)00063-7).

Ohno, S. (1967). *Sex Chromosomes and Sex-Linked Genes* (Berlin, Heidelberg: Springer Berlin Heidelberg) <https://doi.org/10.1007/978-3-642-88178-7>.

Oikawa, K., Ohbayashi, T., Kiyono, T., Nishi, H., Isaka, K., Umezawa, A., Kuroda, M., and Mukai, K. (2004). Expression of a novel human gene, human wings apart-like (hWAPL), is associated with cervical carcinogenesis and tumor progression. *Cancer Res.* *64*, 3545–3549. <https://doi.org/10.1158/0008-5472.CAN-03-3822>.

Okamoto, I., Otte, A.P., Allis, C.D., Reinberg, D., and Heard, E. (2004). Epigenetic dynamics of imprinted X inactivation during early mouse development. *Science* *303*, 644–649. <https://doi.org/10.1126/science.1092727>.

Oldenkamp, R., and Rowland, B.D. (2022). A walk through the SMC cycle: From catching DNAs to shaping the genome. *Mol. Cell* *82*, 1616–1630. <https://doi.org/10.1016/j.molcel.2022.04.006>.

Ottolenghi, A., Merzagora, M., Tallone, L., Durante, M., Paretzke, H.G., and Wilson, W.E. (1995). The quality of DNA double-strand breaks: a Monte Carlo simulation of the end-structure of strand breaks produced by protons and alpha particles. *Radiat. Environ. Biophys.* *34*, 239–244. <https://doi.org/10.1007/BF01209749>.

Otto, S.P., Pannell, J.R., Peichel, C.L., Ashman, T.-L., Charlesworth, D., Chippindale, A.K., Delph, L.F., Guerrero, R.F., Scarpino, S.V., and McAllister, B.F. (2011). About PAR: the distinct evolutionary dynamics of the pseudoautosomal region. *Trends Genet.* *27*, 358–367. <https://doi.org/10.1016/j.tig.2011.05.001>.

Ouyang, Z., Zheng, G., Tomchick, D.R., Luo, X., and Yu, H. (2016). Structural Basis and IP6 Requirement for Pds5-Dependent Cohesin Dynamics. *Mol. Cell* *62*, 248–259. <https://doi.org/10.1016/j.molcel.2016.02.033>.

Ou, H.D., Phan, S., Deerinck, T.J., Thor, A., Ellisman, M.H., and O’Shea, C.C. (2017). ChromEMT: Visualizing 3D chromatin structure and compaction in interphase and mitotic cells. *Science* *357*. <https://doi.org/10.1126/science.aag0025>.

Palecek, J.J., and Gruber, S. (2015). Kite proteins: a superfamily of smc/kleisin partners conserved across bacteria, archaea, and eukaryotes. *Structure* *23*, 2183–2190. <https://doi.org/10.1016/j.str.2015.10.004>.

Panizza, S., Tanaka, T., Hochwagen, A., Eisenhaber, F., and Nasmyth, K. (2000). Pds5 cooperates with cohesin in maintaining sister chromatid cohesion. *Curr. Biol.* *10*, 1557–1564. [https://doi.org/10.1016/s0960-9822\(00\)00854-x](https://doi.org/10.1016/s0960-9822(00)00854-x).

Parelho, V., Hadjur, S., Spivakov, M., Leleu, M., Sauer, S., Gregson, H.C., Jarmuz, A., Canzonetta, C., Webster, Z., Nesterova, T., *et al.* (2008). Cohesins functionally associate with CTCF on mammalian chromosome arms. *Cell* *132*, 422–433. <https://doi.org/10.1016/j.cell.2008.01.011>.

Parenti, I., Diab, F., Gil, S.R., Mulugeta, E., Casa, V., Berutti, R., Brouwer, R.W.W., Dupé, V., Eckhold, J., Graf, E., *et al.* (2020). MAU2 and NIPBL variants impair the heterodimerization of the cohesin loader subunits and cause cornelia de lange syndrome. *Cell Rep.* *31*, 107647. <https://doi.org/10.1016/j.celrep.2020.107647>.

Paull, T.T. (2015). Mechanisms of ATM activation. *Annu. Rev. Biochem.* *84*, 711–738. <https://doi.org/10.1146/annurev-biochem-060614-034335>.

Paull, T.T., Rogakou, E.P., Yamazaki, V., Kirchgessner, C.U., Gellert, M., and Bonner, W.M. (2000). A critical role for histone H2AX in recruitment of repair factors to nuclear foci after DNA damage. *Curr. Biol.* *10*, 886–895. [https://doi.org/10.1016/s0960-9822\(00\)00610-2](https://doi.org/10.1016/s0960-9822(00)00610-2).

Paulson, J.R., and Laemmli, U.K. (1977). The structure of histone-depleted metaphase chromosomes. *Cell* *12*, 817–828. [https://doi.org/10.1016/0092-8674\(77\)90280-x](https://doi.org/10.1016/0092-8674(77)90280-x).

- Payer, B., Lee, J.T., and Namekawa, S.H. (2011). X-inactivation and X-reactivation: epigenetic hallmarks of mammalian reproduction and pluripotent stem cells. *Hum. Genet.* *130*, 265–280. <https://doi.org/10.1007/s00439-011-1024-7>.
- Pękowska, A., Klaus, B., Xiang, W., Severino, J., Daigle, N., Klein, F.A., Oleś, M., Casellas, R., Ellenberg, J., Steinmetz, L.M., *et al.* (2018). Gain of CTCF-Anchored Chromatin Loops Marks the Exit from Naive Pluripotency. *Cell Syst.* *7*, 482–495.e10. <https://doi.org/10.1016/j.cels.2018.09.003>.
- Penny, G.D., Kay, G.F., Sheardown, S.A., Rastan, S., and Brockdorff, N. (1996). Requirement for Xist in X chromosome inactivation. *Nature* *379*, 131–137. <https://doi.org/10.1038/379131a0>.
- Peric-Hupkes, D., Meuleman, W., Pagie, L., Bruggeman, S.W.M., Solovei, I., Brugman, W., Gräf, S., Flicek, P., Kerkhoven, R.M., van Lohuizen, M., *et al.* (2010). Molecular maps of the reorganization of genome-nuclear lamina interactions during differentiation. *Mol. Cell* *38*, 603–613. <https://doi.org/10.1016/j.molcel.2010.03.016>.
- Petela, N.J., Gligoris, T.G., Metson, J., Lee, B.-G., Voulgaris, M., Hu, B., Kikuchi, S., Chapard, C., Chen, W., Rajendra, E., *et al.* (2018). Scc2 Is a Potent Activator of Cohesin's ATPase that Promotes Loading by Binding Scc1 without Pds5. *Mol. Cell* *70*, 1134–1148.e7. <https://doi.org/10.1016/j.molcel.2018.05.022>.
- Petela, N.J., Gonzalez Llamazares, A., Dixon, S., Hu, B., Lee, B.-G., Metson, J., Seo, H., Ferrer-Harding, A., Voulgaris, M., Gligoris, T., *et al.* (2021). Folding of cohesin's coiled coil is important for Scc2/4-induced association with chromosomes. *ELife* *10*. <https://doi.org/10.7554/eLife.67268>.
- Peters, J.-M., Tedeschi, A., and Schmitz, J. (2008). The cohesin complex and its roles in chromosome biology. *Genes Dev.* *22*, 3089–3114. <https://doi.org/10.1101/gad.1724308>.
- Phillips, J.E., and Corces, V.G. (2009). CTCF: master weaver of the genome. *Cell* *137*, 1194–1211. <https://doi.org/10.1016/j.cell.2009.06.001>.
- Phipps, J., and Dubrana, K. (2022). DNA Repair in Space and Time: Safeguarding the Genome with the Cohesin Complex. *Genes (Basel)* *13*. <https://doi.org/10.3390/genes13020198>.
- Piché, J., Van Vliet, P.P., Pucéat, M., and Andelfinger, G. (2019). The expanding phenotypes of cohesinopathies: one ring to rule them all! *Cell Cycle* *18*, 2828–2848. <https://doi.org/10.1080/15384101.2019.1658476>.
- Pidoux, A.L., Uzawa, S., Perry, P.E., Cande, W.Z., and Allshire, R.C. (2000). Live analysis of lagging chromosomes during anaphase and their effect on spindle elongation rate in fission yeast. *J. Cell Sci.* *113 Pt 23*, 4177–4191. <https://doi.org/10.1242/jcs.113.23.4177>.
- Pinkel, D., Landegent, J., Collins, C., Fuscoe, J., Segreaves, R., Lucas, J., and Gray, J. (1988). Fluorescence *in situ* hybridization with human chromosome-specific libraries: detection of trisomy 21 and translocations of chromosome 4. *Proc Natl Acad Sci USA* *85*, 9138–9142. <https://doi.org/10.1073/pnas.85.23.9138>.
- Pontén, J., and Saksela, E. (1967). Two established in vitro cell lines from human mesenchymal tumours. *Int. J. Cancer* *2*, 434–447.
- Pope, B.D., Ryba, T., Dileep, V., Yue, F., Wu, W., Denas, O., Vera, D.L., Wang, Y., Hansen, R.S., Canfield, T.K., *et al.* (2014). Topologically associating domains are stable units of replication-timing regulation. *Nature* *515*, 402–405. <https://doi.org/10.1038/nature13986>.
- Pradhan, B., Kanno, T., Igarashi, M.U., Baaske, M.D., Kei Wong, J.S., Jeppsson, K., Björkegren, C., and Kim, E. (2022). The Smc5/6 complex is a DNA loop extruding motor. *BioRxiv* <https://doi.org/10.1101/2022.05.13.491800>.
- Rabitsch, K.P., Gregan, J., Schleiffer, A., Javerzat, J.-P., Eisenhaber, F., and Nasmyth, K. (2004). Two fission yeast homologs of *Drosophila* Mei-S332 are required for chromosome segregation during meiosis I and II. *Curr. Biol.* *14*, 287–301. <https://doi.org/10.1016/j.cub.2004.01.051>.
- Rankin, S., Ayad, N.G., and Kirschner, M.W. (2005). Sororin, a substrate of the anaphase-promoting complex, is required for sister chromatid cohesion in vertebrates. *Mol. Cell* *18*, 185–200. <https://doi.org/10.1016/j.molcel.2005.03.017>.
- Rao, S.S.P., Huntley, M.H., Durand, N.C., Stamenova, E.K., Bochkov, I.D., Robinson, J.T., Sanborn, A.L., Machol, I.,

Omer, A.D., Lander, E.S., *et al.* (2014). A 3D map of the human genome at kilobase resolution reveals principles of chromatin looping. *Cell* *159*, 1665–1680. <https://doi.org/10.1016/j.cell.2014.11.021>.

Rao, S.S.P., Huang, S.-C., Glenn St Hilaire, B., Engreitz, J.M., Perez, E.M., Kieffer-Kwon, K.-R., Sanborn, A.L., Johnstone, S.E., Bascom, G.D., Bochkov, I.D., *et al.* (2017). Cohesin loss eliminates all loop domains. *Cell* *171*, 305–320.e24. <https://doi.org/10.1016/j.cell.2017.09.026>.

Rastan, S. (1983). Non-random X-chromosome inactivation in mouse X-autosome translocation embryos--location of the inactivation centre. *J. Embryol. Exp. Morphol.* *78*, 1–22.

Rastan, S., and Robertson, E.J. (1985). X-chromosome deletions in embryo-derived (EK) cell lines associated with lack of X-chromosome inactivation. *J. Embryol. Exp. Morphol.* *90*, 379–388.

Raudsepp, T., and Chowdhary, B.P. (2015). The eutherian pseudoautosomal region. *Cytogenet. Genome Res.* *147*, 81–94. <https://doi.org/10.1159/000443157>.

Rausch, C., Weber, P., Prorok, P., Hörl, D., Maiser, A., Lehmkuhl, A., Chagin, V.O., Casas-Delucchi, C.S., Leonhardt, H., and Cardoso, M.C. (2020). Developmental differences in genome replication program and origin activation. *Nucleic Acids Res.* *48*, 12751–12777. <https://doi.org/10.1093/nar/gkaa1124>.

Raznahan, A., and Disteché, C.M. (2021). X-chromosome regulation and sex differences in brain anatomy. *Neurosci. Biobehav. Rev.* *120*, 28–47. <https://doi.org/10.1016/j.neubiorev.2020.10.024>.

Redon, C., Pilch, D., Rogakou, E., Sedelnikova, O., Newrock, K., and Bonner, W. (2002). Histone H2A variants H2AX and H2AZ. *Curr. Opin. Genet. Dev.* *12*, 162–169. [https://doi.org/10.1016/S0959-437X\(02\)00282-4](https://doi.org/10.1016/S0959-437X(02)00282-4).

Remeseiro, S., Cuadrado, A., Carretero, M., Martínez, P., Drosopoulos, W.C., Cañamero, M., Schildkraut, C.L., Blasco, M.A., and Losada, A. (2012a). Cohesin-SA1 deficiency drives aneuploidy and tumorigenesis in mice due to impaired replication of telomeres. *EMBO J.* *31*, 2076–2089. <https://doi.org/10.1038/emboj.2012.11>.

Remeseiro, S., Cuadrado, A., Gómez-López, G., Pisano, D.G., and Losada, A. (2012b). A unique role of cohesin-SA1 in gene regulation and development. *EMBO J.* *31*, 2090–2102. <https://doi.org/10.1038/emboj.2012.60>.

Revenkova, E., Focarelli, M.L., Susani, L., Paulis, M., Bassi, M.T., Mannini, L., Frattini, A., Delia, D., Krantz, I., Vezzoni, P., *et al.* (2009). Cornelia de Lange syndrome mutations in SMC1A or SMC3 affect binding to DNA. *Hum. Mol. Genet.* *18*, 418–427. <https://doi.org/10.1093/hmg/ddn369>.

Rhind, N., and Gilbert, D.M. (2013). DNA replication timing. *Cold Spring Harb. Perspect. Biol.* *5*, a010132. <https://doi.org/10.1101/cshperspect.a010132>.

Rhodes, J.M., Bentley, F.K., Print, C.G., Dorsett, D., Misulovin, Z., Dickinson, E.J., Crosier, K.E., Crosier, P.S., and Horsfield, J.A. (2010). Positive regulation of c-Myc by cohesin is direct, and evolutionarily conserved. *Dev. Biol.* *344*, 637–649. <https://doi.org/10.1016/j.ydbio.2010.05.493>.

Rhodes, J., Mazza, D., Nasmyth, K., and Uphoff, S. (2017). Scc2/Nipbl hops between chromosomal cohesin rings after loading. *ELife* *6*. <https://doi.org/10.7554/eLife.30000>.

Ricci, M.A., Manzo, C., García-Parajo, M.F., Lakadamyali, M., and Cosma, M.P. (2015). Chromatin fibers are formed by heterogeneous groups of nucleosomes *in vivo*. *Cell* *160*, 1145–1158. <https://doi.org/10.1016/j.cell.2015.01.054>.

Rice, W.R. (1987a). The accumulation of sexually antagonistic genes as a selective agent promoting the evolution of reduced recombination between primitive sex chromosomes. *Evolution* *41*, 911–914. <https://doi.org/10.1111/j.1558-5646.1987.tb05864.x>.

Rice, W.R. (1987b). Genetic hitchhiking and the evolution of reduced genetic activity of the Y sex chromosome. *Genetics* *116*, 161–167. <https://doi.org/10.1093/genetics/116.1.161>.

Riedel, C.G., Katis, V.L., Katou, Y., Mori, S., Itoh, T., Helmhart, W., Gálová, M., Petronczki, M., Gregan, J., Cetin, B., *et al.* (2006). Protein phosphatase 2A protects centromeric sister chromatid cohesion during meiosis I. *Nature* *441*, 53–61. <https://doi.org/10.1038/nature04664>.

Rivera, T., and Losada, A. (2006). Shugoshin and PP2A, shared duties at the centromere. *Bioessays* *28*, 775–779. <https://doi.org/10.1002/bies.20448>.

- Rogakou, E.P., Pilch, D.R., Orr, A.H., Ivanova, V.S., and Bonner, W.M. (1998). DNA double-stranded breaks induce histone H2AX phosphorylation on serine 139. *J. Biol. Chem.* *273*, 5858–5868. <https://doi.org/10.1074/jbc.273.10.5858>.
- Rogakou, E.P., Boon, C., Redon, C., and Bonner, W.M. (1999). Megabase chromatin domains involved in DNA double-strand breaks *in vivo*. *J. Cell Biol.* *146*, 905–916. <https://doi.org/10.1083/jcb.146.5.905>.
- Roig, M.B., Löwe, J., Chan, K.-L., Beckouët, F., Metson, J., and Nasmyth, K. (2014). Structure and function of cohesin's Scc3/SA regulatory subunit. *FEBS Lett.* *588*, 3692–3702. <https://doi.org/10.1016/j.febslet.2014.08.015>.
- Rolef Ben-Shahar, T., Heeger, S., Lehane, C., East, P., Flynn, H., Skehel, M., and Uhlmann, F. (2008). Eco1-dependent cohesin acetylation during establishment of sister chromatid cohesion. *Science* *321*, 563–566. <https://doi.org/10.1126/science.1157774>.
- Rothkamm, K., Krüger, I., Thompson, L.H., and Löbrich, M. (2003). Pathways of DNA double-strand break repair during the mammalian cell cycle. *Mol. Cell. Biol.* *23*, 5706–5715. <https://doi.org/10.1128/MCB.23.16.5706-5715.2003>.
- Rowland, B.D., Roig, M.B., Nishino, T., Kurze, A., Uluocak, P., Mishra, A., Beckouët, F., Underwood, P., Metson, J., Imre, R., *et al.* (2009). Building sister chromatid cohesion: smc3 acetylation counteracts an antiestablishment activity. *Mol. Cell* *33*, 763–774. <https://doi.org/10.1016/j.molcel.2009.02.028>.
- Rowntree, R.K., and Lee, J.T. (2006). Mapping of DNA replication origins to noncoding genes of the X-inactivation center. *Mol. Cell. Biol.* *26*, 3707–3717. <https://doi.org/10.1128/MCB.26.10.3707-3717.2006>.
- Rubio, E.D., Reiss, D.J., Welcsh, P.L., Distèche, C.M., Filippova, G.N., Baliga, N.S., Aebersold, R., Ranish, J.A., and Krumm, A. (2008). CTCF physically links cohesin to chromatin. *Proc Natl Acad Sci USA* *105*, 8309–8314. <https://doi.org/10.1073/pnas.0801273105>.
- Ryba, T., Hiratani, I., Lu, J., Itoh, M., Kulik, M., Zhang, J., Schulz, T.C., Robins, A.J., Dalton, S., and Gilbert, D.M. (2010). Evolutionarily conserved replication timing profiles predict long-range chromatin interactions and distinguish closely related cell types. *Genome Res.* *20*, 761–770. <https://doi.org/10.1101/gr.099655.109>.
- Ryu, J.-K., Katan, A.J., van der Sluis, E.O., Wisse, T., de Groot, R., Haering, C.H., and Dekker, C. (2020). The condensin holocomplex cycles dynamically between open and collapsed states. *Nat. Struct. Mol. Biol.* *27*, 1134–1141. <https://doi.org/10.1038/s41594-020-0508-3>.
- Ryu, J.-K., Bouchoux, C., Liu, H.W., Kim, E., Minamino, M., de Groot, R., Katan, A.J., Bonato, A., Marenduzzo, D., Michieletto, D., *et al.* (2021). Bridging-induced phase separation induced by cohesin SMC protein complexes. *Sci. Adv.* *7*. <https://doi.org/10.1126/sciadv.abe5905>.
- Sadoni, N., Cardoso, M.C., Stelzer, E.H.K., Leonhardt, H., and Zink, D. (2004). Stable chromosomal units determine the spatial and temporal organization of DNA replication. *J. Cell Sci.* *117*, 5353–5365. <https://doi.org/10.1242/jcs.01412>.
- Saitoh, N., Goldberg, I., and Earnshaw, W.C. (1995). The SMC proteins and the coming of age of the chromosome scaffold hypothesis. *Bioessays* *17*, 759–766. <https://doi.org/10.1002/bies.950170905>.
- Sakata, R., Niwa, K., Ugarte La Torre, D., Gu, C., Tahara, E., Takada, S., and Nishiyama, T. (2021). Opening of cohesin's SMC ring is essential for timely DNA replication and DNA loop formation. *Cell Rep.* *35*, 108999. <https://doi.org/10.1016/j.celrep.2021.108999>.
- Salo, P., Kääriäinen, H., Petrovic, V., Peltomäki, P., Page, D.C., and de la Chapelle, A. (1995). Molecular mapping of the putative gonadoblastoma locus on the Y chromosome. *Genes Chromosomes Cancer* *14*, 210–214. <https://doi.org/10.1002/gcc.2870140309>.
- Sane, A., Sridhar, S., Sanyal, K., and Ghosh, S.K. (2021). Shugoshin ensures maintenance of the spindle assembly checkpoint response and efficient spindle disassembly. *Mol. Microbiol.* *116*, 1079–1098. <https://doi.org/10.1111/mmi.14796>.
- Santivasi, W.L., and Xia, F. (2014). Ionizing radiation-induced DNA damage, response, and repair. *Antioxid. Redox Signal.* *21*, 251–259. <https://doi.org/10.1089/ars.2013.5668>.

- Saretzki, G., Armstrong, L., Leake, A., Lako, M., and von Zglinicki, T. (2004). Stress defense in murine embryonic stem cells is superior to that of various differentiated murine cells. *Stem Cells* 22, 962–971. <https://doi.org/10.1634/stemcells.22-6-962>.
- Savatier, P., Lapillonne, H., Jirmanova, L., Vitelli, L., and Samarut, J. (2002). Analysis of the cell cycle in mouse embryonic stem cells. *Methods Mol. Biol.* 185, 27–33. <https://doi.org/10.1385/1-59259-241-4:27>.
- Schär, P., Fäsi, M., and Jessberger, R. (2004). SMC1 coordinates DNA double-strand break repair pathways. *Nucleic Acids Res.* 32, 3921–3929. <https://doi.org/10.1093/nar/gkh716>.
- Schindelin, J., Arganda-Carreras, I., Frise, E., Kaynig, V., Longair, M., Pietzsch, T., Preibisch, S., Rueden, C., Saalfeld, S., Schmid, B., *et al.* (2012). Fiji: an open-source platform for biological-image analysis. *Nat. Methods* 9, 676–682. <https://doi.org/10.1038/nmeth.2019>.
- Schipler, A., and Iliakis, G. (2013). DNA double-strand-break complexity levels and their possible contributions to the probability for error-prone processing and repair pathway choice. *Nucleic Acids Res.* 41, 7589–7605. <https://doi.org/10.1093/nar/gkt556>.
- Schmid, W. (1963). Dna replication patterns of human chromosomes. *Cytogenetics* 2, 175–193. <https://doi.org/10.1159/000129778>.
- Schmiesing, J.A., Ball, A.R., Gregson, H.C., Alderton, J.M., Zhou, S., and Yokomori, K. (1998). Identification of two distinct human SMC protein complexes involved in mitotic chromosome dynamics. *Proc Natl Acad Sci USA* 95, 12906–12911. <https://doi.org/10.1073/pnas.95.22.12906>.
- Schmitz, J., Watrin, E., Lénárt, P., Mechtler, K., and Peters, J.-M. (2007). Sororin is required for stable binding of cohesin to chromatin and for sister chromatid cohesion in interphase. *Curr. Biol.* 17, 630–636. <https://doi.org/10.1016/j.cub.2007.02.029>.
- Schultz, L.B., Chehab, N.H., Malikzay, A., and Halazonetis, T.D. (2000). p53 binding protein 1 (53BP1) is an early participant in the cellular response to DNA double-strand breaks. *J. Cell Biol.* 151, 1381–1390. <https://doi.org/10.1083/jcb.151.7.1381>.
- Schwarzer, W., Abdennur, N., Goloborodko, A., Pekowska, A., Fudenberg, G., Loe-Mie, Y., Fonseca, N.A., Huber, W., Haering, C.H., Mirny, L., *et al.* (2017). Two independent modes of chromatin organization revealed by cohesin removal. *Nature* 551, 51–56. <https://doi.org/10.1038/nature24281>.
- Scully, R., Panday, A., Elango, R., and Willis, N.A. (2019). DNA double-strand break repair-pathway choice in somatic mammalian cells. *Nat. Rev. Mol. Cell Biol.* 20, 698–714. <https://doi.org/10.1038/s41580-019-0152-0>.
- Sedelnikova, O.A., Pilch, D.R., Redon, C., and Bonner, W.M. (2003). Histone H2AX in DNA damage and repair. *Cancer Biol. Ther.* 2, 233–235. <https://doi.org/10.4161/cbt.2.3.373>.
- Seitan, V.C., Banks, P., Laval, S., Majid, N.A., Dorsett, D., Rana, A., Smith, J., Bateman, A., Krpic, S., Hostert, A., *et al.* (2006). Metazoan Scc4 homologs link sister chromatid cohesion to cell and axon migration guidance. *PLoS Biol.* 4, e242. <https://doi.org/10.1371/journal.pbio.0040242>.
- Shaltiel, I.A., Datta, S., Lecomte, L., Hassler, M., Kschonsak, M., Bravo, S., Stober, C., Eustermann, S., and Haering, C.H. (2021). A hold-and-feed mechanism drives directional DNA loop extrusion by condensin. *BioRxiv* <https://doi.org/10.1101/2021.10.29.466147>.
- Shi, D., Zhao, S., Zuo, M.-Q., Zhang, J., Hou, W., Dong, M.-Q., Cao, Q., and Lou, H. (2020a). The acetyltransferase Eco1 elicits cohesin dimerization during S phase. *J. Biol. Chem.* 295, 7554–7565. <https://doi.org/10.1074/jbc.RA120.013102>.
- Shi, Z., Gao, H., Bai, X.-C., and Yu, H. (2020b). Cryo-EM structure of the human cohesin-NIPBL-DNA complex. *Science* 368, 1454–1459. <https://doi.org/10.1126/science.abb0981>.
- Sibanda, B.L., Chirgadze, D.Y., Ascher, D.B., and Blundell, T.L. (2017). DNA-PKcs structure suggests an allosteric mechanism modulating DNA double-strand break repair. *Science* 355, 520–524. <https://doi.org/10.1126/science.aak9654>.
- Sinclair, A.H., Berta, P., Palmer, M.S., Hawkins, J.R., Griffiths, B.L., Smith, M.J., Foster, J.W., Frischauf, A.M., Lovell-Badge, R., and Goodfellow, P.N. (1990). A gene from the human sex-determining region encodes a protein with

homology to a conserved DNA-binding motif. *Nature* 346, 240–244. <https://doi.org/10.1038/346240a0>.

Singh, N.P., Madabhushi, S.R., Srivastava, S., Senthilkumar, R., Neeraja, C., Khosla, S., and Mishra, R.K. (2011a). Epigenetic profile of the euchromatic region of human Y chromosome. *Nucleic Acids Res.* 39, 3594–3606. <https://doi.org/10.1093/nar/gkq1342>.

Singh, S.K., Wang, M., Staudt, C., and Iliakis, G. (2011b). Post-irradiation chemical processing of DNA damage generates double-strand breaks in cells already engaged in repair. *Nucleic Acids Res.* 39, 8416–8429. <https://doi.org/10.1093/nar/gkr463>.

Singh, S.K., Bencsik-Theilen, A., Mladenov, E., Jakob, B., Taucher-Scholz, G., and Iliakis, G. (2013). Reduced contribution of thermally labile sugar lesions to DNA double strand break formation after exposure to heavy ions. *Radiat. Oncol.* 8, 77. <https://doi.org/10.1186/1748-717X-8-77>.

Singleton, B.K., Torres-Arzuayus, M.I., Rottinghaus, S.T., Taccioli, G.E., and Jeggo, P.A. (1999). The C terminus of Ku80 activates the DNA-dependent protein kinase catalytic subunit. *Mol. Cell. Biol.* 19, 3267–3277. <https://doi.org/10.1128/MCB.19.5.3267>.

Skibbens, R.V., Corson, L.B., Koshland, D., and Hieter, P. (1999). Ctf7p is essential for sister chromatid cohesion and links mitotic chromosome structure to the DNA replication machinery. *Genes Dev.* 13, 307–319. <https://doi.org/10.1101/gad.13.3.307>.

Soh, Y.-M., Bürmann, F., Shin, H.-C., Oda, T., Jin, K.S., Toseland, C.P., Kim, C., Lee, H., Kim, S.J., Kong, M.-S., *et al.* (2015). Molecular basis for SMC rod formation and its dissolution upon DNA binding. *Mol. Cell* 57, 290–303. <https://doi.org/10.1016/j.molcel.2014.11.023>.

Soh, Y.Q.S., Alföldi, J., Pyntikova, T., Brown, L.G., Graves, T., Minx, P.J., Fulton, R.S., Kremitzki, C., Koutseva, N., Mueller, J.L., *et al.* (2014). Sequencing the mouse Y chromosome reveals convergent gene acquisition and amplification on both sex chromosomes. *Cell* 159, 800–813. <https://doi.org/10.1016/j.cell.2014.09.052>.

Solovei, I., Kreysing, M., Lanctôt, C., Kösem, S., Peichl, L., Cremer, T., Guck, J., and Joffe, B. (2009). Nuclear architecture of rod photoreceptor cells adapts to vision in mammalian evolution. *Cell* 137, 356–368. <https://doi.org/10.1016/j.cell.2009.01.052>.

Song, Q., Khanna, K.K., Lu, H., and Lavin, M.F. (1993). Cloning and characterization of a human protein phosphatase 1-encoding cDNA. *Gene* 129, 291–295. [https://doi.org/10.1016/0378-1119\(93\)90282-8](https://doi.org/10.1016/0378-1119(93)90282-8).

Soriano, P., Keitges, E.A., Schorderet, D.F., Harbers, K., Gartler, S.M., and Jaenisch, R. (1987). High rate of recombination and double crossovers in the mouse pseudoautosomal region during male meiosis. *Proc Natl Acad Sci USA* 84, 7218–7220. <https://doi.org/10.1073/pnas.84.20.7218>.

Sparvoli, E., Levi, M., and Rossi, E. (1994). Replicon clusters may form structurally stable complexes of chromatin and chromosomes. *J. Cell Sci.* 107 (Pt 11), 3097–3103. <https://doi.org/10.1242/jcs.107.11.3097>.

Splinter, E., Heath, H., Kooren, J., Palstra, R.-J., Klous, P., Grosveld, F., Galjart, N., and de Laat, W. (2006). CTCF mediates long-range chromatin looping and local histone modification in the beta-globin locus. *Genes Dev.* 20, 2349–2354. <https://doi.org/10.1101/gad.399506>.

Sporbert, A., Gahl, A., Ankerhold, R., Leonhardt, H., and Cardoso, M.C. (2002). DNA polymerase clamp shows little turnover at established replication sites but sequential de novo assembly at adjacent origin clusters. *Mol. Cell* 10, 1355–1365. [https://doi.org/10.1016/s1097-2765\(02\)00729-3](https://doi.org/10.1016/s1097-2765(02)00729-3).

Sporbert, A., Domaing, P., Leonhardt, H., and Cardoso, M.C. (2005). PCNA acts as a stationary loading platform for transiently interacting Okazaki fragment maturation proteins. *Nucleic Acids Res.* 33, 3521–3528. <https://doi.org/10.1093/nar/gki665>.

Srinivasan, M., Scheinost, J.C., Petela, N.J., Gligoris, T.G., Wissler, M., Ogushi, S., Collier, J.E., Voulgaris, M., Kurze, A., Chan, K.-L., *et al.* (2018). The Cohesin Ring Uses Its Hinge to Organize DNA Using Non-topological as well as Topological Mechanisms. *Cell* 173, 1508–1519.e18. <https://doi.org/10.1016/j.cell.2018.04.015>.

Srinivasan, M., Petela, N.J., Scheinost, J.C., Collier, J., Voulgaris, M., B Roig, M., Beckouët, F., Hu, B., and Nasmyth, K.A. (2019). Scc2 counteracts a Wapl-independent mechanism that releases cohesin from chromosomes during G1. *ELife* 8. <https://doi.org/10.7554/eLife.44736>.

- Srinivasan, M., Fumasoni, M., Petela, N.J., Murray, A., and Nasmyth, K.A. (2020). Cohesion is established during DNA replication utilising chromosome associated cohesin rings as well as those loaded de novo onto nascent DNAs. *ELife* 9. <https://doi.org/10.7554/eLife.56611>.
- Stavropoulos, N., Rowntree, R.K., and Lee, J.T. (2005). Identification of developmentally specific enhancers for Tsix in the regulation of X chromosome inactivation. *Mol. Cell. Biol.* 25, 2757–2769. <https://doi.org/10.1128/MCB.25.7.2757-2769.2005>.
- Stedman, W., Kang, H., Lin, S., Kissil, J.L., Bartolomei, M.S., and Lieberman, P.M. (2008). Cohesins localize with CTCF at the KSHV latency control region and at cellular c-myc and H19/Igf2 insulators. *EMBO J.* 27, 654–666. <https://doi.org/10.1038/emboj.2008.1>.
- Stenerlöv, B., Karlsson, K.H., Cooper, B., and Rydberg, B. (2003). Measurement of prompt DNA double-strand breaks in mammalian cells without including heat-labile sites: results for cells deficient in nonhomologous end joining. *Radiat. Res.* 159, 502–510.
- Stigler, J., Çamdere, G.Ö., Koshland, D.E., and Greene, E.C. (2016). Single-Molecule Imaging Reveals a Collapsed Conformational State for DNA-Bound Cohesin. *Cell Rep.* 15, 988–998. <https://doi.org/10.1016/j.celrep.2016.04.003>.
- Ström, L., Lindroos, H.B., Shirahige, K., and Sjögren, C. (2004). Postreplicative recruitment of cohesin to double-strand breaks is required for DNA repair. *Mol. Cell* 16, 1003–1015. <https://doi.org/10.1016/j.molcel.2004.11.026>.
- Strunnikov, A.V., Larionov, V.L., and Koshland, D. (1993). SMC1: an essential yeast gene encoding a putative head-rod-tail protein is required for nuclear division and defines a new ubiquitous protein family. *J. Cell Biol.* 123, 1635–1648. <https://doi.org/10.1083/jcb.123.6.1635>.
- Sudakin, V., Ganoth, D., Dahan, A., Heller, H., Hershko, J., Luca, F.C., Ruderman, J.V., and Hershko, A. (1995). The cyclosome, a large complex containing cyclin-selective ubiquitin ligase activity, targets cyclins for destruction at the end of mitosis. *Mol. Biol. Cell* 6, 185–197. <https://doi.org/10.1091/mbc.6.2.185>.
- Sumara, I., Vorlaufer, E., Gieffers, C., Peters, B.H., and Peters, J.M. (2000). Characterization of vertebrate cohesin complexes and their regulation in prophase. *J. Cell Biol.* 151, 749–762. <https://doi.org/10.1083/jcb.151.4.749>.
- Sumara, I., Vorlaufer, E., Stukenberg, P.T., Kelm, O., Redemann, N., Nigg, E.A., and Peters, J.-M. (2002). The dissociation of cohesin from chromosomes in prophase is regulated by Polo-like kinase. *Mol. Cell* 9, 515–525. [https://doi.org/10.1016/s1097-2765\(02\)00473-2](https://doi.org/10.1016/s1097-2765(02)00473-2).
- Sutherland, B.M., Bennett, P.V., Sidorkina, O., and Laval, J. (2000). Clustered DNA damages induced in isolated DNA and in human cells by low doses of ionizing radiation. *Proc Natl Acad Sci USA* 97, 103–108. <https://doi.org/10.1073/pnas.97.1.103>.
- Swift, M.L., Beishline, K., Flashner, S., and Azizkhan-Clifford, J. (2021). DSB repair pathway choice is regulated by recruitment of 53BP1 through cell cycle-dependent regulation of Sp1. *Cell Rep.* 34, 108840. <https://doi.org/10.1016/j.celrep.2021.108840>.
- Takagi, N., and Sasaki, M. (1975). Preferential inactivation of the paternally derived X chromosome in the extraembryonic membranes of the mouse. *Nature* 256, 640–642. <https://doi.org/10.1038/256640a0>.
- Takagi, N., Sugawara, O., and Sasaki, M. (1982). Regional and temporal changes in the pattern of X-chromosome replication during the early post-implantation development of the female mouse. *Chromosoma* 85, 275–286. <https://doi.org/10.1007/BF00294971>.
- Takata, M., Sasaki, M.S., Sonoda, E., Morrison, C., Hashimoto, M., Utsumi, H., Yamaguchi-Iwai, Y., Shinohara, A., and Takeda, S. (1998). Homologous recombination and non-homologous end-joining pathways of DNA double-strand break repair have overlapping roles in the maintenance of chromosomal integrity in vertebrate cells. *EMBO J.* 17, 5497–5508. <https://doi.org/10.1093/emboj/17.18.5497>.
- Takebayashi, S., Dileep, V., Ryba, T., Dennis, J.H., and Gilbert, D.M. (2012). Chromatin-interaction compartment switch at developmentally regulated chromosomal domains reveals an unusual principle of chromatin folding. *Proc Natl Acad Sci USA* 109, 12574–12579. <https://doi.org/10.1073/pnas.1207185109>.

- Tang, Z., Shu, H., Qi, W., Mahmood, N.A., Mumby, M.C., and Yu, H. (2006). PP2A is required for centromeric localization of Sgo1 and proper chromosome segregation. *Dev. Cell* *10*, 575–585. <https://doi.org/10.1016/j.devcel.2006.03.010>.
- Tark-Dame, M., van Driel, R., and Heermann, D.W. (2011). Chromatin folding--from biology to polymer models and back. *J. Cell Sci.* *124*, 839–845. <https://doi.org/10.1242/jcs.077628>.
- Tashiro, S., and Lanctôt, C. (2015). The international nucleome consortium. *Nucleus* *6*, 89–92. <https://doi.org/10.1080/19491034.2015.1022703>.
- Telenius, H., Carter, N.P., Bebb, C.E., Nordenskjöld, M., Ponder, B.A., and Tunnacliffe, A. (1992). Degenerate oligonucleotide-primed PCR: general amplification of target DNA by a single degenerate primer. *Genomics* *13*, 718–725. [https://doi.org/10.1016/0888-7543\(92\)90147-K](https://doi.org/10.1016/0888-7543(92)90147-K).
- Thol, F., Bollin, R., Gehlhaar, M., Walter, C., Dugas, M., Suchanek, K.J., Kirchner, A., Huang, L., Chaturvedi, A., Wichmann, M., *et al.* (2014). Mutations in the cohesin complex in acute myeloid leukemia: clinical and prognostic implications. *Blood* *123*, 914–920. <https://doi.org/10.1182/blood-2013-07-518746>.
- Tichy, E.D., and Stambrook, P.J. (2008). DNA repair in murine embryonic stem cells and differentiated cells. *Exp. Cell Res.* *314*, 1929–1936. <https://doi.org/10.1016/j.yexcr.2008.02.007>.
- Tommasino, F., Friedrich, T., Scholz, U., Taucher-Scholz, G., Durante, M., and Scholz, M. (2013). A DNA double-strand break kinetic rejoining model based on the local effect model. *Radiat. Res.* *180*, 524–538. <https://doi.org/10.1667/RR13389.1>.
- Tommasino, F., Friedrich, T., Scholz, U., Taucher-Scholz, G., Durante, M., and Scholz, M. (2015a). Application of the local effect model to predict DNA double-strand break rejoining after photon and high-LET irradiation. *Radiat. Prot. Dosimetry* *166*, 66–70. <https://doi.org/10.1093/rpd/ncv164>.
- Tommasino, F., Friedrich, T., Jakob, B., Meyer, B., Durante, M., and Scholz, M. (2015b). Induction and Processing of the Radiation-Induced Gamma-H2AX Signal and Its Link to the Underlying Pattern of DSB: A Combined Experimental and Modelling Study. *PLoS ONE* *10*, e0129416. <https://doi.org/10.1371/journal.pone.0129416>.
- Tong, K., and Skibbens, R.V. (2014). Cohesin without cohesion: a novel role for Pds5 in *Saccharomyces cerevisiae*. *PLoS ONE* *9*, e100470. <https://doi.org/10.1371/journal.pone.0100470>.
- Tong, K., and Skibbens, R.V. (2015). Pds5 regulators segregate cohesion and condensation pathways in *Saccharomyces cerevisiae*. *Proc Natl Acad Sci USA* *112*, 7021–7026. <https://doi.org/10.1073/pnas.1501369112>.
- Tonkin, E.T., Wang, T.-J., Lisgo, S., Bamshad, M.J., and Strachan, T. (2004). NIPBL, encoding a homolog of fungal Scc2-type sister chromatid cohesion proteins and fly Nipped-B, is mutated in Cornelia de Lange syndrome. *Nat. Genet.* *36*, 636–641. <https://doi.org/10.1038/ng1363>.
- Tóth, A., Ciosk, R., Uhlmann, F., Galova, M., Schleiffer, A., and Nasmyth, K. (1999). Yeast cohesin complex requires a conserved protein, Eco1p(Ctf7), to establish cohesion between sister chromatids during DNA replication. *Genes Dev.* *13*, 320–333. <https://doi.org/10.1101/gad.13.3.320>.
- Tothova, Z., Valton, A.-L., Gorelov, R.A., Vallurupalli, M., Krill-Burger, J.M., Holmes, A., Landers, C.C., Haydu, J.E., Malolepsza, E., Hartigan, C., *et al.* (2021). Cohesin mutations alter DNA damage repair and chromatin structure and create therapeutic vulnerabilities in MDS/AML. *JCI Insight* *6*. <https://doi.org/10.1172/jci.insight.142149>.
- Tsuchiya, K., Reijo, R., Page, D.C., and Distèche, C.M. (1995). Gonadoblastoma: molecular definition of the susceptibility region on the Y chromosome. *Am. J. Hum. Genet.* *57*, 1400–1407.
- Turinetto, V., and Giachino, C. (2015). Multiple facets of histone variant H2AX: a DNA double-strand-break marker with several biological functions. *Nucleic Acids Res.* *43*, 2489–2498. <https://doi.org/10.1093/nar/gkv061>.
- Uhlmann, F., and Nasmyth, K. (1998). Cohesion between sister chromatids must be established during DNA replication. *Curr. Biol.* *8*, 1095–1101. [https://doi.org/10.1016/s0960-9822\(98\)70463-4](https://doi.org/10.1016/s0960-9822(98)70463-4).
- Uhlmann, F., Lottspeich, F., and Nasmyth, K. (1999). Sister-chromatid separation at anaphase onset is promoted by cleavage of the cohesin subunit Scc1. *Nature* *400*, 37–42. <https://doi.org/10.1038/21831>.

- Uhlmann, F., Wernic, D., Poupart, M.A., Koonin, E.V., and Nasmyth, K. (2000). Cleavage of cohesin by the CD clan protease separin triggers anaphase in yeast. *Cell* 103, 375–386. [https://doi.org/10.1016/s0092-8674\(00\)00130-6](https://doi.org/10.1016/s0092-8674(00)00130-6).
- Ulrich, H.D. (2012). Ubiquitin and SUMO in DNA repair at a glance. *J. Cell Sci.* 125, 249–254. <https://doi.org/10.1242/jcs.091801>.
- Unal, E., Arbel-Eden, A., Sattler, U., Shroff, R., Lichten, M., Haber, J.E., and Koshland, D. (2004). DNA damage response pathway uses histone modification to assemble a double-strand break-specific cohesin domain. *Mol. Cell* 16, 991–1002. <https://doi.org/10.1016/j.molcel.2004.11.027>.
- Unal, E., Heidinger-Pauli, J.M., and Koshland, D. (2007). DNA double-strand breaks trigger genome-wide sister-chromatid cohesion through Eco1 (Ctf7). *Science* 317, 245–248. <https://doi.org/10.1126/science.1140637>.
- Unal, E., Heidinger-Pauli, J.M., Kim, W., Guacci, V., Onn, I., Gygi, S.P., and Koshland, D.E. (2008). A molecular determinant for the establishment of sister chromatid cohesion. *Science* 321, 566–569. <https://doi.org/10.1126/science.1157880>.
- Uziel, T., Lerenthal, Y., Moyal, L., Andegeko, Y., Mittelman, L., and Shiloh, Y. (2003). Requirement of the MRN complex for ATM activation by DNA damage. *EMBO J.* 22, 5612–5621. <https://doi.org/10.1093/emboj/cdg541>.
- Valerie, K., and Povirk, L.F. (2003). Regulation and mechanisms of mammalian double-strand break repair. *Oncogene* 22, 5792–5812. <https://doi.org/10.1038/sj.onc.1206679>.
- Vian, L., Pękowska, A., Rao, S.S.P., Kieffer-Kwon, K.-R., Jung, S., Baranello, L., Huang, S.-C., El Khattabi, L., Dose, M., Pruett, N., *et al.* (2018). The energetics and physiological impact of cohesin extrusion. *Cell* 173, 1165–1178.e20. <https://doi.org/10.1016/j.cell.2018.03.072>.
- Vietri Rudan, M., Barrington, C., Henderson, S., Ernst, C., Odom, D.T., Tanay, A., and Hadjur, S. (2015). Comparative Hi-C reveals that CTCF underlies evolution of chromosomal domain architecture. *Cell Rep.* 10, 1297–1309. <https://doi.org/10.1016/j.celrep.2015.02.004>.
- Vignard, J., Mirey, G., and Salles, B. (2013). Ionizing-radiation induced DNA double-strand breaks: a direct and indirect lighting up. *Radiother. Oncol.* 108, 362–369. <https://doi.org/10.1016/j.radonc.2013.06.013>.
- Vogelstein, B., Pardoll, D.M., and Coffey, D.S. (1980). Supercoiled loops and eucaryotic DNA replication. *Cell* 22, 79–85. [https://doi.org/10.1016/0092-8674\(80\)90156-7](https://doi.org/10.1016/0092-8674(80)90156-7).
- Volkov, A., Mascarenhas, J., Andrei-Selmer, C., Ulrich, H.D., and Graumann, P.L. (2003). A prokaryotic condensin/cohesin-like complex can actively compact chromosomes from a single position on the nucleoid and binds to DNA as a ring-like structure. *Mol. Cell. Biol.* 23, 5638–5650. <https://doi.org/10.1128/MCB.23.16.5638-5650.2003>.
- Vrouwe, M.G., Elghalbzouri-Maghrani, E., Meijers, M., Schouten, P., Godthelp, B.C., Bhuiyan, Z.A., Redeker, E.J., Mannens, M.M., Mullenders, L.H.F., Pastink, A., *et al.* (2007). Increased DNA damage sensitivity of Cornelia de Lange syndrome cells: evidence for impaired recombinational repair. *Hum. Mol. Genet.* 16, 1478–1487. <https://doi.org/10.1093/hmg/ddm098>.
- Wada, S., Van Khoa, T., Kobayashi, Y., Funayama, T., Ogihara, K., Ueno, S., and Ito, N. (2005). Prediction of cellular radiosensitivity from DNA damage induced by gamma-rays and carbon ion irradiation in canine tumor cells. *J. Vet. Med. Sci.* 67, 1089–1095.
- Wagner, F.R., Dienemann, C., Wang, H., Stützer, A., Tegunov, D., Urlaub, H., and Cramer, P. (2020). Structure of SWI/SNF chromatin remodeller RSC bound to a nucleosome. *Nature* 579, 448–451. <https://doi.org/10.1038/s41586-020-2088-0>.
- Waizenegger, I.C., Hauf, S., Meinke, A., and Peters, J.M. (2000). Two distinct pathways remove mammalian cohesin from chromosome arms in prophase and from centromeres in anaphase. *Cell* 103, 399–410. [https://doi.org/10.1016/s0092-8674\(00\)00132-x](https://doi.org/10.1016/s0092-8674(00)00132-x).
- Wang, W. (2003). The SWI/SNF family of ATP-dependent chromatin remodelers: similar mechanisms for diverse functions. *Curr. Top. Microbiol. Immunol.* 274, 143–169. https://doi.org/10.1007/978-3-642-55747-7_6.

- Wang, C.-Y., Jégu, T., Chu, H.-P., Oh, H.J., and Lee, J.T. (2018). SMCHD1 Merges Chromosome Compartments and Assists Formation of Super-Structures on the Inactive X. *Cell* *174*, 406-421.e25. <https://doi.org/10.1016/j.cell.2018.05.007>.
- Wang, C.-Y., Colognori, D., Sunwoo, H., Wang, D., and Lee, J.T. (2019). PRC1 collaborates with SMCHD1 to fold the X-chromosome and spread Xist RNA between chromosome compartments. *Nat. Commun.* *10*, 2950. <https://doi.org/10.1038/s41467-019-10755-3>.
- Wang, H., Zeng, Z.C., Bui, T.A., Sonoda, E., Takata, M., Takeda, S., and Iliakis, G. (2001). Efficient rejoining of radiation-induced DNA double-strand breaks in vertebrate cells deficient in genes of the RAD52 epistasis group. *Oncogene* *20*, 2212–2224. <https://doi.org/10.1038/sj.onc.1204350>.
- Wang, X., Ran, T., Zhang, X., Xin, J., Zhang, Z., Wu, T., Wang, W., and Cai, G. (2017). 3.9 Å structure of the yeast Mec1-Ddc2 complex, a homolog of human ATR-ATRIP. *Science* *358*, 1206–1209. <https://doi.org/10.1126/science.aan8414>.
- Ward, J.F. (1994). The complexity of DNA damage: relevance to biological consequences. *Int. J. Radiat. Biol.* *66*, 427–432. <https://doi.org/10.1080/09553009414551401>.
- Watanabe, Y. (2005). Shugoshin: guardian spirit at the centromere. *Curr. Opin. Cell Biol.* *17*, 590–595. <https://doi.org/10.1016/j.ceb.2005.10.003>.
- Watrín, E., Schleiffer, A., Tanaka, K., Eisenhaber, F., Nasmyth, K., and Peters, J.-M. (2006). Human Scc4 is required for cohesin binding to chromatin, sister-chromatid cohesion, and mitotic progression. *Curr. Biol.* *16*, 863–874. <https://doi.org/10.1016/j.cub.2006.03.049>.
- Weber, P., Rausch, C., Scholl, A., and Cardoso, M.C. (2018). Repli-FISH (Fluorescence *In Situ* Hybridization): Application of 3D-(Immuno)-FISH for the Study of DNA Replication Timing of Genetic Repeat Elements. *OBM Genet.* *3*. <https://doi.org/10.21926/obm.genet.1901062>.
- Weitzer, S., Lehane, C., and Uhlmann, F. (2003). A model for ATP hydrolysis-dependent binding of cohesin to DNA. *Curr. Biol.* *13*, 1930–1940. <https://doi.org/10.1016/j.cub.2003.10.030>.
- Wells, J.N., Gligoris, T.G., Nasmyth, K.A., and Marsh, J.A. (2017). Evolution of condensin and cohesin complexes driven by replacement of Kite by Hawk proteins. *Curr. Biol.* *27*, R17–R18. <https://doi.org/10.1016/j.cub.2016.11.050>.
- Wendt, K.S. (2017). Resolving the Genomic Localization of the Kollerin Cohesin-Loader Complex. *Methods Mol. Biol.* *1515*, 115–123. https://doi.org/10.1007/978-1-4939-6545-8_7.
- Wendt, K.S., and Peters, J.-M. (2009). How cohesin and CTCF cooperate in regulating gene expression. *Chromosome Res.* *17*, 201–214. <https://doi.org/10.1007/s10577-008-9017-7>.
- Wendt, K.S., Yoshida, K., Itoh, T., Bando, M., Koch, B., Schirghuber, E., Tsutsumi, S., Nagae, G., Ishihara, K., Mishiro, T., *et al.* (2008). Cohesin mediates transcriptional insulation by CCCTC-binding factor. *Nature* *451*, 796–801. <https://doi.org/10.1038/nature06634>.
- de Wit, E., Vos, E.S.M., Holwerda, S.J.B., Valdes-Quezada, C., Verstegen, M.J.A.M., Teunissen, H., Splinter, E., Wijchers, P.J., Krijger, P.H.L., and de Laat, W. (2015). CTCF binding polarity determines chromatin looping. *Mol. Cell* *60*, 676–684. <https://doi.org/10.1016/j.molcel.2015.09.023>.
- Woodman, J., Fara, T., Dzieciatkowska, M., Trejo, M., Luong, N., Hansen, K.C., and Megee, P.C. (2014). Cell cycle-specific cleavage of Scc2 regulates its cohesin deposition activity. *Proc Natl Acad Sci USA* *111*, 7060–7065. <https://doi.org/10.1073/pnas.1321722111>.
- Wutz, G., Várnai, C., Nagasaka, K., Cisneros, D.A., Stocsits, R.R., Tang, W., Schoenfelder, S., Jessberger, G., Muhar, M., Hossain, M.J., *et al.* (2017). Topologically associating domains and chromatin loops depend on cohesin and are regulated by CTCF, WAPL, and PDS5 proteins. *EMBO J.* *36*, 3573–3599. <https://doi.org/10.15252/embj.201798004>.
- Xiang, S., and Koshland, D. (2021). Cohesin architecture and clustering *in vivo*. *ELife* *10*. <https://doi.org/10.7554/eLife.62243>.
- Xiang, W., Roberti, M.J., Hériché, J.-K., Huet, S., Alexander, S., and Ellenberg, J. (2018). Correlative live and super-

resolution imaging reveals the dynamic structure of replication domains. *J. Cell Biol.* 217, 1973–1984. <https://doi.org/10.1083/jcb.201709074>.

Xiong, B., Lu, S., and Gerton, J.L. (2010). Hos1 is a lysine deacetylase for the Smc3 subunit of cohesin. *Curr. Biol.* 20, 1660–1665. <https://doi.org/10.1016/j.cub.2010.08.019>.

Xue, Y., Canman, J.C., Lee, C.S., Nie, Z., Yang, D., Moreno, G.T., Young, M.K., Salmon, E.D., and Wang, W. (2000). The human SWI/SNF-B chromatin-remodeling complex is related to yeast rsc and localizes at kinetochores of mitotic chromosomes. *Proc Natl Acad Sci USA* 97, 13015–13020. <https://doi.org/10.1073/pnas.240208597>.

Xu, N., Donohoe, M.E., Silva, S.S., and Lee, J.T. (2007). Evidence that homologous X-chromosome pairing requires transcription and Ctfc protein. *Nat. Genet.* 39, 1390–1396. <https://doi.org/10.1038/ng.2007.5>.

Xu, X., Kanai, R., Nakazawa, N., Wang, L., Toyoshima, C., and Yanagida, M. (2018). Suppressor mutation analysis combined with 3D modeling explains cohesin's capacity to hold and release DNA. *Proc Natl Acad Sci USA* 115, E4833–E4842. <https://doi.org/10.1073/pnas.1803564115>.

Yaffe, D., and Saxel, O. (1977). Serial passaging and differentiation of myogenic cells isolated from dystrophic mouse muscle. *Nature* 270, 725–727. <https://doi.org/10.1038/270725a0>.

Yaffe, E., Farkash-Amar, S., Polten, A., Yakhini, Z., Tanay, A., and Simon, I. (2010). Comparative analysis of DNA replication timing reveals conserved large-scale chromosomal architecture. *PLoS Genet.* 6, e1001011. <https://doi.org/10.1371/journal.pgen.1001011>.

Yamamoto, A., Guacci, V., and Koshland, D. (1996a). Pds1p is required for faithful execution of anaphase in the yeast, *Saccharomyces cerevisiae*. *J. Cell Biol.* 133, 85–97. <https://doi.org/10.1083/jcb.133.1.85>.

Yamamoto, A., Guacci, V., and Koshland, D. (1996b). Pds1p, an inhibitor of anaphase in budding yeast, plays a critical role in the APC and checkpoint pathway(s). *J. Cell Biol.* 133, 99–110. <https://doi.org/10.1083/jcb.133.1.99>.

Yamazaki, S., Ishii, A., Kanoh, Y., Oda, M., Nishito, Y., and Masai, H. (2012). Rif1 regulates the replication timing domains on the human genome. *EMBO J.* 31, 3667–3677. <https://doi.org/10.1038/emboj.2012.180>.

Yamazaki, S., Hayano, M., and Masai, H. (2013). Replication timing regulation of eukaryotic replicons: Rif1 as a global regulator of replication timing. *Trends Genet.* 29, 449–460. <https://doi.org/10.1016/j.tig.2013.05.001>.

Yanagida, M. (2000). Cell cycle mechanisms of sister chromatid separation; roles of Cut1/separin and Cut2/securin. *Genes Cells* 5, 1–8. <https://doi.org/10.1046/j.1365-2443.2000.00306.x>.

Yang, Y.-G., Cortes, U., Patnaik, S., Jasin, M., and Wang, Z.-Q. (2004). Ablation of PARP-1 does not interfere with the repair of DNA double-strand breaks, but compromises the reactivation of stalled replication forks. *Oncogene* 23, 3872–3882. <https://doi.org/10.1038/sj.onc.1207491>.

Zachariae, W., and Nasmyth, K. (1996). TPR proteins required for anaphase progression mediate ubiquitination of mitotic B-type cyclins in yeast. *Mol. Biol. Cell* 7, 791–801. <https://doi.org/10.1091/mbc.7.5.791>.

Zachariae, W., Shin, T.H., Galova, M., Obermaier, B., and Nasmyth, K. (1996). Identification of subunits of the anaphase-promoting complex of *Saccharomyces cerevisiae*. *Science* 274, 1201–1204. <https://doi.org/10.1126/science.274.5290.1201>.

Zhang, J., Shi, X., Li, Y., Kim, B.-J., Jia, J., Huang, Z., Yang, T., Fu, X., Jung, S.Y., Wang, Y., *et al.* (2008). Acetylation of Smc3 by Eco1 is required for S phase sister chromatid cohesion in both human and yeast. *Mol. Cell* 31, 143–151. <https://doi.org/10.1016/j.molcel.2008.06.006>.

Zhang, N., Panigrahi, A.K., Mao, Q., and Pati, D. (2011). Interaction of Sororin protein with polo-like kinase 1 mediates resolution of chromosomal arm cohesion. *J. Biol. Chem.* 286, 41826–41837. <https://doi.org/10.1074/jbc.M111.305888>.

Zou, L., and Elledge, S.J. (2003). Sensing DNA damage through ATRIP recognition of RPA-ssDNA complexes. *Science* 300, 1542–1548. <https://doi.org/10.1126/science.1083430>.

Zou, H., McGarry, T.J., Bernal, T., and Kirschner, M.W. (1999). Identification of a vertebrate sister-chromatid separation inhibitor involved in transformation and tumorigenesis. *Science* 285, 418–422.

<https://doi.org/10.1126/science.285.5426.418>.

Zuilkoski, C.M., and Skibbens, R.V. (2022). Integrating sister chromatid cohesion establishment to DNA replication. *Genes (Basel)* *13*. <https://doi.org/10.3390/genes13040625>.

Zuin, J., Dixon, J.R., van der Reijden, M.I.J.A., Ye, Z., Kolovos, P., Brouwer, R.W.W., van de Corput, M.P.C., van de Werken, H.J.G., Knoch, T.A., van IJcken, W.F.J., *et al.* (2014). Cohesin and CTCF differentially affect chromatin architecture and gene expression in human cells. *Proc Natl Acad Sci USA* *111*, 996–1001. <https://doi.org/10.1073/pnas.1317788111>.

4D Nucleome Web Portal. Available at: <https://www.4dnucleome.org/>.

DepMap Data Explorer. Available at:

https://depmap.org/portal/interactive/?yDataset=&yFeature=&x=slice%2Fcopy_number_absolute%2F5524%2Fentity_id.

Subcellular - CTCF - The Human Protein Atlas. Available at:

<https://www.proteinatlas.org/ENSG00000102974-CTCF/subcellular>.

gd online documentation. Available at: <http://bio.gsi.de/DOCS/gd.html>.

Diffraction PSF 3D. Available at: <https://www.optinav.info/Diffraction-PSF-3D.htm>.

Iterative Deconvolve 3D. Available at: <https://www.optinav.info/Iterative-Deconvolve-3D.htm>.

Color Profiler. Available at: <https://imagej.nih.gov/ij/plugins/color-profiler.html>.

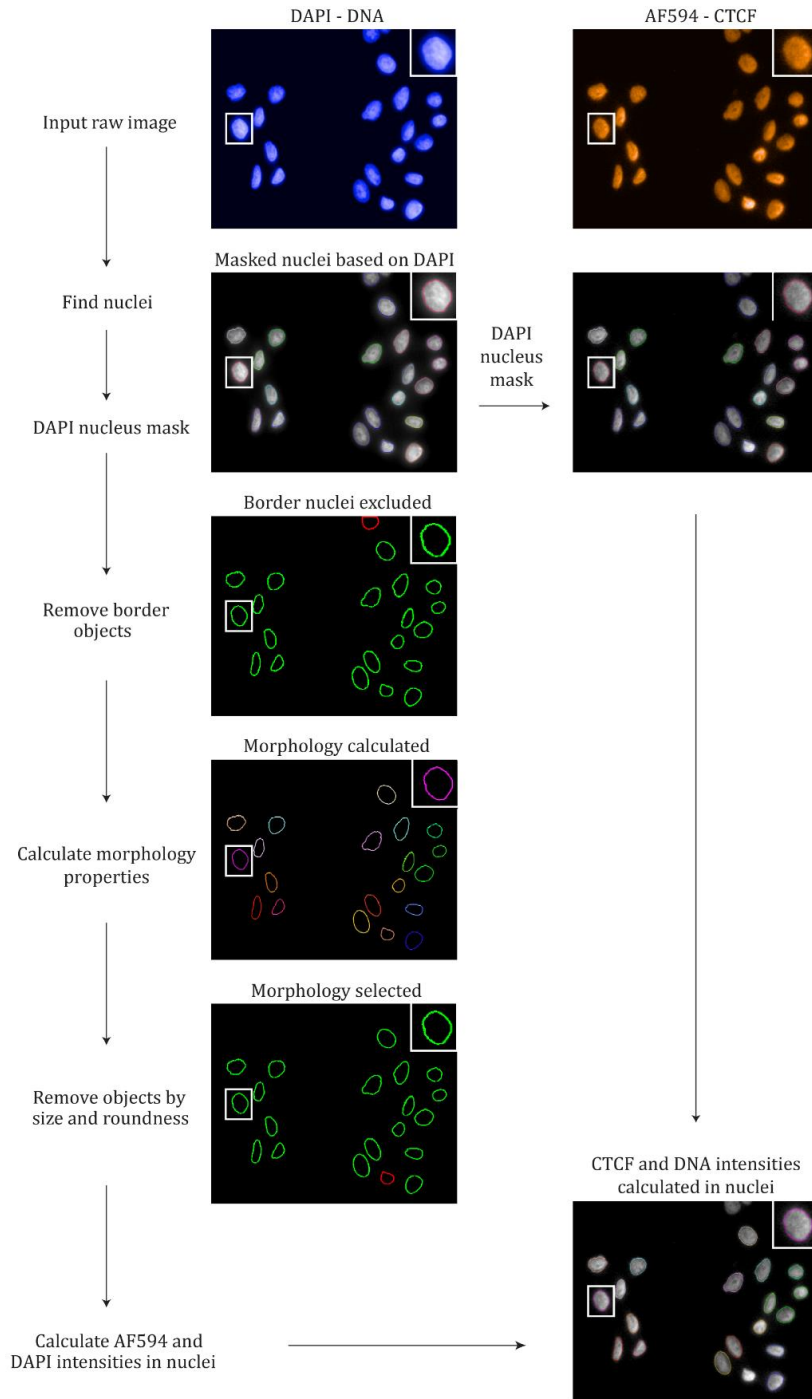
Protein Ontology. Available at: <https://proconsortium.org/pro.shtml>.

OMIM Entry # 122470 - CORNELIA DE LANGE SYNDROME 1. Available at: <https://omim.org/entry/122470>.

8. Supplementary material

8.1. Supplementary figures

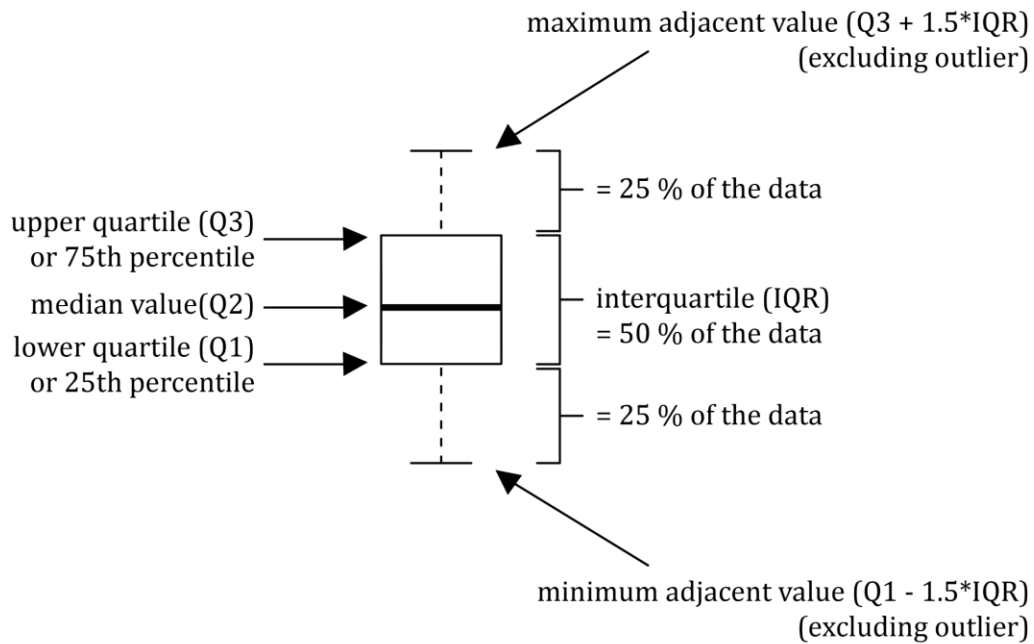
Supplementary Figure SF1: Image analysis pipeline for high-content wide-field images.



| Calculations applied to the measured DNA and CTCF nuclear intensities | |
|---|--|
| Background subtraction | CTCF intensity sample - median (intensity sample without CTCF detection) |
| Normalization to DNA content | Background subtracted CTCF intensity sample / DAPI intensity sample |
| Normalization to control | CTCF intensity sample / median (CTCF intensity control sample) |

Input raw images obtained with a high-content wide-field microscope (Supplementary Table ST3) were analyzed to obtain nuclear intensity values of DNA (DAPI) and CTCF (A594 in HeLa Kyoto and U2OS cells; GFP in mESC-AID-CTCF cells). An example for HeLa Kyoto cells is shown. First, nuclei were identified and segmented based on the DNA signal. The nuclei touching the edge of the image were excluded. The morphological properties of nuclei were calculated and used to select nuclei. The nuclear DNA and CTCF intensities were calculated for the selected nuclei and plotted upon different calculations shown in the above table. Background subtraction was applied in Figure 3.1.1. (C, E), Figure 3.1.5. (B, C), Supplementary Figure SF5 B; for HeLa Kyoto and U2OS, the background was measured in cells stained with the primary antibody being omitted; for mESC-AID-CTCF cells, the background was measured in ES-E14TG2a WT cells which do not have any CTCF-GFP-tag. Normalization to DNA content was applied in Figure 3.1.1. E upon background subtraction. Normalization to control was applied in Figure 3.1.2. (B, C), Figure 3.1.5. (B, C), Supplementary Figure SF5 B.

Supplementary Figure SF2: Boxplot data visualization.



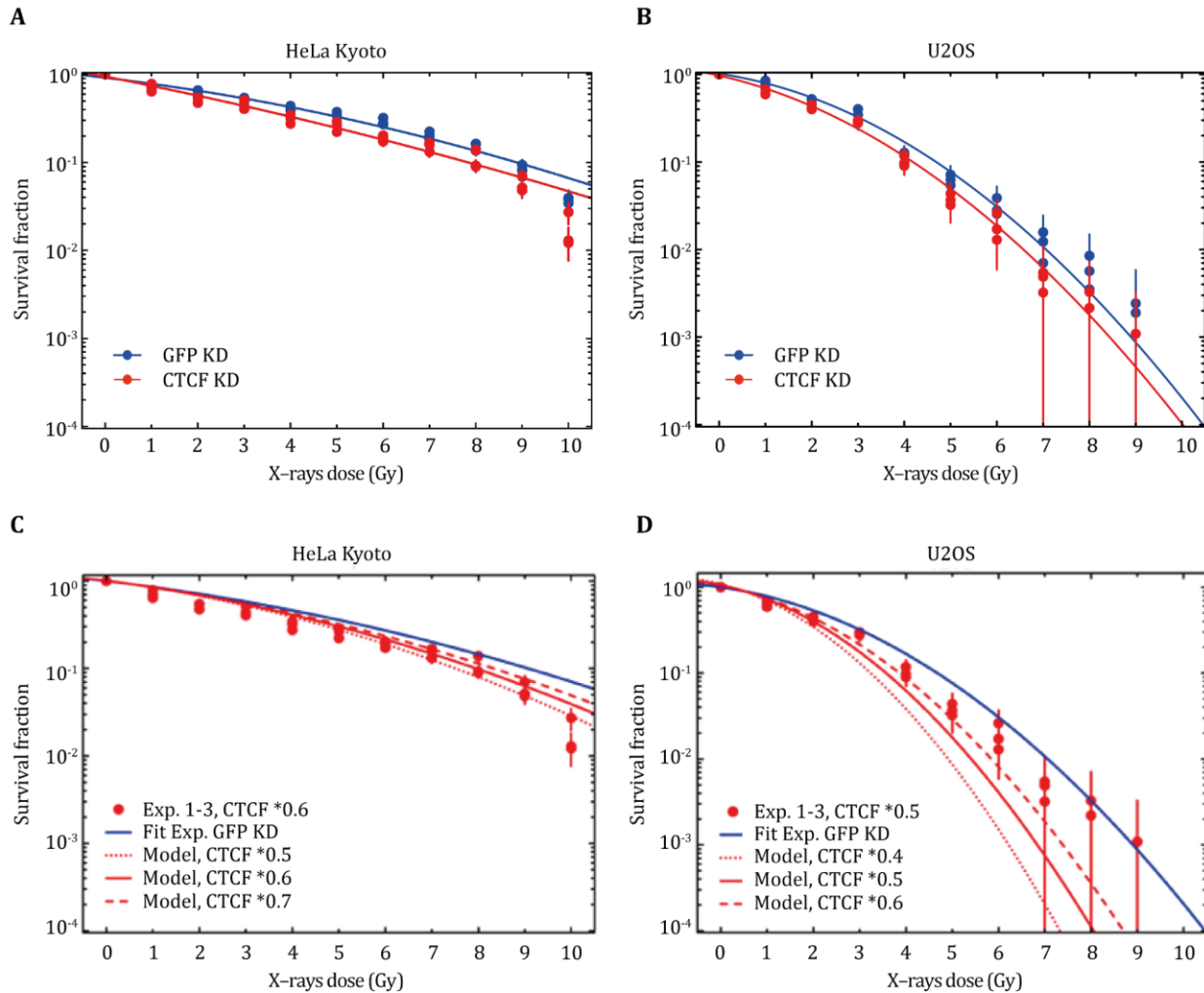
Boxplots allow to visualize the main statistics of a dataset. The “box” contains 50% of the observations, with the median value depicted as a line in it. The higher and lower borders of the box respectively represent the upper and lower quartile of the distribution. The remaining 50% of the observations is contained in the “whiskers” that depart from the box. The extreme values at the whiskers represent instead the maximum and minimum data points that are not considered outliers, as lying at +/- 1.5 times the interquartile range.

Supplementary Figure SF3: Colony formation images.

| D (Gy) | HeLa Kyoto | | U2OS | | mESC-AID-CTCF | | | |
|-----------|------------|---------|--------|---------|---------------|------------|-------------|--------------|
| | GFP KD | CTCF KD | GFP KD | CTCF KD | 0 μ M | 25 μ M | 500 μ M | 1000 μ M |
| 0 | | | | | | | | |
| 1 | | | | | | | | |
| 2 | | | | | | | | |
| 3 | | | | | | | | |
| 4 | | | | | | | | |
| 5 | | | | | | | | |
| 6 | | | | | | | | |
| 7 | | | | | | | | |
| 8 | | | | | | | | |
| 9 | | | | | | | | |
| 10 | | | | | | | | |

A complete set of images of colony formation of HeLa Kyoto, U2OS and mESC-AID-CTCF cells is shown (see methods section 3.1.4.5. for details). D (Gy) = X-rays dose; 0 - 1000 μ M = auxin concentration.

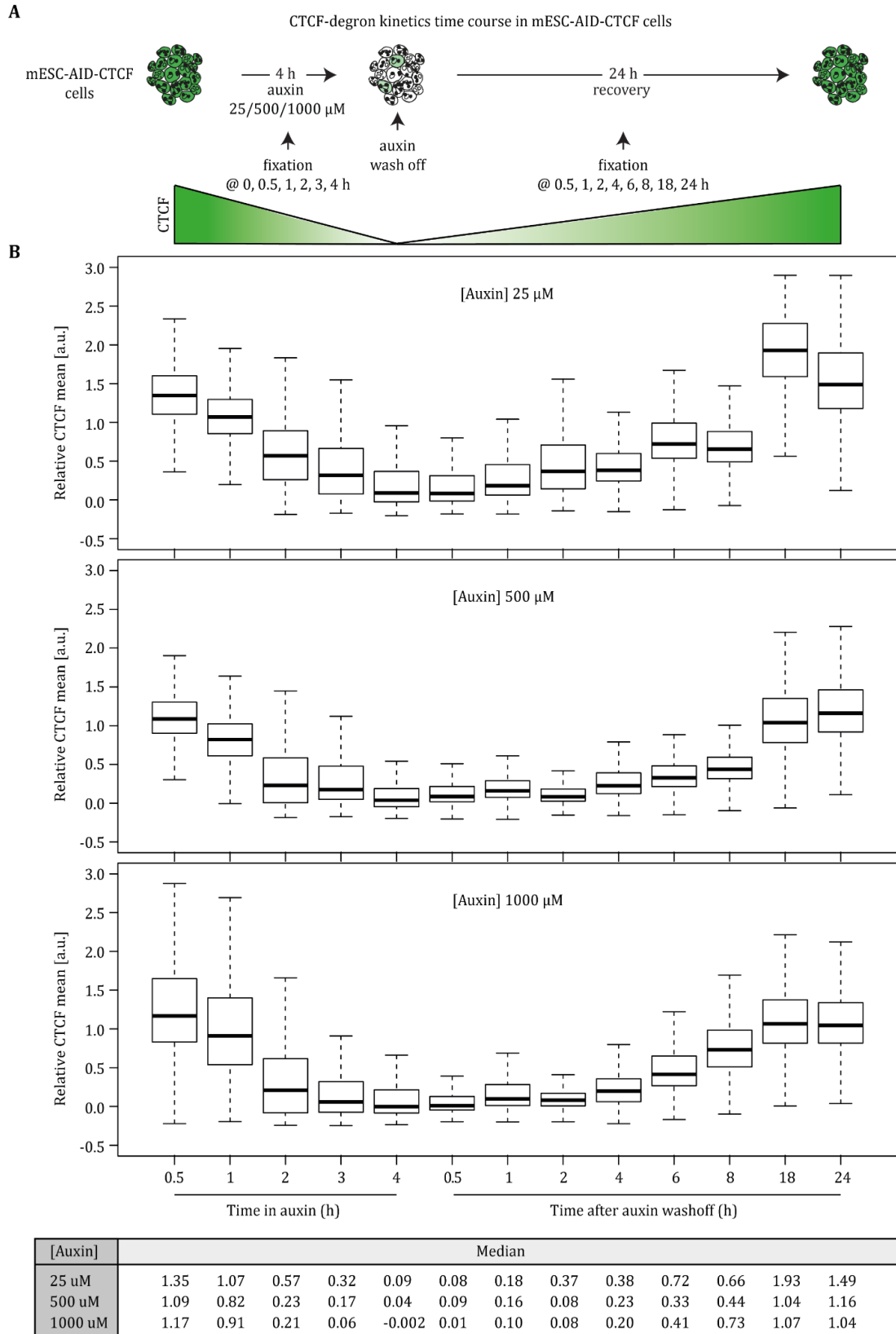
Supplementary Figure SF4: Survival curves and modeling predictions with equal y axis.



The experimental survival curves (Figure 3.1.3.) and relative modeling prediction (Figure 3.1.4.) of HeLa Kyoto and U2OS were plotted with a different scale on the y axis, due to the very different radiosensitivity of the two cell lines, with the scaling that better suited their visualization. Here both the experimental data (A, B) and the model predictions (C, D) are plotted by using the same scaling that was chosen for U2OS, to allow direct comparison. The modeling (C, D) was provided by Dr. Michael Scholz (GSI, Darmstadt). Whiskers = error bars (see the footer of Supplementary Table ST6 for the calculation of the relative error); fitting curve weighted by:

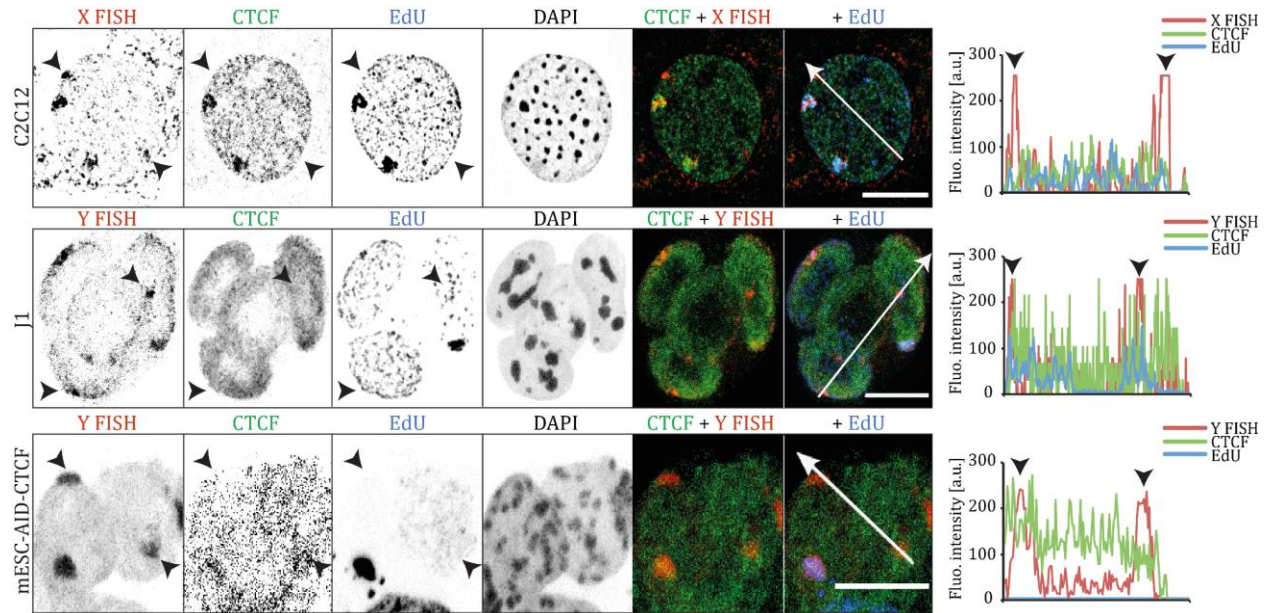
$$\text{Relative error} = \text{mean normalized number of colonies} \times \frac{1}{\sqrt{(\text{mean raw number of colonies})}}$$

Supplementary Figure SF5: Time course validation of the CTCF-degron kinetics.



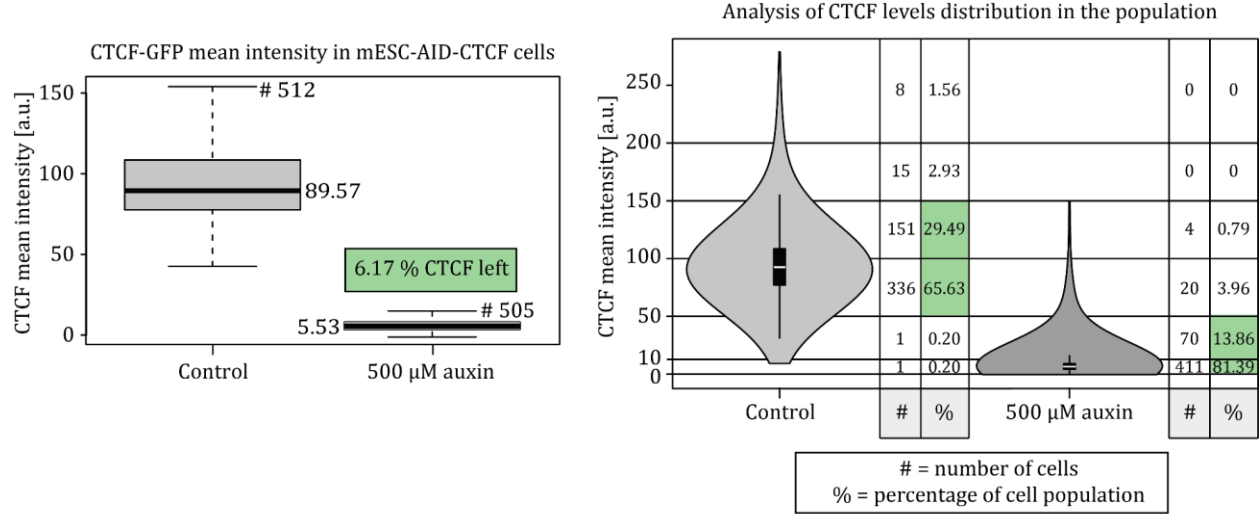
A Experimental scheme of the time course experiment: different auxin concentrations (0, 25, 500, 1000 μM) were applied for 4 hours to mESC-AID-CTCF cells (Supplementary Table ST1), then auxin was washed off and replaced with fresh medium to allow CTCF recovery; cells were collected at different time points during the auxin treatment and upon washing off, imaged with high content microscopy (Supplementary Table ST3) and CTCF intensity values were measured (Supplementary Figure SF1); **B** After subtracting the background measured in untagged WT ES-E14TG2a (Supplementary Table ST1), the mean CTCF-GFP intensities were normalized to (divided by) the median value of the respective time 0 h of each auxin treatment and plotted as boxplots (see Supplementary Figure SF2 for boxplot interpretation). The results are based on three biological replicates.

Supplementary Figure SF6: Anti-colocalization of CTCF and not replicating sex chromosomes.



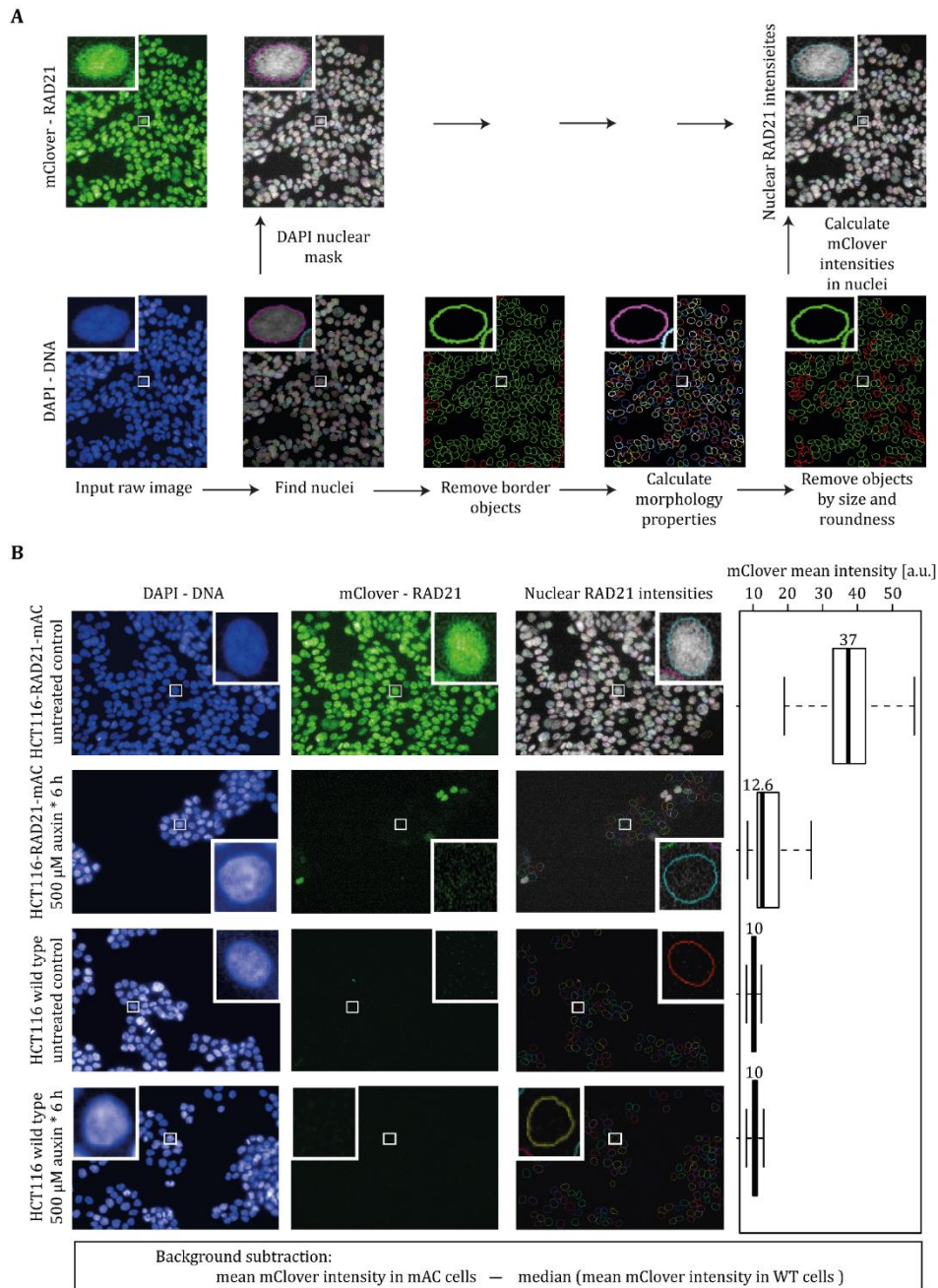
CTCF is not enriched in the not replicating X chromosome (in somatic C2C12 cells) and in the Y chromosome (in J1 and mESC-AID-CTCF mouse embryonic stem cells; Supplementary Table ST1). Cells were processed as described in the legend of Figure 3.2.3. A). In short, cells were fixed upon 30' pulse labeling with 10 μ M EdU. EdU detection, CTCF immunostaining and X or Y chromosome FISH followed (Supplementary Table ST2, ST7 and ST8). After confocal imaging (Supplementary Table ST3), colocalization was visualized with the Fiji software by plotting the color profile along an overlaid arrowed line (white arrow in the merged RGB image of each montage, right side; scale bar: 10 μ m). The corresponding intensity profiles shows that when the sex chromosomes are not replicating, there is no enrichment of CTCF (on the right side of each montage). The not replicating chromosomes are recognized as no EdU signal is overlapping the FISH signal in the images, nor any EdU peak is overlapping the FISH intensity peak in the color profile plots. The overlaid black arrows indicate the not replicating chromosomes in the image montages and the corresponding peak of FISH signal intensity in the color profile plots.

Supplementary Figure SF7: mAID validation relative to Y chromosome experiments.



mESC-AID-CTCF cells (Supplementary Table ST1) were imaged with a high content wide-field microscope (Supplementary Table ST3) and CTCF-GFP-tag nuclear mean intensities were measured. Upon background subtraction as measured in wild type ES-E14TG2a cells (not bearing any GFP-tag; subtracted value: 38.8 a.u.; median in untreated WT: 38.79 a.u., auxin-treated WT: 38.80 a.u.; pipeline in Supplementary Figure SF1), and normalization to the median value in untreated cells, a residual 6% CTCF was calculated in auxin-treated cells. A two-sided Wilcoxon test was performed to test significance ($p < 0.0001$). In particular, circa 80% of auxin-treated cells showed less than 10% residual values and circa 14% cells showed less than 50% residual CTCF, as shown in the right panel (Supplementary Table ST4).

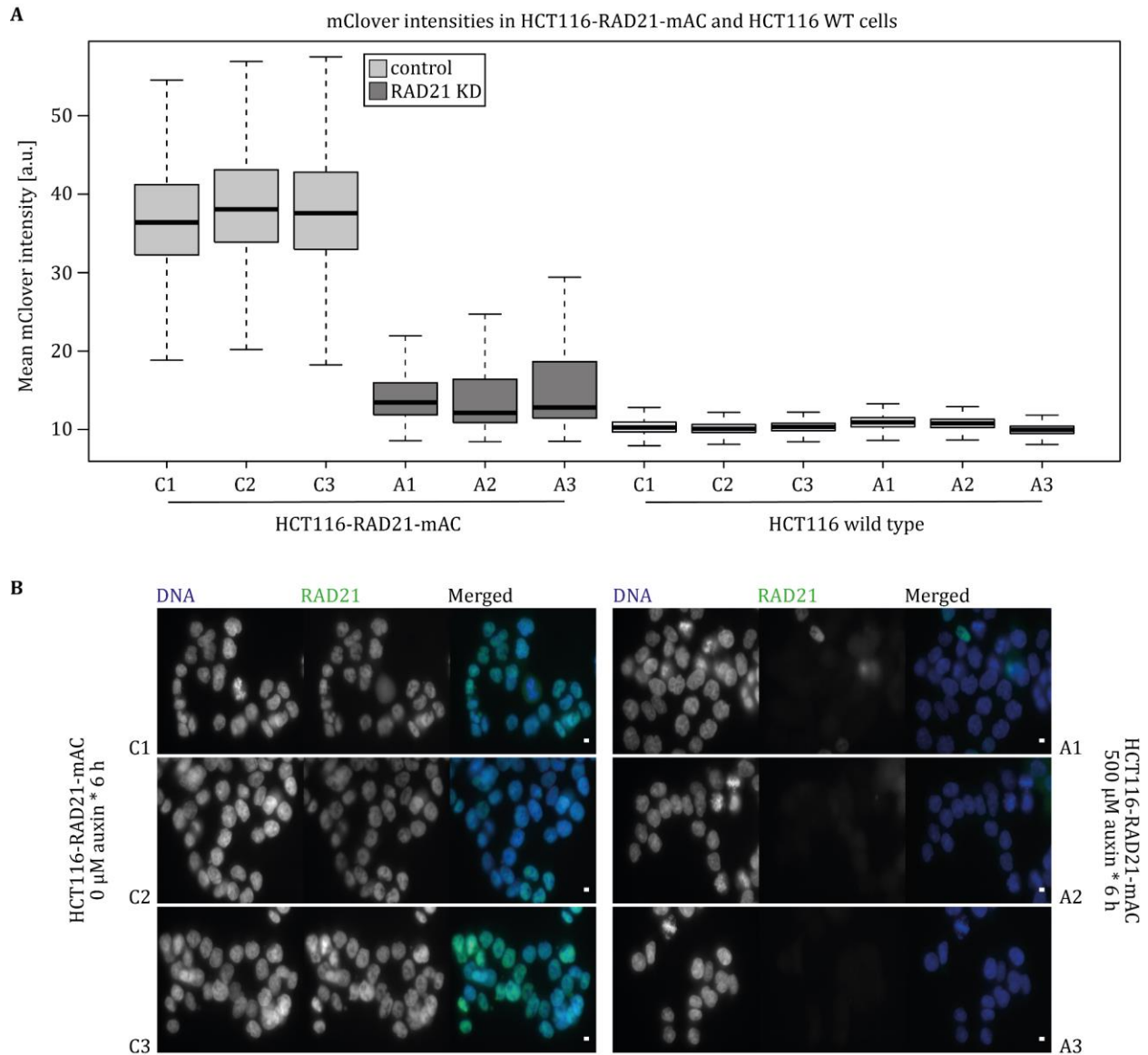
Supplementary Figure SF8: Image analysis pipeline for RAD21 degron validation.



A Pipeline for image analysis of high-content microscopy images. Both untagged WT HCT116 and HCT116-RAD21-mAC cells (Supplementary Table ST1) were imaged with a high-content wide-field microscope (Supplementary Table ST3). White rectangular overlays show a zoom-in of a cell from the shown image field throughout the pipeline. Nuclear masks were segmented based on the DNA - DAPI signal, the nuclei on the borders of each field were removed and the remaining nuclei were selected by morphology characteristics. The RAD21 - mClover (Figure 4.2.1.) nuclear mean intensities were then measured within the selected nuclear masks. For the measurement of SA1 - AF488 (Figure 4.2.3.) or γ H2AX - AF488 (Figure 4.2.4. B) nuclear mean intensities, the same pipeline was used, except background subtraction. **B** Example images of untreated and auxin-treated WT HCT116 and HCT116-RAD21-mAC cells and corresponding mClover nuclear mean intensity.

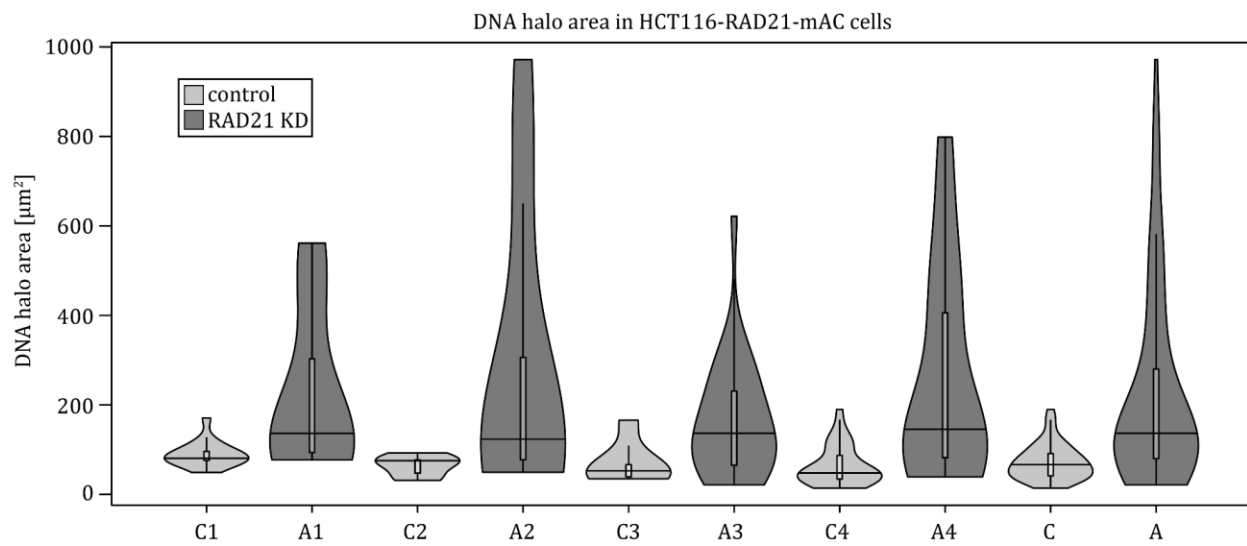
The images on the left side are an example of high-content wide-field microscopy images for each sample. From each image, one cell is selected and shown magnified in the corner (white rectangular areas). The untagged wild type HCT-116 had a median mClover value of 10.23 and 10.56 a.u. in the untreated and auxin-treated WT cells, respectively. A background value of 10 a.u. was therefore subtracted from the engineered HCT116-RAD21-mAC cells to produce the plot shown in Figure 4.2.1. D.

Supplementary Figure SF9: Quantification of RAD21 depletion: single replicates.



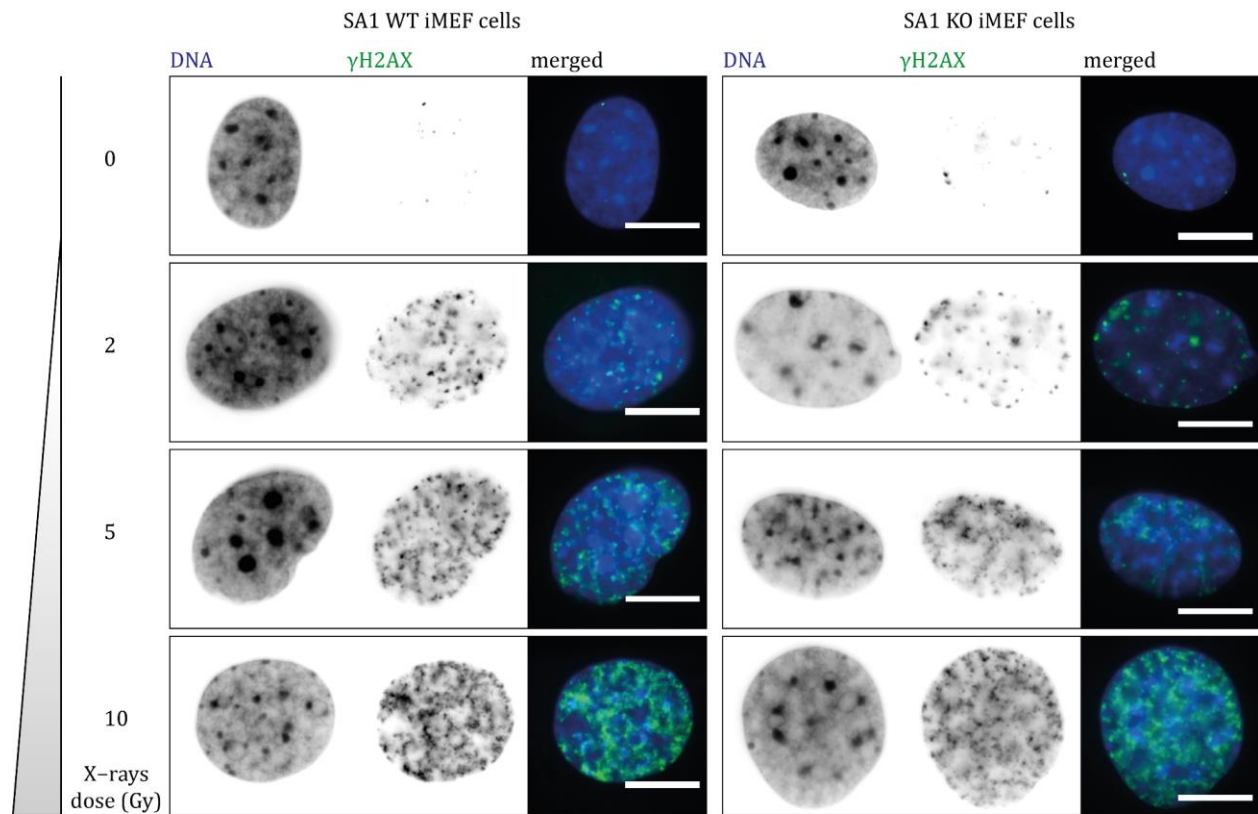
A mClover nuclear mean intensity in WT HCT116 and HCT116-RAD21-mAC cells (Supplementary Table ST1), single replicates. Cells were analyzed as described in Supplementary Figure SF8. The boxplot shows the results for the single biological replicates of each cell line and treatment, which were then merged to obtain the plot in Figure 4.2.1. **D. B** An example of wide-field images is shown as a montage (single channels plus merged image, produced with the Fiji software) for each biological replicate of the untreated and auxin-treated HCT116-RAD21-mAC samples (scale bar: 10 μm). In both **A** and **B**: C = control (0 μM auxin) and A = auxin-treated (500 μM auxin); 1, 2, 3 = number of the biological replicate (statistics in Supplementary Table ST4).

Supplementary Figure SF10: DNA halo area in RAD21-depleted cells: single replicates.



The measurements of DNA halo areas is shown for each biological replicate (1, 2, 3) of the untreated control (C = 0 μM auxin, light gray) and auxin-treated (A = 500 μM auxin, dark gray) HCT116-RAD21-mAC cells (Supplementary Table ST4; see Figure 4.2.2. D for the results comprising all replicates).

Supplementary Figure SF11: Images of SA1 WT/KO iMEF cells after X-rays and γ H2AX detection.



Example of confocal images of X-rays irradiated SA1 WT (left panels) and SA1 KO (right panels) iMEF cells. SA1 WT and KO iMEF cells (Supplementary Table ST1) were irradiated with 0, 2, 5, 10 Gy X-rays and fixed after 30' at 37°C. Upon γ H2AX immunostaining (Supplementary Table ST2), cells were imaged by confocal microscopy (Supplementary Table ST3) and montages of confocal images were produced with the Fiji software (scale bar: 10 μ m). Each montage corresponds to samples irradiated with the X-ray dose indicated on the left side. The corresponding samples were imaged also with high-content wide-field microscopy to measure γ H2AX nuclear mean intensities as shown in Figure 4.2.4. B.

8.2. Supplementary tables

Supplementary Table ST1: Cell line characteristics.

| Name | Species | Type | Identifier | Reference | Thesis chapter |
|---|---------------------|----------------------|---------------------------|-----------------------------------|----------------|
| HeLa Kyoto | <i>Homo sapiens</i> | cervical carcinoma | RRID*: CVCL_1922 | (Erflé <i>et al.</i> , 2007) | 3.1., 3.2. |
| U2OS | <i>Homo sapiens</i> | osteosarcoma | RRID: CVCL_0042 | (Pontén and Saksela, 1967) | 3.1. |
| mESC-AID-CTCF (E14Tg2a OsTir1 CTCF-AID-eGFP) | <i>Mus musculus</i> | embryonic stem | EN52.9.1 | (Nora <i>et al.</i> , 2017) | 3.1., 3.2. |
| ES E14TG2a | <i>Mus musculus</i> | embryonic stem | RRID: CVCL_9108 | (Hooper <i>et al.</i> , 1987) | 3.1., 3.2. |
| ES J1 | <i>Mus musculus</i> | embryonic stem | RRID:CVCL_6412 | (Li <i>et al.</i> , 1992) | 3.2. |
| C2C12 | <i>Mus musculus</i> | myoblast | RRID:CVCL_0188 | (Yaffe and Saxel, 1977) | 3.2. |
| HCT116-RAD21-mAC (HCT116 CMV-OsTIR1 RAD21-mAID-mClover) | <i>Homo sapiens</i> | colon carcinoma | GSE145099 | (Natsume <i>et al.</i> , 2016) | 4.2.1., 4.2.2. |
| HCT116 | <i>Homo sapiens</i> | colon carcinoma | RRID:CVCL_0291 | (Brattain <i>et al.</i> , 1981) | 4.2.1., 4.2.2. |
| iMEF SA1 WT | <i>Mus musculus</i> | embryonic fibroblast | RRID:CVCL_A7BM, AVI2606.3 | (Remeseiro <i>et al.</i> , 2012a) | 4.2.3., 4.2.4. |
| iMEF SA1 KO | <i>Mus musculus</i> | embryonic fibroblast | AVI2606.5 | (Remeseiro <i>et al.</i> , 2012a) | 4.2.3., 4.2.4. |

*RRID: Resource Identification Initiative Identifier

Supplementary Table ST2: Primary and secondary antibody characteristics.

| Reactivity (clone) | Host | Dilution | Application | Cat # | Company/Reference | Thesis chapter |
|--|--------|----------|------------------------|-------------|--|------------------|
| anti-CTCF | rabbit | 1:800 | IF | 2899 | Cell Signaling Technology, Danvers, Massachusetts, USA | 3.1., 3.2. |
| anti-SA1 | rabbit | 1:350 | IF | - | (Remeseiro <i>et al.</i> , 2012a) | 4.2.3. |
| anti-phospho-Histone H2A.X (Ser139) (JBW301) | mouse | 1:800 | IF | 05-636 | Sigma Aldrich, Merck KGaA, Darmstadt, Deutschland | 4.2.4., 5.1. |
| anti-BrdU (for CldU detection) | rabbit | 1:800 | IF | 600-401-C29 | Rockland Immunochemicals, Pottstown, Pennsylvania, USA | 5.1. |
| anti-rabbit IgG AlexaFluor 594 | goat | 1:800 | IF | 111-585-144 | Jackson ImmunoResearch Europe Ltd, Cambridge House, UK | 3.1., 3.2., 5.1. |
| anti-rabbit IgG AlexaFluor 488 | goat | 1:800 | IF | A11034 | Invitrogen, Thermo Fisher, Waltham, Massachusetts, USA | 4.2.3. |
| anti-mouse IgG AlexaFluor 488 | donkey | 1:800 | IF | 715-545-150 | The Jackson Laboratory, Bar Harbor, ME, USA | 4.2.4., 5.1. |
| Streptavidin Cy5 | - | 1:300 | FISH** probe detection | PA45001 | Sigma-Aldrich, St Louis, MO, USA | 3.2.2.3. |

* IF: immunofluorescence; ** FISH: fluorescence *in situ* hybridization.

Supplementary Table ST3: Imaging system characteristics.

| Microscope/ Company | Lasers/ lamps | Filters (ex. & em. [nm]) * | Objectives /lenses | Detection system | Application | Thesis chapter |
|---|---|---|--|---|-----------------------------------|-------------------|
| Operetta® high content screening microscopy/ PerkinElmer Life Sciences, UK | Xenon fiber-optic light source, 300 W, 360 – 640 nm continuous spectrum | 405/488/561** 405: ex.* 360-400 & em.* 410-480 488: ex. 460-490 & em. 500-550 561: ex. 560-580 & em. 590-640 | 40× air (0.95 NA) long WD*** | 14-bit Jenoptik CMOS | high-content screening microscopy | all |
| Leica TCS SP5 II/Leica Microsystems, Wetzlar, Germany | 405 nm diode, 488 nm Argon, 561 nm DPSS, 633 nm HeNe gas | AOBS beam splitter | HCX PL APO 63× / 1.4-0.6 oil lambda blue | 2 HyD Hybrid Detectors | confocal z-stack imaging | 3.2. |
| Axiovert 200/Carl Zeiss Microscopy GmbH, Jena, Germany | HBO100 bulb (FluoArc control) | 405/488/561 405: ex 350-50 & em 460-50 488: ex 482-18 & em 520-28 561: ex 565-30 & em 620-60 | 63×/1.4 NA Plan-Apochromat Oil Ph3 objective | AxioCam mRM/Zeiss | wide-field imaging | 4.2.1. |
| Axioplan 2/Carl Zeiss Microscopy GmbH, Jena, Germany | HBO100 bulb | 405: ex 365-12 & em 397LP | 100×/1.30 NA Plan-Neofluar Oil Ph3 objective | AxioCam mRM/Zeiss | wide-field imaging | 4.2.2. |
| Leica TCS SPE-II/Leica Microsystems, Wetzlar, Germany | 405 nm/25 mW, 488 nm/10 mW, 561 nm/20 mW, 635 nm/18 mW | AOBS beam splitter | 63×/1.30 ACS APO Oil CS 0.17/E 0.16 | Leica SP-Detector | confocal z-stack imaging | 4.2.3., 4.2.4. |
| DeltaVision OMX V3/GE, Chicago, IL, USA | 405, 488 and 593 nm diode lasers | 405: 401-447, 488: 500-550, 594: 603-627 | 100× 1.4 oil immersion objective UPlanSApo (Olympus) | Cascade II:512 EMCCD cameras (Photometrics) | 3D SIM imaging | 5.1. |

*ex.: excitation & em.: emission, ** dichroic specification, *** WD: working distance.

Supplementary Table ST4: Plot statistics.

| Figure | Cell line | # biological replicate / Sample | n* | Median | Mean | StDev** |
|------------------------------------|-----------|------------------------------------|----------|----------|-----------|----------|
| 3.1.1. C | HK | CTCF-stained | 10535 | 211984 | 218612.2 | 71008.61 |
| | U2OS | CTCF-stained | 6189 | 433944 | 472436.1 | 224604.9 |
| | | Secondary Ab | 23062 | 42593 | 44628.13 | 14203.24 |
| 3.1.1. E | HK | CTCF-stained | 10535 | 0.124 | 0.127 | 0.03 |
| | U2OS | CTCF-stained | 6189 | 0.213 | 0.220 | 0.09 |
| 3.1.2. B | HK | #1 GFP KD | 16371 | 119417 | 125964.87 | 48122.56 |
| | | #1 GFP KD ^{norm.} | 16371 | 1 | 1.055 | 0.40 |
| | | #1 CTCF KD – 24 h | 25001 | 74500 | 8018.61 | 34354 |
| | | #1 CTCF KD – 24 h ^{norm.} | 25001 | 0.624 | 0.671 | 0.29 |
| | | #1 CTCF KD – 48 h | 5256 | 106585 | 113491.49 | 46631.52 |
| | | #1 CTCF KD – 48 h ^{norm.} | 5256 | 0.893 | 0.950 | 0.39 |
| | | #1 CTCF KD – 72 h | 10830 | 94238.5 | 96642.94 | 28445.63 |
| | | #1 CTCF KD – 72 h ^{norm.} | 10830 | 0.789 | 0.809 | 0.24 |
| | | #2 GFP KD | 9006 | 187191.5 | 214236.6 | 103824.3 |
| | | #2 GFP KD ^{norm.} | 9006 | 1 | 1.144 | 0.55 |
| | | #2 CTCF KD – 24 h | 1984 | 114575 | 120246.6 | 39725.25 |
| | | #2 CTCF KD – 24 h ^{norm.} | 1984 | 0.612 | 0.642 | 0.21 |
| | | #2 CTCF KD – 48 h | 5325 | 114618 | 120878.1 | 44490.31 |
| | | #2 CTCF KD – 48 h ^{norm.} | 5325 | 0.612 | 0.646 | 0.24 |
| | | #2 CTCF KD – 72 h | 5539 | 122086 | 125749.2 | 40343.11 |
| | | #2 CTCF KD – 72 h ^{norm.} | 5539 | 0.652 | 0.672 | 0.22 |
| | | #3 GFP KD | 25852 | 186725 | 197557.8 | 78690.65 |
| | | #3 GFP KD ^{norm.} | 25852 | 1 | 1.058 | 0.42 |
| | | #3 CTCF KD – 24 h | 4714 | 118828 | 123747 | 39584.56 |
| | | #3 CTCF KD – 24 h ^{norm.} | 4714 | 0.636 | 0.663 | 0.21 |
| | | #3 CTCF KD – 48 h | 4934 | 107419 | 112492.3 | 38473.35 |
| #3 CTCF KD – 48 h ^{norm.} | 4934 | 0.575 | 0.602 | 0.21 | | |
| #3 CTCF KD – 72 h | 8750 | 114225 | 118252.1 | 37748.7 | | |
| #3 CTCF KD – 72 h ^{norm.} | 8750 | 0.612 | 0.633 | 0.20 | | |
| GFP KD ^{merged} | 51229 | 1 | 1.072 | 0.44 | | |
| CTCF KD – 24 h ^{merged} | 31699 | 0.625 | 0.668 | 0.27 | | |
| CTCF KD – 48 h ^{merged} | 15515 | 0.665 | 0.735 | 0.33 | | |
| CTCF KD – 72 h ^{merged} | 25119 | 0.693 | 0.718 | 0.24 | | |

| | | | | | | |
|------------------------------------|------|---------------------------------------|---------|----------|-----------|-----------|
| 3.1.2. C | U2OS | #1 GFP KD | 2648 | 584249.5 | 678319.04 | 351112.56 |
| | | #1 GFP KD ^{norm.} | 2648 | 1 | 1.161 | 0.60 |
| | | #1 CTCF KD – 24 h | 1640 | 298600 | 313054.54 | 87753.73 |
| | | #1 CTCF KD – 24 h ^{norm.} | 1640 | 0.511 | 0.536 | 0.15 |
| | | #1 CTCF KD – 48 h | 2424 | 288488 | 301797.55 | 89412.46 |
| | | #1 CTCF KD – 48 h ^{norm.} | 2424 | 0.494 | 0.517 | 0.15 |
| | | #1 CTCF KD – 72 h | 1174 | 608136.5 | 638074.45 | 260539.93 |
| | | #1 CTCF KD – 72 h ^{norm.} | 1174 | 1.041 | 1.092 | 0.45 |
| | | #2 GFP KD | 1315 | 954110 | 1024028 | 362094.9 |
| | | #2 GFP KD ^{norm.} | 1315 | 1 | 1.073 | 0.38 |
| | | #2 CTCF KD – 24 h | 1040 | 480750 | 536206.3 | 249541.6 |
| | | #2 CTCF – 24 h ^{norm.} | 1040 | 0.504 | 0.562 | 0.26 |
| | | #2 CTCF KD – 48 h | 602 | 534528 | 601806 | 251735.9 |
| | | #2 CTCF KD – 48 h ^{norm.} | 602 | 0.560 | 0.631 | 0.26 |
| | | #2 CTCF KD – 72 h | 471 | 462839 | 478718.1 | 186801.3 |
| | | #2 CTCF KD – 72 h ^{norm.} | 471 | 0.485 | 0.502 | 0.20 |
| | | #3 GFP KD | 317 | 1812784 | 1864035 | 626358.7 |
| | | #3 GFP KD ^{norm.} | 317 | 1 | 1.028 | 0.35 |
| | | #3 CTCF KD – 24 h | 324 | 937947.5 | 985970 | 314408.3 |
| | | #3 CTCF KD – 24 h ^{norm.} | 324 | 0.517 | 0.544 | 0.17 |
| #3 CTCF KD – 48 h | 259 | 1155118 | 1220088 | 467461.1 | | |
| #3 CTCF KD – 48 h ^{norm.} | 259 | 0.637 | 0.673 | 0.26 | | |
| #3 CTCF KD – 72 h | 288 | 1128024 | 1205586 | 470095.8 | | |
| # CTCF KD – 72 h ^{norm.} | 288 | 0.622 | 0.665 | 0.26 | | |
| GFP KD ^{merged} | 4280 | 1 | 1.124 | 0.53 | | |
| CTCF KD – 24 h ^{merged} | 3004 | 0.510 | 0.546 | 0.20 | | |
| CTCF KD – 48 h ^{merged} | 3285 | 0.514 | 0.550 | 0.20 | | |
| CTCF KD – 72 h ^{merged} | 1933 | 0.789 | 0.885 | 0.46 | | |
| 3.1.5. B | AID | #1 – 0 μM ^{AUX} | 2154 | 57.56 | 58.89 | 12.67 |
| | | #2 – 0 μM ^{AUX} | 4292 | 59.69 | 60.00 | 10.85 |
| | | #3 – 0 μM ^{AUX} | 1952 | 57.77 | 58.05 | 11.54 |
| | | #4 – 0 μM ^{AUX} | 3680 | 58.72 | 58.82 | 11.16 |
| | | 0 μM ^{AUX merged} | 12078 | 58.81 | 59.13 | 11.42 |
| | | 0 μM ^{AUX subtr.} | 12078 | 41.86 | 42.18 | 11.42 |
| | | 0 μM ^{AUX norm.} | 12078 | 1 | 1.007 | 0.27 |
| | | #1 – 25 μM ^{AUX} | 3605 | 18.24 | 21.28 | 10.06 |
| | | #2 – 25 μM ^{AUX} | 2284 | 18.16 | 20.27 | 7.55 |
| | | #3 – 25 μM ^{AUX} | 5540 | 19.02 | 20.77 | 6.91 |

| | | | | | | |
|------------|------|--|-------|--------|-------|-------|
| | | #4 – 25 μM ^{AUX} | 6274 | 18.55 | 20.00 | 6.17 |
| | | 25 μM ^{AUX merged} | 17703 | 18.58 | 20.54 | 7.53 |
| | | 25 μM ^{AUX subtr.} | 17703 | 1.63 | 3.59 | 7.53 |
| | | 25 μM ^{AUX norm.} | 17703 | 0.039 | 0.086 | 0.18 |
| | AID | #1 – 500 μM ^{AUX} | 2215 | 17.66 | 19.13 | 6.00 |
| | | #2 – 500 μM ^{AUX} | 3163 | 16.38 | 17.96 | 6.66 |
| | | #3 – 500 μM ^{AUX} | 4349 | 16.22 | 19.37 | 10.37 |
| | | #4 – 500 μM ^{AUX} | 7708 | 15.68 | 16.68 | 4.90 |
| | | 500 μM ^{AUX merged} | 17435 | 16.17 | 17.90 | 7.17 |
| | | 500 μM ^{AUX subtr.} | 17435 | -0.78 | 0.95 | 7.17 |
| | | 500 μM ^{AUX norm.} | 17435 | -0.019 | 0.023 | 0.17 |
| | AID | #1 – 1000 μM ^{AUX} | 2082 | 15.56 | 17.19 | 6.83 |
| | | #2 – 1000 μM ^{AUX} | 3129 | 16.28 | 17.63 | 6.55 |
| | | #3 – 1000 μM ^{AUX} | 1535 | 17.04 | 18.14 | 5.37 |
| | | #4 – 1000 μM ^{AUX} | 4162 | 16.57 | 17.66 | 5.04 |
| | | 1000 μM ^{AUX merged} | 10908 | 16.31 | 17.63 | 5.92 |
| | | 1000 μM ^{AUX subtr.} | 10908 | -0.64 | 0.68 | 5.92 |
| | | 1000 μM ^{AUX norm.} | 10908 | -0.015 | 0.016 | 0.14 |
| | ES14 | WT untagged | 47399 | 16.95 | 18.35 | 5.46 |
| SF5 | AID | #1 – 25 μM – 0 h ^{AUX} | 3480 | 49.53 | 50.03 | 9.05 |
| | | #1 – 25 μM – 0.5 h ^{AUX} | 1763 | 64.69 | 65.08 | 13.12 |
| | | #1 – 25 μM – 1 h ^{AUX} | 1944 | 58.29 | 58.42 | 13.45 |
| | | #1 – 25 μM – 2 h ^{AUX} | 2017 | 34.05 | 34.96 | 12.67 |
| | | #1 – 25 μM – 3 h ^{AUX} | 2910 | 28.04 | 30.54 | 11.27 |
| | | #1 – 25 μM – 4 h ^{AUX} | 4086 | 22.23 | 25.83 | 9.46 |
| | | #1 – 25 μM – 0.5 h ^{WA} | 3411 | 20.53 | 23.25 | 7.62 |
| | | #1 – 25 μM – 1 h ^{WA} | 4325 | 25.83 | 29.51 | 10.25 |
| | | #1 – 25 μM – 2 h ^{WA} | 2981 | 26.75 | 29.62 | 8.98 |
| | | #1 – 25 μM – 4 h ^{WA} | 7432 | 28.37 | 29.98 | 6.89 |
| | | #1 – 25 μM – 6 h ^{WA} | 2725 | 41.23 | 42.83 | 9.84 |
| | | #1 – 25 μM – 8 h ^{WA} | 4082 | 36.71 | 37.28 | 7.15 |
| | | #1 – 25 μM – 18 h ^{WA} | 6337 | 76.32 | 76.21 | 14.50 |
| | | #1 – 25 μM – 24 h ^{WA} | 11137 | 58.32 | 61.36 | 14.15 |
| | | #2 – 25 μM – 0 h ^{AUX} | 2622 | 54.02 | 54.33 | 8.64 |
| | | #2 – 25 μM – 0.5 h ^{AUX} | 2171 | 59.39 | 59.09 | 11.77 |
| | | #2 – 25 μM – 1 h ^{AUX} | 3918 | 51.00 | 51.24 | 9.45 |
| | | #2 – 25 μM – 2 h ^{AUX} | 5749 | 44.53 | 44.69 | 15.06 |
| | | #2 – 25 μM – 3 h ^{AUX} | 2915 | 28.92 | 31.13 | 11.51 |
| | | #2 – 25 μM – 4 h ^{AUX} | 2305 | 22.39 | 27.00 | 11.11 |
| | | #2 – 25 μM – 0.5 h ^{WA} | 2977 | 22.53 | 27.03 | 10.75 |
| | | #2 – 25 μM – 1 h ^{WA} | 2341 | 21.74 | 25.80 | 9.74 |
| | | #2 – 25 μM – 2 h ^{WA} | 4189 | 24.66 | 28.20 | 9.77 |
| | | #2 – 25 μM – 4 h ^{WA} | 4935 | 34.32 | 36.28 | 8.99 |
| | | #2 – 25 μM – 6 h ^{WA} | 3822 | 40.06 | 41.74 | 9.79 |
| | | #2 – 25 μM – 8 h ^{WA} | 3810 | 41.11 | 42.63 | 9.51 |
| | | #2 – 25 μM – 24 h ^{WA} | 9749 | 75.08 | 75.00 | 13.97 |
| | | #3 – 25 μM – 0 h ^{AUX} | 812 | 43.31 | 43.48 | 6.65 |

| | | | | | | |
|--|-----|--|-------|-------|-------|-------|
| | | #3 – 25 μ M – 0.5 h ^{AUX} | 1715 | 60.53 | 61.02 | 10.47 |
| | | #3 – 25 μ M – 1 h ^{AUX} | 3915 | 51.99 | 52.21 | 10.14 |
| | | #3 – 25 μ M – 2 h ^{AUX} | 6539 | 32.95 | 33.20 | 10.32 |
| | | #3 – 25 μ M – 3 h ^{AUX} | 4591 | 29.23 | 32.19 | 12.69 |
| | | #3 – 25 μ M – 4 h ^{AUX} | 3153 | 20.29 | 23.18 | 7.85 |
| | | #3 – 25 μ M – 0.5 h ^{WA} | 3054 | 21.17 | 23.73 | 7.04 |
| | | #3 – 25 μ M – 1 h ^{WA} | 2072 | 24.52 | 27.75 | 10.31 |
| | | #3 – 25 μ M – 2 h ^{WA} | 3046 | 42.70 | 45.09 | 12.88 |
| | | #3 – 25 μ M – 4 h ^{WA} | 846 | 41.35 | 46.53 | 20.77 |
| | | #3 – 25 μ M – 6 h ^{WA} | 769 | 56.41 | 59.07 | 16.39 |
| | | #3 – 25 μ M – 8 h ^{WA} | 1404 | 51.30 | 53.55 | 18.11 |
| | | #3 – 25 μ M – 18 h ^{WA} | 5461 | 83.89 | 83.08 | 14.49 |
| | | #3 – 25 μ M – 24 h ^{WA} | 3929 | 67.43 | 68.02 | 14.81 |
| | | 25 μ M – 0 h ^{AUX merged} | 6914 | 50.29 | 50.89 | 9.27 |
| | | 25 μ M – 0.5 h ^{AUX merged} | 5649 | 61.16 | 61.54 | 12.11 |
| | | 25 μ M – 1 h ^{AUX merged} | 9777 | 52.5 | 53.06 | 10.96 |
| | | 25 μ M – 2 h ^{AUX merged} | 14305 | 36.78 | 38.06 | 13.87 |
| | | 25 μ M – 3 h ^{AUX merged} | 10416 | 28.80 | 31.43 | 12.00 |
| | | 25 μ M – 4 h ^{AUX merged} | 9544 | 21.64 | 25.24 | 9.53 |
| | | 25 μ M – 0.5 h ^{WA merged} | 9442 | 21.42 | 24.60 | 8.73 |
| | | 25 μ M – 1 h ^{WA merged} | 8738 | 24.61 | 28.10 | 10.25 |
| | | 25 μ M – 2 h ^{WA merged} | 10216 | 30.43 | 33.65 | 12.97 |
| | | 25 μ M – 4 h ^{WA merged} | 13213 | 30.87 | 33.39 | 10.26 |
| | | 25 μ M – 6 h ^{WA merged} | 7316 | 41.51 | 43.97 | 11.89 |
| | | 25 μ M – 8 h ^{WA merged} | 9296 | 39.46 | 41.93 | 11.79 |
| | | 25 μ M – 18 h ^{WA merged} | 11798 | 79.51 | 79.39 | 14.90 |
| | | 25 μ M – 24 h ^{WA merged} | 24815 | 65.62 | 67.77 | 15.50 |
| | | 25 μ M – 0 h ^{AUX norm.} | 6914 | 1 | 1.02 | 0.29 |
| | | 25 μ M – 0.5 h ^{AUX norm.} | 5649 | 1.35 | 1.36 | 0.38 |
| | | 25 μ M – 1 h ^{AUX norm.} | 9777 | 1.07 | 1.09 | 0.35 |
| | | 25 μ M – 2 h ^{AUX norm.} | 14305 | 0.57 | 0.61 | 0.44 |
| | | 25 μ M – 3 h ^{AUX norm.} | 10416 | 0.32 | 0.40 | 0.38 |
| | | 25 μ M – 4 h ^{AUX norm.} | 9544 | 0.09 | 0.20 | 0.30 |
| | | 25 μ M – 0.5 h ^{WA norm.} | 9442 | 0.08 | 0.18 | 0.28 |
| | | 25 μ M – 1 h ^{WA norm.} | 8738 | 0.18 | 0.29 | 0.33 |
| | | 25 μ M – 2 h ^{WA norm.} | 10216 | 0.37 | 0.47 | 0.41 |
| | | 25 μ M – 4 h ^{WA norm.} | 13213 | 0.38 | 0.46 | 0.33 |
| | | 25 μ M – 6 h ^{WA norm.} | 7316 | 0.72 | 0.80 | 0.38 |
| | | 25 μ M – 8 h ^{WA norm.} | 9296 | 0.66 | 0.73 | 0.37 |
| | | 25 μ M – 18 h ^{WA norm.} | 11798 | 1.93 | 1.92 | 0.47 |
| | | 25 μ M – 24 h ^{WA norm.} | 24815 | 1.49 | 1.56 | 0.49 |
| | AID | #1 – 500 μ M – 0 h ^{AUX} | 3236 | 54.88 | 55.18 | 10.43 |
| | | #1 – 500 μ M – 0.5 h ^{AUX} | 2996 | 54.77 | 55.74 | 9.32 |
| | | #1 – 500 μ M – 1 h ^{AUX} | 2842 | 46.58 | 46.02 | 12.25 |
| | | #1 – 500 μ M – 2 h ^{AUX} | 2982 | 21.09 | 25.95 | 11.69 |
| | | #1 – 500 μ M – 3 h ^{AUX} | 1640 | 17.92 | 24.51 | 12.61 |
| | | #1 – 500 μ M – 4 h ^{AUX} | 3600 | 16.73 | 19.52 | 7.69 |
| | | #1 – 500 μ M – 0.5 h ^{WA} | 2536 | 19.83 | 22.63 | 8.25 |
| | | #1 – 500 μ M – 1 h ^{WA} | 740 | 15.08 | 16.07 | 3.48 |
| | | #1 – 500 μ M – 2 h ^{WA} | 4373 | 20.89 | 22.99 | 7.52 |

| | | | | |
|---|-------|-------|-------|-------|
| #1 – 500 μ M – 4 h ^{WA} | 2523 | 24.55 | 27.49 | 10.28 |
| #1 – 500 μ M – 6 h ^{WA} | 4198 | 29.00 | 32.74 | 12.38 |
| #1 – 500 μ M – 8 h ^{WA} | 4150 | 31.69 | 32.04 | 6.31 |
| #1 – 500 μ M – 18 h ^{WA} | 4931 | 44.62 | 44.95 | 8.26 |
| #1 – 500 μ M – 24 h ^{WA} | 8888 | 56.60 | 57.00 | 11.75 |
| #2 – 500 μ M – 0 h ^{AUX} | 2471 | 61.28 | 61.95 | 11.04 |
| #2 – 500 μ M – 0.5 h ^{AUX} | 1351 | 64.48 | 64.03 | 13.79 |
| #2 – 500 μ M – 1 h ^{AUX} | 3655 | 46.01 | 46.53 | 9.49 |
| #2 – 500 μ M – 2 h ^{AUX} | 3706 | 25.35 | 29.06 | 12.24 |
| #2 – 500 μ M – 3 h ^{AUX} | 4582 | 25.49 | 30.17 | 12.63 |
| #2 – 500 μ M – 4 h ^{AUX} | 4131 | 19.25 | 22.31 | 8.13 |
| #2 – 500 μ M – 0.5 h ^{WA} | 7104 | 22.60 | 25.83 | 9.26 |
| #2 – 500 μ M – 1 h ^{WA} | 2988 | 26.46 | 29.14 | 8.42 |
| #2 – 500 μ M – 2 h ^{WA} | 2938 | 23.01 | 25.15 | 7.13 |
| #2 – 500 μ M – 4 h ^{WA} | 3342 | 31.27 | 32.93 | 7.95 |
| #2 – 500 μ M – 6 h ^{WA} | 2163 | 29.54 | 30.67 | 7.07 |
| #2 – 500 μ M – 8 h ^{WA} | 4596 | 37.24 | 38.69 | 9.90 |
| #2 – 500 μ M – 18 h ^{WA} | 4765 | 67.91 | 68.95 | 16.30 |
| #2 – 500 μ M – 24 h ^{WA} | 5607 | 54.27 | 54.70 | 9.94 |
| #3 – 500 μ M – 0 h ^{AUX} | 2482 | 45.91 | 46.45 | 8.09 |
| #3 – 500 μ M – 0.5 h ^{AUX} | 2156 | 56.63 | 56.52 | 10.58 |
| #3 – 500 μ M – 1 h ^{AUX} | 3006 | 50.13 | 49.93 | 10.41 |
| #3 – 500 μ M – 2 h ^{AUX} | 3253 | 33.04 | 35.18 | 13.41 |
| #3 – 500 μ M – 3 h ^{AUX} | 4506 | 25.79 | 29.54 | 10.20 |
| #3 – 500 μ M – 4 h ^{AUX} | 3613 | 24.07 | 27.44 | 8.89 |
| #3 – 500 μ M – 0.5 h ^{WA} | 1311 | 21.28 | 24.37 | 8.55 |
| #3 – 500 μ M – 1 h ^{WA} | 2981 | 23.31 | 26.19 | 8.12 |
| #3 – 500 μ M – 2 h ^{WA} | 1690 | 22.33 | 24.43 | 7.06 |
| #3 – 500 μ M – 4 h ^{WA} | 2840 | 24.16 | 26.22 | 8.29 |
| #3 – 500 μ M – 6 h ^{WA} | 2738 | 32.16 | 33.32 | 7.72 |
| #3 – 500 μ M – 8 h ^{WA} | 3708 | 33.98 | 34.79 | 7.02 |
| #3 – 500 μ M – 18 h ^{WA} | 7116 | 56.93 | 58.05 | 11.92 |
| #3 – 500 μ M – 24 h ^{WA} | 6922 | 71.66 | 71.23 | 14.82 |
| 500 μ M – 0 h ^{AUX merged} | 8189 | 53.73 | 54.57 | 11.67 |
| 500 μ M – 0.5 h ^{AUX merged} | 6503 | 56.75 | 57.72 | 11.28 |
| 500 μ M – 1 h ^{AUX merged} | 9503 | 47.47 | 47.45 | 10.80 |
| 500 μ M – 2 h ^{AUX merged} | 9941 | 26.83 | 30.13 | 13.03 |
| 500 μ M – 3 h ^{AUX merged} | 10728 | 24.90 | 29.04 | 11.83 |
| 500 μ M – 4 h ^{AUX merged} | 11344 | 20.16 | 23.06 | 8.85 |
| 500 μ M – 0.5 h ^{WA merged} | 10951 | 21.83 | 24.92 | 9.05 |
| 500 μ M – 1 h ^{WA merged} | 6709 | 24.38 | 26.39 | 8.80 |
| 500 μ M – 2 h ^{WA merged} | 9001 | 21.74 | 23.96 | 7.38 |
| 500 μ M – 4 h ^{WA merged} | 8705 | 26.71 | 29.17 | 9.30 |
| 500 μ M – 6 h ^{WA merged} | 9099 | 30.22 | 32.42 | 10.08 |
| 500 μ M – 8 h ^{WA merged} | 12454 | 34.07 | 35.32 | 8.48 |
| 500 μ M – 18 h ^{WA merged} | 16812 | 55.06 | 57.30 | 15.45 |
| 500 μ M – 24 h ^{WA merged} | 21417 | 59.36 | 60.99 | 14.32 |
| 500 μ M – 0 h ^{AUX norm.} | 8189 | 1 | 1.02 | 0.33 |
| 500 μ M – 0.5 h ^{AUX norm.} | 6503 | 1.09 | 1.11 | 0.32 |

| | | | | | | |
|--|-----|-------------------------------------|-------|-------|-------|-------|
| | | 500 µM – 1 h ^{AUX} norm. | 9503 | 0.82 | 0.82 | 0.31 |
| | | 500 µM – 2 h ^{AUX} norm. | 9941 | 0.23 | 0.32 | 0.37 |
| | | 500 µM – 3 h ^{AUX} norm. | 10728 | 0.17 | 0.29 | 0.34 |
| | | 500 µM – 4 h ^{AUX} norm. | 11344 | 0.04 | 0.12 | 0.25 |
| | | 500 µM – 0.5 h ^{WA} norm. | 10951 | 0.09 | 0.17 | 0.26 |
| | | 500 µM – 1 h ^{WA} norm. | 6709 | 0.16 | 0.22 | 0.25 |
| | | 500 µM – 2 h ^{WA} norm. | 9001 | 0.08 | 0.15 | 0.21 |
| | | 500 µM – 4 h ^{WA} norm. | 8705 | 0.23 | 0.30 | 0.27 |
| | | 500 µM – 6 h ^{WA} norm. | 9099 | 0.33 | 0.39 | 0.29 |
| | | 500 µM – 8 h ^{WA} norm. | 12454 | 0.44 | 0.47 | 0.24 |
| | | 500 µM – 18 h ^{WA} norm. | 16812 | 1.04 | 1.10 | 0.44 |
| | | 500 µM – 24 h ^{WA} norm. | 21417 | 1.16 | 1.21 | 0.41 |
| | AID | #1 – 1000 µM – 0 h ^{AUX} | 2026 | 59.79 | 60.26 | 10.73 |
| | | #1 – 1000 µM – 0.5 h ^{AUX} | 1805 | 71.94 | 71.74 | 14.92 |
| | | #1 – 1000 µM – 1 h ^{AUX} | 4211 | 52.24 | 53.49 | 18.07 |
| | | #1 – 1000 µM – 2 h ^{AUX} | 2863 | 20.56 | 25.09 | 12.04 |
| | | #1 – 1000 µM – 3 h ^{AUX} | 4205 | 22.00 | 24.76 | 10.83 |
| | | #1 – 1000 µM – 4 h ^{AUX} | 5232 | 20.93 | 23.18 | 8.11 |
| | | #1 – 1000 µM – 0.5 h ^{WA} | 4139 | 18.17 | 20.32 | 6.33 |
| | | #1 – 1000 µM – 1 h ^{WA} | 4184 | 19.38 | 21.27 | 6.56 |
| | | #1 – 1000 µM – 2 h ^{WA} | 1070 | 22.05 | 23.68 | 6.99 |
| | | #1 – 1000 µM – 4 h ^{WA} | 2975 | 27.55 | 29.65 | 8.91 |
| | | #1 – 1000 µM – 6 h ^{WA} | 5131 | 29.31 | 31.88 | 9.66 |
| | | #1 – 1000 µM – 8 h ^{WA} | 3891 | 42.12 | 43.90 | 11.39 |
| | | #1 – 1000 µM – 18 h ^{WA} | 6405 | 47.03 | 48.06 | 11.13 |
| | | #1 – 1000 µM – 24 h ^{WA} | 10508 | 55.15 | 55.73 | 11.31 |
| | | #2 – 1000 µM – 0 h ^{AUX} | 5519 | 50.28 | 50.88 | 7.95 |
| | | #2 – 1000 µM – 0.5 h ^{AUX} | 3005 | 61.79 | 61.94 | 14.52 |
| | | #2 – 1000 µM – 1 h ^{AUX} | 1321 | 61.29 | 61.88 | 17.06 |
| | | #2 – 1000 µM – 2 h ^{AUX} | 2386 | 39.20 | 42.63 | 16.36 |
| | | #2 – 1000 µM – 3 h ^{AUX} | 352 | 19.54 | 25.09 | 12.24 |
| | | #2 – 1000 µM – 4 h ^{AUX} | 892 | 24.22 | 27.21 | 10.69 |
| | | #2 – 1000 µM – 0.5 h ^{WA} | 961 | 23.92 | 27.77 | 11.74 |
| | | #2 – 1000 µM – 1 h ^{WA} | 2264 | 30.39 | 33.54 | 12.72 |
| | | #2 – 1000 µM – 2 h ^{WA} | 881 | 21.46 | 24.19 | 8.31 |
| | | #2 – 1000 µM – 4 h ^{WA} | 997 | 31.56 | 34.49 | 11.75 |
| | | #2 – 1000 µM – 6 h ^{WA} | 185 | 34.24 | 36.72 | 10.91 |
| | | #2 – 1000 µM – 8 h ^{WA} | 1634 | 36.32 | 39.25 | 14.13 |
| | | #2 – 1000 µM – 18 h ^{WA} | 1963 | 44.33 | 44.71 | 8.41 |
| | | #2 – 1000 µM – 24 h ^{WA} | 6638 | 60.73 | 61.65 | 14.68 |
| | | #3 – 1000 µM – 0 h ^{AUX} | 2779 | 40.53 | 40.96 | 6.60 |
| | | #3 – 1000 µM – 0.5 h ^{AUX} | 3030 | 43.38 | 43.44 | 7.38 |
| | | #3 – 1000 µM – 1 h ^{AUX} | 2254 | 34.64 | 34.82 | 8.78 |
| | | #3 – 1000 µM – 2 h ^{AUX} | 4731 | 20.44 | 24.50 | 11.02 |
| | | #3 – 1000 µM – 3 h ^{AUX} | 2707 | 18.41 | 23.83 | 12.28 |
| | | #3 – 1000 µM – 4 h ^{AUX} | 10032 | 17.69 | 21.42 | 9.40 |
| | | #3 – 1000 µM – 0.5 h ^{WA} | 3368 | 19.33 | 21.43 | 6.31 |
| | | #3 – 1000 µM – 1 h ^{WA} | 2743 | 22.21 | 24.35 | 6.96 |
| | | #3 – 1000 µM – 2 h ^{WA} | 1687 | 20.64 | 21.66 | 5.15 |
| | | #3 – 1000 µM – 4 h ^{WA} | 3324 | 20.76 | 21.86 | 4.48 |

| | | | | | | |
|-----------------|-------|--|-------|--------|--------|-------|
| | | #3 – 1000 μ M – 6 h ^{WA} | 2638 | 36.11 | 37.62 | 9.34 |
| | | #3 – 1000 μ M – 18 h ^{WA} | 6374 | 59.64 | 60.16 | 12.36 |
| | | #3 – 1000 μ M – 24 h ^{WA} | 12886 | 45.02 | 45.26 | 7.37 |
| | | 1000 μ M – 0 h ^{AUX merged} | 10324 | 49.22 | 50.05 | 10.54 |
| | | 1000 μ M – 0.5 h ^{AUX merged} | 7840 | 54.31 | 57.05 | 16.84 |
| | | 1000 μ M – 1 h ^{AUX merged} | 7786 | 46.52 | 49.51 | 18.58 |
| | | 1000 μ M – 2 h ^{AUX merged} | 9980 | 25.14 | 29.00 | 14.88 |
| | | 1000 μ M – 3 h ^{AUX merged} | 7264 | 20.60 | 24.43 | 11.47 |
| | | 1000 μ M – 4 h ^{AUX merged} | 16156 | 18.76 | 22.31 | 9.20 |
| | | 1000 μ M – 0.5 h ^{WA merged} | 8468 | 19.11 | 21.60 | 7.49 |
| | | 1000 μ M – 1 h ^{WA merged} | 9191 | 21.78 | 25.21 | 9.91 |
| | | 1000 μ M – 2 h ^{WA merged} | 3638 | 21.28 | 22.87 | 6.69 |
| | | 1000 μ M – 4 h ^{WA merged} | 7296 | 24.83 | 26.76 | 9.10 |
| | | 1000 μ M – 6 h ^{WA merged} | 7954 | 31.43 | 33.90 | 9.96 |
| | | 1000 μ M – 8 h ^{WA merged} | 5525 | 41.05 | 42.52 | 12.44 |
| | | 1000 μ M – 18 h ^{WA merged} | 14742 | 51.22 | 52.85 | 13.09 |
| | | 1000 μ M – 24 h ^{WA merged} | 30032 | 50.57 | 52.55 | 12.66 |
| | | 1000 μ M – 0 h ^{AUX norm.} | 10324 | 1 | 1.03 | 0.35 |
| | | 1000 μ M – 0.5 h ^{AUX norm.} | 7840 | 1.17 | 1.26 | 0.55 |
| | | 1000 μ M – 1 h ^{AUX norm.} | 7786 | 0.91 | 1.01 | 0.61 |
| | | 1000 μ M – 2 h ^{AUX norm.} | 9980 | 0.21 | 0.33 | 0.49 |
| | | 1000 μ M – 3 h ^{AUX norm.} | 7264 | 0.06 | 0.18 | 0.38 |
| | | 1000 μ M – 4 h ^{AUX norm.} | 16156 | -0.002 | 0.11 | 0.30 |
| | | 1000 μ M – 0.5 h ^{WA norm.} | 8468 | 0.009 | 0.09 | 0.25 |
| | | 1000 μ M – 1 h ^{WA norm.} | 9191 | 0.10 | 0.21 | 0.33 |
| | | 1000 μ M – 2 h ^{WA norm.} | 3638 | 0.08 | 0.13 | 0.22 |
| | | 1000 μ M – 4 h ^{WA norm.} | 7296 | 0.20 | 0.26 | 0.30 |
| | | 1000 μ M – 6 h ^{WA norm.} | 7954 | 0.41 | 0.50 | 0.33 |
| | | 1000 μ M – 8 h ^{WA norm.} | 5525 | 0.73 | 0.78 | 0.41 |
| | | 1000 μ M – 18 h ^{WA norm.} | 14742 | 1.07 | 1.12 | 0.43 |
| | | 1000 μ M – 24 h ^{WA norm.} | 30032 | 1.04 | 1.11 | 0.42 |
| | ES14 | WT untagged | 13829 | 18.82 | 22.12 | 11.42 |
| 3.2.1. E | HK | 0 h Chase | 64127 | 64.00 | 67.11 | 12.84 |
| | | 2 h Chase | 59362 | 53.33 | 55.57 | 12.23 |
| | | 4 h Chase | 86122 | 44.00 | 45.13 | 9.43 |
| 3.2.2. C | C2C12 | Control | 1250 | 116.79 | 120.70 | 26.97 |
| | | CTCF KD | 1476 | 51.33 | 51.24 | 15.11 |
| 3.2.2. D | C2C12 | Highest CTCF KD | 135 | 25.07 | 24.48 | 3.84 |
| | | Medium CTCF KD | 182 | 35.34 | 35.15 | 2.89 |
| | | Low CTCF KD | 355 | 46.14 | 45.75 | 2.72 |
| 3.2.3. B | C2C12 | Replicating X chromosome | 27 | 22.63 | 23.42 | 3.22 |
| | | Not replicating X chrom. | 28 | 20.41 | 20.15 | 4.81 |

| | | | | | | | |
|-----------------|-----------|--|--|----------|----------|----------|------|
| | | ROIs | 27 | 20.66 | 20.73 | 4.06 | |
| | J1 | Replicating Y chromosome | 6 | 26.09 | 24.44 | 6.85 | |
| | | Not replicating Y chrom. | 6 | 20.22 | 20.56 | 5.08 | |
| | | ROIs | 12 | 24.54 | 22.81 | 4.90 | |
| | AID | Replicating Y chromosome | 12 | 20.82 | 20.68 | 3.32 | |
| | | Not replicating Y chrom. | 7 | 17.88 | 18.50 | 1.67 | |
| | | ROIs | 19 | 17.14 | 16.91 | 2.41 | |
| 3.2.3. E | AID | Control - 0 μM^{AUX} | 12 | 96.25 | 106.83 | 42.47 | |
| | | CTCF-depleted - 500 μM^{AUX} | 37 | 23.59 | 32.93 | 26.02 | |
| 3.2.3. G | AID | Control - 0 μM^{AUX} | 12 | 43042.50 | 46687.92 | 15747.20 | |
| | | 500 μM^{AUX} - synchr. Y | 12 | 16814.00 | 17548.23 | 8878.54 | |
| | | 500 μM^{AUX} - asynchr. Y | 25 | 7987.00 | 9396.76 | 4851.17 | |
| 3.2.3. I | AID | Control - 0 μM^{AUX} | 24 | 7.90 | 8.07 | 3.12 | |
| | | CTCF-depleted - 500 μM^{AUX} | 54 | 6.32 | 7.15 | 3.32 | |
| 3.2.3. J | AID | Control - 0 μM^{AUX} | 24 | 0.39 | 0.37 | 0.08 | |
| | | CTCF-depleted - 500 μM^{AUX} | 54 | 0.34 | 0.34 | 0.07 | |
| 3.2.3. K | AID | Control - 0 μM^{AUX} | 24 | 49.26 | 54.04 | 19.11 | |
| | | CTCF-depleted - 500 μM^{AUX} | 54 | 48.5 | 54.20 | 20.77 | |
| SF7 | AID | 0 μM^{AUX} | 512 | 128.37 | 134.86 | 29.45 | |
| | | 0 μM^{AUX} subtr. | 512 | 89.57 | 96.06 | 29.45 | |
| | | 500 μM^{AUX} | 505 | 44.33 | 49.49 | 17.90 | |
| | | 500 μM^{AUX} subtr. | 505 | 5.53 | 10.69 | 17.90 | |
| | ES14 | WT untagged | 1100 | 38.79 | 39.75 | 5.25 | |
| 4.2.1. D | RAD21-mAC | #1 - 0 μM^{AUX} | 9594 | 36.41 | 37.15 | 7.45 | |
| | | #2 - 0 μM^{AUX} | 9280 | 38.08 | 39.37 | 9.18 | |
| | | #3 - 0 μM^{AUX} | 8645 | 37.59 | 38.44 | 8.46 | |
| | | 0 μM^{AUX} merged | 27519 | 37.34 | 38.30 | 8.43 | |
| | | 0 μM^{AUX} subtr. | 27467 | 27.33 | 28.22 | 8.19 | |
| | | | #1 - 500 μM^{AUX} | 2255 | 13.45 | 16.57 | 8.30 |
| | | | #2 - 500 μM^{AUX} | 8241 | 12.12 | 15.60 | 7.90 |
| | | | #3 - 500 μM^{AUX} | 11008 | 12.80 | 16.61 | 8.43 |
| | | | 500 μM^{AUX} merged | 21504 | 12.63 | 16.22 | 8.23 |
| | | | 500 μM^{AUX} subtr. | 21496 | 2.62 | 6.18 | 8.05 |
| | | RAD21-WT | 0 μM^{AUX} merged | 27653 | 10.23 | 10.48 | 1.96 |
| | | | 500 μM^{AUX} merged | 34097 | 10.56 | 10.69 | 1.55 |
| | | | 0 μM^{AUX} + 500 μM^{AUX} merged | 61750 | 10.40 | 10.60 | 1.74 |

| | | | | | | |
|----------|-----------|---|------|---------|---------|---------|
| 4.2.2. D | RAD21-mAC | #1 - 0 μ M - 6 h ^{AUX} | 16 | 80.95 | 89.28 | 27.95 |
| | | #2 - 0 μ M - 6 h ^{AUX} | 7 | 75.47 | 64.02 | 22.92 |
| | | #3 - 0 μ M - 6 h ^{AUX} | 6 | 52.64 | 68.61 | 49.49 |
| | | #4 - 0 μ M - 6 h ^{AUX} | 27 | 47.82 | 63.60 | 43.63 |
| | | 0 μ M - 6 h ^{AUX} merged | 56 | 66.45 | 71.52 | 39.04 |
| | | #1 - 500 μ M - 6 h ^{AUX} | 12 | 136.37 | 221.01 | 182.78 |
| | | #2 - 500 μ M - 6 h ^{AUX} | 12 | 123.47 | 275.62 | 317.83 |
| | | #3 - 500 μ M - 6 h ^{AUX} | 28 | 136.78 | 164.62 | 130.96 |
| | | #4 - 500 μ M - 6 h ^{AUX} | 28 | 145.52 | 258.55 | 235.71 |
| | | 500 μ M - 6 h ^{AUX} merged | 80 | 136.78 | 222.60 | 213.65 |
| 4.2.3. C | SA1 WT | #1 | 611 | 97.06 | 101.43 | 29.32 |
| | | #2 | 713 | 85.38 | 87.01 | 19.84 |
| | | #3 | 822 | 79.48 | 82.32 | 19.28 |
| | | merged | 2146 | 85.47 | 89.32 | 24.08 |
| | SA1 KO | #1 | 1759 | 31.41 | 34.23 | 9.20 |
| | | #2 | 1013 | 37.55 | 40.76 | 11.56 |
| | | #3 | 1564 | 31.31 | 33.84 | 9.17 |
| | | merged | 4336 | 32.38 | 35.62 | 10.20 |
| 4.2.4. B | SA1 WT | 0 Gy | 167 | 17.10 | 22.75 | 16.11 |
| | | 2 Gy | 80 | 72.15 | 81.11 | 33.37 |
| | | 5 Gy | 206 | 164.65 | 166.09 | 50.34 |
| | | 10 Gy | 106 | 220.07 | 214.38 | 78.94 |
| | SA1 KO | 0 Gy | 261 | 13.48 | 17.64 | 13.61 |
| | | 2 Gy | 188 | 62.63 | 68.39 | 27.81 |
| | | 5 Gy | 213 | 95.86 | 98.82 | 44.29 |
| | | 10 Gy | 267 | 188.02 | 196.17 | 59.60 |
| 4.2.4. D | SA1 WT | 2 Gy | 7 | 579 | 591.71 | 218.82 |
| | SA1 KO | 2 Gy | 10 | 257.50 | 292.40 | 96.72 |
| 4.2.4. E | SA1 WT | 2 Gy | 4142 | 0.035 | 0.069 | 0.089 |
| | SA1 KO | 2 Gy | 1369 | 0.003 | 0.035 | 0.080 |
| 4.2.4. F | SA1 WT | 2 Gy | 4142 | 1040.50 | 2441.60 | 3789.07 |
| | SA1 KO | 2 Gy | 1369 | 79 | 1208.53 | 3049.76 |

*n: number of cells (except n: number of foci in 3.2.1. E, 4.2.4. E, 4.2.4. F; n: number of X/Y chromosomes or ROIs in 3.2.3. B); **StDev: standard deviation;

cell line name abbreviations: HK = HeLa Kyoto, AID = mESC-AID-CTCF, ES14 = ES-E14TG2a; RAD21-mAC = HCT116-RAD21-mAC, RAD21-WT = HCT116 wild type, SA1 WT = iMEF SA1 WT, SA1 KO = iMEF SA1 KO.

sample names: # = biological replicate number, norm. = normalized, merged = pooled replicates, subtr. = background-subtracted, AUX = auxin, WA = auxin wash-off.

Supplementary Table ST5: esiRNA characteristics.

| Name | esiRNA cDNA target Sequence | Accession no. | Application | Reference | Thesis chapter |
|--|--|--|-----------------------------------|--|----------------|
| <p>EHU130111 Sigma-Aldrich MISSION® esiRNA targeting human CTCF</p> | <p>AACAGCAGGAGGGTCTGCTATCAGAGGTTA ATGCAGAGAAAGTGGTTGGTAATATGAAGC CTCCAAAGCCAACAAAAATTA AAAAGAAAAG GTGTAAGAAGACATTCCAGTGTGAGCTTT GCAGTTACACGTGTCCACGGCGTTCAAATTT GGATCGTCACATGAAAAGCCACACTGATGAG AGACCACACAAGTGCCATCTCTGTGGCAGGG CATTCAGAACAGTCACCTCCTGAGGAATCA CCTTAACACACACACAGGTA CTGCTCTCAC AAGTGCCAGACTGCGACATGGCCTTTGTGA CCAGTGGAGAATTGGTTCGGCATCGTCGTTA CAAACACACCCACGAGAAGCCATTCAAGTGT TCCATGTGCGATTACGCCAGTGTAGAAGTCA GCAAATTA AAAACGTACATTTCGCTCTCATA TGGAGAGCGTCCGTTTCAGTGCAGTTTGTGC AGTTATGCCAGCAGGGACACATACAAGCTGA AAAGGCACATGA</p> | <p>Ensembl: ENSG00000102974 NCBI: NM_006565.3</p> | <p>CTCF mRNA silencing</p> | <p>https://www.sigmaaldrich.com/catalog/product/sigma/ehu130111?lang=de&region=DE</p> | <p>3.1.</p> |
| <p>EHUEGFP Sigma-Aldrich MISSION® esiRNA targeting EGFP</p> | <p>GTGAGCAAGGGCGAGGAGCTGTTACCCGGGG TGTTGCCCATCTGGTCGAGCTGGACGGCGA CGTAAACGGCCACAAGTTCAGCGTGTCCGGC GAGGGCGAGGGCGATGCCACCTACGGCAAGC TGACCCTGAAGTTCATCTGCACCACCGGCAA GCTGCCCGTGGCCCTGGCCACCTCGTGACC ACCCTGACCTACGGCGTGCAGTGCTTACGCC GCTACCCCGACCACATGAAGCAGCAGACTT CTTCAAGTCCGCCATGCCGAAGGCTACGTC CAGGAGCGCACCATCTTCTTCAAGGACGACG GCAACTACAAGACCCGCGCGAGGTGAAGTT CGAGGGCGACACCCTGGTGAACCGCATCGAG CTGAAGGGCATCGACTTCAAGGAGGACGGCA ACATCCTGGGGCACAAGCTGGAGTACAATA CAACAGCCACAACGTCTATATCATGGCCGAC AAGCAGAAGAACGGCATCAAGGTGAACTTC AAGATCCGCCACAACATCGAGGACGGCAGCG TGCAGCTCGCCGACCACTACCAGCAGAACAC CCCCATCGGGACGGCCCCGTGCTGTGCCC GACAACCACTACCTGAGCACCCAGTCCGCCC TGAGCAAAGACCCCAACGAGAAGCGCGATCA CATGGTCTGCTGGAGTTCGTGACCGCCGCC GGGATCACTCTCGGCATGGACGAGCTGTA</p> | <p>UniProtKB: C5MKY7 GenBank: MK387175.1</p> | <p>mock control for knockdown</p> | <p>https://www.sigmaaldrich.com/catalog/product/sigma/ehu egfp?lang=de&region=DE</p> | <p>3.1.</p> |

| | | | | | |
|--|---|---|---------------------------------|--|-------------|
| <p>EMU044061</p> <p>Sigma-Aldrich</p> <p>MISSION® esiRNA</p> <p>targeting</p> <p>mouse CTCF</p> | <p>GTGGCAGAGCATTTCAGAACAGTGACCCTCCT GAGGAATCATCTGAACACACACACAGGTACT CGTCCTCACAAGTGCCCAGACTGCGATATGG CCTTTGTGACCAGTGGAGAATTGGTGCGGCA TCGTGTTATAAACACACTCATGAGAAACCA TTTAAGTGTTCATGTGTGATTATGCCAGTG TAGAAGTCAGCAAATTTAAAACGACACATTC GCTCTCATACTGGAGAGCGCCCGTTCCAGTG CAGTTTGTGCAGTTATGCCAGCAGGGACACA TACAAGCTGAAAAGGCATATGAGAACCCAT TCAGGGGAAAAACCTTATGAATGTTATATT TGTCACGCTCGGTTTACCCAGAGTGGTACCA TGAAGATGCACATTTTACAGAAGCACACAG AAAATGTGGCCAAATTTTATTGTCCCATTTG TGACACTGTCATAGCCCGAAAAAGTGATTTG GGTGTCCACTTGCGAAAGCAGCATTCTATA TTGAACAGGGCAAAAAATGTCGCTACTGTG ATGCTGTGTTTCATGAGCGATATGCTCTCAT CCAGCA</p> | <p>Ensembl: ENSMUSG000 00005698</p> <p>NCBI: NM_181322</p> | <p>CTCF mRNA silencing</p> | <p>https://www.sigmaaldrich.com/DE/de/product/sigma/emu044061</p> | <p>3.2.</p> |
|--|---|---|---------------------------------|--|-------------|

Supplementary Table ST6: Survival data.

| Figure | Cell line | # biological replicate / Sample | X-rays dose (Gy) | | | | | | | | | | |
|----------|-----------|--|----------------------|----------------------|----------------------|----------------------|----------------------|----------------------|----------------------|----------------------|----------------------|----------------------|----------------------|
| | | | 0 | 1 | 2 | 3 | 4 | 5 | 6 | 7 | 8 | 9 | 10 |
| 3.1.3. B | HK | #1 GFP ^{KD} raw* | 551 591 475 | 349 342 - | 304 287 - | 270 281 - | 251 222 - | 210 196 200 | 181 178 160 | 124 133 106 | 80 73 74 | 50 49 53 | 18 19 27 |
| | | #1 GFP ^{KD} norm.** | 1.02 1.10 0.88 | 0.65 0.63 - | 0.56 0.53 - | 0.50 0.52 - | 0.47 0.41 - | 0.39 0.36 0.37 | 0.34 0.33 0.30 | 0.23 0.25 0.20 | 0.15 0.14 0.14 | 0.09 0.09 0.10 | 0.03 0.04 0.05 |
| | | #1 GFP ^{KD} mean #1 GFP ^{KD} error*** | 1.00 0.04 | 0.64 0.03 | 0.55 0.03 | 0.51 0.03 | 0.44 0.03 | 0.37 0.03 | 0.32 0.02 | 0.22 0.02 | 0.14 0.02 | 0.09 0.01 | 0.04 0.01 |
| | | #1 CTCF ^{KD} raw | 493 500 478 | 382 386 - | 263 268 - | 250 253 - | 171 167 - | 144 152 130 | 97 100 101 | 82 80 84 | 64 70 70 | 31 37 35 | 14 10 16 |
| | | #1 CTCF ^{KD} norm. | 1.01 1.02 0.97 | 0.78 0.79 - | 0.54 0.55 - | 0.51 0.52 - | 0.35 0.34 - | 0.29 0.31 0.27 | 0.20 0.20 0.21 | 0.17 0.16 0.17 | 0.13 0.14 0.14 | 0.06 0.08 0.07 | 0.03 0.02 0.03 |
| | | #1 CTCF ^{KD} mean #1 CTCF ^{KD} error | 1.00 0.05 | 0.78 0.04 | 0.54 0.03 | 0.51 0.03 | 0.34 0.03 | 0.29 0.02 | 0.20 0.02 | 0.17 0.02 | 0.14 0.02 | 0.07 0.01 | 0.03 0.01 |
| | | #2 GFP ^{KD} raw | 633 662 637 | 469 473 480 | 440 407 432 | 386 350 313 | 265 252 240 | 235 219 208 | 183 171 174 | 135 122 129 | 103 115 97 | 52 48 58 | 29 23 21 |
| | | #2 GFP ^{KD} norm. | 0.98 1.03 0.99 | 0.73 0.73 0.75 | 0.68 0.63 0.67 | 0.60 0.54 0.49 | 0.41 0.39 0.37 | 0.36 0.34 0.32 | 0.28 0.27 0.27 | 0.21 0.19 0.20 | 0.16 0.18 0.15 | 0.08 0.07 0.09 | 0.05 0.04 0.03 |
| | | #2 GFP ^{KD} mean #2 GFP ^{KD} error | 1.00 0.04 | 0.74 0.03 | 0.66 0.03 | 0.54 0.03 | 0.39 0.02 | 0.34 0.02 | 0.27 0.02 | 0.20 0.02 | 0.16 0.02 | 0.08 0.01 | 0.04 0.01 |
| | | #2 CTCF ^{KD} raw | 594 604 607 | 393 367 398 | 341 312 332 | 280 248 261 | 178 180 140 | 168 162 150 | 114 120 108 | 102 90 96 | 60 54 48 | 24 30 33 | 6 9 7 |
| | | #2 CTCF ^{KD} norm. | 0.99 1.00 1.01 | 0.65 0.61 0.66 | 0.57 0.52 0.55 | 0.47 0.41 0.43 | 0.30 0.30 0.23 | 0.28 0.27 0.25 | 0.19 0.20 0.18 | 0.17 0.15 0.16 | 0.10 0.09 0.08 | 0.04 0.05 0.05 | 0.01 0.01 0.01 |
| | | #2 CTCF ^{KD} mean #2 CTCF ^{KD} error | 1.00 0.04 | 0.64 0.03 | 0.55 0.03 | 0.44 0.03 | 0.28 0.02 | 0.27 0.02 | 0.19 0.02 | 0.16 0.02 | 0.09 0.01 | 0.05 0.01 | 0.01 0.00 |
| | | #3 GFP ^{KD} raw | 525 532 511 | 392 400 414 | 293 297 316 | 251 259 273 | 221 207 196 | 189 186 182 | 143 137 156 | 103 90 97 | 62 74 78 | 32 40 36 | 21 18 15 |
| | | #3 GFP ^{KD} norm. | 1.00 1.02 0.98 | 0.75 0.77 0.79 | 0.56 0.57 0.60 | 0.48 0.50 0.52 | 0.42 0.40 0.38 | 0.36 0.36 0.35 | 0.27 0.26 0.30 | 0.20 0.17 0.19 | 0.12 0.14 0.15 | 0.06 0.08 0.07 | 0.04 0.03 0.03 |

| | | | | | | | | | | | | | |
|-----------------------------|-------|-----------------------------|------|------|------|------|------|------|------|------|------|------|------|
| | | #3 GFP ^{KD} mean | 1.00 | 0.77 | 0.58 | 0.50 | 0.40 | 0.36 | 0.28 | 0.18 | 0.14 | 0.07 | 0.03 |
| | | #3 GFP ^{KD} error | 0.04 | 0.04 | 0.03 | 0.03 | 0.03 | 0.03 | 0.02 | 0.02 | 0.02 | 0.01 | 0.01 |
| | | #3 CTCF ^{KD} raw | 470 | 320 | 231 | 193 | 142 | 110 | 87 | 55 | 39 | 26 | 7 |
| | | | 457 | 335 | 213 | 187 | 146 | 98 | 72 | 68 | 48 | 24 | 5 |
| | | | 465 | 325 | 218 | 184 | 157 | 102 | 82 | 61 | 41 | 22 | 6 |
| | | #3 CTCF ^{KD} norm. | 1.01 | 0.69 | 0.50 | 0.42 | 0.31 | 0.24 | 0.19 | 0.12 | 0.08 | 0.06 | 0.02 |
| | | | 0.98 | 0.72 | 0.46 | 0.40 | 0.31 | 0.21 | 0.16 | 0.15 | 0.10 | 0.05 | 0.01 |
| | | | 1.00 | 0.70 | 0.47 | 0.40 | 0.34 | 0.22 | 0.18 | 0.13 | 0.09 | 0.05 | 0.01 |
| | | #3 CTCF ^{KD} mean | 1.00 | 0.70 | 0.48 | 0.41 | 0.32 | 0.22 | 0.17 | 0.13 | 0.09 | 0.05 | 0.01 |
| | | #3 CTCF ^{KD} error | 0.05 | 0.04 | 0.03 | 0.03 | 0.03 | 0.02 | 0.02 | 0.02 | 0.01 | 0.01 | 0.01 |
| 3.1.3. C | U2 OS | #1 GFP ^{KD} raw | 284 | 204 | 119 | 85 | 29 | 17 | 10 | 3 | 1 | 0 | 0 |
| | | | 251 | 213 | 112 | 93 | 22 | 13 | 7 | 4 | 3 | 0 | 0 |
| | | | 104 | 62 | 55 | 36 | 25 | 11 | 6 | 2 | 2 | 1 | 0 |
| | | | 186 | - | - | - | - | 18 | 9 | 4 | 1 | 1 | 0 |
| | | #1 GFP ^{KD} norm. | 1.38 | 0.99 | 0.58 | 0.41 | 0.14 | 0.08 | 0.05 | 0.01 | 0.00 | 0.00 | 0.00 |
| | | | 1.22 | 1.03 | 0.54 | 0.45 | 0.11 | 0.06 | 0.03 | 0.02 | 0.01 | 0.00 | 0.00 |
| | | | 0.50 | 0.30 | 0.27 | 0.17 | 0.12 | 0.05 | 0.03 | 0.01 | 0.01 | 0.00 | 0.00 |
| | | | 0.90 | - | - | - | - | 0.09 | 0.04 | 0.02 | 0.00 | 0.00 | 0.00 |
| | | #1 GFP ^{KD} mean | 1.00 | 0.77 | 0.46 | 0.35 | 0.12 | 0.07 | 0.04 | 0.02 | 0.01 | 0.00 | 0.00 |
| | | #1 GFP ^{KD} error | 0.07 | 0.06 | 0.05 | 0.04 | 0.02 | 0.02 | 0.01 | 0.01 | 0.01 | 0.00 | - |
| | | #1 CTCF ^{KD} raw | 230 | 163 | 114 | 74 | 33 | 10 | 3 | 2 | 1 | 0 | 0 |
| | | | 280 | 178 | 110 | 67 | 22 | 9 | 8 | 1 | 0 | 0 | 0 |
| | 128 | 66 | 86 | 64 | 26 | 12 | 6 | 2 | 2 | 0 | 0 | | |
| | 279 | - | - | - | - | 9 | 7 | 0 | 0 | 1 | 0 | | |
| #1 CTCF ^{KD} norm. | 1.00 | 0.71 | 0.50 | 0.32 | 0.14 | 0.04 | 0.01 | 0.01 | 0.00 | 0.00 | 0.00 | | |
| | 1.22 | 0.78 | 0.48 | 0.29 | 0.10 | 0.04 | 0.03 | 0.00 | 0.00 | 0.00 | 0.00 | | |
| | 0.56 | 0.29 | 0.38 | 0.28 | 0.11 | 0.05 | 0.03 | 0.01 | 0.01 | 0.00 | 0.00 | | |
| | 1.22 | - | - | - | - | 0.04 | 0.03 | 0.00 | 0.00 | 0.00 | 0.00 | | |
| #1 CTCF ^{KD} mean | 1.00 | 0.59 | 0.45 | 0.30 | 0.12 | 0.04 | 0.03 | 0.01 | 0.00 | 0.00 | 0.00 | | |
| #1 CTCF ^{KD} error | 0.07 | 0.05 | 0.04 | 0.04 | 0.02 | 0.01 | 0.01 | 0.00 | 0.00 | 0.00 | - | | |
| #2 GFP ^{KD} raw | 345 | 293 | 170 | 139 | 46 | 19 | 7 | 5 | 3 | 1 | 0 | | |
| | 350 | 301 | 187 | 141 | 40 | 21 | 9 | 3 | 1 | 1 | 0 | | |
| | 362 | 304 | 190 | 145 | 49 | 26 | 11 | 5 | 2 | 0 | 0 | | |
| #2 GFP ^{KD} norm. | 0.98 | 0.83 | 0.48 | 0.39 | 0.13 | 0.05 | 0.02 | 0.01 | 0.01 | 0.00 | 0.00 | | |
| | 0.99 | 0.85 | 0.53 | 0.40 | 0.11 | 0.06 | 0.03 | 0.01 | 0.00 | 0.00 | 0.00 | | |
| | 1.03 | 0.86 | 0.54 | 0.41 | 0.14 | 0.07 | 0.03 | 0.01 | 0.01 | 0.00 | 0.00 | | |
| #2 GFP ^{KD} mean | 1.00 | 0.85 | 0.52 | 0.40 | 0.13 | 0.06 | 0.03 | 0.01 | 0.01 | 0.00 | 0.00 | | |
| #2 GFP ^{KD} error | 0.05 | 0.05 | 0.04 | 0.03 | 0.02 | 0.01 | 0.01 | 0.01 | 0.00 | 0.00 | - | | |
| #2 CTCF ^{KD} raw | 300 | 214 | 133 | 88 | 29 | 13 | 4 | 0 | 1 | 0 | 0 | | |
| | 297 | 210 | 114 | 93 | 24 | 8 | 3 | 1 | 1 | 0 | 0 | | |
| | 333 | 206 | 125 | 95 | 31 | 9 | 5 | 2 | 0 | 0 | 0 | | |
| #2 CTCF ^{KD} norm. | 0.97 | 0.69 | 0.43 | 0.28 | 0.09 | 0.04 | 0.01 | 0.00 | 0.00 | 0.00 | 0.00 | | |
| | 0.96 | 0.68 | 0.37 | 0.30 | 0.08 | 0.03 | 0.01 | 0.00 | 0.00 | 0.00 | 0.00 | | |
| | 1.07 | 0.66 | 0.40 | 0.31 | 0.10 | 0.03 | 0.02 | 0.01 | 0.00 | 0.00 | 0.00 | | |

| | | | | | | | | | | | | | |
|-----------------------------|------------|-----------------------------|------|------|------|------|------|------|------|------|------|------|------|
| | | #2 CTCF ^{KD} mean | 1.00 | 0.68 | 0.40 | 0.30 | 0.09 | 0.03 | 0.01 | 0.00 | 0.00 | 0.00 | 0.00 |
| | | #2 CTCF ^{KD} error | 0.06 | 0.05 | 0.04 | 0.03 | 0.02 | 0.01 | 0.01 | 0.00 | 0.00 | - | - |
| | | #3 GFP ^{KD} raw | 194 | 158 | 97 | 68 | 25 | 12 | 5 | 0 | 1 | 0 | 0 |
| | | | 190 | 164 | 103 | 82 | 27 | 10 | 4 | 3 | 1 | 0 | 0 |
| | | | 187 | 160 | 99 | 79 | 20 | 9 | 7 | 1 | 0 | 0 | 0 |
| | | #3 GFP ^{KD} norm. | 1.02 | 0.83 | 0.51 | 0.36 | 0.13 | 0.06 | 0.03 | 0.00 | 0.01 | 0.00 | 0.00 |
| | | | 1.00 | 0.86 | 0.54 | 0.43 | 0.14 | 0.05 | 0.02 | 0.02 | 0.01 | 0.00 | 0.00 |
| | | | 0.98 | 0.84 | 0.52 | 0.42 | 0.11 | 0.05 | 0.04 | 0.01 | 0.00 | 0.00 | 0.00 |
| | | #3 GFP ^{KD} mean | 1.00 | 0.84 | 0.52 | 0.40 | 0.13 | 0.05 | 0.03 | 0.01 | 0.00 | 0.00 | 0.00 |
| | | #3 GFP ^{KD} error | 0.07 | 0.07 | 0.05 | 0.05 | 0.03 | 0.02 | 0.01 | 0.01 | 0.00 | - | - |
| | | #3 CTCF ^{KD} raw | 139 | 84 | 60 | 39 | 13 | 5 | 2 | 1 | 0 | 0 | 0 |
| | | | 141 | 85 | 57 | 35 | 12 | 4 | 3 | 0 | 0 | 0 | 0 |
| | | | 130 | 79 | 53 | 40 | 15 | 6 | 2 | 1 | 0 | 0 | 0 |
| | | #3 CTCF ^{KD} norm. | 1.02 | 0.61 | 0.44 | 0.29 | 0.10 | 0.04 | 0.01 | 0.01 | 0.00 | 0.00 | 0.00 |
| | | | 1.03 | 0.62 | 0.42 | 0.26 | 0.09 | 0.03 | 0.02 | 0.00 | 0.00 | 0.00 | 0.00 |
| | | | 0.95 | 0.58 | 0.39 | 0.29 | 0.11 | 0.04 | 0.01 | 0.01 | 0.00 | 0.00 | 0.00 |
| | | #3 CTCF ^{KD} mean | 1.00 | 0.60 | 0.41 | 0.28 | 0.10 | 0.04 | 0.02 | 0.00 | 0.00 | 0.00 | 0.00 |
| | | #3 CTCF ^{KD} error | 0.09 | 0.07 | 0.06 | 0.05 | 0.03 | 0.02 | 0.01 | 0.01 | - | - | - |
| 3.1.6. | AID | #1 - 0 μ M AUX raw | 309 | 263 | 226 | 170 | 154 | 142 | 118 | 85 | 73 | 52 | 24 |
| | | #1 - 0 μ M AUX norm. | 1.00 | 0.85 | 0.73 | 0.55 | 0.50 | 0.46 | 0.38 | 0.28 | 0.24 | 0.17 | 0.08 |
| | | #1 - 25 μ M AUX raw | 263 | 210 | 176 | 150 | 141 | 65 | 53 | 42 | 33 | 25 | 15 |
| | | #1 - 25 μ M norm. | 1.00 | 0.80 | 0.67 | 0.57 | 0.54 | 0.25 | 0.20 | 0.16 | 0.13 | 0.10 | 0.06 |
| | | #1 - 500 μ M AUX raw | 280 | 223 | 153 | 90 | 82 | 74 | 66 | 53 | 31 | 24 | 17 |
| | | #1 - 500 μ M AUX norm. | 1.00 | 0.80 | 0.55 | 0.32 | 0.29 | 0.26 | 0.24 | 0.19 | 0.11 | 0.09 | 0.06 |
| | | #1 - 1000 μ M AUX raw | 268 | 206 | 165 | 104 | 92 | 85 | 76 | 54 | 43 | 26 | 13 |
| | | #1 - 1000 μ M AUX norm. | 1.00 | 0.77 | 0.62 | 0.39 | 0.34 | 0.32 | 0.28 | 0.20 | 0.16 | 0.10 | 0.05 |
| | | #2 - 0 μ M AUX raw | 473 | 418 | 387 | 328 | 261 | 188 | 159 | 101 | 89 | 60 | 43 |
| | | #2 - 0 μ M AUX norm. | 1.00 | 0.88 | 0.82 | 0.69 | 0.55 | 0.40 | 0.34 | 0.21 | 0.19 | 0.13 | 0.09 |
| | | #2 - 25 μ M AUX raw | 430 | 375 | 353 | 270 | 212 | 184 | 137 | 110 | 69 | 56 | 30 |
| #2 - 25 μ M norm. | 1.00 | 0.87 | 0.82 | 0.63 | 0.49 | 0.43 | 0.32 | 0.26 | 0.16 | 0.13 | 0.07 | | |
| #2 - 500 μ M AUX raw | 433 | 383 | 324 | 279 | 214 | 171 | 115 | 101 | 74 | 67 | 20 | | |
| #2 - 500 μ M AUX norm. | 1.00 | 0.88 | 0.75 | 0.64 | 0.49 | 0.39 | 0.27 | 0.23 | 0.17 | 0.15 | 0.05 | | |
| #2 - 1000 μ M AUX raw | 430 | 358 | 323 | 257 | 234 | 150 | 130 | 95 | 55 | 42 | 20 | | |
| #2 - 1000 μ M AUX norm. | 1.00 | 0.83 | 0.75 | 0.60 | 0.54 | 0.35 | 0.30 | 0.22 | 0.13 | 0.10 | 0.05 | | |
| #3 - 0 μ M AUX raw | 430 | 370 | 340 | 270 | 240 | 153 | 124 | 97 | 76 | 57 | 36 | | |
| #3 - 0 μ M AUX norm. | 1.00 | 0.86 | 0.79 | 0.63 | 0.56 | 0.36 | 0.29 | 0.23 | 0.18 | 0.13 | 0.08 | | |
| #3 - 25 μ M AUX raw | 376 | 336 | 275 | 205 | 180 | 134 | 110 | 93 | 64 | 53 | 25 | | |
| #3 - 25 μ M norm. | 1.00 | 0.89 | 0.73 | 0.55 | 0.48 | 0.36 | 0.29 | 0.25 | 0.17 | 0.14 | 0.07 | | |
| #3 - 500 μ M AUX raw | 427 | 368 | 327 | 230 | 200 | 170 | 128 | 100 | 73 | 59 | 16 | | |
| | | | 1.00 | 0.86 | 0.77 | 0.54 | 0.47 | 0.40 | 0.30 | 0.23 | 0.17 | 0.14 | 0.04 |

| | | | | | | | | | | | | |
|--|--------------|--------------|--------------|--------------|--------------|--------------|--------------|--------------|--------------|--------------|--------------|--|
| #3 – 500 μM AUX norm. | | | | | | | | | | | | |
| #3 – 1000 μM AUX raw #3 – 1000 μM AUX norm. | 400 1.00 | 345 0.86 | 286 0.72 | 221 0.55 | 158 0.40 | 121 0.30 | 109 0.27 | 79 0.20 | 54 0.14 | 31 0.08 | 17 0.04 | |
| #4 – 0 μM AUX raw #4 – 0 μM AUX norm. | 399 1.00 | 354 0.89 | 324 0.81 | 270 0.68 | 194 0.49 | 160 0.40 | 121 0.30 | 91 0.23 | 77 0.19 | 44 0.11 | 37 0.09 | |
| #4 – 25 μM AUX raw #4 – 25 μM norm. | 284 1.00 | 249 0.88 | 233 0.82 | 175 0.62 | 135 0.48 | 118 0.42 | 86 0.30 | 66 0.23 | 47 0.17 | 32 0.11 | 18 0.06 | |
| #4 – 500 μM AUX raw #4 – 500 μM AUX norm. | 346 1.00 | 304 0.88 | 263 0.76 | 217 0.63 | 162 0.47 | 113 0.33 | 84 0.24 | 52 0.15 | 39 0.11 | 30 0.09 | 17 0.05 | |
| #4 – 1000 μM AUX raw #4 – 1000 μM AUX norm. | 338 1.00 | 230 0.68 | 210 0.62 | 166 0.49 | 117 0.35 | 101 0.30 | 84 0.25 | 52 0.15 | 30 0.09 | 21 0.06 | 19 0.06 | |
| 0 μM AUX mean 0 μM AUX error | 1.00 0.05 | 0.87 0.05 | 0.79 0.04 | 0.64 0.04 | 0.52 0.04 | 0.40 0.03 | 0.33 0.03 | 0.24 0.02 | 0.20 0.02 | 0.13 0.02 | 0.09 0.01 | |
| 25 μM AUX mean 25 μM error | 1.00 0.05 | 0.86 0.05 | 0.76 0.05 | 0.59 0.04 | 0.50 0.04 | 0.36 0.03 | 0.28 0.03 | 0.22 0.03 | 0.16 0.02 | 0.12 0.02 | 0.06 0.01 | |
| 500 μM AUX mean 500 μM AUX error | 1.00 0.05 | 0.86 0.05 | 0.71 0.04 | 0.53 0.04 | 0.43 0.03 | 0.35 0.03 | 0.26 0.03 | 0.20 0.02 | 0.14 0.02 | 0.12 0.02 | 0.05 0.01 | |
| 1000 μM AUX mean 1000 μM AUX error | 1.00 0.05 | 0.79 0.05 | 0.68 0.04 | 0.51 0.04 | 0.41 0.03 | 0.32 0.03 | 0.28 0.03 | 0.19 0.02 | 0.13 0.02 | 0.08 0.02 | 0.05 0.01 | |

*raw = raw number of colonies counted; ** norm. = normalized to the average of the respective unirradiated samples; ***mean & error = mean of normalized values and calculated relative error values (see calculation below), respectively shown as dots and error bars in the survival curves;
cell line name abbreviations: HK = HeLa Kyoto, AID = mESC-AID-CTCF;
sample names: # = biological replicate number, AUX = auxin.

$$\text{Relative error} = \text{mean normalized number of colonies} \times \frac{1}{\sqrt{(\text{mean raw number of colonies})}}$$

Supplementary Table ST7: Oligonucleotide characteristics.

| Name | Sequence [5' - 3'] | Application | Reference | Thesis chapter |
|------------|----------------------------------|---------------------------------------|------------------------------------|----------------|
| 6MW primer | CCG ACT CGA GNN NNN NAT GTG G | X chromosome FISH probe generation | (Telenius <i>et al.</i> , 1992) | 3.2. |
| 6AI primer | CCG ACT CGA GNN NNN TAC ACC | Y chromosome FISH probe generation | (Jentsch <i>et al.</i> , 2001) | 3.2. |

Supplementary Table ST8: Nucleotide characteristics.

| Name | Application | Detection | Cat # | Company | Thesis chapter |
|--|-------------------------------------|-----------------------|----------|---|----------------|
| Biotin-16-dUTP | Labeling of FISH probes | Streptavidin | - | Home made (Weber <i>et al.</i> , 2018) | 3.2. |
| dATP, dTTP, dCTP & dGTP | Generation of FISH probes/PCR | - | 10297018 | Thermo Fisher Scientific, Waltham, MA, USA | 3.2. |
| 5-Ethynyl-2'- deoxyuridine (EdU) | Pulse labeling of nascent DNA | ClickIT chemistry | E10415 | Thermo Fisher Scientific, Waltham, MA, USA | 3.2. |
| 5-Chloro-2'- deoxyuridine (ClU) | Pulse labeling of nascent DNA | Antibody detection | C6891 | Sigma-Aldrich, St Louis, MO, USA | 5.1. |

9. Annex

9.1. List of abbreviations

| | |
|----------|--|
| AAVS1 | <u>a</u> deno- <u>a</u> ssociated <u>v</u> irus integration <u>s</u> ite <u>1</u> |
| ABC | <u>A</u> TP <u>b</u> inding <u>c</u> assette |
| AID | <u>a</u> xin- <u>i</u> nducible <u>d</u> egron |
| AKB | <u>A</u> urora <u>k</u> inase <u>B</u> |
| APC/C | <u>a</u> naphase <u>p</u> romoting <u>c</u> omplex/ <u>c</u> yclosome |
| ATM | <u>a</u> taxia <u>t</u> elangiectasia <u>m</u> utated |
| ATR | <u>A</u> TM and <u>R</u> AD3-related |
| 53BP1 | <u>p</u> 53- <u>b</u> inding <u>p</u> rotein <u>1</u> |
| BRCA1 | <u>b</u> reast <u>c</u> ancer gene <u>1</u> |
| BSA | <u>b</u> ovine <u>s</u> erum <u>a</u> lbumin |
| Bub1 | <u>b</u> udding <u>u</u> ninhibited by <u>b</u> enzimidazole <u>1</u> |
| CBS | <u>C</u> TCF <u>b</u> inding <u>s</u> ite |
| 3C | <u>c</u> hromosome <u>c</u> onformation <u>c</u> apture |
| CDC5 | <u>c</u> ell <u>d</u> ivision <u>c</u> ontrol <u>5</u> |
| CDCA5 | <u>c</u> ell <u>d</u> ivision <u>c</u> ycle- <u>a</u> ssociated protein <u>5</u> |
| CdLS | <u>C</u> ornelia <u>d</u> e <u>L</u> ange <u>s</u> yndrome |
| cDSB | <u>c</u> lustered <u>D</u> SBs |
| ChIP-Seq | <u>c</u> hromatin <u>i</u> mmunoprecipitation- <u>s</u> equencing |
| CoAT | <u>C</u> ohesin <u>N</u> - <u>a</u> cetyl <u>t</u> ransferase |
| CoDAC | <u>C</u> ohesin <u>d</u> eacetylase |
| CTCF | <u>C</u> CTC-binding <u>f</u> actor |
| Ctf7 | <u>c</u> hromosome <u>t</u> ransmission <u>f</u> idelity <u>7</u> |
| DAPI | <u>4</u> ', <u>6</u> - <u>d</u> iamidino- <u>2</u> - <u>p</u> henyl <u>i</u> ndole |
| DDR | <u>D</u> NA <u>d</u> amage <u>r</u> esponse |
| DMEM | <u>D</u> ulbecco's <u>m</u> odified <u>E</u> agle's <u>m</u> edium |
| DNA-PKcs | <u>D</u> NA-dependent protein <u>k</u> inase, <u>c</u> atalytic <u>s</u> ubunit |
| DSB | <u>D</u> ouble <u>s</u> trand <u>b</u> reak |
| Eco1 | <u>e</u> stablishment of sister <u>c</u> ohesion <u>1</u> |
| EdU | <u>5</u> - <u>e</u> thynyl- <u>2</u> '- <u>d</u> eoxy <u>u</u> ridine |
| EM | <u>e</u> lectron <u>m</u> icroscopy |
| ESPL1 | <u>e</u> xtra <u>s</u> pindle <u>p</u> oles- <u>l</u> ike <u>1</u> |

| | |
|------------|---|
| FCS | <u>f</u> etal <u>c</u> alf <u>s</u> erum |
| FISH | <u>f</u> luorescent <i><u>i</u>n <u>s</u>itu</i> hybridization |
| FRAP | <u>f</u> luorescence <u>r</u> ecovery <u>a</u> fter <u>p</u> hoto <u>b</u> leaching |
| FSG | <u>f</u> ish <u>s</u> kin <u>g</u> elatin |
| GLOBLE | <u>G</u> iant- <u>L</u> oop- <u>B</u> inary- <u>L</u> Esion |
| Hawk | <u>H</u> EAT proteins <u>a</u> ssociated <u>w</u> ith <u>k</u> leisins |
| HDAC8 | <u>h</u> istone <u>d</u> eacetylase <u>8</u> |
| HEAT | <u>H</u> untingtin, <u>E</u> F3, <u>P</u> P2 <u>A</u> , <u>T</u> OR1 |
| Hi-C | <u>h</u> igh-throughput <u>c</u> hromosome <u>c</u> onformation <u>c</u> apture |
| HiP-HoP | <u>h</u> ighly <u>p</u> redictive <u>h</u> eteromorphi <u>c</u> <u>p</u> olymer |
| HR | <u>h</u> omologous <u>r</u> ecombination |
| IAA | 3- <u>i</u> ndole <u>a</u> cetic <u>a</u> cid |
| ICM | <u>i</u> nn <u>e</u> r <u>c</u> ell <u>m</u> ass |
| iDSB | <u>i</u> solated <u>D</u> SBs |
| iMEF | <u>i</u> mmortalized <u>m</u> ouse <u>e</u> mbryonic <u>f</u> ibroblast |
| IOD | <u>i</u> nter- <u>o</u> ri <u>g</u> in <u>d</u> istance |
| Irr1 | <u>i</u> rr <u>e</u> gular cell behavior <u>1</u> |
| Kite | <u>k</u> leisin <u>i</u> nteracting winged-helix <u>t</u> andem <u>e</u> lements |
| Ku70-Ku86 | <u>K</u> <u>u</u> , first two letters of the Japanese patient's surname |
| lncRNA | <u>l</u> ong <u>n</u> on <u>c</u> oding <u>R</u> NA |
| MAU2 | <u>m</u> aternal-effect <u>u</u> ncoordinated <u>2</u> |
| Mcd1 | <u>m</u> itotic <u>c</u> hromosome <u>d</u> eterminant <u>1</u> |
| MeCP2 | <u>m</u> ethyl- <u>C</u> pG-binding <u>p</u> rotein <u>2</u> |
| mESC | <u>m</u> ouse <u>e</u> mbryonic <u>s</u> tem <u>c</u> ell |
| MRN | <u>M</u> RE11- <u>R</u> AD50- <u>N</u> BS1 |
| MSY | <u>m</u> ale-specific <u>Y</u> |
| NBD | <u>n</u> ucleotide- <u>b</u> inding "head" <u>d</u> omain |
| NHEJ | <u>n</u> on- <u>h</u> omologous <u>e</u> nd- <u>j</u> oining |
| NIPBL | <u>n</u> ipped- <u>B</u> - <u>l</u> ike protein |
| PAR | <u>p</u> seudo <u>a</u> utosomal <u>r</u> egion |
| PARP-1 | <u>p</u> oly[<u>A</u> D <u>P</u> - <u>r</u> ibose] <u>p</u> olymerase <u>1</u> |
| PARylation | <u>p</u> oly[<u>A</u> D <u>P</u> - <u>r</u> ibosyl]ation |
| PBS | <u>p</u> hosphate- <u>b</u> uffered <u>s</u> aline |

| | |
|------------|---|
| Pds1/5 | precocious <u>d</u> issociation of <u>s</u> isters <u>1</u> or <u>5</u> |
| Plk1 | polo- <u>l</u> ike <u>k</u> inase <u>1</u> |
| PP1/2A | Protein phosphatase <u>1</u> or <u>2A</u> |
| PRC1/2 | Polycomb repressive <u>c</u> omplex <u>1</u> or <u>2</u> |
| PSF | point <u>s</u> pread <u>f</u> unction |
| PTTG1 | pituitary <u>t</u> umor- <u>t</u> ransforming gene <u>1</u> protein |
| RAD | <u>R</u> IF1- <u>a</u> ssociated <u>d</u> omain |
| RAD21/51 | radiation-sensitive mutant <u>21</u> or <u>51</u> |
| RD | replication <u>d</u> omain |
| RFi | replication units or nano- <u>f</u> oci |
| RIF1 | <u>R</u> ap1- <u>i</u> nteracting- <u>f</u> actor- <u>1</u> |
| ROI | region <u>o</u> f <u>i</u> nterest |
| ROS | reactive <u>o</u> xygen <u>s</u> pecies |
| RPA-ATRIP | replication <u>p</u> rotein <u>A</u> - <u>A</u> TR- <u>i</u> nteracting <u>p</u> rotein |
| RSC | remodels the <u>s</u> tructure of <u>c</u> hromatin complex |
| RT | replication <u>t</u> iming |
| RTD | replication <u>t</u> iming <u>d</u> ecision point |
| SAC | spindle <u>a</u> ssembly <u>c</u> heckpoint |
| 3D-SIM | <u>3D</u> -structured <u>i</u> llumination <u>m</u> icroscopy |
| SBS | <u>s</u> trings and <u>b</u> inders <u>s</u> witch model |
| Scc1/3 | <u>s</u> ister <u>c</u> hromatid <u>c</u> ohesion <u>1</u> or <u>3</u> |
| SCF | <u>S</u> kp1, <u>C</u> ullin and <u>F</u> -box |
| Sgo1 | <u>S</u> hugoshin <u>1</u> |
| Smc | structural <u>m</u> aintenance of <u>c</u> hromosomes |
| <i>SRY</i> | <u>s</u> ex <u>r</u> egion <u>Y</u> |
| SSB | <u>s</u> ingle <u>s</u> trand <u>b</u> reak |
| SSC | <u>s</u> aline- <u>s</u> odium <u>c</u> itrate |
| STAG1/2 | <u>s</u> tromal <u>a</u> ntigen (SA1/2) |
| STED | <u>s</u> timulated <u>e</u> mission <u>d</u> epletion |
| STORM | <u>s</u> tochastic <u>o</u> ptical <u>r</u> econstruction <u>m</u> icroscopy |
| SUMO | <u>s</u> mall <u>u</u> biquitin-like <u>m</u> odifier |
| SWI/SNF | <u>s</u> witch/ <u>s</u> ucrose <u>n</u> on-fermentable |
| TAD | topologically <u>a</u> ssociated <u>d</u> omain |

| | |
|-------------|---|
| TSPY | testis-specific protein <u>Y</u> |
| WAPL | <u>w</u> ings <u>a</u> part- <u>l</u> ike |
| WHD | <u>w</u> inged- <u>h</u> elix <u>d</u> omain |
| Xa | <u>a</u> ctive <u>X</u> chromosome |
| XCI | <u>X</u> chromosome <u>i</u> nactivation |
| Xi | <u>i</u> nactive <u>X</u> chromosome |
| <i>Xic</i> | <u>X</u> - <u>i</u> nactivation <u>c</u> enter locus |
| <i>Xist</i> | <u>X</u> - <u>i</u> nactive <u>s</u> pecific <u>t</u> ranscript |
| <i>Xite</i> | <u>X</u> - <u>i</u> nactivation <u>i</u> ntergenic <u>t</u> ranscription <u>e</u> lements |
| Xp | <u>p</u> aternally-inherited <u>X</u> chromosome |

9.2. List of figures

Main figures:

| | |
|---|----|
| 1.1. Hierarchical folding of DNA through chromatin organization and major hallmarks. | 2 |
| 1.2. Timeline of measurements and modeling of chromatin structures. | 7 |
| 1.3. Timeline of measurements and concepts of chromatin functions. | 14 |
| 2.1. Do the chromatin architectural proteins CTCF and cohesin affect genomic functions by structuring chromatin domains? | 18 |
| 3.1.1. Genome size and CTCF basal levels differ in HeLa Kyoto and U2OS. | 23 |
| 3.1.2. CTCF knockdown is efficiently achieved in 24 hours in HeLa Kyoto and U2OS. | 25 |
| 3.1.3. Radiosensitivity is increased and relative survival is decreased upon CTCF depletion. | 27 |
| 3.1.4. GLOBLE predictions of clonogenic survival upon different levels of CTCF depletion in HeLa Kyoto and U2O cells, in comparison to the experimental data. | 30 |
| 3.1.5. Degron system validation in mESC-AID-CTCF cells. | 32 |
| 3.1.6. Clonogenic assay of mESC-AID-CTCF cells upon auxin-induced CTCF depletion and irradiation. | 33 |
| 3.1.7. GLOBLE predictions of clonogenic survival upon different levels of auxin-induced CTCF depletion in mESC-AID-CTCF cells, in comparison to the experimental data. | 34 |
| 3.1.8. GLOBLE predictions of radiation sensitivity analyzing the impact of CTCF depletion on differentially sized control chromatin domains. | 35 |
| 3.1.9. Lower CTCF levels lead to less chromatin domains and higher probability that DSBs will not be separated into different chromatin domains (cDSBs). | 37 |
| 3.2.1. CTCF is enriched at the time and at the sites of DNA replication. | 51 |
| 3.2.2. CTCF depletion impairs cell cycle and S-phase progression in mammalian cells. | 53 |
| 3.2.3. CTCF is enriched at the replicating Xi and Y chromosomes and its depletion impairs the synchrony of Y replication. | 56 |
| 4.1.1. Cohesin components and conformations within the ATP cycle. | 71 |
| 4.1.2. Cohesin major functions. | 75 |
| 4.1.3. Models of chromatin loop extrusion by cohesin. | 78 |
| 4.2.1. Cohesin major component RAD21 is efficiently depleted up to 10% in HCT116-RAD21-mAC cells. | 80 |
| 4.2.2. Cohesin is essential to regulate chromatin loop sizes. | 82 |

| | |
|--|-----|
| 4.2.3. SA1 KO validation in iMEF SA1 KO cells. | 84 |
| 4.2.4. The signaling of DNA damage is impaired in iMEF SA1 KO cells. | 85 |
| 5.1. DNA replication and repair units in human HeLa Kyoto cells using 3D-structured illumination microscopy. | 97 |
| 6.1. CTCF and cohesin orchestrate the spatio-temporal regulation of global genomic functions by structuring chromatin into functional loops and domains. | 103 |
| Supplementary figures: | |
| SF1: Image analysis pipeline for high-content wide-field images. | 137 |
| SF2: Boxplot data visualization. | 139 |
| SF3: Colony formation images. | 140 |
| SF4: Survival curves and modeling predictions with equal y axis. | 141 |
| SF5: Time course validation of the CTCF-degron kinetics. | 142 |
| SF6: Anti-colocalization of CTCF and not replicating sex chromosomes. | 144 |
| SF7: mAID validation relative to Y chromosome experiments. | 145 |
| SF8: Image analysis pipeline for RAD21 degron validation. | 146 |
| SF9: Quantification of RAD21 depletion: single replicates. | 148 |
| SF10: DNA halo area in RAD21-depleted cells: single replicates. | 149 |
| SF11: Images of SA1 WT/KO iMEF cells after X-rays and γ H2AX detection. | 150 |

9.3. List of tables

Main tables:

| | |
|--|----|
| 1.1. Sizes of structural chromatin units measured with different methods. | 4 |
| 1.2. Sizes of functional chromatin units measured with different methods. | 12 |
| 3.1. Parameters that were used in the GLOBLE model for prediction of the impact of CTCF depletion. | 29 |
| 3.2. Equations of the GLOBLE model applied to CTCF depletion. | 44 |
| 4.1. Protein subunits of the cohesin complex and its regulators in human and budding yeast. | 69 |

Supplementary tables:

| | |
|--|-----|
| ST1 Cell line characteristics. | 151 |
| ST2 Primary and secondary antibody characteristics. | 152 |
| ST3 Imaging system characteristics. | 153 |
| ST4 Plot statistics. | 154 |
| ST5 esiRNA characteristics. | 163 |
| ST6 Survival data. | 165 |
| ST7 Oligonucleotide characteristics. | 169 |
| ST8 Nucleotide characteristics. | 169 |

9.4. Declaration - Ehrenwörtliche Erklärung

Ich erkläre hiermit ehrenwörtlich, dass ich die vorliegende Arbeit entsprechend den Regeln guter wissenschaftlicher Praxis selbstständig und ohne unzulässige Hilfe Dritter angefertigt habe.

Sämtliche aus fremden Quellen direkt oder indirekt übernommenen Gedanken sowie sämtliche von Anderen direkt oder indirekt übernommenen Daten, Techniken und Materialien sind als solche kenntlich gemacht. Die Arbeit wurde bisher bei keiner anderen Hochschule zu Prüfungszwecken eingereicht. Die eingereichte elektronische Version stimmt mit der schriftlichen Version überein.

Darmstadt, den 06.10.2022

Stefania Mamberti



9.5. Own and external contributions

All experiments were conceived and performed by me, except for the following:

Dr. Michael Scholz (GSI Helmholtzzentrum für Schwerionenforschung, Darmstadt, Germany) conceived our publication on the impact of CTCF on radiosensitivity together with Prof. Dr. M. Cristina Cardoso, Dr. Alexander Rapp and myself, and performed physical modeling and survival predictions based on my experimental results relative to Chapter 3.1. (Figures 3.1.4., 3.1.7., 3.1.8. and Supplementary Figure SF4 C – D).

During their Bachelor thesis internships under my direct supervision, Alexandra Clemens and Marlisa Helen Ködel respectively performed the experiments relative to Figure 3.2.2. and Figure 3.2.1. C – E.

Andreas Maiser (Ludwig-Maximilians-Universität LMU, Munich, Germany) kindly performed the 3D SIM imaging of my samples relative to Figure 5.1.

Dr. Cathia Rausch (Technische Universität TU, Darmstadt, Germany) performed the preparation of FISH probes for the painting of the X and Y chromosomes that I used to perform the experiments relative to Figure 3.2.3. and Supplementary Figure SF6.

mESC-AID-CTCF cells were kindly provided by Elphège P. Nora and Benoit G. Bruneau, Gladstone Institute of Cardiovascular Disease, San Francisco, USA.

HCT116-RAD21-mAC cells were kindly provided by Masato Kanemaki, National Institute of Genetics, Mishima, Japan.

SA1 WT and SA1 KO iMEF cells and the anti-SA1 primary antibody were kindly provided by Ana Losada, Centro Nacional de Investigaciones Oncológicas (CNIO), Madrid, Spain.

9.6. Acknowledgements

I am immensely thankful to Prof. Dr. M. Cristina Cardoso for welcoming me in her own lab. Thank you for accepting me as a PhD student despite my previous absolute lack of experience with mammalian cell cultures and fluorescent microscopy, it has been a dream to me to access this fluorescent microscopic world. Thank you for the great trust and freedom of movement that you give to any PhD student, it was a huge gift to be able to experiment “anything” I was curious about. Thank you for all the training with teaching, meetings, seminars, and for always being open to never ending discussions about chromatin loops which at times reached a metaphysical level. Thank you for all the constructive kicking, the loud laughs, the deep patience and the reassuring speeches too. Thank you for all the knowledge and wisdom you openly gifted to me, from the biological to the career and private issues.

I am really grateful to Prof. Dr. Gisela Taucher-Scholz for accepting to be my second supervisor. Thank you for the enthusiastic interest you have always shown to my project, for the nice scientific discussions and for your kindness in suggesting possible thesis developments.

I am very grateful to Prof. Dr. Alexander Löwer and to Prof. Dr. Barbara Drossel for accepting the roles of third and fourth thesis supervisors, respectively, and to have added important points of view for the initial development of my thesis project, which allowed me to focus the future work in relevant directions. Thank you Prof. Dr. Alexander Löwer also for the kind words of support about project management, for helping me and Ksenia in the organization of one of our GRK1657 retreats and for offering us the opportunity to invite Dr. Britta Mädge, previous Cell editor now in DFG.

I am very thankful to Prof. Dr. Burkhard Jakob for accepting my sudden request to take over the role of Prof. Dr. Gisela Taucher-Scholz in the last months of my PhD. Thank you for the exchanges of ideas during our time within the GRK1657 and for the friendly chat about science and career options we had on our way back to Darmstadt from one of our retreats in Kleinwalsertal.

I am really grateful to Prof. Dr. Helle Ulrich and Prof. Dr. Dominik Niopek for accepting to join the PhD examination committee for the evaluation of my thesis. Thank you for your contribution, I am sure we will have interesting discussions during my thesis defense.

Thanks to Alexandra Clemens and Marlisa Helen Ködel for having chosen me as supervisor for their Bachelor thesis internship and hence giving me the opportunity to improve my planning, managing and teaching skills. Thanks also to my girls’ squad of the MTB10 (2017) practical course, it was a funny adventure in my very early months of PhD. I know I expected a lot from all of you. Thank you for your contribution to the development of my project, I hope we have grown together in this.

Thank you Katrin for always having a smile for anyone, for your humor, for having patiently dealt with my allergy to bureaucracy and for all the help with any private issue too.

Thank you Anne, Manu and Diana for your irreplaceable technical support and for being an excellent emotional buffering system for the oscillating mood of the whole lab. No words would ever be enough.

Thank you Alex for all the help with basically anything in the lab, from experiment planning, through microscopy and analysis, till finding the key points in scientific discussions. From the earlier days of

my PhD when you tutored me for my very first immunostaining till my last day in the lab when we cheered for our manuscript being accepted.

Thanks to all the present and past PostDocs of the lab for sharing your expertise and advices, and for the chats about science and career. You all are an important piece of the lab puzzle.

Thanks to all the present and past PhD fellows of the lab, it has been a pleasure to share this path with you. No need to say, you became a lovely extravagant family for me in Darmstadt.

I am grateful to the whole Graduate College of Radiation Biology GRK1657 for having created such a friendly environment for networking and collaborations, especially important in the first years.

I am really grateful to Dr. Michael Scholz for the nice collaboration which started with a chat at my poster session at the GBS Meeting (Frankfurt, 2018) and brought us to publish together.

I am grateful to Andreas Maiser for his kindness in taking care of the 3D SIM imaging of my samples.

I am grateful to Dr. Katharina Brandstetter, Dr. med. Marion Cremer, Prof. Dr. Thomas Cremer, Prof. Dr. Heinrich Leonhardt and Dr. Hartmann Harz for our fruitful collaboration and for the interesting discussions we had when me and Katharina were preparing to present our paper together at a seminar hosted by the SPP2202 program.

9.7. Curriculum vitae

Stefania Mamberti

PERSONAL INFORMATION

Year and Place of Birth: 1990 Como (CO), Italy

Nationality: Italian

EDUCATION and WORKING EXPERIENCE

- 07/2017 – 12/2022 **Technische Universität Darmstadt**, Darmstadt, Germany
PhD in Cellular Biology
Laboratory of Prof. Dr. M. Cristina Cardoso
Project: Interplay of DNA replication, repair and chromatin: structure versus function
- 10/2020 – 12/2021 Research assistant contract by the Technische Universität Darmstadt
- 04/2020 – 09/2020 PhD scholarship funded by the Deutsche Forschungsgemeinschaft (DFG)
- 07/2017 – 03/2020 Graduate College in Molecular Radiation Biology GRK 1657,
PhD scholarship funded by the Deutsche Forschungsgemeinschaft (DFG)
- 03/2017 – 06/2017 **Università degli Studi di Pavia**, Pavia, Italy
Research scholarship funded by the Fondazione Bussolera Branca
Laboratory of Prof. Dr. Alessandra M. Albertini
Project: Screening of larvicidal activities of bacterial origin against the tiger mosquito
Aedes albopictus
- 10/2013 – 11/2015 **Università degli Studi di Pavia**, Pavia, Italy
Master of Science in Molecular Biology and Genetics
Laboratory of Prof. Dr. Cinzia Calvio
Experimental Thesis: γ -PGA hydrolases of phage origin in *Bacillus subtilis* and other
microbial genomes
- 09/2011 – 03/2012 **Ruprecht-Karls-Universität Heidelberg**, Heidelberg, Germany
LLP Erasmus Program
- 09/2009 – 09/2013 **Università degli Studi di Pavia**, Pavia, Italy
Bachelor of Science in Biological Sciences
Laboratory of Prof. Dr. Cinzia Calvio
Experimental Thesis: Functional annotation of a new gene of *B. subtilis*: from cloning
to the enzymatic activity
- 09/2004 – 07/2009 **Liceo Scientifico Paolo Giovio**, Como, Italy
High School Diploma in Science and Foreign Languages

LANGUAGES AND IT

Italian: mother tongue; **English, German, French:** fluent; **Spanish:** basic

Microsoft Office, Adobe Illustrator, RStudio, Volocity, ImageJ: intermediate level

PUBLICATIONS

Mamberti S., Pabba M. K., Rapp A., Cardoso M. C., Scholz M. (2022). The chromatin architectural protein CTCF is critical for cell survival upon irradiation-induced DNA damage. *International Journal of Molecular Sciences*; 23(7):3896. DOI: 10.3390/ijms23073896.

Barbieri G., Ferrari C., Mamberti S., Gabrieli P., Castelli M., Sassera D., Ursino E., Scoffone V. C., Radaelli G., Clementi E., Sacchi L., Ferrari E., Gasperi G., Albertini A. M. (2021). Identification of a novel *Brevibacillus laterosporus* strain with insecticidal activity against *Aedes albopictus* larvae. *Frontiers of Microbiology*; 12:624014. DOI: 10.3389/fmicb.2021.624014.

Cremer M., Brandstetter K., Maiser A., Rao S. S. P., Schmid V. J., Guirao-Ortiz M., Mitra N., Mamberti S., Klein K. N., Gilbert D. M., Leonhardt H., Cardoso M. C., Aiden E. L., Harz H., Cremer T. (2020). Cohesin depleted cells rebuild functional nuclear compartments after endomitosis. *Nature Communications*; 11(1):6146. DOI: 10.1038/s41467-020-19876-6.

Mamberti S. and Cardoso M. C. (2020). Are the processes of DNA replication and DNA repair reading a common structural chromatin unit? *Nucleus*; 11: 66-82. DOI: 10.1080/19491034.2020.1744415.

Mamberti S., Prati P., Cremaschi P., Seppi C., Morelli C. F., Galizzi A., Fabbi M., Calvio C. (2015). γ -PGA hydrolases of phage origin in *Bacillus subtilis* and other microbial genomes. *PLoS ONE*; 10(7): e0130810. DOI: 10.1371/journal.pone.0130810.

“Πάντες ἄνθρωποι τοῦ εἰδέναι ὀρέγονται φύσει.”

“All men by nature desire to know.”

Aristotélēs

*“Τῆς παιδείας ἔφη τὰς μὲν ρίζας εἶναι πικράς,
τὸν δὲ καρπὸν γλυκύν.”*

*“He said that the root of education is bitter,
but the fruit is sweet.”*

Dioghénēs Laértios

